Synthesis and Thermodynamic Integrated Machine Learning Modelling of Deep Eutectic Solvents: Applications in CO_2 Capture, Azeotrope Separation, and Biodiesel Production

Thesis submitted in partial fulfillment

for the Award of Degree

Doctor of Philosophy

by

Amit Kumar Gomey

Rajiv Gandhi Institute of Petroleum Technology

Jais-229304

20CE0003 **2026**

CERTIFICATE

It is certified that the work contained in the thesis titled ***"Synthesis and Thermodynamic Integrated Machine Learning Modelling of Deep Eutectic Solvents: Applications in CO_2 Capture, Azeotrope Separation, and Biodiesel Production"*** has been carried out under my supervision and that this work has not been submitted elsewhere for a degree.

It is further certified that the student has fulfilled all the requirements of Comprehensive, Candidacy, and SOTA.

Dr. Rakesh Kumar
(Supervisor)

DECLARATION BY THE CANDIDATE

I, ***Amit Kumar Gomey***, certify that the work embodied in this thesis is my own bonafide work and was carried out by me under the supervision of ***Dr. Rakesh Kumar*** from ***August 2020*** to ***January 2026***, at the *Department of Chemical and Biochemical Engineering,* Rajiv Gandhi Institute of Petroleum Technology, Jais. The matter embodied in this thesis has not been submitted for the award of any other degree. I declare that I have faithfully acknowledged and given credits to the research workers wherever their works have been cited in my work in this thesis. I further declare that I have not wilfully copied any other's work, paragraphs, text, data, results, etc., reported in journals, books, magazines, reports, dissertations, theses, etc., or available on websites and have not included them in this thesis and have not cited as my work.

Date:

Place: RGIPT, Jais, Amethi **Amit Kumar Gomey**

CERTIFICATE BY THE SUPERVISOR

It is certified that the above statement made by the student is correct to the best of my knowledge.

Dr. Rakesh Kumar

(Supervisor) Signature & Seal of Head of Department

CERTIFICATE

CERTIFIED that the work contained in the thesis titled **"*Synthesis and Thermodynamic Integrated Machine Learning Modelling of Deep Eutectic Solvents: Applications in CO_2 Capture, Azeotrope Separation, and Biodiesel Production*"** by **Mr. Amit Kumar Gomey** has been carried out under my supervision. It is also certified that he fulfilled the mandatory requirement of TWO quality publications that arose out of his thesis work.

It is further certified that the two publications (copies enclosed) of the aforesaid **Mr. Amit Kumar Gomey** have been published in the Journals indexed by –

(a) SCI

(b) SCI Extended

(c) SCOPUS

Dr. Rakesh Kumar

(Supervisor) (Convener,DPGC)

COPYRIGHT TRANSFER CERTIFICATE

Title of the Thesis: Synthesis and Thermodynamic Integrated Machine Learning Modelling of Deep Eutectic Solvents: Applications in CO_2 Capture, Azeotrope Separation, and Biodiesel Production

Name of the Student: Amit Kumar Gomey

Copyright Transfer

The undersigned hereby assigns to the Rajiv Gandhi Institute of Petroleum Technology Jais all rights under copyright that may exist in and for the above thesis submitted for the award of the **"DOCTOR OF PHILOSOPHY".**

Date:

Place: RGIPT, Jais, Amethi **Amit Kumar Gomey**

Note: However, the author may reproduce or authorize others to reproduce material extracted verbatim from the thesis or derivative of the thesis for the author's personal use provided that the source and the Institute's copyright notice are indicated

---

To Papa, Mummy, and Moti

—the steady state in all my chaos.

Acknowledgement

It brings me immense joy to finally arrive at the moment when I can present my doctoral thesis. Before I proceed, I pay my humble respects to the *great visionary* whose foresight and enduring legacy laid the foundation for my journey. I am deeply conscious that I stand here today only because of the path he paved.

I extend my deepest and most sincere appreciation to my doctoral supervisor, *Dr. Rakesh Kumar*, for his unwavering guidance and continuous encouragement throughout my research journey. His open-minded approach allowed me the scientific freedom to explore my own ideas, while his patience served as a steady anchor during the challenging phases of my work. Working under his supervision has been an immense privilege.

I would like to acknowledge my RPEC committee members, *Prof. M. S. Balathanigaimani* (Department of Chemical and Biochemical Engineering) and, *Dr. Tushar Sharma* (Department of Petroleum Engineering) for their constructive feedback and valuable suggestions that significantly enhanced the quality and rigor of my research.

I would like to thank *Prof. Amit Ranjan, Dr. V. S. Sistla, Dr. Gunjan Kumar Agrahari, Dr. Deepak Dwivedi, Dr. Vivek Kumar, Dr. Arvind Kumar,* and *Dr. K. G. Biswas* for their valuable contributions to my learning and development during my time at the institute.

I place on record my sincere thanks to the Head of the Department, Chemical and Biochemical Engineering, for providing the infrastructure and resources that fueled this research.

I am profoundly grateful to my senior, *Dr. Mohd Belal Haider*, who has been instrumental in guiding me through the intricacies of research. He was the craftsman who taught me the tools of the trade, from the first experiment to the final full stop of a manuscript and guided me through the maze of academic publishing.

My heartfelt thanks go to my lab mates, particularly *Ajeet Kumar Prajapati*. He has been more than a colleague; he was my sanity keeper who saw through my anger, absorbed my frustrations, and always guided me toward the light. I also thank *Sunil Kumar Singh* and *Syed Saim Ali* for being the reliable hands that helped me through the rigors of experimental work.

I would like to express my sincere appreciation to my closest friends, *Sujeet Kumar Pandey, Suvadeep Panda,* and *Deepak Yadav*. The shared high-spirited evenings, and their unwavering support through thick and thin were the lifeline that made this journey not just bearable but truly memorable.

I also want to thank *Rohit Kumar Singh*, whose sharp intellect and smart techniques often challenged me to think sharply, and *Aash Mohammad*, my fellow Chemical Engineer, who shared not just his lunch but also his wisdom and time, and kept me sane. I also thank my batchmates *Niyamat Ullah Khan* and *Harikeshwar Pandey* for their friendship, support, and the light-hearted moments that made this journey more enjoyable.

I thank my seniors *Vinamra Bhushan Sharma* and *Yogendra Yadawa* for their valuable guidance. I also want to thank my colleagues *Ashish Yadav, Saurabh Mishra, Amarendra, Bhupendra, Nirmal, Waseem, Akanksha, Pooja, Ekansh Kumar* for their camaraderie, and *Siddharth Atal*, who has been like the younger brother I never had and whose respect and affection I deeply cherish.

I would like to thank the administrative staff of the department, particularly *Mr. Anuj Shrivastava*, who was more like a friend than just an office staff member. I extend my sincere appreciation to the non-teaching staff for their support*: Arun ji* and *Mahesh ji* for their valuable assistance during my Teaching Assistantship; *Rajesh* and *Chotu* for their diligence in maintaining the laboratory; and *Surjeet* for his efficiency in handling documentation and office workflow.

On a personal note, I would like to acknowledge *Jyotsna Rani Mallick*. Thank you for being the love of my life, and frequently, my favourite "headache." You have tested my patience as much as you have filled my heart, and I wouldn't have it any other way.

Above all, I owe an immeasurable debt to my family. My father, *Sri Satya Prakash Gomey*, whose progressive outlook and open-minded nature paved the way for my dreams. My mother, *Smt. Sumitra Gomey*, whose prayers and delicious food were the fuel that kept me going. And my little sister, *Ankita aka "Moti"*, who fulfils her duty as an annoying sibling but has always been there to care for our parents while I was away pursuing this goal.

This journey would have been impossible without the love, sacrifices, and encouragement of every person mentioned here. To each of you, I extend my deepest gratitude.

अनन्तपारं किल शब्दशास्त्रं

स्वल्पं तथायुर्बहवश्च विघ्नाः।

यत् सारभूतं तदुपासनीयं

हंसैर्यथा क्षीरमिवाम्बुमध्यात्॥

Table of Contents

List of Figures

List of Tables

Nomenclature

AARD	Absolute Average Relative Deviation	IEA	International Energy Agency
AMP	2-amino-2-methyl-1-propanol	IL	Ionic Liquid
ANN	Artificial Neural Network	IPCC	Intergovernmental Panel on Climate Change
ARD	Absolute Relative Deviation	IPA	Isopropyl Alcohol / Isopropanol
ASTM	American Society for Testing and Materials	LA	Levulinic Acid
BSFC	Brake Specific Fuel Consumption	LCA	Life Cycle Assessment
BTBAC	Benzyltributylammonium Chloride	LJR	Lydersen-Joback-Reid
BTE	Brake Thermal Efficiency	LODO	Leave-One-DES-Out
BTEAC	Benzyltriethylammonium Chloride	LTTM	Low Transition Temperature Mixture
CCUS	Carbon Capture, Utilization, and Storage	MAE	Mean Absolute Error
ChCl	Choline Chloride	MDEA	Methyldiethanolamine
CO	Carbon Monoxide	MEA	Monoethanolamine
CO_2	Carbon Dioxide	ML	Machine Learning
COSMO-RS	Conductor-like Screening Model for Real Solvents	MLP	Multilayer Perceptron
DEA	Diethanolamine	MOF	Metal-Organic Framework
DEG	Diethylene Glycol	MTPPBr	Methyltriphenylphosphonium Bromide
DES	Deep Eutectic Solvent	NO_x	Nitrogen Oxides
DMSO	Dimethyl Sulfoxide	NRTL	Non-Random Two-Liquid
DSC	Differential Scanning Calorimetry	PCT Pro	Pressure-Composition-Temperature Analyzer
[EMIM][BF_4]	1-ethyl-3-methylimidazolium tetrafluoroborate	PI	Performance Index
FA	Furfuryl Alcohol	PID	Proportional-Integral-Derivative
FFA	Free Fatty Acid	ppm	Parts Per Million

FTIR	Fourier Transform Infrared Spectroscopy
GB	Gradient Boosting
GBT	Gradient-Boosted Trees
GCN	Graph Convolutional Network
GNN	Graph Neural Network
HBA	Hydrogen Bond Acceptor
HBD	Hydrogen Bond Donor
HC	Hydrocarbon
HRR	Heat Release Rate
TAC	Total Annual Cost
TBAB	Tetrabutylammonium Bromide
TEG	Triethylene Glycol
TGA	Thermogravimetric Analysis
TPAB	Tetrapropylammonium Bromide
QSPR	Quantitative Structure-Property Relationship
R^2	Coefficient of Determination
RD	Relative Deviation
RF	Random Forest
RMSE	Root Mean Square Error
SHAP	SHapley Additive exPlanations
SQP	Sequential Quadratic Programming
SVR	Support Vector Regression
VCR	Variable Compression Ratio
VFT	Vogel-Fulcher-Tammann
VFTH	Vogel-Fulcher-Tammann-Hesse
VLE	Vapor-Liquid Equilibrium
WMO	World Meteorological Organization

Roman Symbols

a, b, c, d	Fitting parameters
A, B, C, D	Constants in property estimation equations
a_{ij}, a_{ji}	NRTL binary interaction parameters
b_{ij}, b_{ji}	NRTL temperature-dependent parameters
C_p	Heat capacity (J/mol·K)
D	Distillate flow rate (kmol/h)
E_a	Activation energy (kJ/mol)
F	Objective function

Greek Symbols

α	Nonrandomness parameter / Thermal expansion
β	Temperature exponent parameter
γ	Activity coefficient
Δ	Change/difference operator
ΔG	Gibbs free energy change (kJ/mol)
ΔS	Entropy change (J/mol·K)
η	Dynamic viscosity (mPa·s)
ν	Kinematic viscosity (m^2/s)

f	Fugacity (MPa)	ρ	Density (g/cm^3)
g^E	Molar excess Gibbs energy (kJ/mol)	σ	Surface tension (mN/m)
h	Leverage value	τ_{ij}	NRTL interaction parameter
h^*	Critical leverage threshold	ω	Acentric factor
H_x	Henry's constant (molar fraction basis)	φ	Fugacity coefficient
ΔH	Enthalpy of dissolution (kJ/mol)	**Subscripts**	
k_{ij}	Binary interaction parameter	c	Critical property
M_w	Molecular weight (g/mol)	calc	Calculated value
n	Refractive index / Number of groups	DES	Deep eutectic solvent
p	Number of descriptors	dis	Dissolution
P	Pressure (bar or MPa)	exp	Experimental value
P_c	Critical Pressure (bar)	free	Free volume
P_b	Boiling point pressure (bar)	i, j	Component indices
Q_c	Condenser duty (kW)	m	Molar basis
Q_r	Reboiler duty (kW)	**Superscripts**	
R	Universal gas constant (8.314 J/mol·K)	E	Excess property
T	Temperature (K)	∞	Infinite dilution
T_b	Boiling temperature (K)	*	Critical value/threshold
T_c	Critical temperature (K)	a	Footnote
T_g	Glass transition temperature (K)		
V_c	Critical volume (cm³/mol)		
V_m	Molar volume (cm³/mol)		
x	Mole fraction in liquid phase		
y	Mole fraction in vapor phase		
Z_c	Critical compressibility factor		

Preface

The thesis research originated from an interest in using green solvents for CO_2 capture. Initial efforts focused on establishing a reliable protocol for synthesizing pure DES. Various methods were tested, including synthesis under nitrogen, vacuum degassing, and argon blanketing. Through these trials, an optimized protocol was established to ensure solvent purity.

However, the early experimental phase faced significant challenges. Persistent leakage in the AMAR high-pressure sorption analyzer and the non-functionality of the PCT Pro equipment made the collection of reliable solubility data impossible. These equipment failures created a period of uncertainty regarding the experimental progression of the work.

To overcome this setback, a computational approach was adopted. A comprehensive literature review was conducted to compile a database of CO_2 solubility for 102 distinct DESs. It was recognized that this data could be used for systematic screening rather than simple compiling. Thermophysical properties were estimated using Group Contribution Methods in Microsoft Excel. This involved implementing complex nested formulas for the Modified Lydersen-Joback-Reid method, Haghbakhsh correlations, and Lorentz-Lorentz equations. This process provided a fundamental understanding of the thermodynamic equations and formed the basis for **Chapters 2 and 3**.

The availability of this dataset led to a key realization: machine learning could predict CO_2

solubility using simple thermophysical properties (like density and viscosity) rather than complex molecular descriptors. To implement this, Python programming was learned and applied to

develop Random Forest and Gradient Boosting models. These models achieved high prediction accuracy and offered a new methodology for solvent screening.

The experimental validation was performed using a High Pressure Sorption Analyser (PCT PRO). Based on the computational screening, eight novel DESs were synthesized and tested for high-pressure CO_2 solubility. As detailed in **Chapter 4**, this experimental work was supported by advanced analysis, including Quantitative Structure-Property Relationship (QSPR) modeling, SHAP analysis for feature importance, and the development of a Performance Index to balance absorption capacity against viscosity.

The scope of the research was expanded in **Chapter 5** for the separation of azeotropic mixtures, specifically the isopropanol-water azeotrope. Process simulations were conducted using Aspen Plus to compare the performance of DESs with conventional entrainers. During the peer-review process, a comprehensive technoeconomic analysis was required. The Aspen Economic Analyzer was mastered, and a full cost analysis was performed. The results demonstrated that the proposed DES-based process could significantly reduce total annual costs compared to conventional methods.

In **Chapter 6**, the application of DESs was extended to biofuel synthesis and their effect on fuel performance. Biodiesel was synthesized from neem oil using DES as a catalyst and tested in a variable compression ratio diesel engine. The study confirmed that the fuel met ASTM standards and analyzed its emission characteristics.

Finally, **Chapter 7** outlines the future scope of this research. Concepts were developed for using DES as electrolytes in energy storage applications. Additionally, the potential for suspending

graphene and Metal-Organic Frameworks (MOFs) in DES to enhance solubility was proposed, along with the investigation of DES as a functional coating material for selective separation.

This research demonstrates that experimental setbacks can be transformed into opportunities by developing complementary computational capabilities. The integration of property estimation, machine learning screening, experimental synthesis, and process-level economic evaluation provides a systematic framework for rational solvent design, offering a versatile approach for future industrial applications.

Chapter 1

Introduction

1.1. The novel green solvents for industrial applications

The intensification of industrial activities over the past century has significantly altered the Earth's atmospheric composition, with carbon dioxide concentrations rising from pre-industrial levels of approximately 280 ppm to 426.9 ppm as of December 2025[1]. Global energy-related CO_2 emissions reached 37.8 Gt in 2024, marking a continued upward trajectory despite international commitments to climate stabilization. The National Oceanic and Atmospheric Administration reported that Earth's average temperature has increased by 0.06°C per decade since the pre-industrial era (1850-1900), totalling a 1.1°C rise in global surface temperature, with 2024 recorded as the hottest year since 1850, confirmed by NASA, WMO, and NOAA[2-4]. These alarming consequences extend beyond heatwaves, droughts, extreme weather, and rising sea levels to encompass ocean acidification, biodiversity loss, food and water security threats, ecosystem collapse, and public health emergencies, demanding immediate technological interventions across multiple fronts, particularly in industrial sectors responsible for over seventy percent of anthropogenic CO_2 emissions[5], [6]. Fossil fuel combustion for electricity generation and heating accounts for roughly 30% of anthropogenic CO_2 emissions globally, as shown in **Figure 1.1**, with the cement, steel, and chemical industries contributing substantially through both energy consumption and process-inherent carbon release[7].

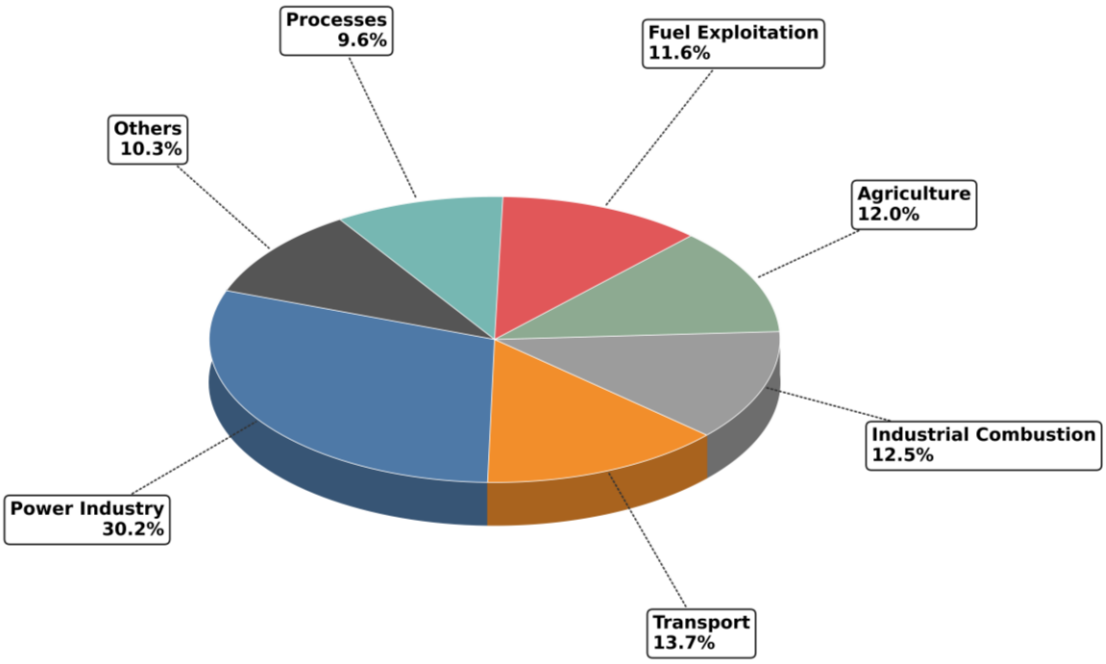

Figure 1.1 Global Greenhouse Gas Emissions by Sector (2024)

At the global scale, China remains the largest source of energy-related CO_2 emissions, while the United States ranks second, as shown in **Figure 1.2**, although emissions trajectories differ markedly between these economies, with growth persisting in China and structural declines observed in the United States.

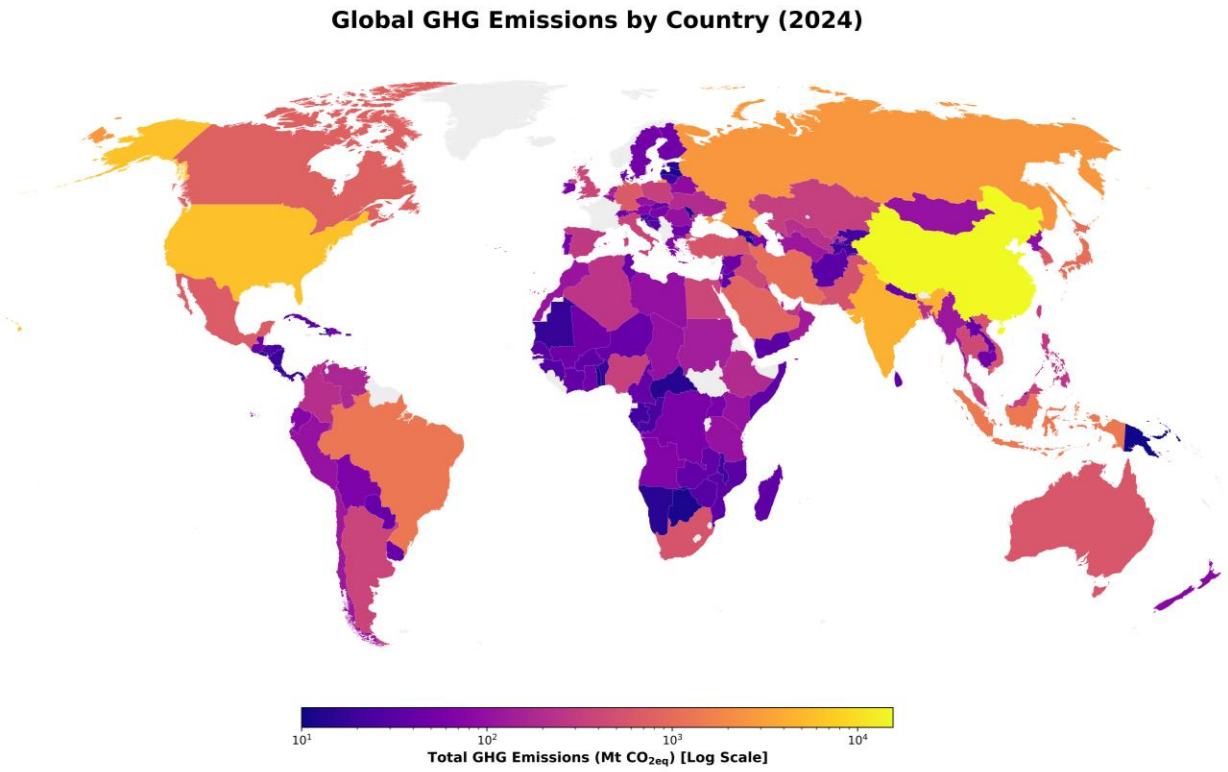

Figure 1.2 Global Greenhouse Gas Emissions by Country (2024)

Within this differentiated global landscape, India's trajectory exemplifies the challenge facing rapidly developing economies. While its absolute emissions remain significantly lower than those of China and the United States, India's per-capita CO_2 emissions have nearly doubled, increasing from approximately 1 tonne in 2000 to around 2 tonnes in 2022, as reported by the International Energy Agency, reflecting the persistent tension between economic growth imperatives and long-term environmental sustainability[8]. The International Energy Agency's Energy Technology Perspectives-2024 report projects that CO_2 emissions from energy-based industries will rise by 130% by 2050 if current fossil fuel dependency continues[7], [9]. Carbon capture, utilization, and storage (CCUS) technologies have emerged as essential components of any comprehensive climate

strategy, with studies demonstrating that excluding CO_2 capture from mitigation portfolios increases climate stabilization costs by approximately 70%.

Beyond carbon capture, chemical process industries face persistent separation challenges that consume disproportionate energy and generate substantial chemical waste. Distillation operations alone account for 40-70% of capital investment and operating costs in typical chemical complexes, yet many industrially significant separations are thermodynamically impossible through conventional distillation[10]. Azeotropic mixtures, compositions where vapor and liquid phases possess identical composition at equilibrium, cannot be separated beyond the azeotropic point regardless of reflux ratio or column configuration. The isopropanol-water system, for example, forms a minimum-boiling azeotrope at 87.5 wt% of isopropanol at atmospheric pressure[11]. Isopropanol serves as a critical cleaning solvent in pharmaceutical manufacturing, microelectronics, and precision optics production, with the global market projected to reach from USD 3.6 billion in 2025 to USD 4.6 billion by 2035[12]. Current industrial practice relies on energy-intensive pressure-swing distillation to shift azeotropic compositions. Alternatively, extractive distillation is employed using organic entrainers. While effective, solvents such as dimethyl sulfoxide (DMSO) and N-methylpyrrolidone (NMP) raise environmental and occupational concerns due to volatility, skin permeability, and regulatory classification, necessitating elaborate recovery infrastructure[11-14].

The biodiesel industry, which has grown to produce over 59 billion liters annually across Europe, North America, and Asia, faces similar technical bottlenecks in separating transesterification products[15-17]. Conventional processes using homogeneous base catalysts generate crude glycerol contaminated with soap, unreacted triglycerides, and sodium salts[18]. This necessitates water washing and neutralization steps that multiply both energy demand and waste volume. High-

free-fatty-acid feedstocks derived from used cooking oil cannot be processed directly without pre-treatment to remove free fatty acids through separate esterification reactions[20]. These constraints impose additional operational costs and environmental liabilities, thereby constraining the large-scale deployment of biodiesel as a sustainable transport fuel[21].

Just as distillation and extraction processes face thermodynamic and operational limits, the chemical absorption methods currently deployed for carbon capture are constrained by severe material limitations. Aqueous amine solutions-the industrial standard for post-combustion CO_2 capture-achieve high absorption rates through chemical reaction mechanisms. However, regeneration requires heating to 110-150°C, imposing a substantial energetic penalty[20-22]. A typical pulverized-coal-fired power plant equipped with 30 wt% monoethanolamine (MEA) capture technology consumes 3.5-4.0 gigajoules of thermal energy per tonne of CO_2 captured, reducing overall plant efficiency by 8-12%[25]. Additionally, amines suffer from oxidative degradation, equipment corrosion, and volatility[24]. Despite these operational and economic challenges, the strategic importance of CO_2 capture remains undisputed. IPCC assessments indicate that removing carbon capture from the climate mitigation portfolio could more than double the overall cost of achieving climate stabilization targets, underscoring the urgent need to develop more efficient, cost-effective, and environmentally benign capture technologies[26].

Ionic liquids (ILs) emerged in the 1990s as a potential solution, offering negligible vapor pressure and high thermal stability[27]. Room-temperature ionic liquids such as 1-butyl-3-methylimidazolium hexafluorophosphate ($[C_4mim][PF_6]$) attracted intensive research for their ability to absorb CO_2 up to 0.6 mole fraction at 8MPa[28]. However, practical deployment encountered formidable obstacles. Synthesis routes require multi-step reactions and extensive purification to remove halide byproducts[29]. Consequently, production costs, even at scale,

typically remain one to two orders of magnitude higher than conventional organic solvents. Moreover, concerns regarding toxicity, biodegradability, and overall environmental footprint have emerged from comprehensive sustainability assessments[30]. Furthermore, the high viscosity of many ionic liquids (often 50-100 times that of water) creates severe mass transfer limitations[31]. The initial characterization of ionic Liquids as 'green solvents' has been critically re-evaluated in light of lifecycle assessments (LCA), highlighting the significant environmental burdens associated with their synthesis and end-of-life disposal[30], [32], [33], [34], [35].

These limitations have catalyzed interest in novel deep eutectic solvents (DESs). First characterized by Abbott et al. in 2003, DESs comprise eutectic mixtures of hydrogen bond acceptors (HBAs) and hydrogen bond donors (HBDs) that spontaneously form liquids at ambient temperature[36]. DES synthesis requires only mixing and mild heating without chemical reactions or purification. With raw material costs often 10-20 times lower than ionic liquids and tunable physicochemical properties, DESs offer a unifying platform to address the limitations in carbon capture, azeotropic separations, and biofuel processing[37]. This thesis establishes the scientific foundation for their systematic design and optimization.

1.2. Deep eutectic solvents

Deep eutectic solvents (DESs) are broadly defined as solvents formed from a eutectic mixture of Lewis or Brønsted acids and bases, which can contain a variety of anionic and/or cationic species[38]. The concept was first formalized by Abbott et al. in 2003, who demonstrated that mixing a quaternary ammonium salt (the hydrogen bond acceptor, HBA) with a metal salt or hydrogen bond donor (HBD) yields a liquid with a melting point significantly lower than that of either individual component. The most commonly used DES comprised of choline chloride (ChCl)

and urea in a 1:2 molar ratio. While ChCl melts at 302°C and urea at 133°C, the resulting eutectic mixture remains liquid at 12°C, a melting point depression of nearly 130°C relative to an ideal mixture[39]. This behavior is attributed to substantial attractive interactions that exist between the HBA and HBD, typically in the form of hydrogen bonds, which contribute to charge delocalization and effectively frustrate the ability of the DES to freeze. From a thermodynamic perspective, this significant depression of the eutectic point temperature compared to an ideal mixture of the constituents implies that DESs are markedly non-ideal mixtures, characterized by a strong tendency of the components to mix with each other. The extent of this non-ideality is reflected in the negative molar excess Gibbs energy ($g^E<0$), which represents the difference between the actual molar Gibbs energy change upon mixing and that of a hypothetical ideal mixture at the same temperature, pressure, and composition[40].

The most extensively studied DESs utilize organic salts like choline chloride combined with organic HBDs such as amides, carboxylic acids, or alcohols. **Figure 1.3** and **Figure 1.4** illustrate the most common HBAs and HBDs utilized in contemporary DES research.

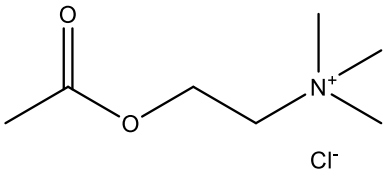

Acetylcholine chloride

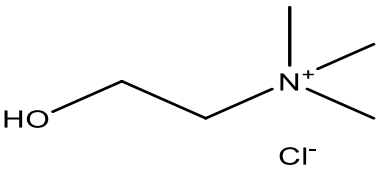

Choline chloride

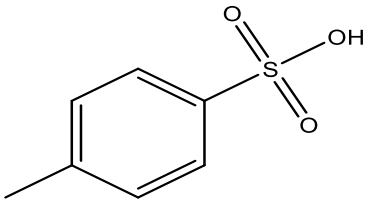

p-toluene sulfonic acid

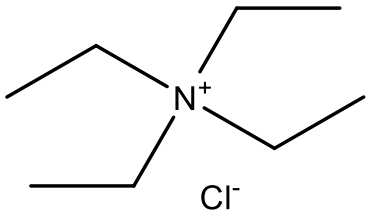

Tetraethylammonium chloride

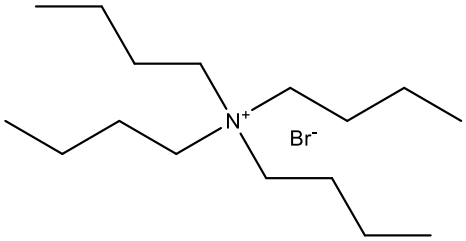

Tetrabutylammonium bromide

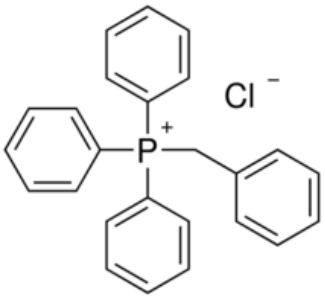

Benzyltriphenylphosphonium chloride

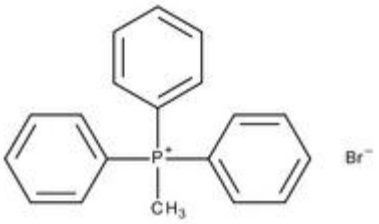

Methyl triphenyl phosphonium bromide

Figure 1.3 Molecular structures of common hydrogen bond acceptors

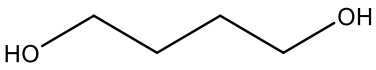

1,4-butanediol

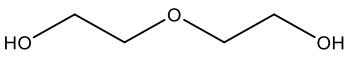

Diethylene glycol

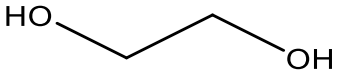

Ethylene glycol

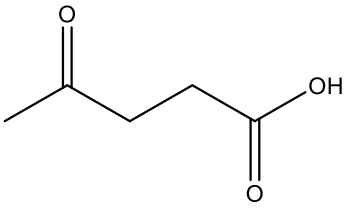

Levulinic acid

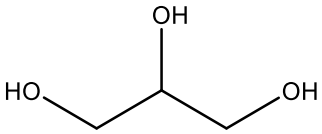

Glycerol

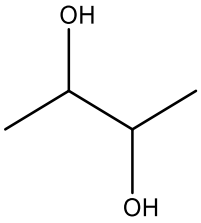

2,3-butanediol

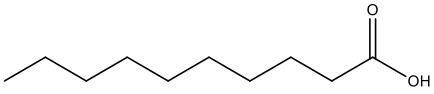

Decanoic acid

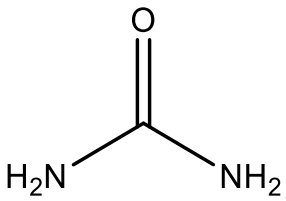

Urea

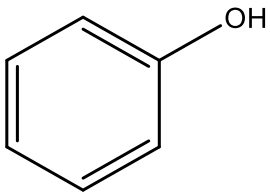

Phenol

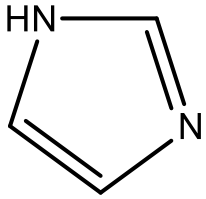

Imidazole

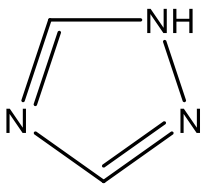

1,2,4-triazole

Triethylene glycol

Figure 1.4 Molecular structures of common hydrogen bond donors

1.3. CO_2 solubility in deep eutectic solvents

Li et al. studied the initial CO_2 solubility in a choline chloride and urea eutectic mixture. The DESs were prepared with molar ratios of 1:1.5, 1:2, and 1:2.5. The investigation was conducted at pressures of 13 MPa and temperatures of 313.15 K, 323.15 K, and 333.15 K[41]. Their research revealed that the solubility of carbon dioxide is affected by the molar ratio of deep eutectic solvents, with the highest solubility observed at a 1:2 molar ratio. Subsequent research focused mainly on the solubility of CO_2, with further studies conducted on other gases, including CO, CH_4, N_2, and SO_2. Garcia et al. published the initial review study on the CO_2 dissolution in deep eutectic solvents[42]. This field has experienced exponential growth in recent years.

The initial synthesis of DESs by Abbott et al. using ammonium salts marked the beginning of a research focus on these ammonium-based compounds[39]. An extensive investigation was undertaken to assess the solubility of carbon dioxide in various ammonium salts. The primary salt examined was choline chloride, with subsequent studies expanding to include tetra-butyl ammonium bromide, tetra-butyl ammonium chloride, and other related ammonium salts. Leron et al. explored the carbon dioxide solubility in Choline Chloride:2ethylene glycol (ethaline) and Choline Chloride:2Glycerol (glyceline) DESs [43], [44]. At 303.15 K and 5.86 MPa, ethaline achieved 3.13 mol/kg while glyceline reached 3.69 mol/kg. For comparison, [BMIM][PF_6] showed 3.98 mol/kg at 293.15 K and 4.75 MPa, indicating that DES performance is within the range of conventional ionic liquids[45], [46]. Lu et al. examined the synthesized deep eutectic solvents of levulinic acid (LA) and furfuryl alcohol (FA) as HBDs and choline chloride (ChCl) as the HBA. The solvents were produced in molar ratios of 3:1, 4:1, and 5:1 of HBD to HBA to investigate their effectiveness in capturing CO_2[47]. The study indicates that ChCl:Levulinic acid (LA)-based DESs exhibit the highest CO_2 solubility, which further increases as the molar ratio of HBD to HBA

increases. Chen et al. experimented to determine CO_2 dissolution in DESs made up of ChCl and dihydric alcohol[48]. ChCl-1,4-butanediol of molar ratio 1:3 DES demonstrated the most significant CO_2 solubility, whereas the ChCl:1,2-propanediol of molar ratio 1:4 DES exhibited the lowest, which indicates that the carbon dioxide solubility increases when the length of the alkyl chain of the hydrogen bond donor (HBD) increases. Furthermore, it was observed that as the molar ratio of HBD to HBA increased, the CO_2 solubility decreased. However, compared to the research done by Leron et al., it was clearly observed that ethaline (ChCl:2Ethylene Glycol) exhibits a higher CO_2 solubility capacity than dihydric alcohols.

Haider et al. studied 15 distinct DESs to study the CO_2 dissolution in them. These DESs were synthesised utilising ChCl and TBAB as the hydrogen bond acceptors. The study illustrates a direct relationship between the length of the HBA chain and the CO_2 solubility. Specifically, as the length of the HBA chain grows, the CO_2 absorption capability also increases[49]. Similarly, Sarmad et al. also found that a rise in the carbon atom in the alkyl chain length of HBA leads to a higher absorption of CO_2 [50].

Li et al. and Leron et al. investigated ChCl:urea DESs at molar ratios of 1:1.5, 1:2, and 1:2.5, finding that reline (ChCl:2urea) achieved the highest CO_2 absorption, comparable to imidazolium-based ionic liquids and surpassing both ethaline and glyceline[51], [52]. Water content significantly reduced CO_2 solubility in reline, limiting its applicability for aqueous systems.

Screening 17 DES formulations, Ali et al. established that amine-functionalized DESs outperformed glycol-based systems[53]. While increasing HBD chain length (ethanolamine → diethanolamine) decreased solubility for a given HBA, extending the HBA alkyl chain (choline chloride → tetrabutylammonium bromide) with constant HBD enhanced CO_2 uptake, revealing opposing structure-property relationships.

Task-specific DESs capable of chemical CO_2 binding were pioneered by Sze et al., who attributed enhanced solubility to alkyl carbonate formation via superbase-mediated deprotonation[54]. While ammonium-based systems dominate current research, their structural limitations-particularly viscosity increases upon CO_2 loading and restricted tunability-have prompted investigation of alternative cation architectures, notably phosphonium salts, which offer distinct electronic properties and expanded design space for optimizing physical absorption mechanisms.

Recent investigations by Ghaedi et al. revealed that phosphonium-based DESs achieve markedly higher CO_2 absorption capacities than their ammonium counterparts, a finding attributed to the larger ionic radius and enhanced polarizability of the phosphorus center[55], [56]. However, this cation class exhibits distinct structure-property relationships: while extended alkyl chains improve solubility in choline chloride systems, phosphonium-based DESs with longer hydrophobic chains show reduced CO_2 uptake, likely due to increased viscosity outweighing free-volume gains.

Haider et al. systematically compared methyltriphenylphosphonium bromide (MTPPhBr)-based DESs with conventional ethaline (ChCl:2EG), using polyethylene glycol homologs as HBDs[57]. The MTPPhBr:4DEG formulation achieved 0.062 mol CO_2/mol DES, 2.7-fold higher than ethaline (0.023 mol/mol) and 17% superior to MTPPhBr:4EG (0.053 mol/mol), demonstrating that polyethylene glycol chain extension enhances absorption when paired with bulky phosphonium cations (**Figure 1.5**). This synergy between cation size and HBD flexibility represents a key design principle absent in rigid ammonium architectures.

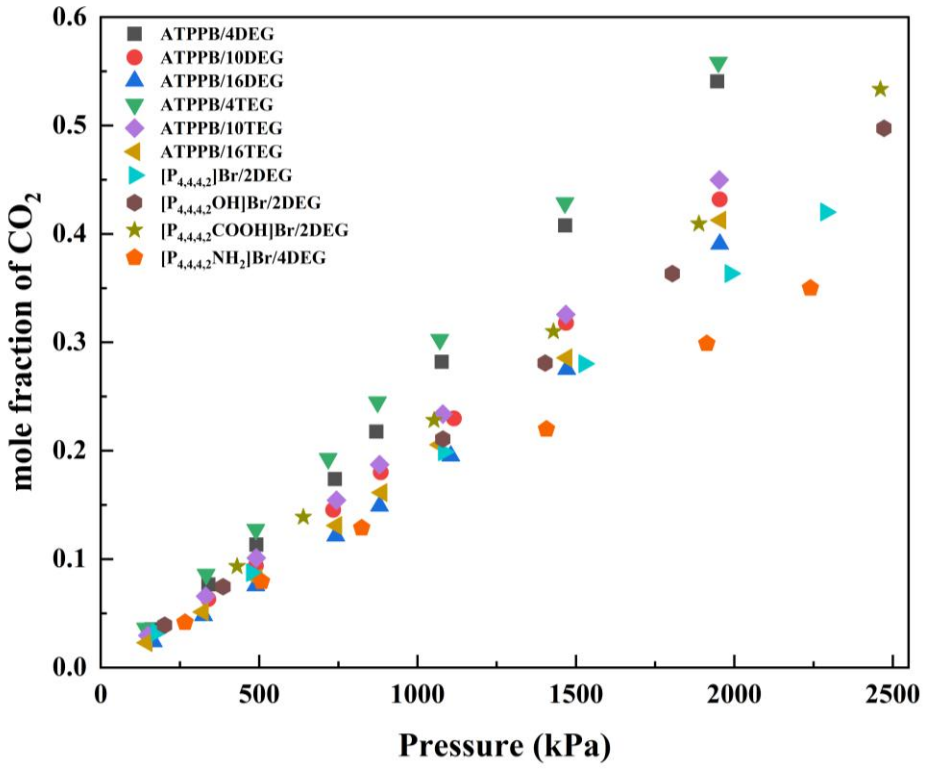

Figure 1.5 CO_2 solubility in DESs based on phosphonium salts at 303.15 K

Functional group modification further amplifies performance. Cui et al. grafted amino, hydroxyl, and carboxyl moieties onto phosphonium alkyl chains, with [P4,4,4,2COOH][Br]:DEG reaching 0.5335 mole fraction CO_2 at 2500 kPa and 303.15 K, K-among the highest reported for non-amine DESs[58]. The carboxyl-functionalized system likely enables dual physisorption-chemisorption pathways without the viscosity penalties of traditional amine solvents.

Beyond molecular design, phosphonium DESs exhibit emergent properties in hybrid materials. Ahmed et al. demonstrated that coating cerium oxide nanoparticles with phosphonium-based DESs increased CO_2 adsorption by 27% relative to pristine CeO_2, despite reduced BET surface area, a counterintuitive result suggesting that the DES layer creates favourable interfacial binding sites rather than merely blocking pores[59]. This finding opens pathways for DES-functionalized

adsorbents that combine the rapid kinetics of solid capture with the high selectivity of liquid absorption[59].

1.4. Machine Learning and neural network approach for the prediction of CO_2 in DES

The vast chemical space of DESs, arising from combinatorial HBA-HBD pairing, variable stoichiometry, and functional modifications, renders exhaustive experimental screening impractical. Machine learning (ML) has emerged as a transformative tool for accelerating solvent discovery by predicting physicochemical properties, identifying structure-performance relationships, and prioritizing candidates for synthesis, thereby reducing experimental costs and development timelines[60], [61]. This section examines the evolution of ML architectures applied to DES-CO_2 systems, from classical descriptor-based models to physics-informed neural networks and graph representations.

1.4.1. Descriptor-Based Models: Establishing Predictive Frameworks

Wang et al. pioneered quantitative structure-property relationship (QSPR) modelling for CO_2 absorption by compiling 1011 solubility measurements spanning 59 DESs (11 HBAs, 16 HBDs) across pressures of 0.036-12.73 MPa and temperatures of 293.15-343.15 K[62]. Employing a random forest (RF) regressor trained on molecular descriptors, their model achieved $R^2 = 0.9758$ and ranked feature importance as: pressure > HBA type > HBD type > molar ratio > temperature, revealing that thermodynamic driving forces dominate over compositional nuances. This hierarchy challenged the prevailing focus on HBD functionalization, redirecting attention toward operating conditions and cation selection.

Expanding this foundation, Mohan et al. curated a physisorption-focused dataset of 1973 data points covering 132 DESs (23 HBAs, 25 HBDs) with molar ratios from 1:1 to 1:16[63]. Their RF

model delivered exceptional performance (R^2 = 0.99, AARD = 2.72%, MAE = 0.087), demonstrating that purely physical absorption-often overlooked in favor of reactive amine systems-can be accurately predicted using structural and thermodynamic descriptors alone. The model's robustness across diverse stoichiometries underscores the viability of ML-guided design for non-reactive DESs.

1.4.2. Neural Network Architectures: Capturing Non-Linear Interactions

Recognizing the limitations of tree-based ensembles in capturing complex molecular interactions, Lemaoui et al. deployed a multilayer perceptron (MLP) trained on 2327 solubility measurements (0.31-320.71 g/kg CO_2) from 94 DESs with 150 unique compositions[64]. Critically, their inputs derived from COSMO-RS σ-profiles-quantum-chemical descriptors encoding electrostatic and hydrogen-bonding potentials, rather than empirical molecular features. The optimized architecture (10-19-13-1 topology with hyperbolic tangent activation) achieved $R^2 = 0.998 \pm 0.001$ (training) and 0.986 ± 0.002 (testing), demonstrating that physics-informed descriptors enhance generalization. This approach bridges ab initio thermodynamics with data-driven prediction, enabling in silico screening without prior experimental data.

Makarov et al. extended predictive scope by merging datasets from Mohan and Song (1971 training points, 534 test points) and comparing Random Forest with Extended Connectivity Fingerprints (RF-ECFP) against the TransCNF model[63], [65], [66]. Their analysis identified 1447 chemisorptive DESs and 5 physisorptive candidates (e.g., tetrabutylphosphonium bromide:4-pyridinepropanol, trioctylphosphine oxide:2-ethyl-1-butanol), highlighting the divergent design criteria for reactive versus non-reactive systems. The molecular fingerprint approach proved particularly effective for interpolation within known chemical families but struggled with extrapolation to novel cation-HBD combinations.

1.4.3. Physics-Informed Deep Learning: Integrating First Principles

Mohan et al. advanced beyond purely empirical correlations by incorporating COSMO-RS-derived σ-profile descriptors into gradient-boosted trees (GBT), support vector regression (SVR), random forest (RF), and artificial neural networks (ANN) to predict CO_2 solubility in chemically reactive DESs[67]. The ANN outperformed all competitors with AARD = 2.94%, successfully capturing carbamate formation kinetics and hydrogen-bond disruption phenomena invisible to conventional descriptors. This hybrid framework demonstrates that embedding quantum-mechanical insights into ML architectures enables accurate prediction of reactive absorption, a regime where traditional QSPR models fail due to non-equilibrium chemisorption dynamics.

1.4.4. Graph Neural Networks: Molecular Representation Learning

Most recently, Morales et al. explored graph neural networks (GNNs) to encode DES molecular structures directly as node-edge representations, bypassing manual feature engineering. Testing on Mohan's dataset, they found that standard Graph Convolutional Networks (GCNs) underperformed relative to RF baselines, but the Graph Neural Network-Mixture Graph (GNN-MG) model, which explicitly represents HBA-HBD interactions as graph edges, achieved superior accuracy[63], [64], [68]. However, performance degraded for structurally dissimilar test cases, revealing a fundamental challenge: current GNN architectures learn pattern recognition rather than generalizable chemical principles, limiting their utility for de novo solvent design beyond training manifolds.

1.4.5. Critical Outlook: Bridging Prediction and Implementation

Despite remarkable predictive accuracies ($R^2 > 0.95$ across multiple studies), no ML-designed DES has yet reached pilot-scale demonstration, a disconnect attributable to models optimizing

solubility alone while neglecting viscosity, regeneration energy, material compatibility, and cost. Wang's feature-importance ranking paradoxically suggests that pressure is an operational variable, not a molecular property, is the strongest predictor, implying that current models excel at interpolating experimental conditions rather than discovering transformative chemistries.

Future progress requires multi-objective optimization frameworks that balance CO_2 capacity, kinetic accessibility (viscosity < 100 mPa·s), thermodynamic reversibility ($|\Delta H| < 40$ kJ/mol), and economic feasibility. Integrating ML predictions with process simulation (e.g., Aspen Plus coupling) and experimental validation loops will transition DES design from in silico curiosity to industrial reality, addressing the critical gap between predictive power and practical deployment.

1.4.6. Toward Process-Level Applications: A Unified Design Platform

The preceding sections have established deep eutectic solvents as solvents whose properties can be systematically tailored through computational design and validated through rigorous characterization. Machine learning models were developed for rapid candidate screening. Thermodynamic frameworks were applied to predict absorption and regeneration efficiency. Predictions were validated experimentally. This progression demonstrates the transition from empirical discovery toward rational design.

Yet the true measure of DES utility lies not in their chemical novelty or computational tractability, but in their performance within integrated industrial processes. **Sections 1.3** and **1.4** demonstrated DES superiority in CO_2 absorption, lower regeneration energy, enhanced stability, and cost advantages compared to conventional amines and ionic liquids. These achievements, while substantial, address a single industrial challenge: CO_2 separation from gas streams. Beyond gas-

liquid absorption, distinctive advantages emerge. The tunable properties of DES and spontaneous phase behavior create opportunities in different application domains.

The following two sections examine azeotropic distillation and biodiesel synthesis. These applications differ profoundly from CO_2 capture in their thermodynamic basis and separation mechanisms yet are unified by the same structure-property relationships governing DES performance. In azeotropic distillation, DES selectivity arises from polarity-based entrainer interactions and non-volatility, eliminating entrainer losses. In biodiesel synthesis, acid functionality and phase behavior jointly enable catalysis and product separation, precisely the integrated functionality in which DESs excel.

Section 1.5 demonstrates DES superiority in azeotropic distillation through rigorous process modeling and comparison with DMSO and pressure-swing alternatives. **Section 1.6** presents a comprehensive fuel quality and engine performance assessment of biodiesel synthesized using DES catalysts, establishing technical equivalence with conventional biodiesel while validating the process simplification and economic advantages that DES catalysis provides.

1.5. DESs for Azeotropic Separations

Azeotropes are binary mixtures characterized by identical vapor-liquid compositions at equilibrium, thereby eliminating the driving force for separation through conventional distillation, independent of reflux ratio or column configuration. The isopropanol-water system exemplifies this challenge, forming a minimum-boiling azeotrope at 87.7 wt% IPA and 80.4°C at atmospheric pressure. With global IPA consumption exceeding 4 billion liters annually in semiconductor cleaning and pharmaceutical manufacturing, recovery of high-purity IPA is economically critical[12].

Industrial separations are accomplished through three primary approaches: pressure-swing distillation (elevated pressure shifting azeotropic composition), azeotropic distillation (added volatile solvent), and extractive distillation (added high-boiling entrainer solvent). Extractive distillation is often selected in preference to azeotropic distillation, as the entrainer remains predominantly in the liquid phase, thereby minimizing vaporization losses. Conventional entrainers-dimethyl sulfoxide (DMSO), N-methylpyrrolidone (NMP), and glycerol-have been established as effective; however, significant drawbacks are encountered: volatility causing atmospheric emissions and recovery costs, thermal degradation at regeneration temperatures (120-150°C), and generation of hazardous byproducts. The negligible vapor pressure of DESs (<0.01 kPa at 150°C) addresses these limitations by eliminating entrainer losses and atmospheric emissions. Owing to their non-volatile nature, such solvents enable alternative process designs in which entrainer recovery is performed by low-pressure flash separation rather than conventional stripping columns, leading to a reduction in overall system energy demand of 20-30%[11]. Furthermore, DES thermal stability eliminates degradation concerns, ensuring reliable performance over extended cycling. Glyceline (choline chloride:glycerol, 1:2) and ethaline (choline chloride:ethylene glycol, 1:2) have demonstrated selectivity and capacity comparable to or exceeding DMSO while offering substantial cost and environmental advantages.

The advantages demonstrated for azeotropic separations-low volatility, thermal stability, and selective interactions-extend beyond distillation operations. Acidic DESs have been shown to catalyze chemical synthesis while simultaneously enabling product separation, a capability absent in conventional solvents. Biodiesel synthesis exemplifies this integrated functionality.

1.6. DESs in Biodiesel Production and Fuel Quality Assessment

Biodiesel production via transesterification of triglycerides with methanol has expanded to over 59 billion liters annually, driven by renewable fuel mandates[17], [18], [19]. Conventional biodiesel synthesis relies on homogeneous base catalysts such as NaOH and KOH, which enable high triglyceride conversion but are ineffective for the simultaneous esterification of free fatty acids present in waste-derived feedstocks[69], [70], [71]. Acidic DESs, particularly choline chloride paired with carboxylic acids (levulinic acid, decanoic acid, p-toluene sulfonic acid), have been proposed as alternatives.

The critical question is whether DES-catalyzed biodiesel meets fuel quality standards and demonstrates acceptable engine performance. Chapter 6 presents a comprehensive assessment of biodiesel produced via DES catalysis: characterization against ASTM D6751 fuel specifications, single-cylinder research engine testing measuring thermal efficiency and emissions, and comparative analysis with conventional biodiesel and petroleum diesel. This work was conducted to establish whether DES catalysis produces commercially viable, performance-equivalent biodiesel while retaining process simplification and economic advantages.

1.7. Problem Statement and Research Gaps

Despite the promising potential of DESs as sustainable alternatives to conventional solvents, their industrial deployment is currently hindered by distinct scientific and technical gaps across the domains of carbon capture, chemical separations, and biofuel production.

1. Conventional amine-based CO_2 capture suffers from high regeneration energy costs, solvent degradation, and equipment corrosion. While Ionic Liquids (ILs) were proposed as

stable alternatives, their high synthesis costs and viscosity have limited their commercial viability. In the context of DESs, the majority of existing research has prioritized chemisorption-based solvents to maximize uptake capacity. However, this often comes at the expense of high regeneration energy, similar to amines. There is a significant lack of research focused on designing physisorption-based DESs, which rely on weaker van der Waals interactions to offer lower regeneration energies. Furthermore, the selection of DESs is often trial-and-error based. There is a critical absence of robust Quantitative Structure-Property Relationship (QSPR) and Machine Learning (ML) frameworks capable of predicting CO_2 solubility based on thermodynamic and thermophysical properties, which is essential for the rational design of new solvents. This research gap is addressed in **Chapters 2, 3, and 4**.

2. The separation of azeotropic mixtures, such as Isopropyl Alcohol (IPA) and water, remains a major energy consumer in the chemical industry. Conventional extractive distillation relies on entrainers like dimethyl sulfoxide (DMSO), which raise environmental and occupational safety concerns due to their toxicity and volatility. DESs have been proposed as greener alternatives because of their negligible vapor pressure and tunable properties. However, the energy and economic performance of DES-based extractive distillation has rarely been evaluated at the industrial process level through rigorous simulation and comparison with established entrainer systems, which is addressed in **Chapter 5**.
3. Biodiesel production from non-edible, high Free Fatty Acid (FFA) feedstocks (e.g., Azadirachta indica or Neem oil) is technically challenging. Conventional homogeneous base catalysts lead to soap formation, while ammonium-based DESs often suffer from limited thermal stability and high viscosity, hindering mass transfer. There is a need to

explore DESs that offer better thermal stability and lipophilicity. Moreover, existing literature is largely confined to synthesis kinetics; there is a scarcity of comprehensive "well-to-wheel" studies that connect the chemical synthesis method directly to engine performance and emission characteristics, which is addressed in **Chapter 6**.

This thesis addresses these interconnected challenges by developing a unified platform for the design, synthesis, and application of specific DESs tailored to these three critical industrial processes.

1.8. Thesis Roadmap

This thesis is structured to systematically address the design, characterization, and application of Deep Eutectic Solvents, represented by **Figure 1.6**. The subsequent chapters are organized as follows:

Chapter 2 and Chapter 3: These chapters focus on the thermodynamic foundations of solvent design. Chapter 2 presents a comprehensive evaluation of the physical and thermodynamic properties of 102 DESs. Critical properties were estimated using the modified Lydersen-Joback-Reid method, while dissolution enthalpy and entropy were calculated using the Clausius-Clapeyron equation. These properties establish the criteria for "tuning" DESs to achieve energy-efficient CO_2 capture. Chapter 3 discusses the screening of DESs using machine learning modeling. The estimated properties from Chapter 2 were used as input features for Random Forest and Gradient Boosting models to predict CO_2 solubility.

Chapter 4: This chapter moves from theoretical design to experimental validation and predictive modeling. It details the synthesis of novel ammonium and phosphonium-based DESs and the measurement of their CO_2 solubility at high pressures (up to 20 bar). Crucially, it introduces

Machine Learning (ML) and Quantitative Structure-Property Relationship (QSPR) models to predict CO_2 uptake, along with a "Performance Index" that balances absorption capacity against viscosity constraints.

Chapter 5: This chapter explores the application of DESs in process separation. It addresses the challenge of separating azeotropic mixtures (specifically IPA-water). It utilizes Aspen Plus process simulation to compare the performance of DESs (Ethaline, Glyceline) against Ionic Liquids ([EMIM][BF_4]) and conventional solvents (DMSO). The chapter evaluates process parameters, energy consumption, and proposes alternative process designs (such as flash recovery) to minimize the energy footprint of industrial separations.

Chapter 6: The final chapter explores the use of DESs as catalysts for biodiesel production from high-FFA Neem oil. It investigates the efficacy of phosphonium-based DESs in esterification reactions compared to traditional methods. Uniquely, this chapter extends the analysis beyond synthesis to a full evaluation of the produced fuel in a Variable Compression Ratio (VCR) diesel engine, analyzing combustion characteristics, brake thermal efficiency, and exhaust emissions.

Chapter 7: This chapter summarizes the key findings of the research, highlighting the versatility of DESs across the studied applications and offering recommendations for future scale-up and industrial implementation.

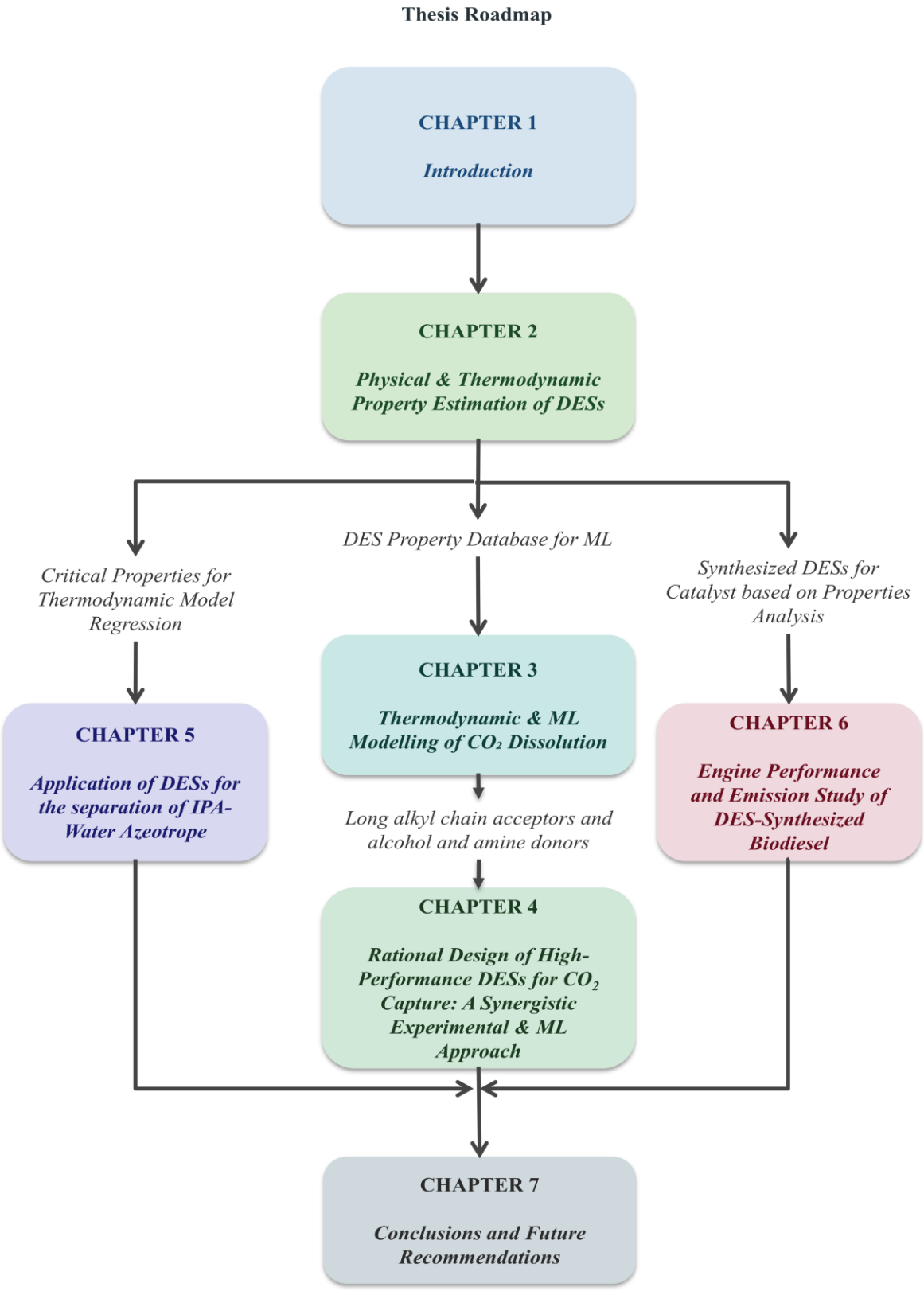

Figure 1.6 Thesis Roadmap

Chapter 2

Physical & Thermodynamic Property Estimation of DESs

2.1. Introduction

In this chapter, a total of one hundred and two different DESs, which were composed of different hydrogen bond acceptors and hydrogen bond donors, were chosen. Critical properties such as critical temperature, critical volume, and critical pressure of HBD and HBA were determined using the Modified Lydersen-Joback-Reid Method. Thereafter, the Lee-Kesler Method was employed to assess the critical properties of DESs. The physical properties, such as the density and the refractive index of the DESs, were calculated using the group contribution method given by Haghbakhsh et al. The free volume of DES was calculated using the Lorentz-Lorentz Relation.

2.2. Selection of DESs from the literature

A total of 102 DESs were selected from the literature. These systems comprised 27 hydrogen bond acceptors and 29 hydrogen bond donors. The selection covered quaternary ammonium salts, amino acids, organic amines, and other functional categories to ensure broad structural diversity. **Figure 2.1** and **Figure 2.2** show the structures of HBA and HBD of some of the selected DESs, and **Table 2.1** represents the list of DESs.

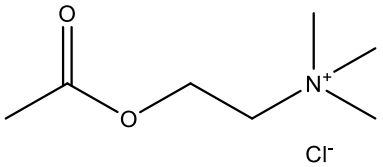

Acetylcholine Chloride

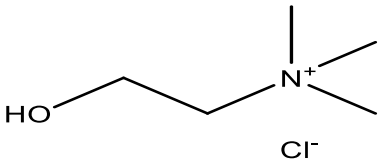

Choline Chloride

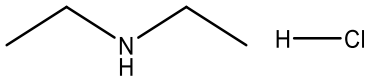

Diethylamine Hydrochloride

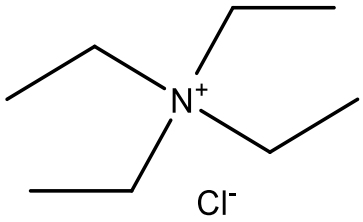

Tetraethylammonium Chloride

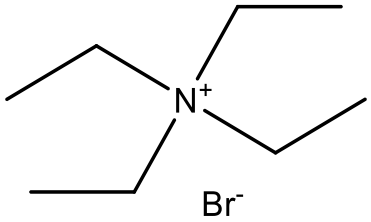

Tetraethylammonium Bromide

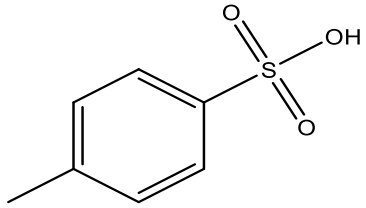

p-toluene sulfonic acid

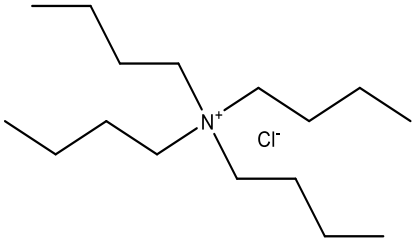

Tetrabutylammonium Chloride

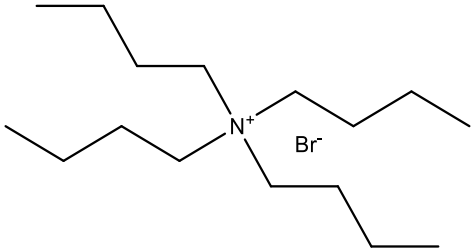

Tetrabutylammonium Bromide

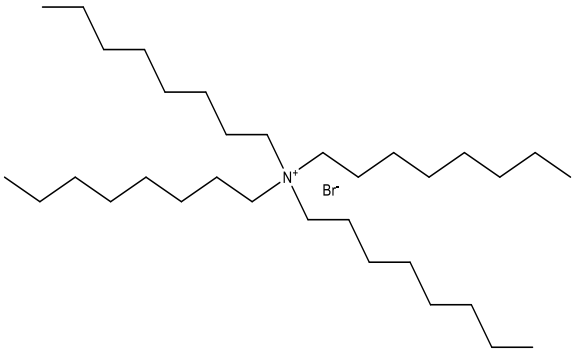

Tetraoctylammonium Bromide

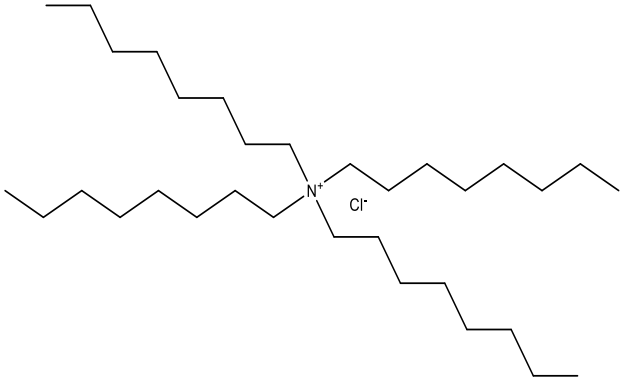

Tetraoctylammonium Chloride

Figure 2.1 Chemical structure of the hydrogen bond acceptors

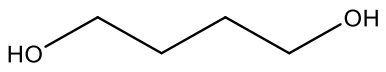

1,4-butanediol

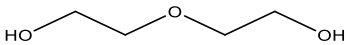

Diethylene Glycol

Ethylene Glycol

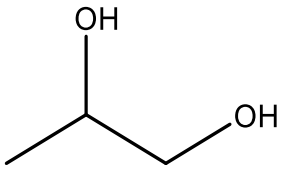

1,2-propanediol

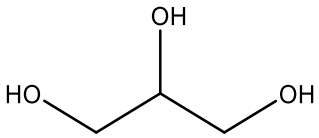

Glycerol

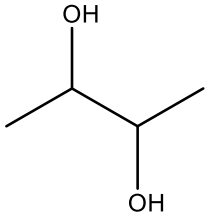

2,3-butanediol

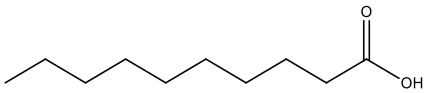

Decanoic Acid

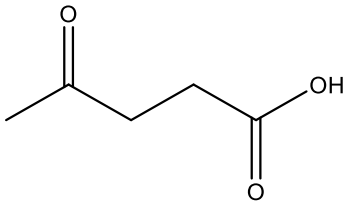

Levulinic Acid

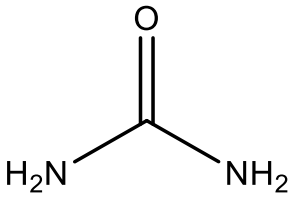

Urea

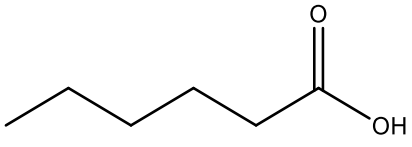

Hexanoic Acid

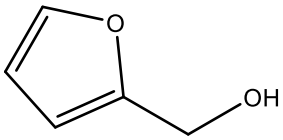

Furfuryl Alcohol

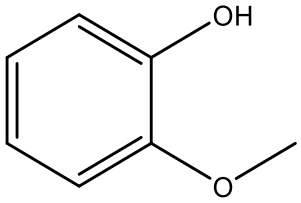

Guaiacol

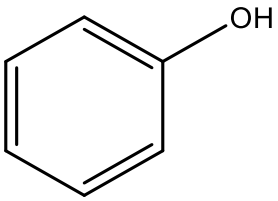

Phenol

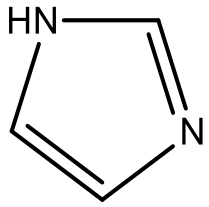

Imidazole

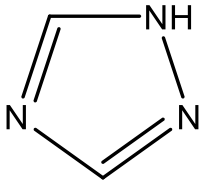

1,2,4-triazole

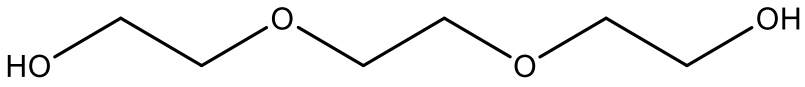

Triethylene Glycol

Figure 2.2 Chemical structure of the hydrogen bond donors

Table 2.1 List of the selected deep eutectic solvents

DES Name	HBA	HBD	Molar Ratio	References
DES1	Choline Chloride	Urea	1:1.5	[41]
DES2	Choline Chloride	Urea	1:2	[41]
DES3	Choline Chloride	Urea	1:2.5	[41]
DES4	Choline Chloride	Glycerol	1:2	[43]
DES5	Choline Chloride	Ethylene Glycol	1:2	[44]
DES6	Choline Chloride	Phenol	1:2	[51]
DES7	Choline Chloride	Phenol	1:3	[51]
DES8	Choline Chloride	Phenol	1:4	[51]
DES9	Choline Chloride	Diethylene Glycol	1:3	[51]
DES10	Choline Chloride	Diethylene Glycol	1:4	[48]
DES11	Choline Chloride	Triethylene Glycol	1:3	[51]
DES12	Choline Chloride	Triethylene Glycol	1:4	[51]
DES13	Choline Chloride	Levulinic Acid	1:3	[47]
DES14	Choline Chloride	Levulinic Acid	1:4	[47]
DES15	Choline Chloride	Levulinic Acid	1:5	[47]
DES16	Choline Chloride	Furfuryl Alcohol	1:3	[47]
DES17	Choline Chloride	Furfuryl Alcohol	1:4	[47]
DES18	Choline Chloride	Furfuryl Alcohol	1:5	[47]
DES19	Choline Chloride	1,4-butanediol	1:3	[48]
DES20	Choline Chloride	1,4-butanediol	1:4	[48]
DES21	Choline Chloride	2,3-butanediol	1:3	[48]
DES22	Choline Chloride	2,3-butanediol	1:4	[48]
DES23	Choline Chloride	1,2-propanediol	1:3	[48]
DES24	Choline Chloride	1,2-propanediol	1:4	[48]
DES25	Choline Chloride	Guaiacol	1:3	[72]
DES26	Choline Chloride	Guaiacol	1:4	[72]
DES27	Choline Chloride	Guaiacol	1:5	[72]
DES28	Diethylamine Hydrochloride	Guaiacol	1:3	[72]
DES29	Diethylamine Hydrochloride	Guaiacol	1:4	[72]
DES30	Diethylamine Hydrochloride	Guaiacol	1:5	[72]
DES31	Acetylcholine Chloride	Guaiacol	1:3	[72]
DES32	Acetylcholine Chloride	Guaiacol	1:4	[72]
DES33	Acetylcholine Chloride	Guaiacol	1:5	[72]
DES34	Tetrabutylammonium Chloride	Decanoic Acid	1:2	[73]
DES35	Tetraoctylammonium Chloride	Decanoic Acid	1:2	[73]

DES36	Tetraoctylammonium Chloride	Decanoic Acid	1:1.5	[73]
DES37	Tetraoctylammonium Bromide	Decanoic Acid	1:2	[73]
DES38	Tetrabutylammonium Bromide	Hexanoic acid	1:2	[74]
DES39	Tetrabutylammonium Bromide	Hexanoic acid	1:3	[74]
DES40	Tetrabutylammonium Bromide	Hexanoic acid	1:4	[74]
DES41	Tetraethylammonium Chloride	Hexanoic acid	1:2	[74]
DES42	Tetraethylammonium Chloride	Hexanoic acid	1:4	[74]
DES43	p-toluene sulfonic acid	Imidazole	1:3	[75]
DES44	p-toluene sulfonic acid	Imidazole	1:3.5	[75]
DES45	p-toluene sulfonic acid	Imidazole	1:4	[75]
DES46	Acetylcholine Chloride	Imidazole	1:2	[76]
DES47	Acetylcholine Chloride	Imidazole	1:3	[76]
DES48	Acetylcholine Chloride	Imidazole	2:3	[76]
DES49	Acetylcholine Chloride	1,2,4-triazole	1:1	[76]
DES50	Acetylcholine Chloride	Levulinic Acid	1:3	[77]
DES51	Tetraethylammonium Chloride	Levulinic Acid	1:3	[77]
DES52	Tetraethylammonium Bromide	Levulinic Acid	1:3	[77]
DES53	Tetrabutylammonium Chloride	Levulinic Acid	1:3	[77]
DES54	Tetrabutylammonium Bromide	Levulinic Acid	1:3	[77]
DES55	Choline Chloride	1,2-Butanediol	1:4	[78]
DES56	Sodium Bromide	Ethylene Glycol	1:6	[79]
DES57	L-Lysine	Hexanoic acid	1:2	[80]
DES58	L-Alanine	Hexanoic acid	1:2	[80]
DES59	L-Histidine	Hexanoic acid	1:2	[80]
DES60	L-Cystine	Hexanoic acid	1:2	[80]
DES61	L-Lysine	Oxalic acid	1:2	[80]
DES62	L-Alanine	Oxalic acid	1:2	[80]
DES63	L-Histidine	Oxalic acid	1:2	[80]
DES64	L-Cystine	Oxalic acid	1:2	[80]
DES65	L-Lysine	Decanoic Acid	1:2	[80]
DES66	L-Alanine	Decanoic Acid	1:2	[80]
DES67	L-Histidine	Decanoic Acid	1:2	[80]
DES68	L-Cystine	Decanoic Acid	1:2	[80]
DES69	L-Lysine	Dodecanoic acid	1:2	[80]
DES70	L-Alanine	Dodecanoic acid	1:2	[80]

DES71	L-Histidine	Dodecanoic acid	1:2	[80]
DES72	L-Cystine	Dodecanoic acid	1:2	[80]
DES73	Decanoic acid	Lidocaine	2:1	[81]
DES74	Menthol	Decanoic acid	2:1	[81]
DES75	Menthol	Decanoic acid	3:1	[81]
DES76	Tetrapropylammonium Bromide	Formic Acid	1:1	[82]
DES77	Tetrapropylammonium Bromide	Formic Acid	1:2	[82]
DES78	Ethanolamine hydrochloride	Tetraethylenepentamine	1:9	[83]
DES79	L-menthol	Thymol	1:2	[84]
DES80	Thymol	2,6-Xylenol	1:1	[84]
DES81	Betaine	1,2-propanediol	1:3	[85]
DES82	Betaine	1,2-propanediol	1:4	[85]
DES83	Betaine	1,2-propanediol	1:5	[85]
DES84	Betaine	1,2-propanediol	1:6	[85]
DES85	Betaine	Diethylene Glycol	1:4	[85]
DES86	Betaine	Diethylene Glycol	1:6	[85]
DES87	Tetrabutylammonium Bromide	Ethylene Glycol	1:3	[86]
DES88	Tetrabutylphosphonium Bromide	Ethylene Glycol	1:3	[86]
DES89	Pyrazole	Glycerol	1:1	[87]
DES90	Pyrazole	Glycerol	1:2	[87]
DES91	Guanidine Isothiocyanate	Acetamide	1:2	[88]
DES92	Guanidine Isothiocyanate	Acetamide	1:3	[88]
DES93	Guanidine Isothiocyanate	Acetamide	1:4	[88]
DES94	Tetrabutylammonium Bromide	Octanoic acid	1:2	[89]
DES95	Tetrabutylammonium Bromide	Decanoic acid	1:2	[89]
DES96	DL-Menthol	Dodecanoic acid	2:1	[89]
DES97	Acetamide	Diethylene glycol	1:4	[90]
DES98	Acetamide	Diethylene glycol	1:5	[90]
DES99	Acetamide	1,2-propanediol	1:4	[90]
DES100	Acetamide	1,2-propanediol	1:5	[90]
DES101	Acetamide	1,3-Propanediol	1:4	[90]
DES102	Acetamide	1,3-Propanediol	1:5	[90]

2.3. Critical properties of DESs

Critical properties such as critical volume (V_c), critical pressure (P_c), and critical temperature (Tc) of a new component are essential for understanding the phase diagram. These are used to predict the transport and thermodynamic properties. The experimental determination of critical properties is challenging, particularly for heavier components that can chemically deteriorate at their extremely high critical temperatures[91], [92]. Therefore, these are estimated by the predictive thermodynamic modelling approach. The critical properties of each hydrogen bond donor and acceptor were determined by employing the modified Lydersen-Joback-Reid (LJR) technique. Valderrama et al. devised the modified LJR approach by merging the Lydersen and Joback Reid methods to assess the critical properties of ionic liquids and molecules of high molecular weight[32-34]. Therefore, it was employed to determine the critical properties of HBA and HBD via the following equations (2.1) to (2.6)

$$T_b(K) = 198.2 + \sum n\Delta T_b \tag{2.1}$$

$$T_C(K) = \frac{T_b}{[A + B\sum n\Delta T_c - (\sum n\Delta T_c)^2]} \tag{2.2}$$

$$P_C(bar) = \frac{M}{[C+\sum n\Delta P_c]^2} \tag{2.3}$$

$$V_C(cm^3/mol) = D + \sum n\Delta V_c \tag{2.4}$$

$$Z_C = \frac{P_c * V_c}{R * T_c} \tag{2.5}$$

$$\omega = \frac{(T_b - 43)(T_c - 43)}{(T_c - T_b)(0.7T_c - 43)} \log\left(\frac{P_c}{P_b}\right) - \frac{(T_c - 43)}{(T_c - T_b)} \log\left(\frac{P_c}{P_b}\right) + \log\left(\frac{P_c}{P_b}\right) - 1 \tag{2.6}$$

where constants A = 0.5703, B = 1.021, C = 0.2573, and D = 6.75, M represents the molecule's molar mass in grams per mole, and n is the quantity of groups within the molecule. ΔV_c, ΔP_c, ΔT_c, and ΔT_b, epitomise atom's group contribution within the molecule to their critical molar volume (cm^3/mol), critical pressure (bar), critical temperature (K), and boiling point (K), respectively.

The critical properties of all the DESs, as shown in **Table A1,** were determined using the Lee-Kesler mixing method after estimating the critical properties of the hydrogen bond donor and hydrogen bond acceptor using equations (2.7) to (2.12) [95];

$$T_{cDES} = \left(\frac{1}{V_{cDES}^{0.25}}\right)\sum_i\sum_j x_i x_j V_{cij}^{0.25} T_{cij} \tag{2.7}$$

where

$$T_{cij} = \left(T_{ci}T_{cj}\right)^{0.5} k_{ij} \tag{2.8}$$

$$V_{cij} = 0.125\left(V_{ci}^{(1/3)} + V_{cj}^{(1/3)}\right)^3 \tag{2.9}$$

$$V_{cDES} = \sum_i\sum_j x_i x_j V_{cij} \tag{2.10}$$

and

$$P_{cDES} = (0.2905 - 0.085\omega_{DES})\frac{RT_{cDES}}{V_{cDES}} \tag{2.11}$$

where

$$\omega_{DES} = \sum_i x_i \omega_i \tag{2.12}$$

M_{wDES} (g/mol), T_{cDES} (K), V_{cDES} (cm^3/mol), and P_{cDES} (bar) represent the molecular weight, critical temperature, critical volume, and critical pressure of DESs, respectively. The k_{ij} denotes binary interaction parameters of DESs, while ω_{DES} represents the acentric factor, respectively. The k_{ij}

values vary from 0.95-1.06 for polar substances and 1.0-1.3 for mixtures of nonpolar compounds[95]. The k_{ij} value was considered to be equal to one for all calculations.

2.4. Physical properties of DESs

The thermophysical properties, including molar volume, free molar volume, surface tension, density, and heat capacity, were determined using the group contribution method established by Haghbaksh et al.[96] using Equations (2.13) to (2.18), as detailed below:

$$X_1 = m_{HBA} \sum_{i=1}^{p} k_i (\Delta X_{1,i})_{HBA} + m_{HBD} \sum_{i=1}^{q} l_i (\Delta X_{1,i})_{HBD} \tag{2.13}$$

$$X_2 = m_{HBA} \sum_{i=1}^{p} k_i (\Delta X_{2,i})_{HBA} + m_{HBD} \sum_{i=1}^{q} l_i (\Delta X_{2,i})_{HBD} \tag{2.14}$$

$$\rho_{DES}\ (g/cm^3) = \left(\frac{\rho_1}{M_{wDES}}\right)^{-0.2045} + \left(\frac{\rho_2}{M_{wDES}}\right)(T^{-0.6785}) + 0.2818 \tag{2.15}$$

$$n_{DES} = (n_1)^{-0.3597} + (n_2)T^{-1.8254} + 1.3695 \tag{2.16}$$

$$C_{pDES}\ (J/mol\ K) = {C_{p1}}^{0.8653} + (C_{p2})(T^{-0.4528}) + 341.4081 \tag{2.17}$$

$$\sigma_{DES}(mN/m) = \sigma_1 - (\sigma_2)T^{0.0115} + 40.8235 \tag{2.18}$$

Additionally, the molar free volume was determined using the refractive index value through the Lorentz-Lorenz connection, as shown in Equation (2.19) [97], [98].

$$V_{free}(cm^3/mol) = V_M \left(\frac{3}{n_{DES}^2 + 2}\right) \tag{2.19}$$

Where

$$V_M \text{is the molar volume of DES } (cm^3/mol) = \frac{M_{wDES}}{\rho_{DES}} \tag{2.20}$$

2.5. Conclusion

This chapter established the foundational computational framework for screening deep eutectic solvents for CO_2 capture applications. The methods shown here enable systematic characterization of DES physical and critical properties.

A total of 102 DESs were selected from the literature. These systems comprised 27 hydrogen bond acceptors and 29 hydrogen bond donors. The selection covered quaternary ammonium salts, amino acids, organic amines, and other functional categories to ensure broad structural diversity.

Critical properties of individual HBA and HBD components were estimated using the Modified Lydersen-Joback-Reid method. The Lee-Kesler mixing rules were then applied to determine critical temperature, critical pressure, and critical volume of complete DES systems. This predictive approach provides the necessary thermodynamic parameters when experimental measurement is impractical.

Physical properties such as density and refractive index were calculated using the group contribution method proposed by Haghbakhsh et al. Molar free volume was subsequently estimated through the Lorentz-Lorentz relation.

The property estimation framework established in this chapter directly enables the work in subsequent chapters. **Chapter 3** extends this foundation by correlating these calculated properties with CO_2 dissolution behavior. Henry's constants and thermodynamic properties are determined, followed by machine learning-based screening of the entire DES library. The computational insights from **Chapter 2** and **Chapter 3** guide the rational design in **Chapter 4**, where novel DESs are synthesized and experimentally characterized for physisorption-based CO_2 capture. **Chapter 5** applies similar property estimation principles to evaluate DES performance in extractive

distillation for azeotrope separation. **Chapter 6** explores a different application domain-DES-catalyzed biodiesel synthesis with integrated engine performance analysis. Together, these chapters demonstrate how fundamental property estimation enables the design of DESs across diverse industrial applications.

Declaration of Publication

This chapter draws its substance and methodology from the research originally disseminated in the following peer-reviewed publication:

Gomey, A. K., Haider, M. B., & Kumar, R. (2025). Designing of energy-efficient deep eutectic solvents for CO_2 capture: insights from physical and thermodynamic property evaluation. *Journal of Molecular Liquids*, 434, 127996. https://doi.org/10.1016/j.molliq.2025.127996

Chapter 3

Thermodynamic and Machine Learning Modelling of CO_2 Dissolution in DESs

Graphical Abstract

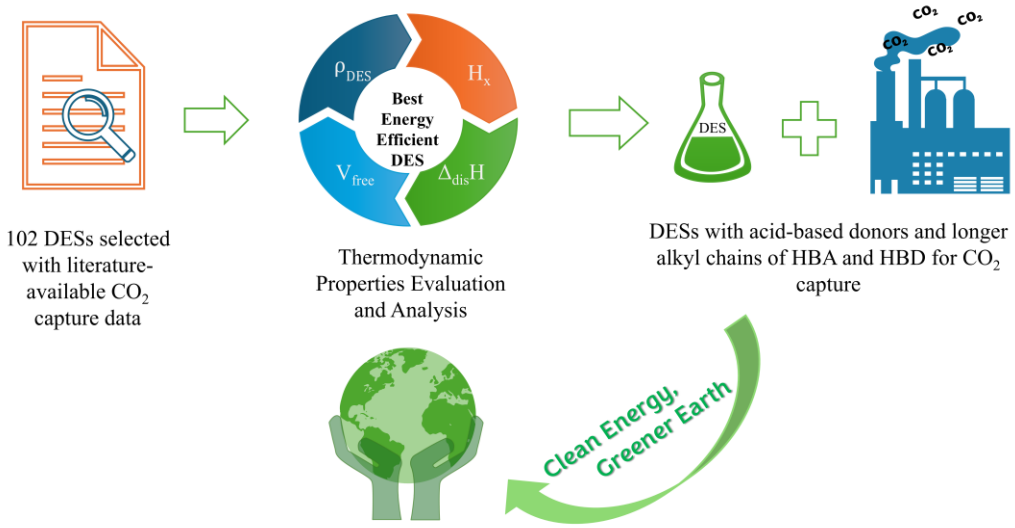

3.1. Introduction

In this chapter, the thermophysical and thermodynamic properties estimated for 102 DESs in **Chapter 2** were analyzed for their effect on CO_2 dissolution behavior. Machine learning screening was employed to identify structure-property relationships. Literature CO_2 solubility data at different temperatures were collected for all selected DESs to enable a comprehensive thermodynamic analysis.

The primary objective was to establish quantitative relationships between DES molecular properties and CO_2 capture performance. Calculated densities were validated against experimental literature data to ensure accuracy of the computational framework. Viscosity data collected from the literature provide insight into mass transfer characteristics and process feasibility. The CO_2 solubilities in DESs were correlated with Henry's law, and the values of Henry's constants were determined from the linear plot of fugacity versus molality of CO_2. Thermodynamic properties such as standard enthalpy of dissolution, standard entropy of dissolution, and standard Gibbs free energy of dissolution of the DES-CO_2 systems were calculated using the Clausius-Clapeyron equation.

Understanding these structure-property relationships is essential for rational solvent design and process optimization. Industrial CO_2 capture requires balancing high absorption capacity against low regeneration energy. Density affects equipment sizing and operational costs. Viscosity governs mass transfer rates and pumping requirements. Lower viscosity facilitates faster CO_2 diffusion. Henry's constant indicates solubility at low pressure. Dissolution enthalpy determines regeneration energy. Dissolution entropy and Gibbs free energy reveal whether CO_2 uptake occurs spontaneously. Henry's constants and dissolution thermodynamics subsequently revealed absorption capacity and regeneration energy requirements.

The nature of hydrogen bond donors and acceptors significantly influences both physical properties and CO_2 dissolution. Acid-based donors show different behavior compared to alcohol and amine-based systems. The length of alkyl chains affects molar free volume, which impacts gas accommodation capacity. Systematic analysis identifies design principles for energy-efficient DESs.

Machine learning complements thermodynamic analysis. Random Forest and Gradient Boosting algorithms identify which properties most strongly influence CO_2 solubility. Statistical correlation analysis reveals relationships between molecular descriptors and dissolution behavior. These insights form the basis of the experimental design in Chapter 4.

3.2. Physical properties of DESs

3.2.1. Density of the DESs

The densities of DESs were calculated at a fixed temperature of 303.15 K, using equation **(2.15)**, and validated with the experimental densities, as listed in **Table A2.** Relative deviation(RD) and absolute relative deviation(ARD) were estimated to assess the accuracy of calculated density using the following equations[99];

$$\mathrm{RD}\ (\%) = \frac{\rho_i^{calc} - \rho_i^{exp}}{\rho_i^{exp}} \times 100 \tag{3.1}$$

$$\mathrm{ARD}\ (\%) = \frac{\left|\rho_i^{calc} - \rho_i^{exp}\right|}{\rho_i^{exp}} \times 100 \tag{3.2}$$

where ρ_i^{calc} is calculated density using the group contribution model given by Reza Haghbakhsh et al.[96], and ρ_i^{exp} is the experimental density reported in the literature.

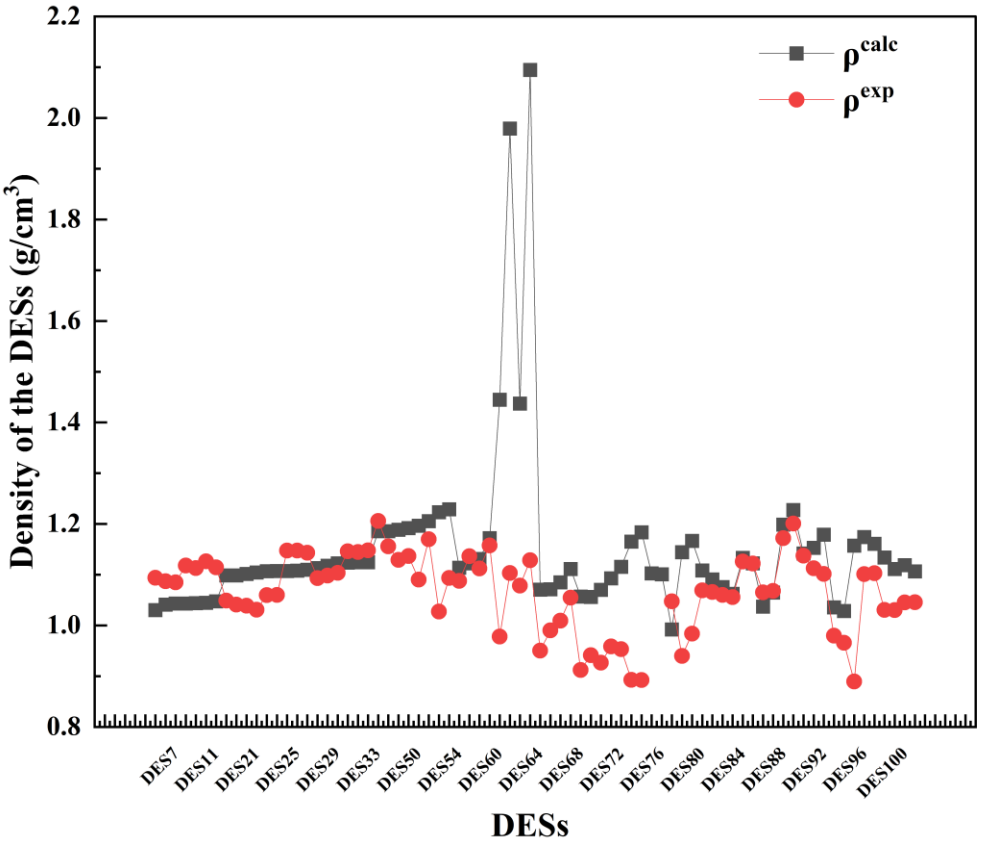

Figure 3.1 Calculated vs. experimental DES densities (in g/cm^3)

The comparison between predicted and experimental values of densities can be observed in **Figure 3.1**. Diethylamine hydrochloride- guaiacol-based DESs were found to have relatively higher deviations due to the negative value of critical volume for the phenolic -OH- group[48].

The density of DESs plays a vital role in CO_2 dissolution. The lower density of DESs results from the larger free volume of DES, which enables higher CO_2 dissolution in the DESs[100]. This relates well with the densities of DESs 34-37, as they have lower density and higher CO_2 dissolution. Additionally, it was observed that the DESs having larger alkyl chain lengths of HBAs possess lower densities as compared to DESs containing shorter alkyl chain lengths, which was found to be in agreement with the reported densities of various ionic liquids[44-46]. Furthermore,

due to the hydrophobic nature of Tetraoctylammonium bromide and decanoic acid, the densities of DESs 34-37 are lower than those of hydrophilic DESs [104]. In general, the acid donor-based DESs had lower densities than alcohol and amine donor-based DESs.

3.2.2. Refractive index and molar free volume of DESs

The refractive index provides information about the polarizability of the solvent molecules, which in turn influences the magnitude of the intermolecular interactions between the solvent and the gas molecules. The prediction of n_{DES} is important in determining the molar free volume of the deep eutectic solvent. Equation (2.19) was used to determine the molar free volume of DESs, and their values are shown in **Table A3.** According to the Lorentz-Lorentz relation, it can be concluded that a lower refractive index corresponds to a greater molar free volume. Additionally, a higher molar volume corresponds to a higher molar free volume, as shown in **Table A3.** Decanoic-based DESs were found to have higher molar free volume, while the lowest was observed in DES62. Furthermore, it was noted that donors based on alcohol have higher refractive indices in comparison to donors based on acid and amines[97], [105], indicating a lower molar-free volume in alcohol-based DESs. Therefore, this suggests that CO_2 has a lower ability to dissolve in alcohol-based DESs, but acid donor-based DESs exhibit a higher molar free volume, suggesting a greater ability to dissolve CO_2. Generally, it was observed that HBA/HBD with longer alkyl chain lengths had greater molar free volume. Therefore, it is recommended that acid-based donors and longer alkyl chain length groups be selected for the synthesis of DES in order to achieve efficient CO_2 absorption.

3.2.3. Viscosity of the DESs

Viscosity is a critical parameter in DESs because it governs their fluidity, mass transfer rates, and overall processability, directly impacting the efficiency of mixing, pumping, and chemical transformations in applications. Across the temperature range 293-323 K, the viscosities of representative DESs drop markedly with increasing temperature, reflecting the thermal disruption of extensive hydrogen-bond networks in these liquids[106]. **Table A4** reports the viscosities of the DESs studied in mPa.s. It was observed that amino acid acceptors based DESs were found to have lower viscosities than other DESs because of the long hydrophobic alkyl chain and ionic pairing, limiting the density of hydrogen bonds. Overall, viscosity in DESs is predominantly governed by the strength and density of hydrogen-bond interactions and the molecular size/structure of the HBA and HBD, making it a key design factor for optimizing DES performance in practical applications.

3.3. Henry's constant

The CO_2 dissolution in DESs can be accurately described using Henry's Law. According to Henry's Law, the molar fraction of a gas dissolved in a solvent is directly proportional to its fugacity in the gaseous phase, as given by equation (3.3)

$$H_x = \lim_{x \to 0} \frac{f^{CO_2}(p, T, x)}{x} \tag{3.3}$$

Where H_x = Henry's law constant (molar fraction basis), f^{CO_2}= fugacity of CO_2 in the gas phase, x = molar fraction of CO_2 in DES, and p, T are the pressure and temperature of the system, respectively.

DESs have negligible vapour pressure; therefore, pure carbon dioxide (CO_2) was assumed to be present in the vapour phase at the equilibrium of the DES-CO_2 system under experimental

conditions. Hence, the fugacity of CO_2 in the vapour phase at equilibrium can be considered as the pressure of pure CO_2[73], [74]. Henry's constants (Hx) were determined from the pressure against CO_2 mol fraction graph by analysing the slope of the graph, as shown in **Figure 3.2** and **Figure 3.3**. The calculated values of Henry's constant for all the DESs are reported in **Table 3.1.** It is pretty evident from Equation (3.3) that the higher the value of Henry's constant, the lower the dissolution of CO_2 in DES.

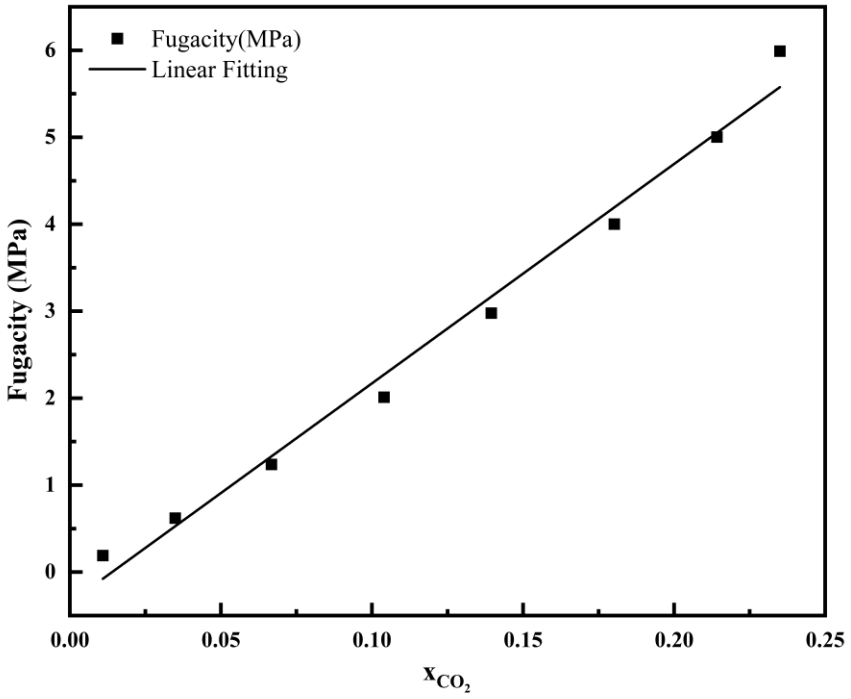

Figure 3.2 Fugacity vs mole fraction of CO_2 dissolved in DES4

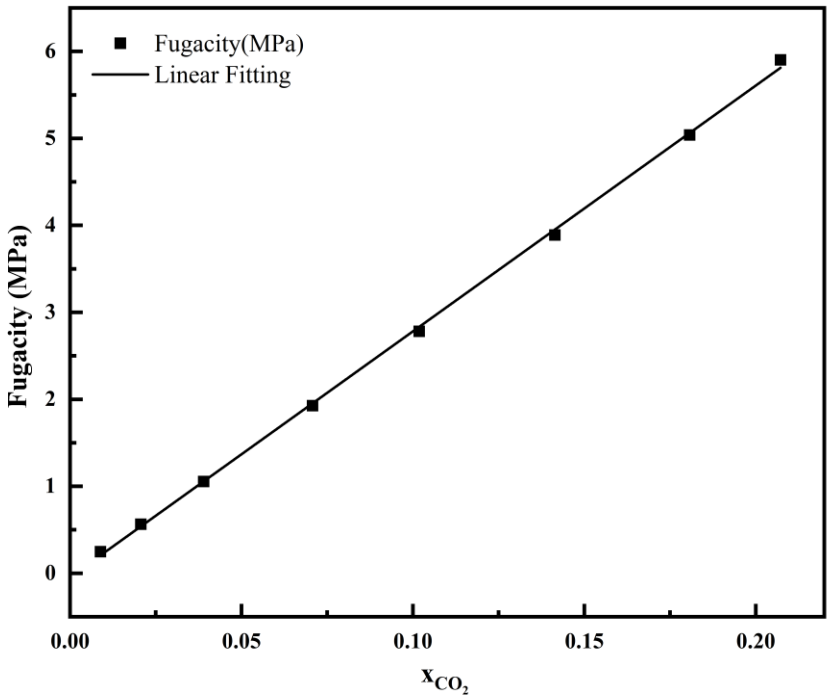

Figure 3.3 Fugacity vs mole fraction of CO_2 dissolved in DES5

Table 3.1 Increasing order of Henry's constant (H_x) of CO_2-DESs at 313.15K

DES Name	Henry's Constants, H_x/MPa	Literature
DES78	2.87	[83]
DES67	4.53	[80]
DES36	6.93	Current work
DES35	7.48	Current work
DES65	7.51	[80]
DES85	28.74	[85]
DES37	7.52	Current work
DES73	7.91	Current Work
DES74	8.58	Current Work
DES34	9.41	Current work
DES79	9.61	[84]
DES95	10.523	Current work
DES68	10.71	[80]
DES80	11.46	[84]

DES38	11.62	[74]
DES39	12.06	[74]
DES2	12.30	[41]
DES96	12.462	Current work
DES40	12.59	[74]
DES94	13.361	Current work
DES53	14.20	[77]
DES41	14.29	[74]
DES42	14.95	[74]
DES54	15.17	[77]
DES45	17.21	[75]
DES44	17.27	[75]
DES43	17.57	[75]
DES61	17.85	[80]
DES50	18.15	[77]
DES60	18.34	[80]
DES1	18.50	[41]
DES66	19.65	[80]
DES15	20.12	[47]
DES59	20.16	[80]
DES77	20.22	Current Work
DES14	20.39	[47]
DES51	20.49	[77]
DES52	20.81	[77]
DES97	20.947	[90]
DES64	21.86	[80]
DES13	21.91	[47]
DES3	22.40	[41]
DES63	22.47	[80]
DES98	23.04	[90]
DES57	23.45	[80]
DES88	24.368	Current work
DES47	24.53	[76]
DES76	24.63	Current work
DES71	24.86	[80]
DES87	25.073	Current work
DES30	25.15	[72]
DES4	25.23	Current work
DES12	25.50	[51]

DES49	25.58	[76]
DES58	26.45	[80]
DES29	26.61	[72]
DES33	26.96	[72]
DES46	27.07	[76]
DES11	27.10	[51]
DES32	27.12	[72]
DES28	27.41	[72]
DES48	27.70	[76]
DES18	28.14	[47]
DES5	28.26	Current work
DES99	28.345	[90]
DES100	28.38	[90]
DES62	28.67	[80]
DES31	28.89	[72]
DES86	29.66	[85]
DES69	29.87	[80]
DES17	29.95	[47]
DES27	30.71	[72]
DES102	31.671	[90]
DES101	31.761	[90]
DES26	32.75	[72]
DES8	33.00	[51]
DES7	33.1	[51]
DES16	33.11	[47]
DES55	33.74	[78]
DES6	34.60	[51]
DES22	34.79	[48]
DES10	35.40	[51]
DES25	35.40	[72]
DES84	36.28	[85]
DES9	36.4	[51]
DES70	38.12	[80]
DES83	39.08	Current Work
DES21	40.68	[48]
DES82	40.74	Current Work
DES81	41.31	Current Work
DES72	41.61	[80]
DES20	42.32	[48]
DES19	43.66	[48]

DES93	44.21	Current Work
DES23	44.88	[48]
DES91	45.27	Current Work
DES92	46.32	Current Work
DES24	50.29	[48]
DES89	51.71	Current Work
DES90	65.21	Current Work
DES56	70.31	[79]
DES75	N.A.	[81]

*N.A – Not Applicable

3.4. Thermodynamic properties of DESs

Gas dissolution properties such as enthalpy, entropy, and Gibbs' free energy provide useful information for the designing of an efficient solvent-based industrial absorption process. The enthalpy of CO_2 dissolution ($\Delta_{dis}H$) gives a sense of the strength of the interaction of gas molecules in liquid solvents. The smaller the absolute values of $\Delta_{dis}H$, easier is the regeneration of the CO_2-rich solvent. The dissolution entropy ($\Delta_{dis}S$) provides us with an idea of the degree of order of the liquid/gas system. Enthalpy of the dissolution, entropy, and Gibbs' free energy of DES-CO_2 systems were calculated from the temperature and pressure dependency of CO_2 solubility in DESs using the following equations[41], [111]:

$$\Delta_{dis}H = R\left(\frac{\partial ln(P)}{\partial\left(\frac{1}{T}\right)}\right)x_{CO_2} \tag{3.4}$$

$$\Delta_{dis}S = \left(\frac{\Delta_{dis}H}{T_{eq}}\right) = -R\left(\frac{\partial ln(P)}{\partial ln(T)}\right)x_{CO_2} \tag{3.5}$$

$$\Delta_{dis}G = \Delta_{dis}H - T\,\Delta_{dis}S \tag{3.6}$$

where x_{CO_2} is the mole fraction of CO_2 in the liquid phase.

The calculated CO_2 dissolution enthalpies($\Delta_{dis}H$), entropies($\Delta_{dis}S$), and Gibbs' free energy($\Delta_{dis}G$) for all the DESs are shown in **Table 3.2**. It is evident from the table that dissolution enthalpies are negative for all DESs, indicating that CO_2 dissolution in DESs is exothermic in nature[78]. The $\Delta_{dis}S$ is mostly associated with the DES structure surrounding the soluble CO_2 at the molecular sites, which indicates the order of intermolecular structure in the CO_2-DES system[47]. The positive values of $\Delta_{dis}G$ demonstrate that DESs cannot dissolve CO_2 spontaneously, and negative values imply that CO_2 dissolution is spontaneous in DESs[41], [77].

Table 3.2 Thermodynamic properties of CO_2-DES system in the increasing order of ΔH (kJ/mol)

DES	ΔH (kJ/mol)	ΔS (J/mol-K)	ΔG (kJ/mol) at 303.15K
DES90	-0.09	-33.61	10.10
DES89	-0.10	-30.74	9.22
DES79	-5.45	-36.31	5.56
DES73	-6.42	-56.83	10.81
DES80	-7.33	-43.66	5.91
DES21	-7.55	-73.18	14.63
DES74	-7.56	-61.15	10.98
DES43	-7.64	-67.49	12.82
DES94	-7.91	-65.40	11.92
DES44	-8.16	-69.04	12.77
DES55	-8.17	-74.39	14.38
DES96	-8.26	-66.05	11.77
DES95	-8.71	-66.42	11.42
DES45	-8.86	-71.12	12.70
DES56	-9.18	-83.82	16.23
DES18	-9.45	-76.84	13.84
DES99	-9.75	-59.00	8.14
DES22	-9.75	-78.65	14.09
DES100	-9.80	-59.21	8.15
DES20	-9.89	-80.80	14.60
DES33	-10.28	-80.27	14.05
DES32	-10.37	-80.80	14.12
DES36	-10.40	-33.60	-0.21

DES102	-10.43	-62.04	8.37
DES35	-10.50	-33.90	-0.22
DES37	-10.50	-33.90	-0.22
DES29	-10.66	-80.47	13.73
DES9	-10.69	-82.92	14.45
DES28	-10.72	-81.91	14.11
DES30	-10.95	-79.78	13.24
DES81	-10.99	-85.13	14.82
DES41	-11.31	-78.51	12.49
DES82	-11.50	-86.70	14.78
DES34	-11.60	-37.30	-0.29
DES16	-11.67	-85.49	14.25
DES31	-11.81	-85.78	14.19
DES27	-11.83	-85.40	14.06
DES69	-11.88	-62.31	8.68
DES26	-11.95	-86.32	14.22
DES65	-11.96	-52.28	7.80
DES12	-12.01	-84.03	13.46
DES70	-12.09	-72.05	13.95
DES88	-12.12	-65.26	7.66
DES62	-12.15	-72.94	8.23
DES87	-12.26	-66.03	7.76
DES101	-12.30	-68.08	8.34
DES61	-12.31	-64.34	7.19
DES68	-12.35	-60.52	11.72
DES72	-12.38	-73.89	14.04
DES66	-12.62	-67.93	13.64
DES8	-12.63	-89.37	14.46
DES7	-12.66	-89.15	14.37
DES42	-12.76	-84.83	12.96
DES71	-12.82	-69.37	14.81
DES19	-12.82	-89.84	14.41
DES97	-12.87	-66.35	7.25
DES83	-12.87	-90.69	14.62
DES86	-13.03	-88.93	13.93
DES64	-13.11	-76.74	9.16
DES76	-13.16	-87.60	13.40
DES98	-13.29	-67.97	7.31
DES63	-13.39	-79.24	9.35
DES25	-13.44	-91.71	14.36
DES93	-13.62	-44.95	0.01
DES67	-13.65	-65.61	13.55

DES11	-13.91	-90.93	13.66
DES10	-13.92	-93.75	14.50
DES54	-13.92	-86.22	12.22
DES85	-14.10	-92.10	13.82
DES84	-14.25	-94.49	14.39
DES53	-14.25	-86.71	12.04
DES23	-14.45	-95.28	14.43
DES15	-14.46	-90.20	12.88
DES17	-14.47	-93.53	13.88
DES6	-14.55	-95.19	14.31
DES14	-14.75	-91.70	13.05
DES52	-14.83	-91.73	12.98
DES39	-15.05	-89.50	12.08
DES51	-15.13	-92.58	12.94
DES40	-15.13	-90.12	12.19
DES92	-15.14	-49.98	0.01
DES91	-15.17	-50.07	0.01
DES13	-15.35	-94.05	13.16
DES49	-15.61	-78.77	8.27
DES38	-16.12	-92.70	11.98
DES48	-16.13	-79.93	8.10
DES77	-16.18	-95.90	12.90
DES46	-16.86	-81.21	7.76
DES3	-17.74	-54.93	-1.09
DES2	-17.96	-55.58	-1.11
DES47	-18.33	-84.97	7.43
DES24	-18.82	-109.67	14.43
DES78	-18.86	-68.81	2.00
DES50	-20.27	-107.97	12.46
DES5	-20.53	-63.78	-1.20
DES4	-21.08	-65.45	-1.24
DES58	-26.70	-112.32	7.35
DES1	-27.81	-86.04	-1.73
DES57	-28.99	-118.94	7.06
DES60	-31.86	-125.95	6.32
DES59	-38.80	-147.46	5.91
DES75			

3.4.1. Effect of hydrogen bond donors

Hydrogen bond donors were classified based on their nature: Acids, amines, and alcohols. Among acid-based DESs, DES59 was found to have the highest ΔH value of -38.80 kJ/mol, while DES74 had the lowest ΔH of -7.56 kJ/mol. A trend was observed that shorter alkyl-chain acids, such as formic, oxalic, and hexanoic acids, exhibit more exothermic values and therefore require higher regeneration energy, whereas longer-chain acids like octanoic, decanoic, and dodecanoic acids are less exothermic and need lower regeneration energy. For the same HBD, more exothermic ΔH was produced by amino-acid HBAs than by quaternary ammoniums. The length and function of HBD chains can be changed to achieve a balance between the amount of CO_2 taken in and the ease of regeneration.

Among alcohol-based DESs, DES4 (ChCl:glycerol 1:2) exhibited the most exothermic ΔH at -21.08 kJ/mol, while DES17 (ChCl:furfuryl alcohol 1:4) showed the least exothermic value of -14.47 kJ/mol. Poly-ol donors (glycerol, ethylene glycol, triethylene glycol) yielded more negative ΔH than monohydric or aromatic alcohols (furfuryl alcohol, guaiacol), reflecting stronger multiple -OH interactions with CO_2. For a given HBD, DESs with amino-acid or choline-derived HBAs were slightly more exothermic than those with quaternary ammoniums, indicating that HBA-HBD affinity modulates CO_2 binding. These results imply that while polyol-based DESs absorb more CO_2, they will demand higher regeneration energy compared to single -OH donors. It was interesting to observe that for the same HBD glycerol, DES4 had the highest enthalpy of dissolution of -21.08 kJ/mol, while DES90 (Pyrazole-Glycerol 1:2 had the lowest enthalpy of dissolution of -0.093 kJ/mol. It is clearly evident that the type of HBA plays a role in lowering the regeneration energy.

Among amine-based DESs, DES1 showed the most exothermic ΔH at -27.81 kJ/mol, and DES43 the least at -7.64 kJ/mol. Primary amine donors (urea) produced more exothermic ΔH than secondary amides (acetamide) or heterocycles (imidazole, triazole), consistent with stronger HBD-CO_2 interactions in polyfunctional systems. In most of the amine donor-based DESs, CO_2 dissolution occurs via chemisorption, forming carbamates or carbonates; hence, amine donor-based DESs were found to have higher dissolution enthalpy[112]. The moderate enthalpies of amine-based DESs point to a favourable balance between CO_2 uptake and regeneration energy.

After analysing the effect of hydrogen bond donor on the enthalpy of dissolution, the trend for the enthalpy of dissolution may be established as:

Acids (-7.56 to -38.80 kJ/mol) < Amines (-6.42 to -27.81 kJ/mol) < Alcohols (-0.09 to -21.08 kJ/mol)

3.4.2. Effect of hydrogen bond acceptors

A systematic variation of CO_2 dissolution enthalpies was observed across the six HBA categories: quaternary ammonium salts (ChCl, TBAB, etc.), amino acids & derivatives (L-Cystine, betaine, etc.), organic amine salts & amides (ethanolamine hydrochloride, acetamide), organic acids & sulfonates (p-TSA), neutral organics (heterocycles & terpenoids) (L-Menthol, thymol, etc.), and inorganic salts (sodium bromide). In the case of quarternary ammonium salts, DES21(choline chloride-2,3 butanediol) has the lowest enthalpy of dissolution of -7.55 kJ/mol due to the two hydroxyl groups present in the 2,3-butanediol whereas DES1 (choline chloride-urea) has the highest enthalpy of dissolution of -27.81 kJ/mol, due to the chemisorption of CO_2 in the presence of urea[113], [114], [115]. Furthermore, amino acid-based HBAs yield the most exothermic ΔH values (-11 to -39 kJ/mol), with several systems reaching ~-30 to -39 kJ/mol that reflect very strong

CO_2 interactions. These high enthalpies greatly enhance CO_2 solubility due to the chemisorption occurring in them, but release substantial heat, implying a higher energy requirement for solvent regeneration. For the case of organic amine salts and amides based HBAs, they showed moderate heat release during CO_2 uptake, with enthalpy values mostly falling between -19 and -10 kJ/mol. This level of interaction seems to strike a useful balance-it's strong enough to encourage good solubility but not so strong that regeneration becomes energy-intensive. In contrast, DESs formed using organic acid or sulfonate-based HBAs tended to have lower enthalpies, around -9 to -7 kJ/mol, which points to weaker physical binding. These are easier to regenerate but won't hold as much CO_2. Systems based on neutral organics like menthol, thymol, or pyrazole had very mild interactions, sometimes approaching zero enthalpy, which implies that dissolution was driven almost entirely by weak physical forces.

Based on this chapter, DES35 to DES37, consisting of tetraoctylammonium bromide as HBA and decanoic acid as HBD, were found to have a lower density ~ 0.956 g/cm^3, lower Henry's constant ~ 7.835 MPa, and lower enthalpy of dissolution ~ -10.75 kJ/mol as compared to the other DESs. Hence, for the energy-efficient industrial CO_2 capture process, it is recommended to utilise these DESs.

3.5. Statistical analysis and machine learning modelling of CO_2 dissolution

Statistical analysis was performed to identify significant relationships between thermodynamic properties of DESs and their CO_2 dissolution. The correlation matrix exhibited strong interdependency of DESs-CO_2 solubility on thermodynamic properties, as shown in **Figure 3.4**. The strong positive correlations were observed for CO_2 dissolution with respect to V_{cDES}, T_{cDES}, and V_{free}, suggesting that the higher the values of these parameters, the higher the CO_2 dissolution,

which can also be observed from the data provided in **Table 3.2** and **Table 3.2**. The correlation matrix highlights that CO_2 dissolution in DESs is predominantly governed by physical properties of the solvents. The CO_2 solubility having the strongest positive correlation with pressure suggests that the physical absorption mechanism plays a central role, with structural and volumetric characteristics of DESs being key contributors to CO_2 solubility.

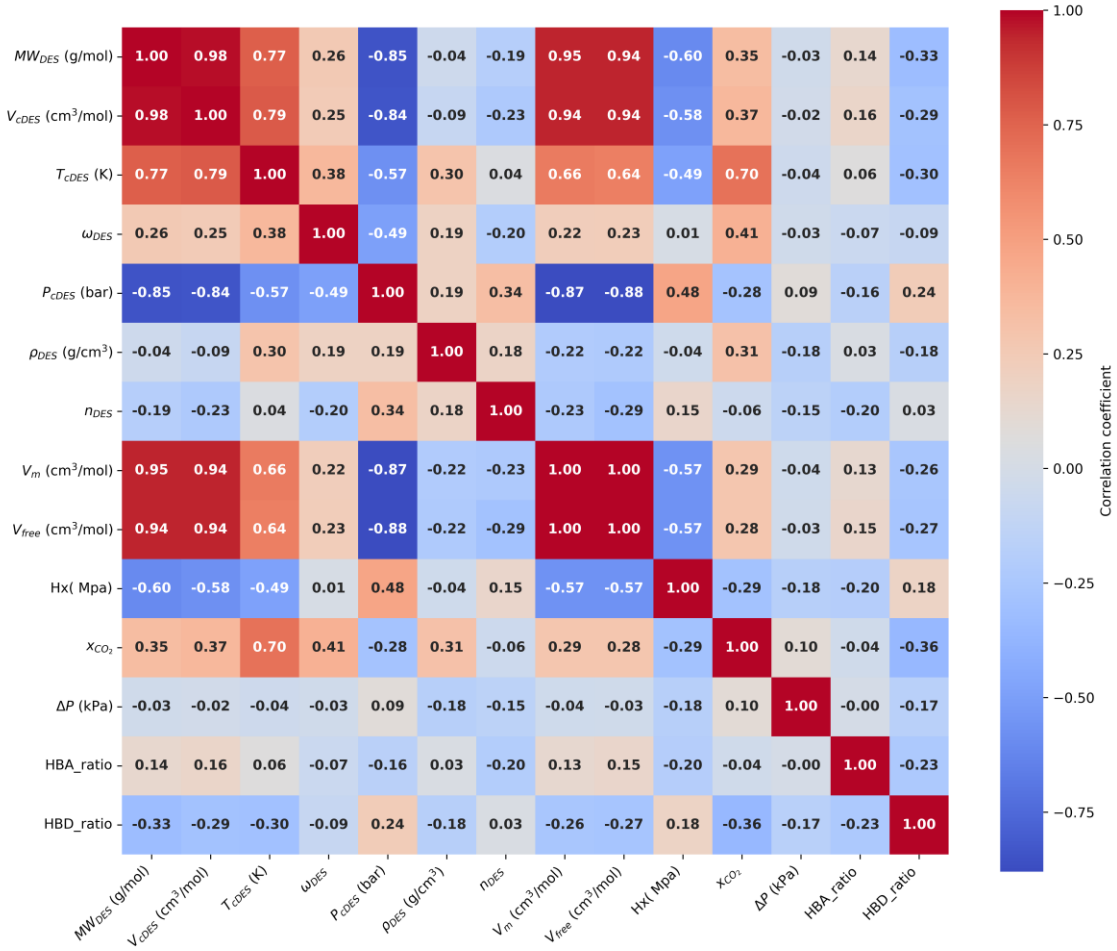

Figure 3.4 Correlation matrix of CO_2 dissolution in DESs

Two machine learning models, Random Forest (RF) and Gradient Boosting (GB), were used to develop predictive models for CO_2 dissolution.

Random Forest (RF) is a bagging-based ensemble learning method that constructs a large number of decision trees during training, each built on an independently bootstrapped subset of the training data. At every internal node of each tree, only a randomly selected subset of input features is considered for splitting, which introduces structural diversity or decorrelation among the individual learners. The final prediction is obtained by averaging the outputs of all trees, which substantially reduces model variance and lowers the risk of overfitting inherent to single decision trees. This "wisdom of the crowd" principle makes RF particularly robust for datasets with moderate dimensionality and complex feature interactions. It is worth noting, however, that RF may still overfit when trees are allowed to grow excessively deep on noisy data, making tree depth a key hyperparameter to monitor.

Gradient Boosting (GB), in contrast, is a sequential ensemble technique rooted in boosting. Trees are constructed in a stage-wise additive manner, where each successive tree is explicitly trained to minimize the residual errors of the combined model up to that point. This correction is governed by the gradient of a differentiable loss function, and each new tree's contribution is scaled by a learning rate (shrinkage parameter), which serves as the primary defence against overfitting by preventing aggressive updating at each stage. This iterative error-minimization strategy allows GB to capture intricate, non-linear structure-property relationships that averaging-based methods may not fully resolve, making it particularly effective at reducing model bias. While the sequential nature of GB training historically imposed a computational cost relative to the parallelizable RF, modern implementations have largely offset this through histogram-based splitting strategies that achieve competitive training speeds.

The dataset (n = 100) was split into training (80%, n = 80) and testing (20%, n = 20) sets. The performance of both models was evaluated using the coefficient of determination (R^2), root mean

square error (RMSE) and mean absolute error (MAE) on both splits. The Random Forest model achieved a training R^2 of 0.979 (RMSE = 0.045, MAE = 0.021) and a testing R^2 of 0.658 (RMSE = 0.105, MAE = 0.048), as illustrated in **Figure 3.5**. The notable gap between training and testing performance reflects a degree of overfitting, consistent with the tendency of RF to memorize training patterns when tree depth is unconstrained. The Gradient Boosting model achieved a training R^2 of 1.000 (RMSE = 0.000, MAE = 0.000) and a testing R^2 of 0.956 (RMSE = 0.037, MAE = 0.019), as illustrated in **Figure 3.6**. While a perfect training fit may appear to indicate overfitting, the strong generalization to unseen data confirms that the model has learned the underlying structure of CO_2 dissolution rather than merely memorizing the training set. Overall, the Gradient Boosting model demonstrated superior predictive capability and was identified as the more reliable model for CO_2 solubility prediction in DES systems. These machine learning models identify the key physicochemical properties of DESs governing CO_2 dissolution, which in turn provides a valuable foundation for techno-economic analysis of the CO_2 capture process at industrial scale.

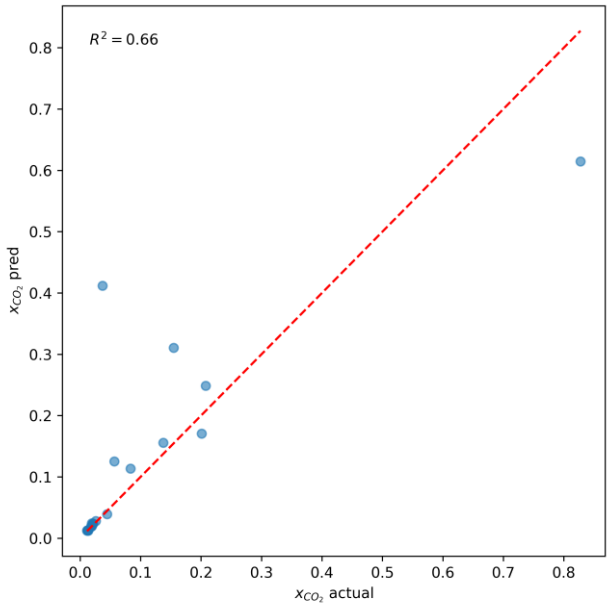

Figure 3.5 Random forest model prediction for CO_2 dissolution

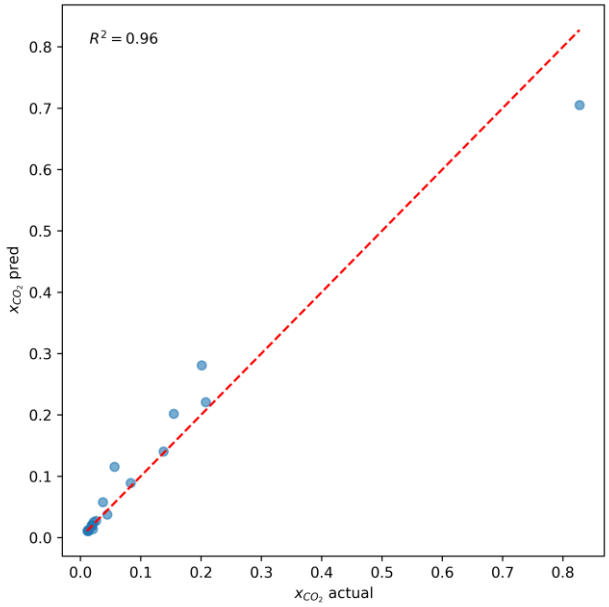

Figure 3.6 Gradient boosting model prediction for CO_2 dissolution

An external validation exercise conducted using the six experimentally synthesized DESs from Chapter 4 revealed that these systems possess Henry's constants in the range of 2.61 to 3.39 MPa, significantly below the training domain mean of 25.39 MPa. The model's predictions carry high uncertainty in this high-performance region, which motivated the development of a dedicated experimental QSPR model in Chapter 4 for this class of DESs.

3.6. Conclusion

This chapter analyzed the thermophysical and thermodynamic properties of 102 DESs to understand their influence on CO_2 dissolution behavior. The properties estimated in **Chapter 2,** such as critical properties, density, refractive index, molar volume, and molar free volume, were correlated with CO_2 capture performance through Henry's constants and dissolution thermodynamics.

Systematic analysis revealed distinct trends based on hydrogen bond donor type. Acid donor-based DESs exhibited lower density and higher molar free volume compared to alcohol and amine donor-based systems. These structural differences directly influenced CO_2 solubility. Henry's constants for acid donor-based DESs were lower than those for amine and alcohol donor-based systems, indicating higher CO_2 absorption capacity. Both hydrogen bond donors and acceptors significantly affected dissolution enthalpy. Alcohol-based donors showed lower enthalpy of dissolution than acid and amine-based donors, suggesting lower regeneration energy requirements.

Statistical correlation analysis identified critical properties and molar free volume as key descriptors. Strong positive correlations were observed between CO_2 dissolution and critical volume, critical temperature, and molar free volume. Machine learning models were developed using these properties as input features. The Gradient Boosting model achieved superior

performance (R^2 = 0.96) compared to the Random Forest model (R^2 = 0.66), demonstrating effective prediction of CO_2 solubility from calculated properties.

Based on the combined analysis of physical and thermodynamic properties, potential DESs for industrial application were identified. The selection criteria included lower density, lower refractive index, higher molar free volume, lower Henry's constant, and lower dissolution enthalpy. DESs comprising tetraoctylammonium bromide as a hydrogen bond acceptor and decanoic acid as a hydrogen bond donor (DES35-37) emerged as promising candidates. These systems exhibited optimal characteristics-lower density, lower Henry's constant, and lower dissolution enthalpy-making them suitable for energy-efficient CO_2 capture processes.

The analysis established clear design principles for rational DES selection. Longer alkyl chains in both HBA and HBD components enhance molar free volume and CO_2 accommodation capacity. Acid-based donors provide favorable thermodynamic properties with lower regeneration energy requirements. These computational insights guided the experimental synthesis and characterization of novel physisorption-based DESs presented in **Chapter 4**.

Declaration of Publication

This chapter draws its substance and methodology from the research originally disseminated in the following peer-reviewed publication:

Gomey, A. K., Haider, M. B., & Kumar, R. (2025). Designing of energy-efficient deep eutectic solvents for CO_2 capture: insights from physical and thermodynamic property evaluation. *Journal of Molecular Liquids*, 434, 127996. https://doi.org/10.1016/j.molliq.2025.127996

Chapter 4

Rational Design of High-Performance DESs for CO_2 Capture: A Synergistic Experimental and Machine Learning Approach

Graphical Abstract

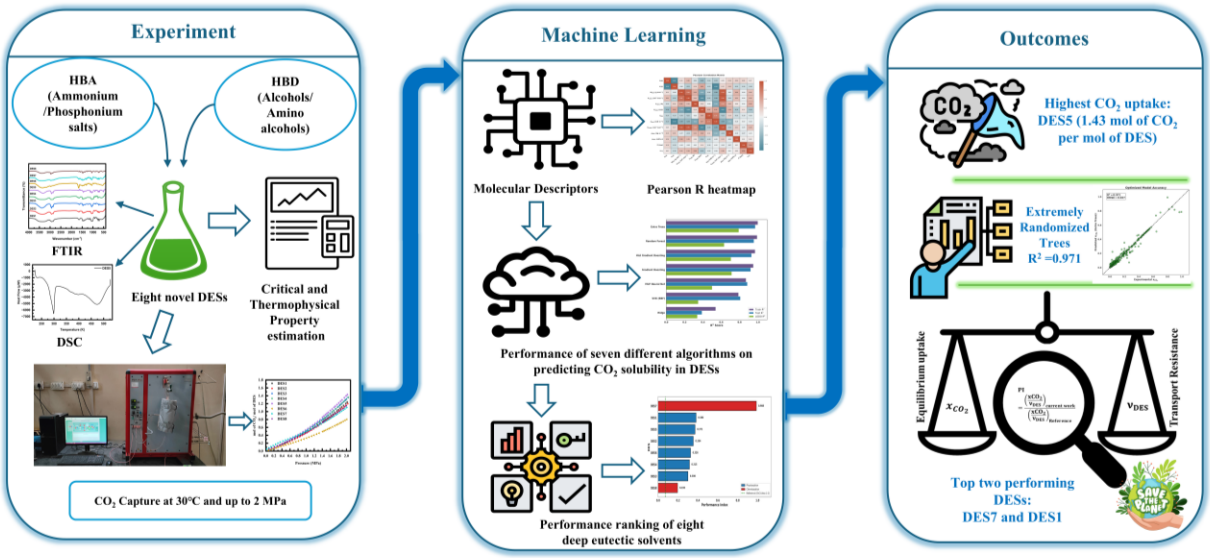

4.1. Introduction

Chapter 2 and 3 established the computational foundation for DES screening and identified key design principles for CO_2 capture. The analysis of 102 DESs revealed that longer alkyl chains and higher molar free volume correlated with enhanced CO_2 dissolution. Thermodynamic analysis showed that alcohol-based donors exhibited the lowest dissolution enthalpy, indicating easier solvent regeneration, though they also demonstrated lower CO_2 uptake capacity compared to acid-based systems. Machine learning models successfully predicted CO_2 solubility from calculated

properties. However, these insights were derived entirely from literature data and theoretical property estimations requiring experimental validation.

This chapter presents the synthesis, characterization, and CO_2 solubility evaluation of eight novel DESs. The design strategy combined ammonium and phosphonium-based hydrogen bond acceptors with a diol donor (1,6-hexanediol) and amino-alcohol donors (2-ethylaminoethanol and 2-amino-2-methyl-1-propanol). The single alcohol donor, 1,6-hexanediol, was selected based on Chapter 3 findings regarding favorable regeneration energetics and the potential for enhanced free volume through longer alkyl chains. Amino-alcohol donors were included to investigate chemical absorption mechanisms alongside physical absorption, enabling comparative analysis of different CO_2 capture pathways within a single experimental framework.

The synthesized DESs were characterized using multiple analytical techniques, including density measurements, viscosity analysis, FTIR spectroscopy, and differential scanning calorimetry. CO_2 solubility experiments were conducted using high-pressure volumetric sorption at 303.15 K up to 20 bars. Henry's constants were determined from low-pressure isotherms for physisorption-based systems. Six DESs (DES1-DES6) exhibited linear physisorption behavior, while two amino-alcohol-based systems (DES7 and DES8) demonstrated mixed-mode absorption involving chemisorption.

Comprehensive quantitative structure-property relationship models were developed using seven machine learning algorithms with rigorous leave-one-out cross-validation. A practical performance index was introduced to balance CO_2 uptake capacity against viscosity constraints, providing rational criteria for industrial solvent selection.

4.2. Materials and Methods

4.2.1. Materials

The chemicals utilized for the synthesis of deep eutectic solvents are listed in **Table 4.1.** All chemicals were used as received without further purification.

Table 4.1 List of chemicals

Chemical	Supplier	CAS number	Purity
Benzyl(triethyl)azanium chloride	S D Fine Chemical Limited	56-37-1	≥ 98%
Benzyl(tributyl)azanium chloride	S D Fine Chemical Limited	23616-79-7	≥ 98%
Tetrapropylazanium bromide	Sisco Research Laboratories	1941-30-6	≥ 99%
Methyl(triphenyl)phosphanium bromide	Molychem	1779-49-3	≥ 98%
Guanidinium chloride	S D Fine Chemical Limited	50-01-1	≥ 98%
Hexane-1,6-diol	Otto Chemie Pvt. Ltd.	629-11-8	≥ 99%
2-(Ethylamino)ethan-1-ol	Acros Organics	110-73-6	≥ 98%
Argon	Purshottam Gas Suppliers	7440-37-1	99.999%
Carbon dioxide	Purshottam Gas Suppliers	124-38-9	99.999%
Dinitrogen	Purshottam Gas Suppliers	7727-37-9	99.999%
Helium	Purshottam Gas Suppliers	7440-59-7	99.999%

4.2.2. Synthesis of deep eutectic solvent

The deep eutectic solvents were synthesized using the process as described by Abbott et al.[36]. The choice of HBA and HBD combinations for the eight DESs was guided by the trends identified in the previous theoretical study[37], specifically favoring long alkyl chains and alcohol/amino-alcohol donors for optimal physisorption. **Table 4.2** presents the structures of HBAs and HBDs

used for the synthesis of the DESs, and **Table 4.3** lists the synthesized DESs. The hydrogen bond acceptors and donors were mixed in a round-bottom flask and placed in a silicone oil bath to maintain a constant temperature of 80 °C. Argon gas served as the inert medium. The mixture was stirred continuously at 500 RPM until a clear, homogeneous solvent was obtained. The solvents were then dried in a vacuum oven for 12 h to eliminate residual moisture [54].

Table 4.2 Structure of hydrogen bond donors and acceptors

S.No.	HBA/ HBD	Chemical Name	Chemical formula	Structure
1.	HBA	Benzyltributylammonium chloride (BTBAC)	$C_6H_5CH_2N(Cl)(C4H_9)_3$	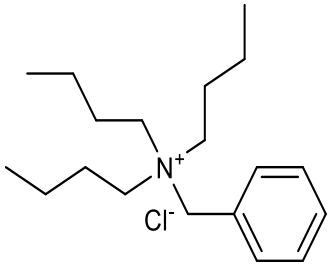
2.	HBA	Benzyltriethylammonium chloride (BTEAC)	$C_6H_5CH_2N(Cl)(C_2H_5)_3$	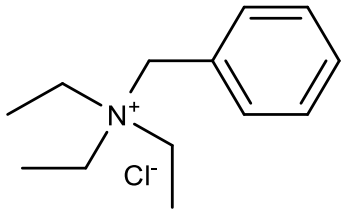
3.	HBA	Guanidine hydrochloride	$NH_2C(=NH)NH_2 \cdot HCl$	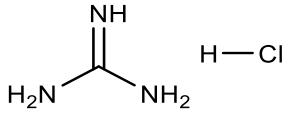
4.	HBA	Tetrapropylammonium bromide (TPAB)	$(CH_3CH_2CH_2)_4N(Br)$	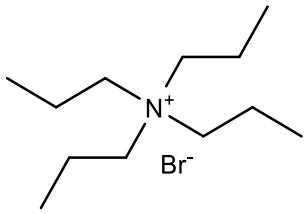

5.	HBA	Methyltriphenylphosphonium bromide (MTPPBr)	$C_{19}H_{18}P.Br$	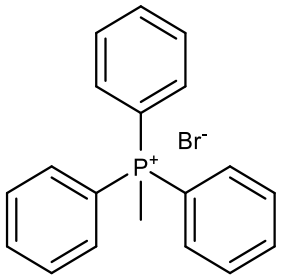
6.	HBD	1,6-hexanediol	$HO(CH_2)_6OH$	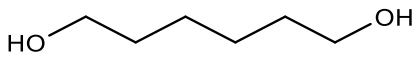
7.	HBD	2-ethylamino ethanol	$C_2H_5NHCH_2CH_2OH$	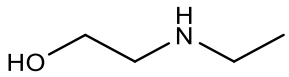
8.	HBD	2-amino-2-methylpropanol	$(CH_3)_2C(NH_2)CH_2OH$	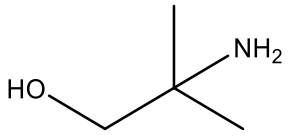

Table 4.3 List of deep eutectic solvents synthesized

DES	Hydrogen bond acceptors	Hydrogen bond donors	Molar ratio	M_{wDES} (g/mol)
DES1	Benzyltriethylammonium chloride	1,6-hexanediol	1:2	140.10
DES2	Benzyltriethylammonium chloride	1,6-hexanediol	1:4	154.71
DES3	Benzyltributylammonium bromide	1,6-hexanediol	1:3	166.61
DES4	Tetrapropylammonium bromide	1,6-hexanediol	1:2	167.54
DES5	Methyltriphenylphosphonium bromide	1,6-hexanediol	1:4	165.98
DES6	Guanidine hydrochloride	2-ethylaminoethanol	1:2	91.27
DES7	Benzyltriethylammonium chloride	2-ethylaminoethanol	1:4	116.87
DES8	Benzyltributylammonium chloride	2-amino-2-methyl-1-propanol	1:4	133.69

4.3. Critical Properties Estimation

Critical properties such as T_c, P_c, and V_c serve as essential parameters in thermodynamic property estimation and phase equilibrium calculations. Measuring these properties through experimental methods proves particularly challenging for heavy molecular compounds, which frequently decompose when exposed to the elevated temperatures required to reach critical conditions[91], [92]. In this study, the critical properties of DESs were determined by employing the computational framework used in **Chapter 2**, given in **Equations (2.1) to (2.12)**[16-18].

Table 4.4 Critical properties of DESs[a]

DES	V_{cDES} (cm^3/mol)	T_{cDES} (K)	ω_{DES}	P_{cDES} (bar)	T_{bDES} (K)
DES1	475.90	704.13	0.98	25.51	531.99
DES2	521.35	714.28	0.92	24.16	539.16
DES3	564.00	737.19	1.02	22.18	569.00
DES4	540.49	699.93	0.94	22.64	532.21
DES5	506.11	766.25	0.98	26.13	580.49
DES6	329.17	637.34	0.68	37.45	441.35
DES7	428.63	642.66	0.70	28.75	461.77
DES8	433.65	684.99	0.72	30.12	504.53

[a]Model uncertainties are approximately $u(V_{cDES}) = \pm 10$ cm^3/mol, $u(T_{cDES}) = \pm 15$ K, $u(\omega_{DES}) = \pm 0.05$, $u(P_{cDES}) = \pm 2$ bar, $u(T_{bDES}) = \pm 10$ K based on typical group contribution method validation.

4.4. Thermophysical properties of DESs

The thermophysical properties, including molar volume, free molar volume, surface tension, density, and heat capacity, were determined using **Equations (2.13) to (2.20)** given in **Chapter 2**. **Table 4.5** presents the computed thermophysical parameters of the deep eutectic solvents.

Table 4.5 Calculated thermophysical properties of deep eutectic solvents at 303.15K[a]

DES	ρ_{DES} (g/cm^3)	n_{DES}	C_{pDES} (J/mol-K)	σ_{DES} (mN/m)	V_m (cm^3/mol)	V_{free} (cm^3/mol)
DES1	1.00	1.48	366.13	18.30	140.22	100.51
DES2	1.04	1.49	355.48	32.78	149.11	106.02
DES3	1.00	1.48	435.49	14.67	166.47	119.16
DES4	1.03	1.47	452.12	30.55	162.00	116.73
DES5	1.09	1.51	435.69	21.00	152.36	107.03
DES6	1.03	NA	463.03	39.38	88.96	NA
DES7	0.94	1.52	352.52	80.51	123.77	86.07
DES8	1.13	1.51	811.30	82.00	118.56	82.86

[a]Standard uncertainties based on model validation are $u(\rho_{DES})$ = 0.015 g/cm^3, $u(n_{DES})$ = 0.01, $u(C_{pDES})$ = 15 J/mol-K, $u(\sigma_{DES})$ = 4 mN/m, $u(V_m)$ = 5 cm^3/mol, $u(V_{free})$ = 5 cm^3/mol.

4.5. CO_2 uptake experiment setup

CO2 absorption capacity was determined employing a SETARAM PCT Pro model D6350 instrument. The experimental setup used CO_2 as the sorbate gas and nitrogen/helium as non-reactive carrier gases. The sample holder valve interfaced with the sample volume cell, which was equipped with a surrounding heating jacket and appropriate thermal insulation. A proportional-integral-derivative (PID) temperature controller ensured isothermal conditions throughout the

experiments. After confirming system hermeticity through leak detection procedures, the apparatus and sample materials were subjected to fifteen hourly purge sequences to eliminate residual atmospheric gases and adsorbed water. Vapor-liquid equilibrium data were acquired using the PCT operational protocol at a constant temperature of 30°C, with pressure conditions ranging from ambient to 20 bar. **Table A1 and A2** show the VLE data for CO_2 in synthesized DESs.

4.6. Characterization

4.6.1. Fourier transform infrared spectroscopy (FTIR) of DESs

Fourier-transform infrared spectroscopy analysis of the prepared deep eutectic solvents was performed using the Thermo Scientific Nicolet iS20 instrument to elucidate intermolecular interactions and hydrogen bonding mechanisms originating from the synergistic interplay between HBAs and HBDs. **Figure 4.1** shows the FTIR spectra of DES1-DES8. The spectral region between 3300 and 3500 cm^{-1} exhibited broad absorption bands attributed to O-H and N-H stretching vibrations, which signify intermolecular hydrogen bonding among the DES constituents. A characteristic downshift of the hydroxyl peak from 3545 cm^{-1} to frequencies below 3500 cm^{-1} was observed consistently across all deep eutectic solvents, confirming the establishment of hydrogen bonding networks[116]. Compared to DES1, DES2 shows a broader absorption band, which reflects more extensive hydrogen bonding interactions resulting from increased HBD availability. In contrast, the absorption feature for DES3 in the 3300-3500 cm^{-1} range appears narrower than those of DES1 and DES2, signifying a less robust hydrogen bonding framework. This attenuation arises from steric effects associated with the voluminous tributyl groups present in the DES3 hydrogen bond acceptor, which impede close-range HBA-HBD associations. Additionally, the halide contribution plays a role, as bromide anions possess lower electronegativity values and diminished hydrogen bonding potential compared to other halides.

Moreover, the coexistence of hydroxyl and amine moieties in the hydrogen bond donor causes superposition of O-H and N-H stretching bands, which is apparent in the spectra of DES6, DES7, and DES8. DES6 displayed the most robust hydrogen bonding network, as confirmed by the intense, broad spectral feature observed in the 3300-3500 cm^{-1} region.

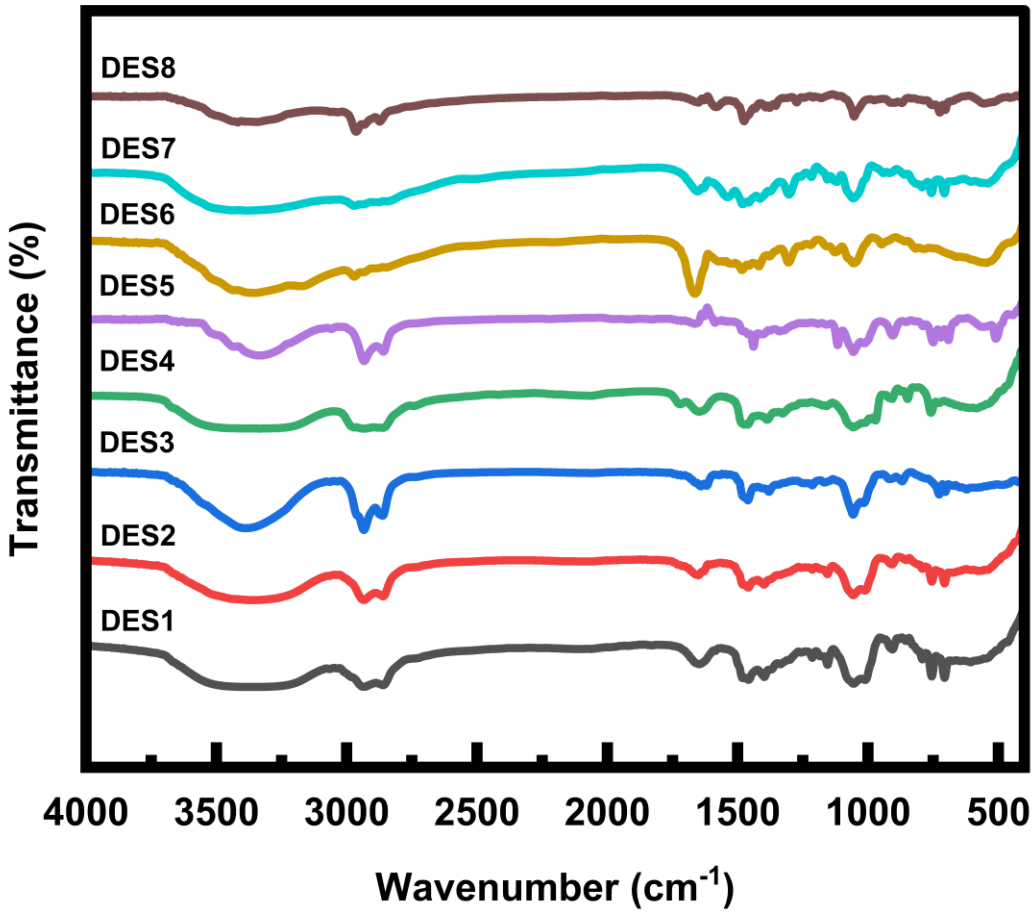

Figure 4.1 FTIR spectra of synthesized DESs[a]

[a]Spectra recorded using Thermo Scientific Nicolet iS20 FTIR Spectrometer with wavenumber accuracy of ±0.01 cm^{-1}. Temperature maintained at 25 ± 0.1°C.

4.6.2. Thermal analysis and phase transition behavior

Determination of the liquid operational window represents a fundamental criterion in solvent screening. The selected solvents should retain their liquid phase during CO_2 absorption operations while avoiding vaporization under desorption temperature conditions. Phase behavior and thermal operating limits of the synthesized DESs were investigated using a Hitachi DSC7020 Differential Scanning Calorimeter. The calorimetric data indicated structural differentiation primarily influenced by the nature of the hydrogen bond donor. DESs containing 1,6-hexanediol (DES1-DES5) presented well-defined melting endothermic peaks, whereas those incorporating amine functionality (DES6-DES8) exhibited glass-forming behavior characteristic of Low Transition Temperature Mixtures (LTTMs). The DSC thermogram of all synthesized DESs is shown in **Figures A1-A8 i**n the **Appendix.** Moreover, considerable disparity in thermal stability characteristics was noted between DESs. In contrast to the thermally stable diol-based systems, amine-functionalized glasses showed erratic baseline deviations beginning at 398.15 K. Such baseline perturbations result from thermal decomposition or vaporization of the amine moiety. Consequently, 398.15K defines the maximum safe temperature for solvent regeneration. **Table 4.6** shows the melting/freezing points of the synthesized DESs.

For 1,6-hexanediol-containing DES formulations, crystallization kinetics proved highly responsive to cation identity and molar ratio modifications. Thermal analysis of DES1 (BTEAC:1,6-Hexanediol, 1:2) revealed complex non-equilibrium phase transitions, including an exothermic cold-crystallization event preceding melting at 268.089 K **(Figure A1)**. These calorimetric features confirm DES1's existence as a kinetically stabilized glass under ambient conditions, where the restricted molecular free volume (100.51 cm^3/mol) impedes rapid crystalline lattice formation during cooling. The resulting elevated viscosity kinetically constrains ionic

reorganization, trapping the system in an amorphous state-a behavior analogous to that observed in ionic liquids, which can potentially hinder CO_2 transport during absorption operations[117]. This metastability was eliminated through stoichiometric modification to a 1:4 molar ratio in DES2, keeping the same HBA-HBD pair, which elevated the fusion onset to 274.861 K **(Figure A2)**. This phase stabilization effect correlates with free volume expansion to 106.02 cm^3/mol. The compositional variation implies that excess 1,6-hexanediol increasingly dictates supramolecular organization, reaching HBD saturation limits and enhancing the lattice cohesive energy required for melting. DES3 (BTBAB:1,6-Hexanediol, 1:3) registered the highest melting transition at 277.474 K **(Figure A3)**, despite exhibiting the largest free volume (119.16 cm^3/mol) among the systems investigated. This counterintuitive observation can be rationalized by the elongated butyl moieties on the cationic species creating interstitial voids (augmenting V_{free}) while concurrently establishing significant hydrophobic associations with the aliphatic framework of the diol molecule. DES4 (TPAB:1,6-Hexanediol, 1:2) presented a broad, attenuated endotherm at 265.982 K **(Figure A4)**. This aligns with the wide eutectic trough seen in its phase diagram, as shown in **Figure 4.2**. The minimum melting point on the phase diagram was identified at 242.380 K for a 1,6-hexanediol mole fraction of 0.8. The substantial width of the eutectic trough correlates with the symmetrical configuration of the tetrapropylammonium cation, which does not possess the aromatic functionality required for π-π stacking interactions exhibited by benzyl-based HBAs[118].

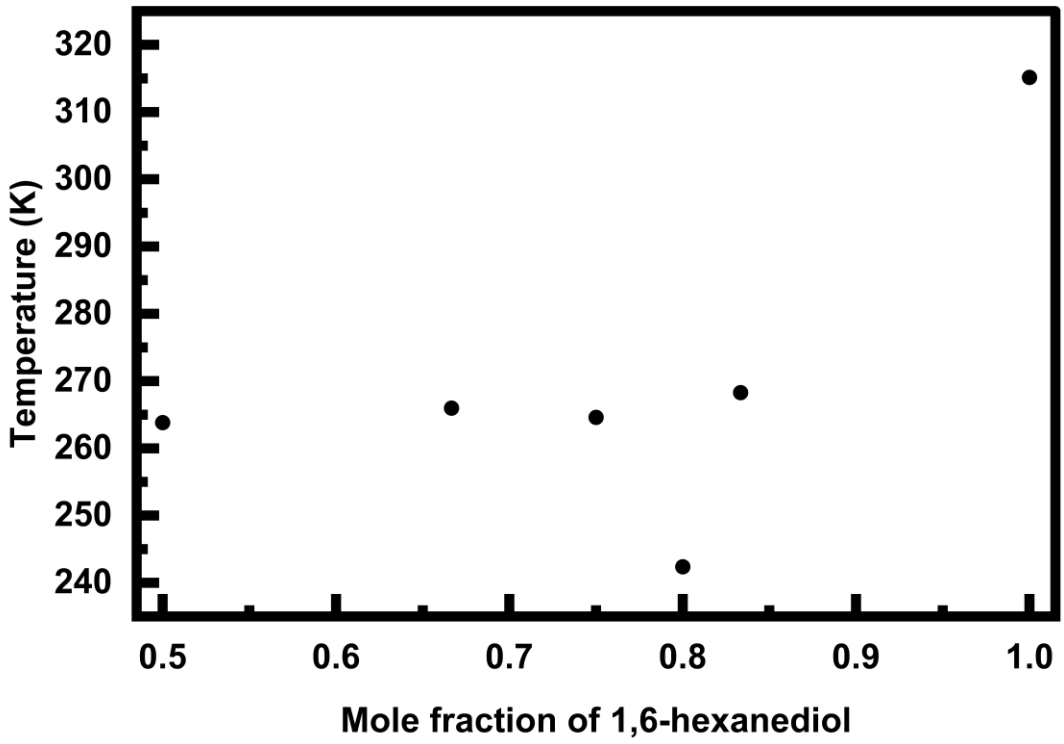

Figure 4.2 Freezing point of tetrapropylammonium bromide with 1,6-hexanediol[a]

[a]Standard uncertainty u(T) = 0.5 K, u(composition) = 0.01 mole fraction. DSC measurements performed with a heating/cooling rate of 10 K/min using Hitachi DSC7020.

DES5 (MTPPB:1,6-Hexanediol, 1:4) exhibited optimal thermal properties for low-temperature operation, characterized by a sharp crystallization exotherm at 259.045 K **(Figure A5)**. This substantial freezing point reduction comes from the expanded atomic radius of the central phosphorus atom, which facilitates charge distribution across the coordinated phenyl moieties through resonance stabilization [119]. The delocalization of positive charge reduces the effective charge concentration on the cation, attenuating ionic interactions with the anion and yielding a considerably lower melting transition temperature than observed in corresponding ammonium salts [120], [121]. A eutectic melting temperature of 250.30 K was identified for the DES

synthesized from methyltriphenylphosphonium bromide and 1,6-hexanediol at a diol composition of 0.75 mole fraction, as shown in **Figure 4.3**.

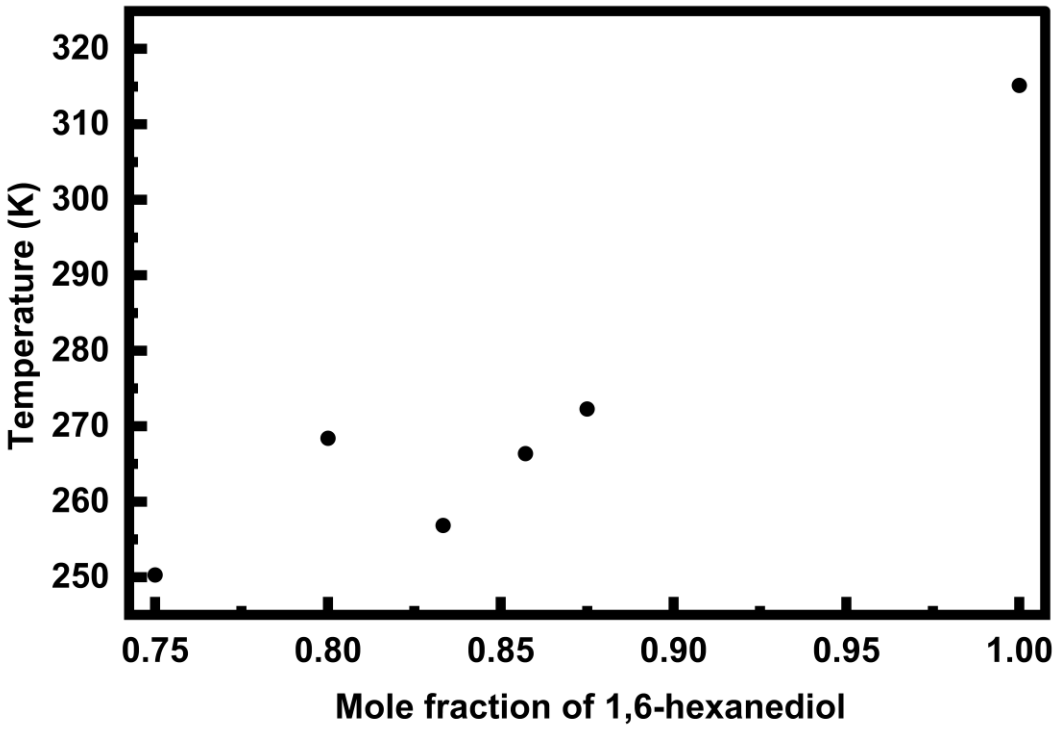

Figure 4.3 Freezing point of MTPPBr with 1,6-hexanediol[a]

[a]Standard uncertainty u(T) = 0.5 K, u(composition) = 0.01 mole fraction. DSC measurements performed with a heating/cooling rate of 10 K/min using Hitachi DSC7020.

The crystalline behaviour was notably absent in amine-functionalized variants (DES6-DES8). The amine-based DESs exhibited a featureless baseline across the melting temperature range, with only a glass transition manifesting near 228.15 K (T_g) in the DSC thermogram. This thermal pattern represents the defining signature of Low Transition Temperature Mixtures (LTTMs), as shown in **Figures A6-A8.** Moreover, considerable disparity in thermal stability characteristics was noted

between DESs. In contrast to the thermally stable diol-based systems, amine-functionalized glasses showed erratic baseline deviations beginning at 398.15 K. Such baseline perturbations result from thermal decomposition or vaporization of the amine moiety. Consequently, 398.15K defines the maximum safe temperature for solvent regeneration.

Table 4.6 Thermal Transitions and Phase Behavior of synthesized DESs

DES	Phase Behavior	Freezing/melting temperature (K)
DES1	Crystalline (Metastable)	268.089
DES2	Crystalline	274.861
DES3	Crystalline	277.474
DES4	Semi-Cryst.	265.982
DES5	Crystalline	259.045
DES6	Glass (LTTM)	Liquid at room temperature
DES7	Glass (LTTM)	Liquid at room temperature
DES8	Glass (LTTM)	Liquid at room temperature

4.6.3. Density of DESs

Density is an essential physicochemical property of DESs, offering insight into their molecular structures and interactions. Precise density measurements facilitate the validation of the quality and composition of synthesized DESs, while also offering critical insights into the viability of several industrial uses of these DESs [122]. The systematic study of density helps us understand how molecules are packed together and how forces work between molecules in these systems. This is important knowledge for designing and improving processes[123]. The density of the deep eutectic solvents was measured using an Anton Par density meter model DMA 4100 M at different temperatures: 293.15 K, 303.15 K, and 313.15 K, as listed in **Table 4.7**.

Table 4.7 Densities of deep eutectic solvents at different temperatures[a].

DES	Temperature (K)/ Density (g/cm^3)		
	293.15	**303.15**	**313.15**
DES1	1.0263	1.0205	1.0147
DES2	1.0071	1.004	0.9957
DES3	0.9899	0.982	0.9786
DES4	1.0504	1.0442	1.0380
DES5	1.1003	1.0933	1.0877
DES6	1.0430	1.0303	1.0293
DES7	0.9842	0.9770	0.9699
DES8	0.9678	0.9604	0.9531

[a]Standard uncertainties u are u(T) = 0.03 K, u(ρ) = 0.0001 g/cm^3. Densities measured using Anton Paar DMA 4100 M density meter with calibration verified against ultrapure water and air at 20°C.

The experimental density values were fitted using the following linear equation:

$$\rho = a + bT \quad (4.1)$$

where ρ is the density in kg/m^3, T is the temperature in Kelvin, and a and b are the fitting parameters. The fitting parameters and standard regression metrics are presented in **Table 4.8**.

Table 4.8 Fitting parameters of the linear density equation of DESs[a]

DES	a*(g/cm^3)	(-b*10^3) (g/cm^3-K)
DES1	1.196	0.580
DES2	1.175	0.570
DES3	1.155	0.565
DES4	1.232	0.620
DES5	1.285	0.630
DES6	1.242	0.680
DES7	1.194	0.710
DES8	1.183	0.740

[a]Standard uncertainties in parameters are u(a) ≤ 0.002 g/cm^3, u(b) ≤ 5×10^{-5} g/cm^3-K.

The densities of the DESs were also calculated using **Equation (2.15)** and compared with the experimental values as reported in **Table 4.9**.

Table 4.9 Experimental and calculated densities of DESs at 303.15 K[a]

DES	ρ_{exp}	ρ_{calc}	Error	RD%	ARD%
DES1	1.004	0.999	0.005	0.489	0.489
DES2	1.021	1.038	-0.017	-1.642	1.642
DES3	0.982	1.014	-0.032	-3.139	3.139
DES4	1.044	1.034	0.010	0.967	0.967
DES5	1.093	1.089	0.004	0.355	0.355
DES6	1.030	1.026	0.004	0.424	0.424
DES7	0.977	0.944	0.033	3.473	3.473
DES8	0.960	1.128	-0.167	-14.830	14.830

[a]Standard uncertainties u are u(T) = 0.03 K, u(ρexp) = 0.0001 g/cm^3. Calculated densities from group contribution method with u(ρcalc) = 0.015 g/cm^3.

The theoretical density predictions showed satisfactory harmony with experimental data, with maximum deviations remaining within 3%. The phosphonium-based DES from MTPPBr and 1,6-hexanediol of a 1:4 molar ratio exhibited the greatest density (1.093 g/cm^3), which can be rationalized by the higher molecular mass and compact structure of the phosphonium cation [124]. The role of HBD molar composition is evident in BTEAC-1,6-hexanediol systems, where increasing the diol ratio from 1:2 to 1:4 results in density enhancement from 1.004 g/cm^3 to 1.021 g/cm^3. This systematic variation demonstrates that elevated 1,6-hexanediol concentrations promote more compact molecular arrangements in the eutectic mixture [122]. BTBAC-based DESs exhibited lower densities relative to their BTEAC-based DESs, with the BTBAC-AMP DES (1:4) having the minimum density of 0.960 g/cm^3 among all DESs. An increase in density was observed to scale proportionally with the degree of hydroxyl substitution in the hydrogen bond donor. This hydroxyl-density relationship rationalizes the elevated densities characteristic of hexanediol-based DESs compared to DESs incorporating 2-ethylaminoethanol or AMP as HBD components [122], [125].

4.6.4. Viscosity of DESs

Viscosity constitutes one of the most pivotal thermophysical characteristics governing operational costs and the industrial viability of DES systems. Comprehensive evaluation of viscosity behavior is vital for process engineering applications, as it exerts significant influence on equipment design, mass transfer rates, energy requirements, and overall process economics [27-29]. Dynamic viscosity determination was carried out using an Anton Paar Modular Compact Rheometer (MCR 302e) within the operational temperature window of 20-50 °C, as depicted in **Figure 4.4**. The corresponding experimental data are provided in Appendix **Tables A3-A4**. All synthesized deep eutectic solvents exhibited Arrhenius-type viscosity behavior, characterized by viscosity reduction

with increasing temperature, a transport phenomenon ubiquitous in conventional molecular solvents [49]. This phenomenon can be explained by the weakening of interactions between HBDs and HBAs as thermal energy increases. The elevated temperature promotes enhanced molecular mobility, subsequently leading to a reduction in viscosity.

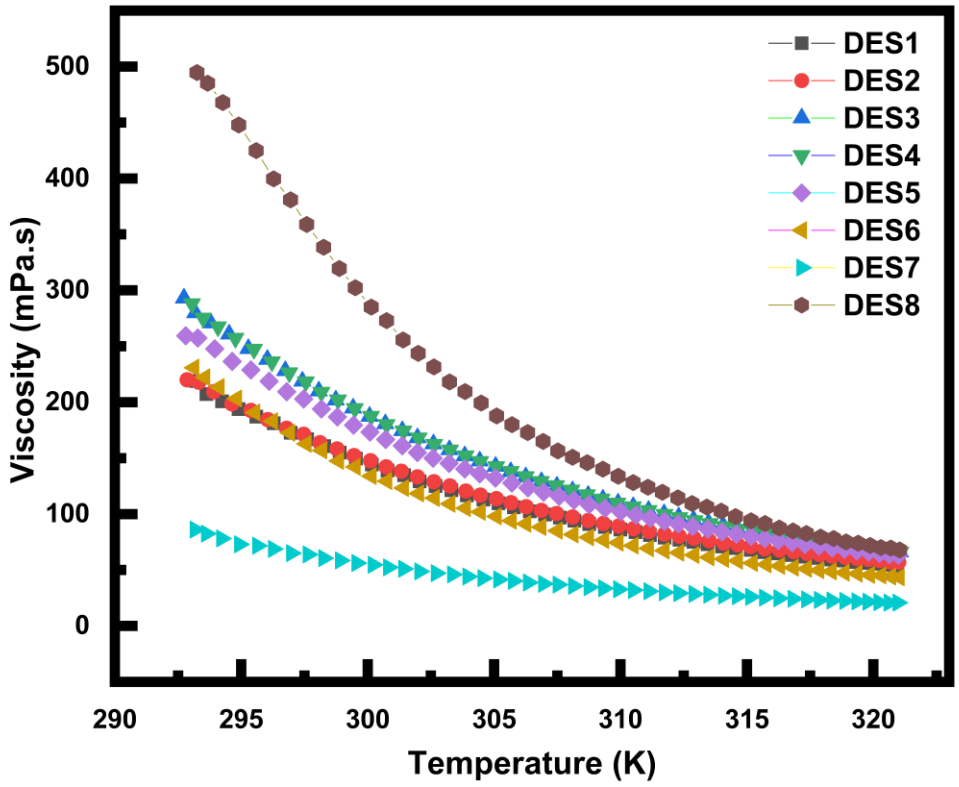

Figure 4.4 Viscosity of DESs at different temperatures[a]

[a]Standard uncertainty u(η) = 1.0% of reading (relative) and u(T) = 0.05 K.

Two empirical models: the Arrhenius equation (containing two adjustable parameters) and the Vogel-Fulcher-Tammann-Hesse (VFTH) equation (containing three adjustable parameters), represented by Equations **(4.2) and (4.3)**, respectively, were employed to validate the experimental viscosity of the DESs as shown in **Figures 4.5-4.6**[127].

$$\eta = \eta_{arr} e^{\frac{E_a}{RT}} \quad (4.2)$$

$$\eta = \eta_{vft} e^{\frac{B}{T-T_\circ}} \quad (4.3)$$

The parameters of both equations are given in **Table 4.10**.

Table 4.10 Correlation coefficients of Arrhenius and VFT equations

DES	Arrhenius Equation[a]			VFT Equation[a]			
	η_{arr} (mPa.s)	Ea (kJ/mol)	R^2	η_{VFT} (mPa.s)	B (K)	$T_\circ$ (K)	R^2
DES1	2.130E-05	39251.23	0.998	0.16	829.22	177.94	0.999
DES2	3.043E-05	38428.14	0.997	0.74	503.06	205.07	0.999
DES3	1.367E-05	41002.15	0.992	0.03	1306.12	148.63	0.999
DES4	1.262E-05	41204.00	0.999	0.02	1446.27	140.88	0.999
DES5	1.610E-05	40414.40	0.998	0.25	744.46	186.32	0.999
DES6	1.216E-06	46267.47	0.995	0.47	470.28	217.10	0.999
DES7	5.951E-06	40053.53	0.992	0.76	303.56	229.17	0.997
DES8	2.701E-08	57598.56	0.998	0.05	920.31	194.65	0.999

[a]Standard uncertainties in experimental viscosity are u(η) = 1.0% of reading (relative), u(T) = 0.05 K. Fitting parameters uncertainties are u(ln A) = 3%, u(Ea) = 5 kJ/mol, u(B) = 50K, u($T_\circ$) =5 K.

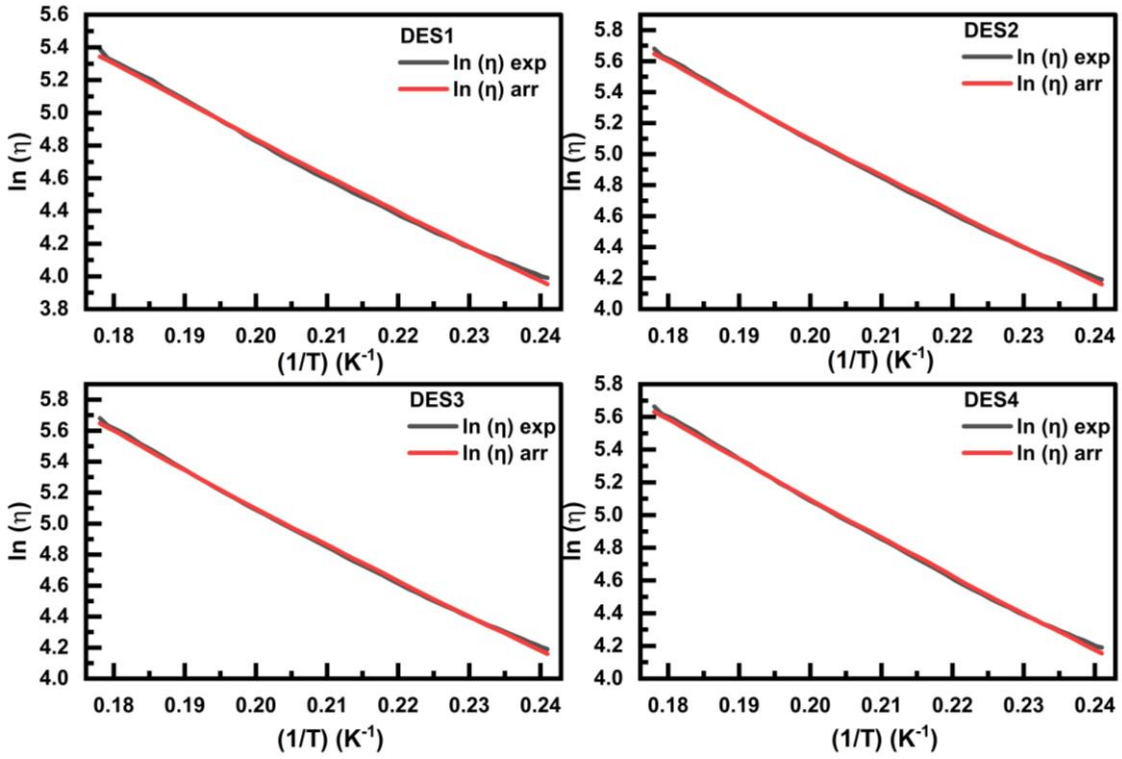

(a)

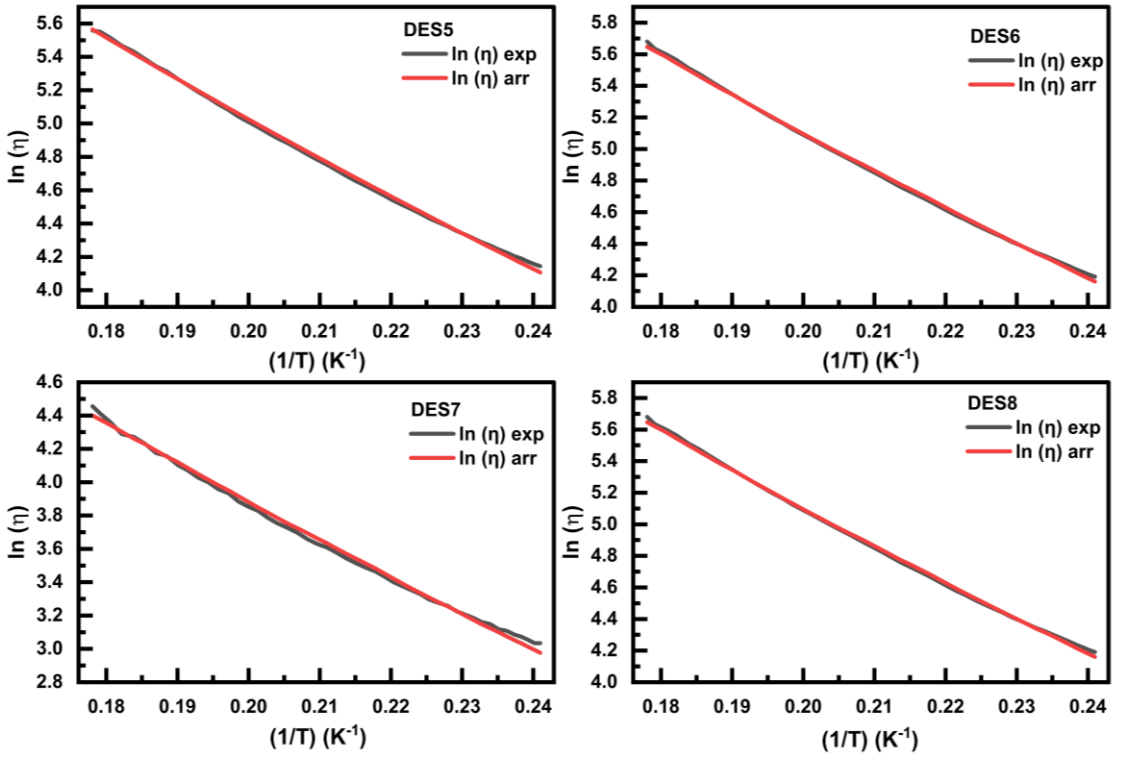

(b)

Figure 4.5 ln η vs 1/T plot for Arrhenius equation (a) DES1-4 (b) DES5-8

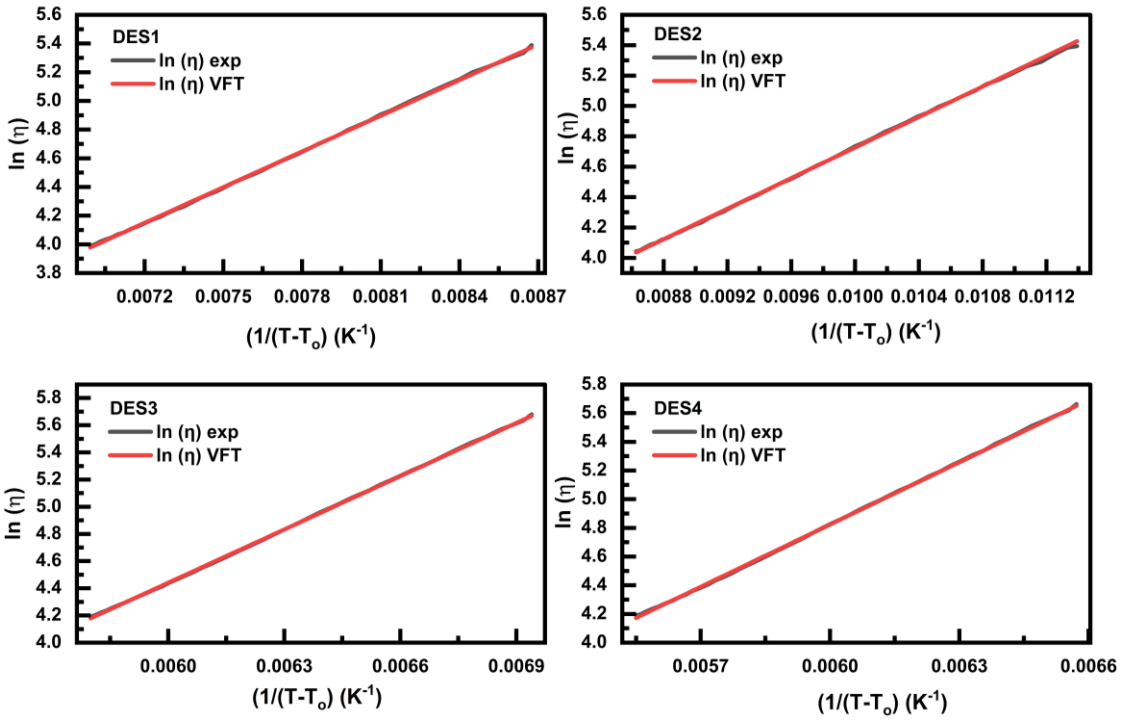

(a)

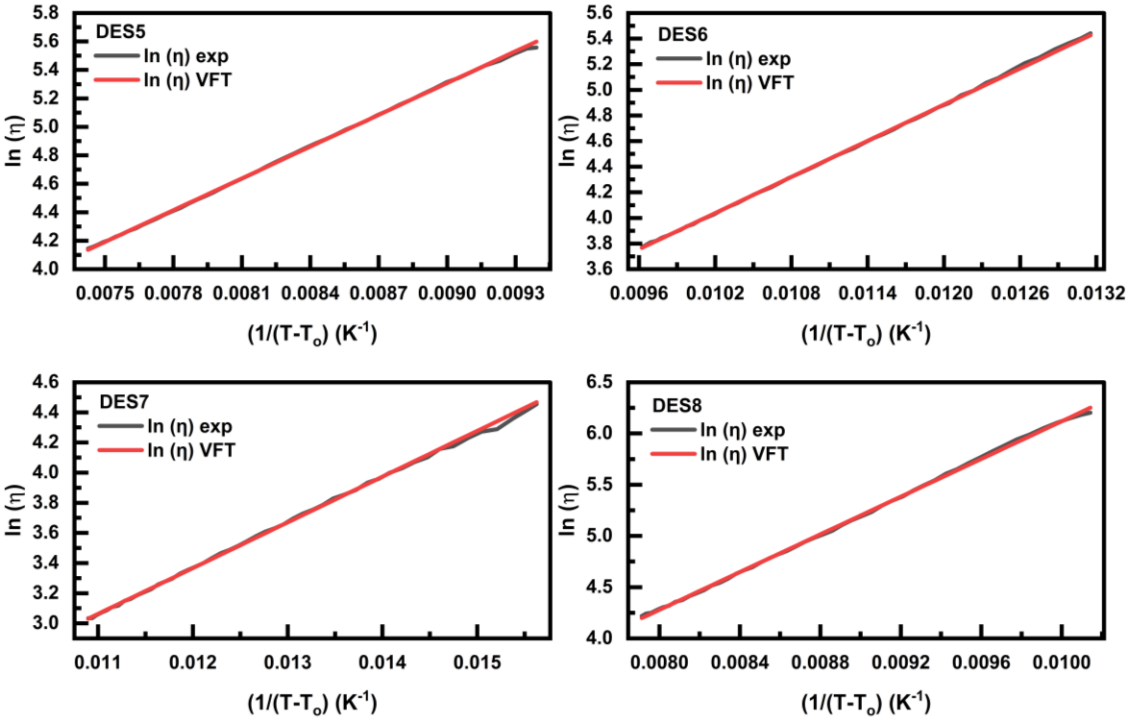

(b)

Figure 4.6 ln η vs 1/(T-T$_o$) plot for VFT equation (a) DES1-4 (b) DES5-8

4.7. CO_2 solubility in DESs

The CO_2 uptake behavior of the synthesized DESs was examined at 30°C under pressures ranging up to 20 bar using a high-pressure volumetric sorption analyzer, as discussed in **Section 4.5**. The solubility curve representing the CO_2 uptake capability of various DESs is shown in **Figure 4.7 and Tables A1-A2.** It was observed that DES5 showed the highest solubility compared to other DESs. This can be attributed to its phosphonium-based aromatic cation, enhancing van der Waals interactions and the high HBD ratio, providing abundant hydroxyl groups for physical absorption[32-36]. Furthermore, as illustrated in **Figure 4.7**, DES3 demonstrates greater CO2 uptake than both DES1 and DES2. This is because DES3 has a higher $V_{free,}$ as evident from **Table 4.5**, which arises from the longer alkyl chains of the BTBAC cation creating greater void space that accommodates CO_2 molecules and facilitating physical absorption[55]. Additionally, comparison of DES1 (1:2) and DES2 (1:4), which have the same HBA-HBD pairs, revealed a positive correlation between HBD molar ratio and CO_2 solubility. This compositional effect was likely attributed to the increased concentration of diol molecules at higher HBD ratios, which expanded both the hydrogen bonding network and the available free volume (DES2: 106.02 cm^3/mol; DES1: 100.51 cm^3/mol), thereby enhancing CO_2 capture capacity[132]. It was also observed that alcohol-based DESs (DES1-5) performed better than amino-alcohol-based DESs (DES6-8), which reflects that amino-alcohol DESs form stronger hydrogen-bond networks, which reduce free volume and hinder CO_2 diffusion[133].

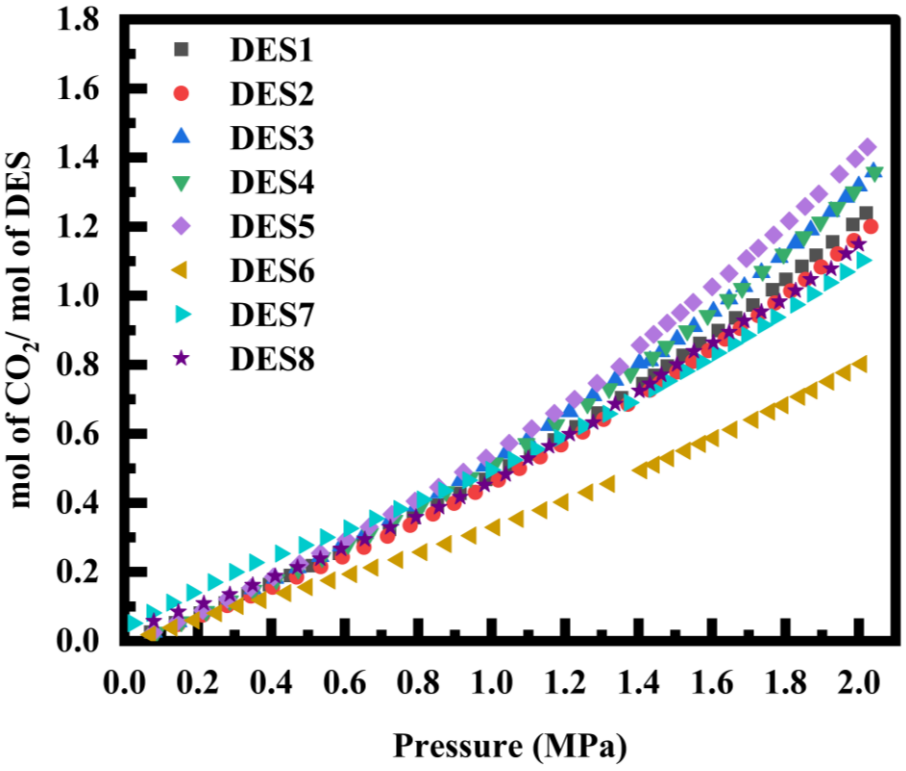

Figure 4.7 CO_2 solubility isotherms for DES1-DES8 at 30°C (0-2 MPa)

4.7.1. Henry's Constant

The CO_2 solubility in DESs can be described using Henry's Law, which was estimated by **Equation (3.3)**. Although solubility data were acquired across pressures up to 2 MPa, Henry's law constants (H_x) were strictly extracted from the initial slope of the isothermal solubility curves in the low-pressure limit ($P \rightarrow 0$), where the fugacity-mole fraction relationship remains linear. This approach fulfils the infinite dilution criteria $\lim_{x \to 0} \frac{f^{CO_2}}{x_{CO_2}}$ essential for Henry's law validity, ensuring that the calculated constants accurately capture the solvent's inherent CO_2 dissolution capacity unperturbed by non-idealities arising at higher pressures. For the DES-CO_2 system under experimental conditions, since deep eutectic solvents have negligible vapor pressure, the vapor phase consists entirely of CO_2, and therefore the fugacity of CO_2 in the vapor phase equals the

fugacity of pure CO_2 in the system conditions. **Table 4.11** compares Henry's constant of current work with the literature.

Table 4.11 Henry's law constants for CO_2 solubility in DESs at 303.15K[a]

DES	Henry's Constant	References
DES1	2.78	Current work
DES2	3.01	Current work
DES3	2.70	Current work
DES4	2.77	Current work
DES5	2.61	Current work
DES6	3.39	Current work
DES7	NA	Current work
DES8	NA	Current work
Bet-1,2Pro-DBU (1:6.002:1.001)	2.56	[134]
Bet-1,2Pro-DBN (1:6.001:0.999)	2.69	[134]
Bet-1,2Pro-TMG (1:5.999:1.003)	2.62	[134]
Bet-DEG-DBU (1:6.001:1.003)	2.58	[134]
Bet-DEG-DBN (1:5.998:0.998)	2.72	[134]
Bet-DEG-TMG (1:6.003:0.999)	3.54	[134]
ChCl/6MDEA	10.32	[49]
ChCl/7MDEA	6.162	[49]
ChCl/6DEA	7.155	[49]
L-Histidine-Hexanoic acid (1:2)	20.16	[80]
L-Cystine-Hexanoic acid (1:2)	18.34	[80]
L-Lysine-Oxalic acid (1:2)	17.85	[80]
L-Lysine-Decanoic acid (1:2)	7.51	[80]
L-Alanine-Decanoic acid (1:2)	19.65	[80]
L-Histidine-Decanoic acid (1:2)	4.53	[80]
L-Cystine-Decanoic acid (1:2)	10.71	[80]
Decanoic acid-Lidocaine (2:1)	7.91	[81]
Menthol-Decanoic acid (2:1)	8.58	[81]
Tetrapropylammonium Bromide-Formic Acid (1:2)	20.22	[82]
Ethanolamine hydrochloride - Tetraethylenepentamine (1:9)	2.87	[83]
L-menthol-Thymol (1:2)	9.61	[84]
Thymol-2,6-Xylenol (1:1)	11.46	[84]
Tetrabutylammonium bromide-Octanoic acid (1:2)	13.36	[90]

Tetrabutylammonium bromide-Decanoic acid (1:2)	10.52	[90]
DL-Menthol-Dodecanoic acid (2:1)	12.46	[90]

*NA: Henry's constant is not applicable due to non-linear solubility behavior at low pressure, indicating mixed-mode absorption (chemisorption + physisorption).

[a]Standard uncertainties u are u(T) = 0.1 K and u(P) = 1.0% of reading. The uncertainty in Henry's constant (u(Hx)) is estimated at ± 5%.

It is evident from **Table 4.11** that six out of eight DESs: DES1-DES6 exhibited Henry's law constants within the 2.61-3.39 MPa range at 303.15 K, indicating favorable CO_2 physisorption characteristics under mild pressure conditions. Among these, DES5 (2.61 MPa) and DES3 (2.70 MPa) registered the lowest Henry's constants, remarkably achieving this performance with uncomplicated binary formulations. Literature values for established choline chloride-amine eutectic systems, specifically ChCl/6MDEA (10.32 MPa) and ChCl/6DEA (7.16 MPa), demonstrate that these benchmark solvents demand markedly higher operating pressures to deliver comparable CO_2 absorption.[49].

Amine-functionalized deep eutectic solvents exhibited a distinctive shift in absorption behavior. For DES7 and DES8, thermodynamically consistent Henry's constants were unattainable (indicated as NA in **Table 4.11**) due to significant isotherm non-linearity observed in the low-pressure regime ($P < 0.2$ MPa). This deviation signifies hybrid absorption kinetics, where nucleophilic amine groups (2-ethylaminoethanol and AMP) participate in swift chemical reaction with CO_2 molecules at low fugacity, subsequently transitioning to physical dissolution at higher pressures. Consequently, Henry's law formalism, predicated on non-reactive infinite dilution conditions, yields values lacking thermodynamic validity for these two systems.

In contrast, DES6 (Guanidine·HCl:2-ethylaminoethanol, 1:2) demonstrated primarily physisorption-driven uptake, notwithstanding the presence of identical amine functionality found in DES7. This mechanistic differentiation was substantiated by dual experimental evidence: (i) DES6 exhibited the lowest absolute CO_2 absorption (0.80 mol/mol) among the complete solvent series, inconsistent with the high-capacity performance characteristic of amine-based eutectic solvents; and (ii) the solubility curve maintained linear behavior in the dilute pressure region ($P < 0.35$ MPa), enabling determination of a valid Henry's constant (3.39 MPa). This phenomenon indicates that amine moieties in DES6 are either sterically restricted or extensively integrated within the robust supramolecular hydrogen bonding network characteristic of the eutectic structure (in agreement with observed glass-forming behavior), consequently limiting their thermodynamic availability for CO_2 chemical binding.

Although select ternary compositions (e.g., Bet-1,2Pro-DBU and Bet-DEG-DBN) have been reported to yield slightly reduced Henry's constants (2.56-2.72 MPa), their multi-component nature and exacting compositional control requirements complicate large-scale manufacturing processes. Binary DES5 synthesized herein achieved virtually identical CO_2 affinity (2.61 MPa) while circumventing ternary formulation complexity. This work thus demonstrates that strategically engineered binary deep eutectic solvents can effectively integrate high physical absorption efficiency with straightforward synthetic procedures and practical industrial scalability.

4.8. Machine Learning-QSPR analysis of CO_2 uptake

The CO_2 solubility behavior of DESs is influenced by various interrelated thermophysical and thermodynamic parameters [90], [135]; therefore, a comprehensive evaluation of structural descriptors was required to isolate parameters exhibiting the strongest correlation with absorption

performance. A robust Quantitative Structure-Property Relationship (QSPR) methodology was developed to expedite the identification of promising DES candidates for CO_2 capture applications. The QSPR model development was based on two datasets: primary experimental data produced herein, and a larger secondary dataset aggregated from published studies [37], [136], [137], [138] of 3694 datapoints, harmonized for the QSPR modelling for CO_2 solubility in DESs. This computational framework strategically integrates mechanistic interpretability with accelerated virtual screening, incorporating systematic robustness validation throughout the model development pipeline. The inclusion of a binary flag (Is_Chemisorption) facilitated discrimination between DESs operating via physisorption or chemisorption pathways. This classification parameter enabled the algorithm to concurrently model distinct CO_2 solubility behaviors exhibited by both chemically active and inert eutectic solvents within a unified QSPR architecture.

4.8.1. Pearson R

This section explores linear correlations between measurable DES properties and carbon dioxide solubility (xCO_2) across the experimental formulations. A descriptor set comprising twelve physicochemical variables was established to elucidate structure-property relationships governing CO_2 uptake: thermodynamic operating parameters (T, P); bulk physical properties encompassing ρ_{DES} and M_{wDES}; transport characteristics represented by μ_{DES}; interfacial tension denoted by σ_{DES}; stoichiometric composition (x_{HBA}, x_{HBD}); and critical state properties (T_{cDES}, P_{cDES}, and V_{cDES}). Pearson's correlation coefficients (r) were calculated to assess bivariate linear associations, with values ranging from -1 (perfect negative relationship) to +1 (perfect positive relationship)[139], [140]. These associations are visualized in the color-coded heat map as shown in **Figure 4.8**.

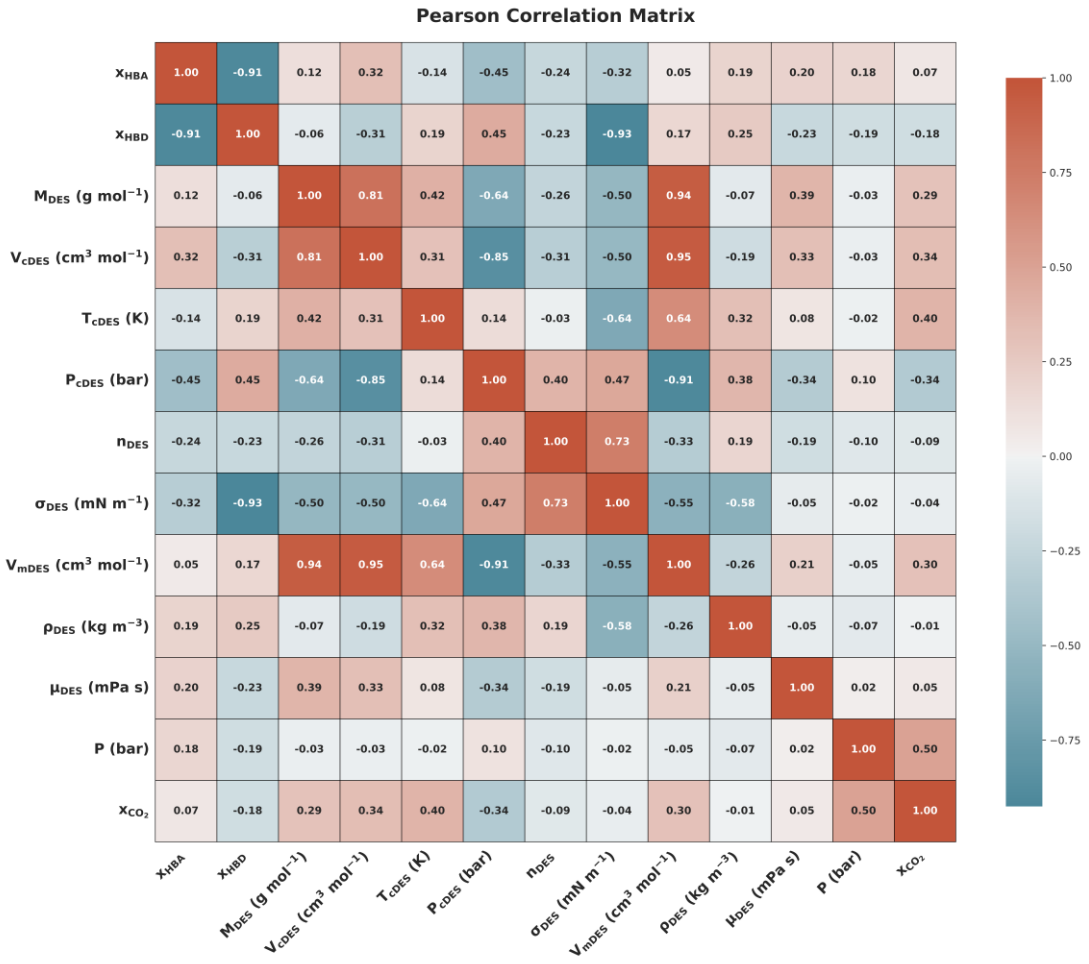

Figure 4.8 Pearson correlations between CO_2 solubility and DES descriptors

Positive correlation coefficients were identified between xCO_2 and the following descriptors: M_{wDES} (r = 0.29), V_{cDES} (r = 0.3), T_{cDES} (r = 0.40), V_{mDES} (r = 0.30), and pressure P (r = 0.50), validating that molecular cavity dimensions, volumetric parameters, and thermodynamic potential collectively enhance gas solubility within the experimental range studied. Notably, critical pressure exhibited an inverse relationship (r = -0.34), implying that elevated lattice energy and stronger cohesive forces restrict CO_2 accommodation within the DES matrix.[141]. Other physicochemical properties, such as density, refractive index, surface tension, viscosity, and

compositional stoichiometry (HBA:HBD ratio) displayed weak linear associations ($|r| < 0.25$) with xCO_2, implying that these factors do not substantially govern equilibrium gas solubility in the examined DES systems.

4.8.2. Rigorous model selection, benchmarking and optimization

A fundamental concern in developing predictive models for DESs involves the risk of algorithmic overfitting, wherein the model captures system-specific patterns rather than underlying physicochemical relationships governing solubility. To address this challenge, a stringent validation methodology termed Leave-One-DES-Out (LODO) cross-validation, derived from the Leave-One-Group-Out (LOGO) validation paradigm, was employed to evaluate model robustness. The predictive performance of several machine learning approaches was assessed: tree-based ensemble methods including Random Forest, Extremely Randomized Trees, Gradient Boosting, and Histogram-based Gradient Boosting; Ridge regression as a regularized linear baseline; and a multilayer perceptron representing deep learning methodologies. As shown in **Figure 4.9**, it was revealed that tree-based ensemble algorithms outperformed both linear regression and neural network models in terms of generalization accuracy.

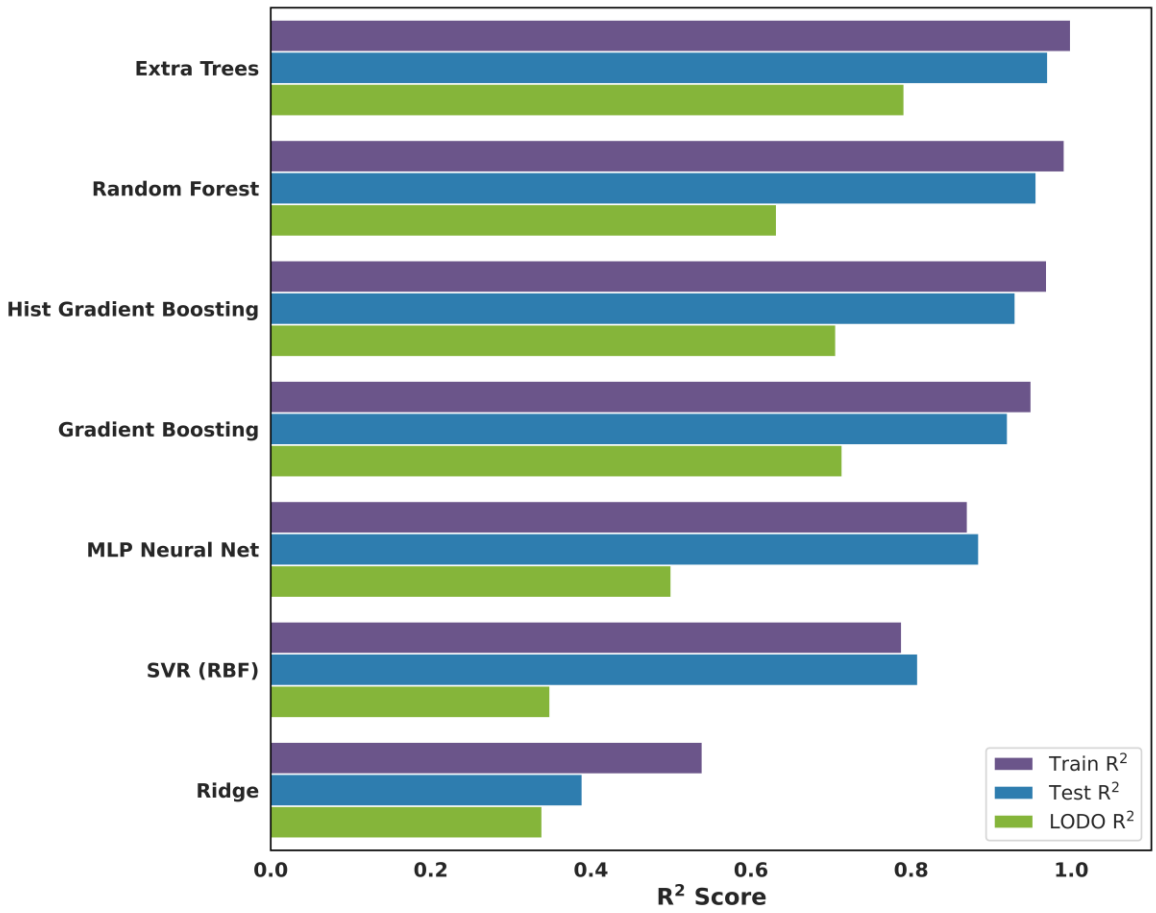

Figure 4.9 Comparison of seven algorithms predicting CO_2 solubility in DESs

Among the evaluated algorithms, Extremely Randomized Trees emerged as the optimal model, delivering a training coefficient of determination (R^2) of 0.969 and a robust LODO validation R^2 of 0.766. This validation performance significantly surpasses that of the Random Forest algorithm, which achieved a training R^2 of 0.952 but suffered substantial generalization degradation with a LODO R^2 of 0.646. The divergent validation performance stems directly from algorithmic architectural differences in decision tree construction. Extremely Randomized Trees conducts randomized split threshold selection following optimization of the random selection process, utilizing the entire training dataset. This stochastic splitting strategy facilitates learning of generalizable physicochemical relationships while avoiding overfitting to dataset-specific

artifacts, thereby yielding superior predictions for previously unencountered solvent systems. Conversely, Random Forest implements bootstrap sampling combined with greedy optimization to identify locally optimal split criteria. While this deterministic optimization approach appears advantageous, it paradoxically promotes model memorization of training examples, resulting in degraded predictive capability when extrapolating to structurally novel DES compositions [59].

The Extremely Randomized Trees algorithm was designated as the optimal modeling approach and subsequently underwent hyperparameter tuning to enhance prediction precision. Model performance assessment via parity plot analysis (**Figure 4.10**) demonstrated that predicted solubility values exhibit tight clustering along the unity line (y = x), indicating robust predictive capability. These results confirm that the curated set of molecular and thermodynamic descriptors provides sufficient information content for accurate CO_2 solubility prediction in DES systems.

Interpretability analysis was performed using the SHAP (SHapley Additive exPlanations) framework to quantify individual feature contributions and reveal the underlying prediction logic. The feature importance hierarchy, illustrated in **Figure 4.11**, established that system pressure (P) exerted the strongest influence on model predictions, with density (ρ_{DES}) and viscosity (μ_{DES}) ranking as the second and third most critical descriptors, respectively exceeding the importance of compositional parameters (HBA and HBD fractions). This pattern indicates that the model extracts predictive information from readily measurable bulk thermophysical properties, which serve as implicit representations of molecular-scale characteristics, including void space distribution and intermolecular packing efficiency, the fundamental determinants of gas dissolution capacity.

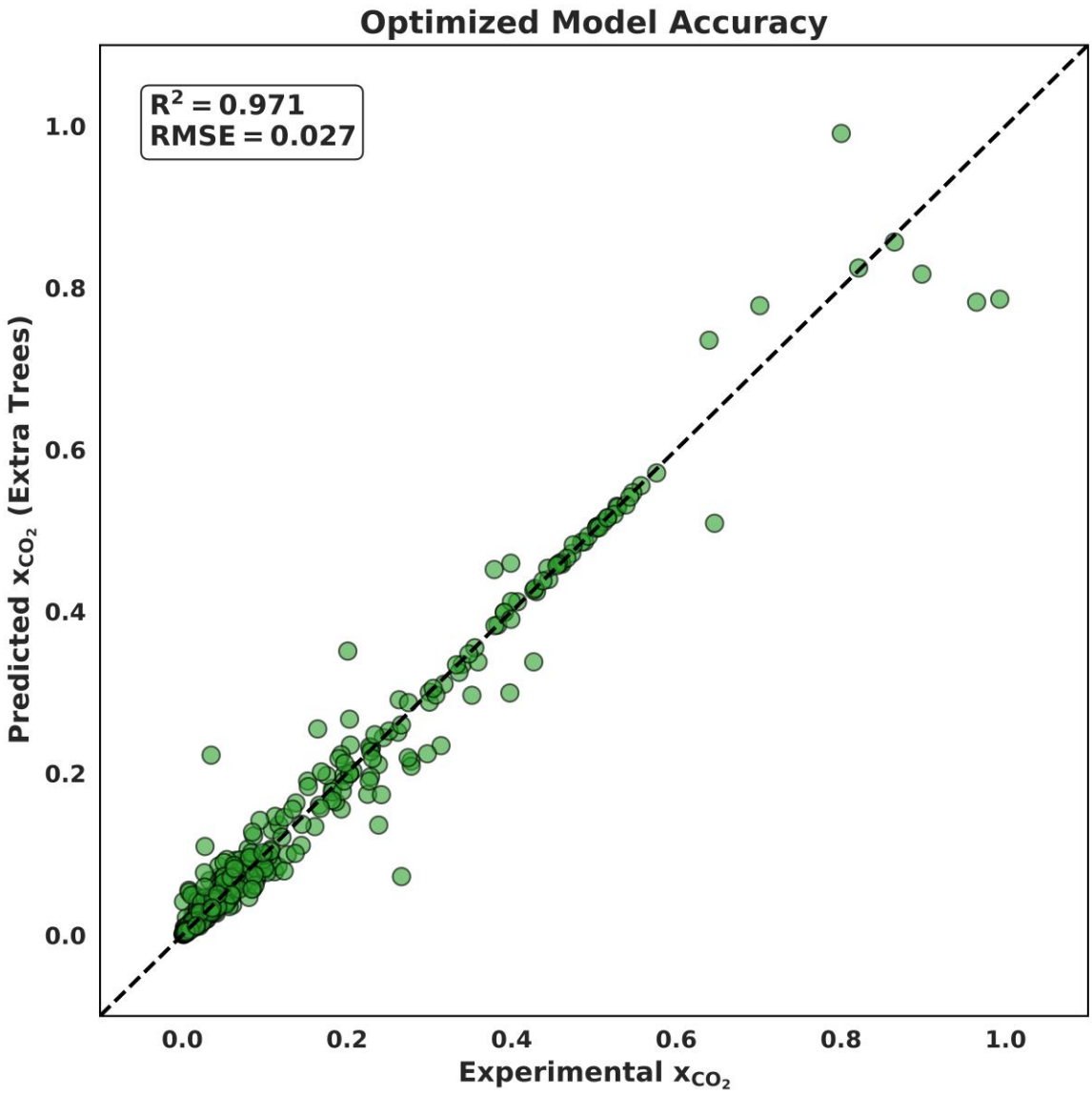

Figure 4.10 Experimental versus predicted xCO_2 for the multivariate QSPR model

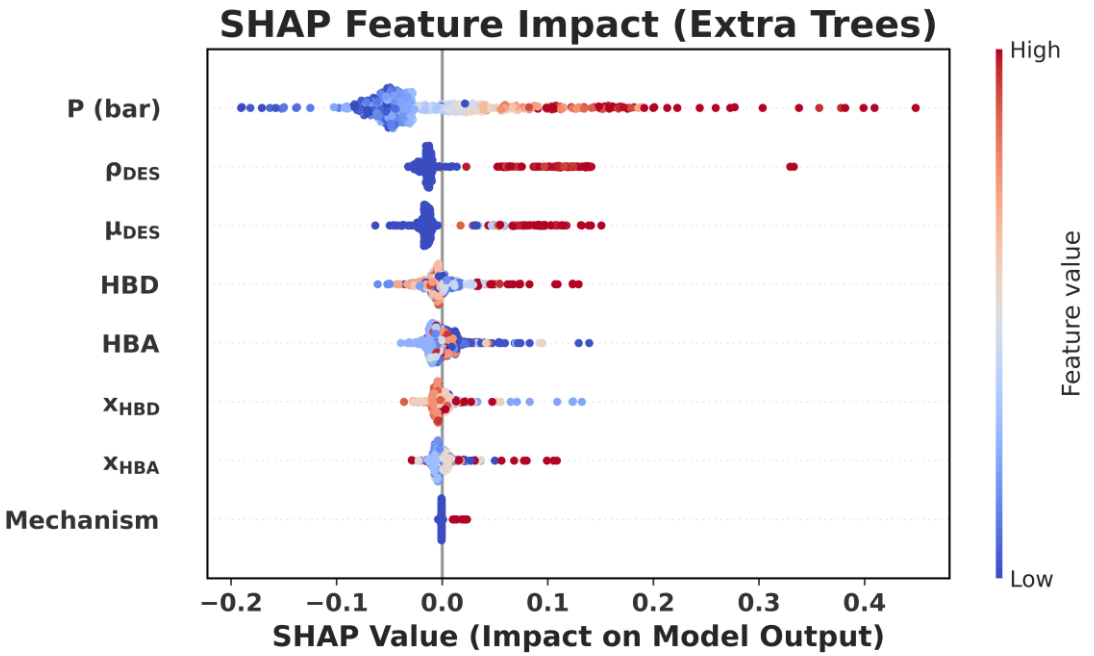

Figure 4.11 SHAP analysis of the dataset

4.8.3. Applicability domain assessment

Applicability Domain (AD) characterization was performed using Williams plot analysis to establish the interpolation space within which model predictions maintain statistical credibility. The Williams plot provides a two-dimensional diagnostic representation wherein standardized residuals (δ) are plotted versus leverage values (h) for each observation, permitting simultaneous identification of response outliers (high residual error) and structurally influential compounds (high leverage). The critical leverage threshold (h^*), computed from the relationship $h^* = 3(p+1)/n$ where p represents the number of descriptors and n denotes training samples, yielded a value of 0.0123 as shown in **Figure 4.12**.

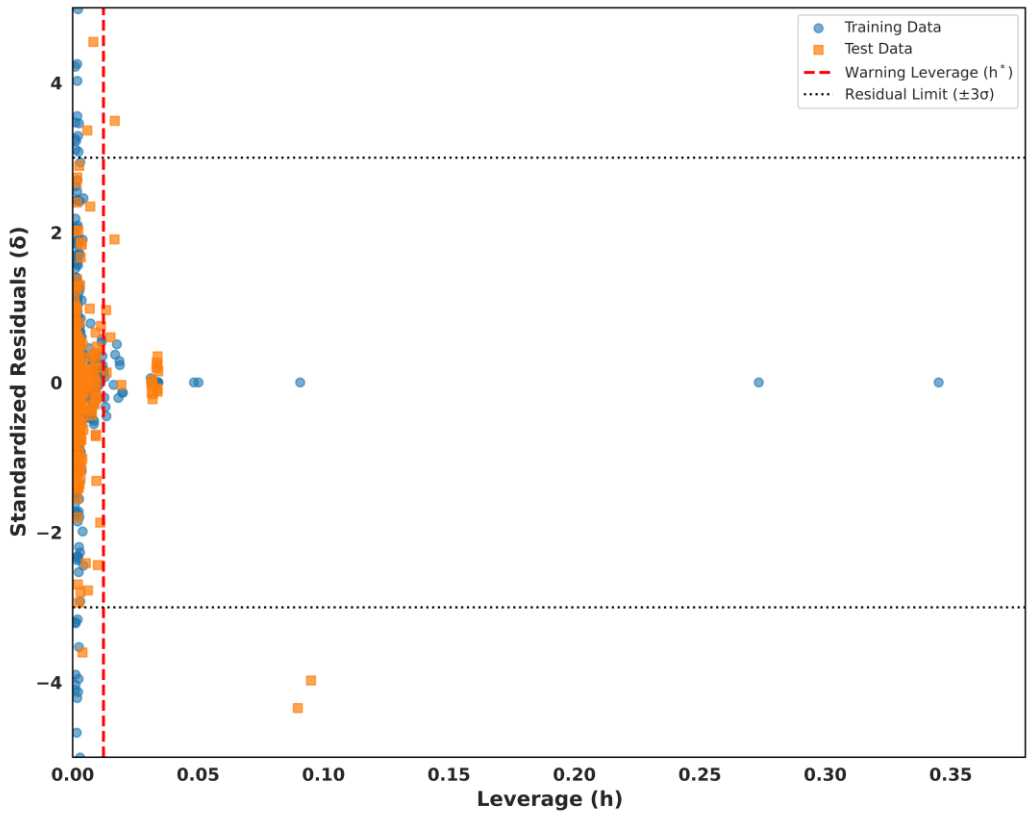

Figure 4.12 Williams plot demonstrating the applicability domain of the QSPR model

As can be seen from **Figure 4.12**, the defined applicability domain contained 94.36% of the test dataset points, determined by simultaneous satisfaction of two validation criteria: standardized prediction residuals within the ±3σ interval and leverage statistics below the critical value ($h < h^*$). Compounds surpassing the leverage threshold ($h > h^*$) were found to correspond primarily to DES systems exhibiting high molecular weight or viscosity values, physicochemical property ranges sparsely represented in the training data distribution. Importantly, while these observations possessed high leverage, indicating structural dissimilarity from the training set mean, their standardized residuals remained constrained within the ±3 acceptance limits. This outcome substantiates the model's capacity for reliable extrapolation: despite these DESs occupying

structurally distinct regions of the chemical space, the algorithm successfully generalized the learned structure-property relationships to deliver accurate solubility predictions.

4.8.4. Practical performance index (PI)

A practical Performance Index (PI) was constructed following the established paradigm of Ashby-type material selection indices, wherein performance is quantified as the quotient of a beneficial property 'benefit' to a detrimental property 'penalty', enabling rational DES screening and ranking[142]. To systematically rank DES candidates based on the trade-off between thermodynamic absorption capacity and hydrodynamic transport limitations, the PI was established with Reline (choline chloride-urea, 1:2 molar composition) designated as the reference solvent for performance benchmarking, as shown by **Equation (4.4)** at 303.15K:

$$PI = \frac{\left(\frac{xCO_2}{\nu_{DES}}\right)_{current\ work}}{\left(\frac{xCO_2}{\nu_{DES}}\right)_{Reference}} \tag{4.4}$$

Where xCO_2 is the mole fraction of CO_2 in DES at a fixed pressure of 1MPa and ν_{DES} is the kinematic viscosity of the DES at 303.15K in m^2/s, which is calculated using **Equation (4.5)**

$$\nu_{DES} = \frac{\eta_{DES}}{\rho_{DES}} \tag{4.5}$$

For this study, the reference value was established as 0.0706, based on the properties of Reline under identical conditions[41], [143]. **Table 4.12** shows the kinematic viscosity and PI of all the DESs

Table 4.12 Kinematic viscosities (303.15 K) and corresponding performance indices of the synthesized DESs[a].

DES	ν_{DES} at 303.15K (cm^2/s)	PI
DES1	1.199	3.815
DES2	1.253	3.539
DES3	1.610	3.001
DES4	1.515	3.151
DES5	1.335	3.715
DES6	1.068	3.262
DES7	0.475	9.876
DES8	2.292	1.953

[a]Standard uncertainties u are u(T) = 0.05 K, u(ρ) = 0.0001 g/cm^3, and u(η) = 1.0% of the measured value. Combined standard uncertainties for derived properties are u(ν) ≈ 2% and u(PI) ≈ 6%.

The index was constructed to encompass both equilibrium absorption performance and the energetic cost associated with solvent transport through the capture system as shown in **Figure 4.13**, established DES7 as the superior candidate (PI ≈ 9.88), primarily attributable to its minimal kinematic viscosity (0.475 cm^2/s), which substantially diminishes the parasitic energy load imposed by circulation pumps. By comparison, DES8 yielded the poorest performance metric (PI ≈ 1.95), a consequence of its elevated kinematic viscosity (2.29 cm^2/s, approximately 4.8-fold higher than DES7), which translates to disproportionately higher pumping energy requirements. From a process engineering perspective, the hydraulic power consumption of recirculation pumps demonstrates linear dependence on both fluid viscosity and operation duration, establishing viscosity as a critical parameter in solvent selection for energy-efficient CO_2 capture[144]. Therefore, DESs exhibiting persistently low ν represent intrinsically more energy-efficient options for absorption-based CO_2 capture. Performance Index analysis establishes DES7 and DES1 as the superior solvent candidates, combining favorable thermodynamic solubility with substantially reduced hydraulic power requirements for continuous circulation.

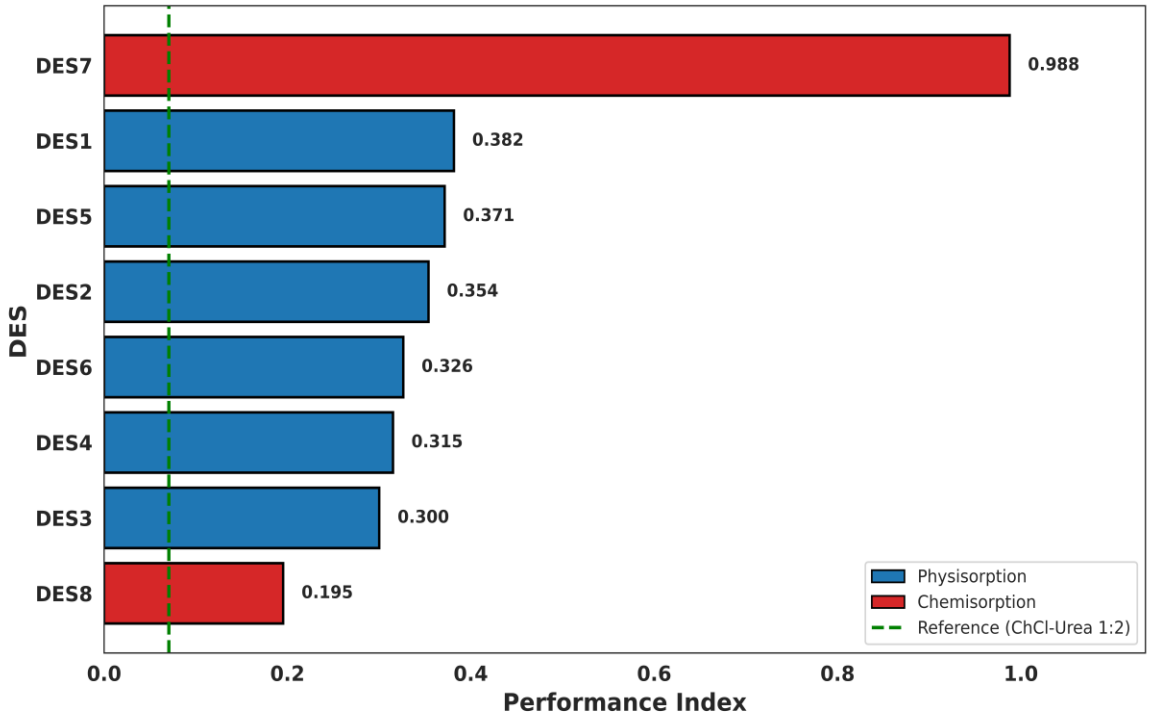

Figure 4.13 Performance ranking of eight deep eutectic solvents

4.9. Conclusion

In this chapter, eight novel deep eutectic solvents were synthesized and subjected to comprehensive physicochemical characterization for CO_2 capture applications. CO_2 solubility measurements were conducted at 303.15 K across pressures extending to 2 MPa using a high-pressure volumetric sorption apparatus. Critical properties (T_{cDES}, P_{cDES}, V_{cDES}) were estimated via Modified-Lydersen group contribution methodology and Lee Kesler method, while thermophysical parameters, including density, surface tension, and transport properties, were predicted using Haghbakhsh's group contribution framework. Experimental density and dynamic viscosity data were successfully correlated with Arrhenius and Vogel-Fulcher-Tammann-Hesse (VFTH) equations, demonstrating excellent predictive agreement.

Fourier-transform infrared spectroscopy confirmed extensive hydrogen bonding networks between acceptors and donors, validating eutectic complex formation. Differential scanning calorimetry revealed distinct thermal behaviors: 1,6-hexanediol-based systems (DES1-DES5) exhibited crystalline melting transitions, whereas amine-functionalized formulations (DES6-DES8) demonstrated glass-forming characteristics with glass transition temperatures near 228 K.

CO_2 absorption capacity ranged from 0.80 (DES6) to 1.43 mol/mol (DES5). Six formulations (DES1-DES6) displayed linear solubility isotherms at low pressures, confirming physisorption with Henry's constants ranging from 2.61 to 3.39 MPa. Conversely, DES7 and DES8 exhibited pronounced non-linearity indicative of chemical absorption, precluding Henry's law application.

A Quantitative Structure-Property Relationship (QSPR) framework was developed using Pearson correlation analysis for descriptor selection. Among seven machine learning algorithms evaluated under Leave-One-DES-Out cross-validation, Extremely Randomized Trees achieved optimal performance (R^2 = 0.971). A Performance Index (PI = xCO_2/ν_{DES}) was formulated to balance absorption capacity against viscosity-induced transport resistance, identifying DES7 and DES1 as superior candidates. This integrated experimental-computational workflow enables rapid, systematic DES screening, though mixed-gas selectivity and industrial operating conditions warrant future investigation.

Declaration of Publication

This chapter draws its substance and methodology from the research originally disseminated in the following peer-reviewed publication:

Gomey, A. K., Singh, S. K., Haider, M. B., & Kumar, R. (2026). Rational design of deep eutectic solvents for CO_2 capture: integrated experimental analysis and machine learning-guided screening. Energy & Fuels. https://doi.org/10.1021/acs.energyfuels.6c01833.

Chapter 5

Application of DESs for the separation of IPA-Water Azeotrope

5.1. Introduction

The separation of azeotropic mixtures represents a persistent challenge in chemical process industries. Isopropyl alcohol (IPA) forms a minimum boiling azeotrope with water at 87.5 wt%. IPA, making conventional distillation ineffective due to the near-unity relative volatility at the azeotropic composition. High-purity IPA finds extensive use in pharmaceutical formulations, semiconductor manufacturing, and specialty chemical synthesis, with the global market projected to reach from USD 3.6 billion in 2025 to USD 4.6 billion by 2035 [12]. Consequently, developing energy-efficient separation processes for IPA recovery holds both economic and environmental significance.

Extractive distillation has emerged as the preferred industrial approach, wherein a high-boiling entrainer selectively alters the relative volatility between azeotropic components. Traditional solvents such as dimethyl sulfoxide (DMSO) have proven effective; however, their moderate volatility necessitates energy-intensive regeneration and presents solvent loss concerns. Recent advances in ionic liquids (ILs) and deep eutectic solvents (DESs) offer compelling alternatives due to their negligible vapor pressure, thermal stability, and tunable physicochemical properties.

Building upon the thermodynamic and CO_2 absorption investigations presented in **Chapters 2, 3, and 4**, this chapter extends the application scope of DESs to azeotrope separation. While previous chapters demonstrated the efficacy of DESs for gas capture through systematic property

characterization and machine learning modeling, the present work explores whether these designer solvents can deliver comparable advantages in liquid-phase separations. Specifically, we evaluate 1-ethyl-3-methylimidazolium tetrafluoroborate ([EMIM][BF_4]) as the representative IL, alongside Ethaline (choline chloride/ethylene glycol) and Glyceline (choline chloride/glycerol) as DES candidates, benchmarked against conventional DMSO.

The investigation employs rigorous NRTL thermodynamic modeling with regressed binary interaction parameters, implemented through Aspen Plus (v.8.6) process simulations. Beyond sensitivity analyses of conventional two-column configurations, an alternative process design exploiting the non-volatile nature of ILs and DESs is proposed, substituting the traditional stripper column with a flash drum to reduce energy consumption. The chapter presents thermodynamic modeling frameworks, process synthesis and simulation methodology, sensitivity analysis results, optimization outcomes with the alternative design, and techno-economic comparisons. Through this systematic investigation, this chapter demonstrated the potential of DESs to serve as viable and energy-efficient entrainers for industrial azeotrope separation.

5.2. Critical properties estimation

The critical properties of EMIM[BF4], Ethaline, Glyceline, and DMSO were estimated using the computational framework described in **Chapter 2**, as shown in **Table 5.1.**

Table 5.1 Estimated critical properties

	Units	Ethaline	Glyceline	[EMIM][BF_4]		DMSO	
		Old work	This work	This work	Literature[145]	This work	Literature[146]
T_{cDES}	K	601.99	680.69	596.23	585.30	729.00	720.15
V_{cDES}	cc/mol	259.70	315.19	540.78	557.80	227.00	238.00
P_{cDES}	bar	40.40	33.93	23.59	23.60	56.50	57.05
ω		0.92	1.22	0.81	0.77	0.28	
T_{bDES}	K			449.46	438.90	464.00	462.15
Z_{cDES}		0.21	0.19	0.26		0.21	

5.3. Process Synthesis

The typical process flow diagram of the extractive distillation is shown in **Figure 5.1**[147], [148]. The process consisted of two columns, one for extractive distillation and the other for entrainer recovery. The azeotropic mixture and the entrainer had been fed to the first column, where the more volatile component was collected at the top, and a less volatile component, along with the entrainer, was collected at the bottom. The bottom product (entrainer and low volatile component) was fed to the second column, in which the entrainer was recovered at the bottom. The recovered entrainer had been cooled down by using a heat exchanger and recycled back to the extractive distillation column. The addition of the entrainer altered the relative volatility between IPA-water, which eventually led to the separation of IPA as the top product and the water-entrainer mixture as the bottom product from the first column. High-purity IPA and entrainer were obtained from the top of the extractive distillation column and from the bottom of the solvent regeneration column, respectively.

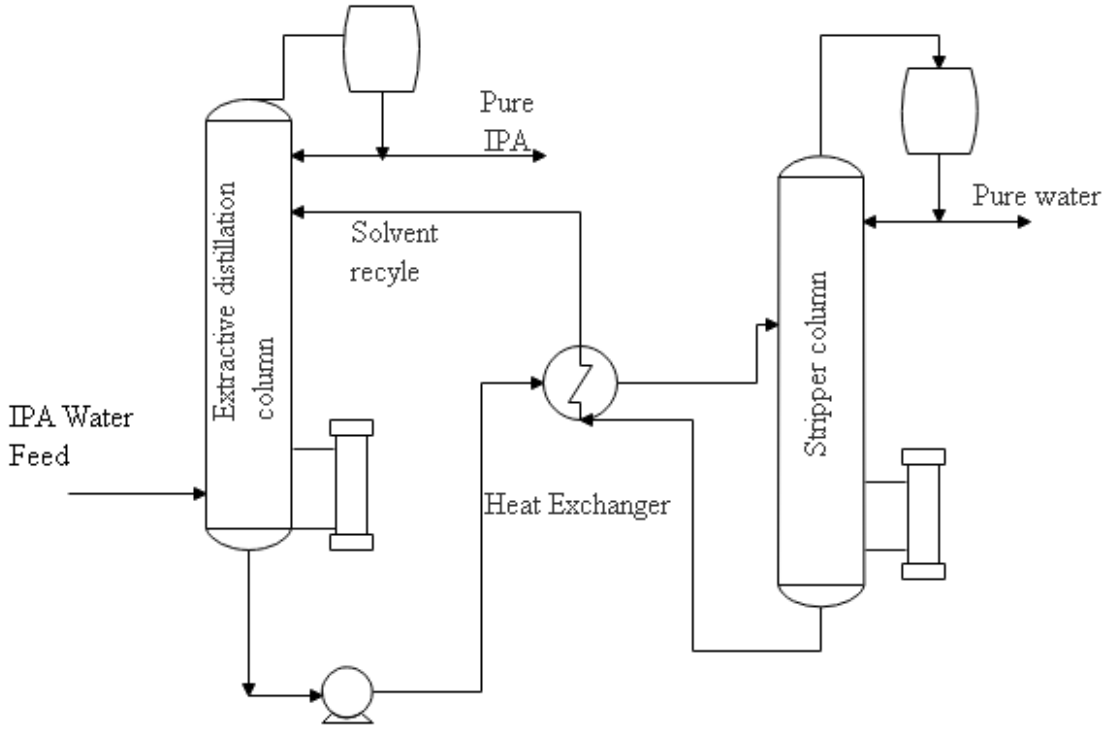

Figure 5.1 Conventional extractive distillation process

5.4. Modelling and Simulation

5.4.1. Thermodynamic modelling

The modelling and simulation were carried out on the Aspen Plus simulator (v 12) of Aspen Technology Inc., Cambridge. The vapour-liquid equilibrium data for the water-IPA-DMSO system were available in the Aspen data bank, and they were used for the simulation. The vapour-liquid equilibrium data for water-IPA with [EMIM][BF_4], Ethaline, and Glyceline systems were not available in the Aspen databank; therefore, they were taken from the literature[149]-[150], [151].

The temperature-dependent properties, such as surface tension, density, and viscosity, were further estimated using the experimental data previously reported [152], [153], [154], [155], [156]. For density, the DNLDIP method was used as given by the equation,

$$\rho = k_1 + k_2\tau^{.35} + k_3\tau^{2/3} + k_4\tau^1 \tag{5.1}$$

Where τ is given by

$$\tau = 1 - T/T_c \tag{5.2}$$

Similarly, the Andrade viscosity model was used for viscosity,

$$\ln\eta = A + \frac{B}{T} + C\ln T \tag{5.3}$$

Surface tension was modelled using the IK-CAPE module,

$$\sigma = w + x * T + y * T^2 + z * T^3 \tag{5.4}$$

It could be observed from **Figures 5.2, 5.3, and 5.4** that experimental data has been correlated well with the **Equations (5.1), (5.3), and (5.4)**, respectively. The model parameters obtained have been shown in **Tables 5.2-5.3.**

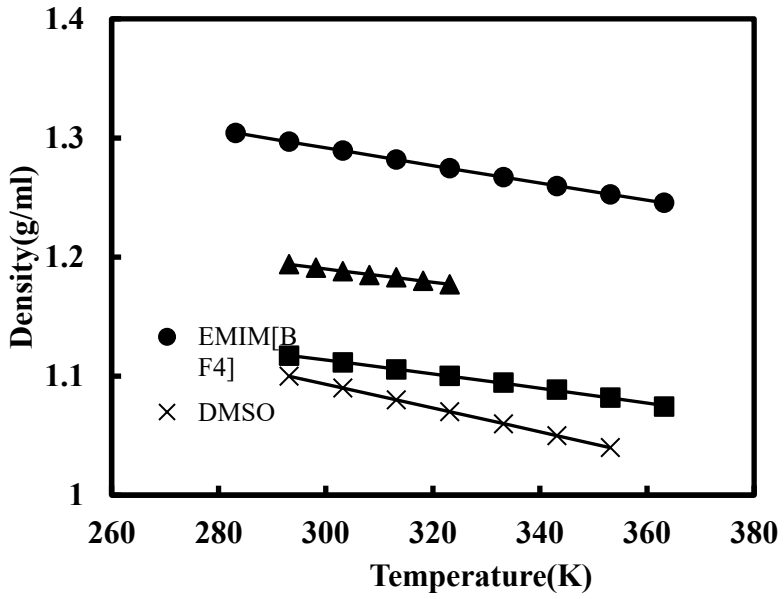

Figure 5.2 Experimental and calculated densities of [EMIM][BF_4], DMSO, and DESs (283.15-363.15 K) [157]

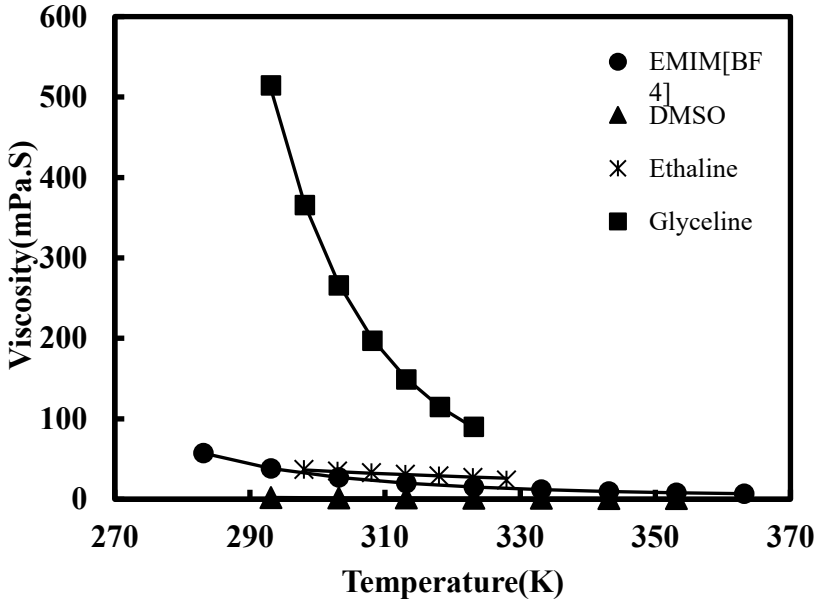

Figure 5.3 Experimental and calculated viscosities of [EMIM][BF_4], DMSO, and DESs (283.15–363.15 K) [157]

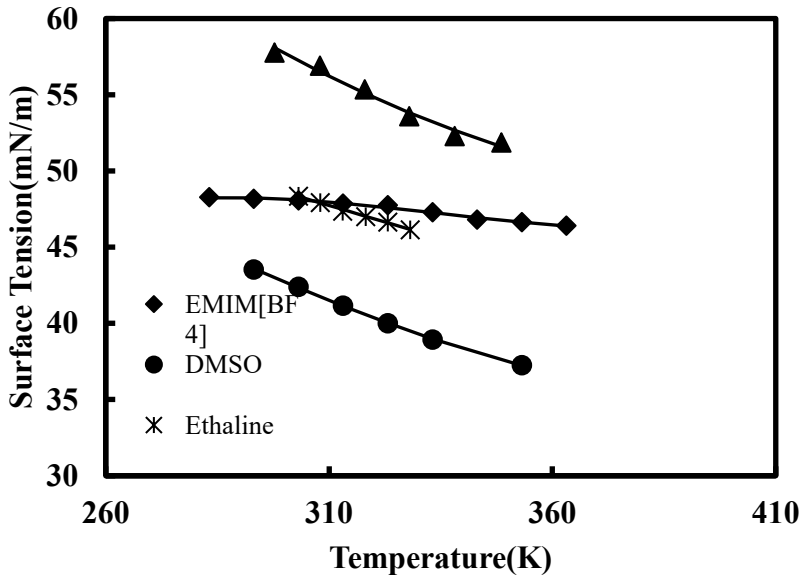

Figure 5.4 Experimental and calculated surface tension of [EMIM][BF_4], DMSO, and DESs (283.15–363.15 K) [157]

Table 5.2 Calculated density and viscosity parameters of [EMIM][BF_4], DESs and DMSO in the temperature range of 283.15-363.15 K

Property	**Density (g/ml)**					**Viscosity (mPa.S)**			
parameter	**k_1**	**k_2**	**k_3**	**k_4**	**SD**	**A**	**B**	**C**	**SD**
[EMIM][BF_4]	1.06	0.31	-0.72	0.88	1.4E-4	-131.86	8671.39	18.65	0.14
Ethaline	0.713	0.385	0.156	0	5.5E-4	267.213	-11071.13	-39.75	0.42
Glyceline	0.001	0.262	10388.80	3.99	2.6E-4	-110.844	10000.00	14.60	2.63
DMSO	0.44	0.34	0.21	0.38	1.1E-4	-101.09	6103.62	14.27	0.011

Table 5.3 Calculated Surface tension analysed over temperature range of 283.15–363.15 K of [EMIM][BF_4], DESs and DMSO

Property	Surface Tension				
parameter	**W**	**x**	**Y**	**z**	**SD**
[EMIM][BF_4]	-131.82	1.67	-0.01	5.1E-6	0.0812
Ethaline	59.27	0.07	0.0274	0.333	0.0504
Glyceline	248.73	4.50	-4.51	0.00	0.3445
DMSO	0.66	0.73	0.00	3.6E-6	0.0376

The experimental VLE data of water-IPA-[EMIM][BF_4], water-IPA-Ethaline, and water-IPA-Glyceline obtained from the literature were regressed using a non-random two-liquid (NRTL) thermodynamic model, and binary interaction parameters were calculated[149], [150], [151]. It should be noted that for the water-IPA-DESs system, DESs have been assumed as the non-dissociative single component, which is opposed to previously reported data[150], [151]. The NRTL model uses the following equation to calculate activity coefficients;

$$\ln\gamma_i = \frac{\sum_j \tau_{ij} G_{ji} X_j}{\sum_k G_{ki} X_k} + \sum_j \frac{(X_j G_{ij})}{\sum_k G_{kj} X_k}\left[\tau_{ij} - \frac{\sum_n X_n \tau_{ij} G_{ji}}{\sum_k G_{kj} X_k}\right] \tag{5.5}$$

where,

$$\tau_{ij} = \frac{\Delta g_{ij}}{T};\ \tau_{ii} = 0\ \&G_{ij} = \exp\left(-\alpha_{ij}\tau_{ij}\right);\ G_{ii} = 1 \tag{5.6}$$

The temperature dependency of the activity coefficient was accounted by using the extended version of the basic NRTL model, provided by the Aspen plus® as given in eq-11.

$$\tau_{ij} = a_{ij} + \frac{b_{ij}}{T} \text{ and } \alpha_{ij} = c_{ij} + d_{ij}\,(T - 273.15K) \tag{5.7}$$

At equilibrium, the fugacity of each component in both phases will be equal. However, for both

IL and DESs, it is assumed to have negligible volatility and therefore the vapour phase is essentially entrainer-free. For low to moderate pressures, the objective function for regression of NRTL binary interaction parameters takes the following form;

$$y_i P = x_i \gamma_i P_i^* \quad (5.8)$$

The binary interaction parameters obtained after regression for both systems are shown in **Table 5.4**

Tables 5.5, 5.6, and 5.7. The calculated VLE data for IPA-Water-[EMIM][BF_4] system was compared with experimental data, as shown in **Figure 5.5**. The binary molar concentration of IPA in the vapor phase was plotted against the Pseudo-binary molar concentration of IPA in the liquid phase at various concentrations of [EMIM][BF_4]. The result shows that NRTL model predictions are in close agreement with the experimental data. Similar results with ethaline and glyceline show that the NRTL model best predicted the experimental results.

Table 5.4 NRTL[a] parameters obtained through regression of IPA-Water-[EMIM][BF_4] system

component i	IPA	IPA	WATER
component j	WATER	[EMIM][BF_4]	[EMIM][BF_4]
a_{ij}	-11.53	13.60	-9.04
a_{ji}	59.25	1.11	12.02
b_{ij}	4690.38	75.05	3500.00
b_{ji}	-16318.00	00.67	-4699.70
α_{ij}	0.30	0.30	0.30

[a]Standard uncertainties u were u(T) = 0.05 K

Table 5.5 NRTL[a] parameters obtained through regression of IPA-Water-Ethaline system

component i component j	Water IPA	Ethaline IPA	Ethaline Water
a_{ij}	6.83	3.79	1.86
a_{ji}	-1.31	0.00	0.00
b_{ij}	-1483.16	-1172.07	-1227.54
b_{ji}	426.39	371.37	375.65
α_{ij}	0.30	0.30	0.30

[a]Standard uncertainties u were u(T) = 0.05 K

Table 5.6 NRTL[a] parameters obtained through regression of IPA-Water-Glyceline system

component i component j	IPA WATER	Glyceline IPA	Glyceline water
a_{ij}	-2.50	-1.94	-2.32
a_{ji}	5.38	0.00	0.00
b_{ij}	850.87	819.92	43.97
b_{ji}	-1005.06	606.74	639.64
α_{ij}	0.30	0.30	0.30

[a]Standard uncertainties u were u(T) = 0.05 K

Table 5.7 NRTL[a] parameters obtained through regression of IPA-Water-DMSO system.

component i component j	IPA WATER	IPA DMSO	WATER DMSO
a_{ij}	-1.31	0.00	-1.25
a_{ji}	6.83	0.00	1.75
b_{ij}	426.39	115.28	586.80
b_{ji}	-1483.46	-25.01	-1130.20
α_{ij}	0.30	0.30	0.30

[a]Standard uncertainties u were u(T) = 0.05 K

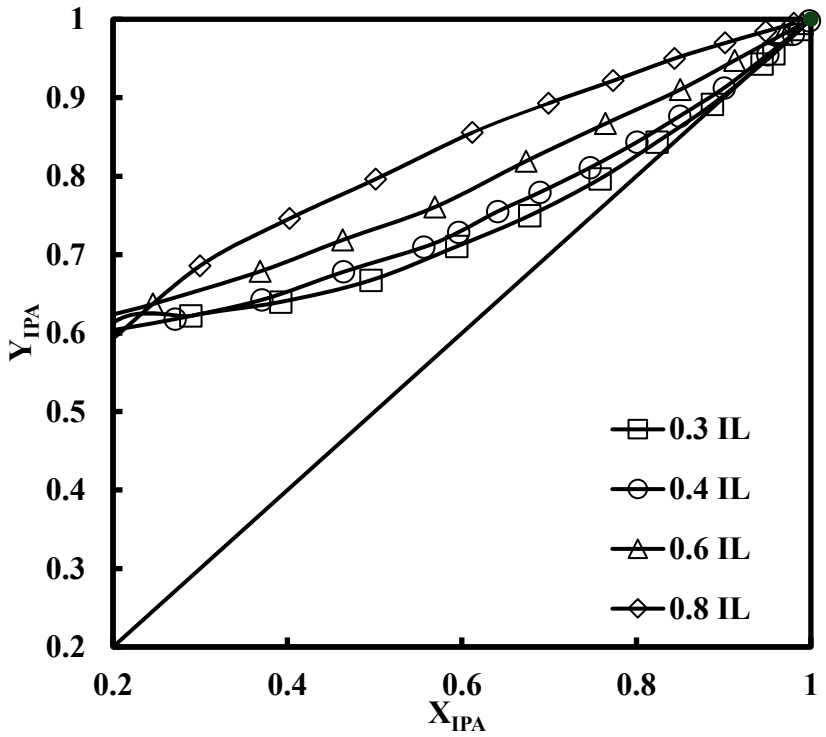

Figure 5.5 Experimental and NRTL predicted VLE of water-IPA-[EMIM][BF_4]

5.4.2. Steady-state simulation

The extractive distillation column and recovery column were both modelled as the RADFRAC subroutine of the Aspen Plus. Each stage was assumed to be an equilibrium stage. The number of theoretical stages for the extractive distillation column and solvent recovery column was fixed at 41 and 24, respectively [21]. The fresh feed of 100 kmol/h containing an equimolar mixture of IPA and water was fed at the lower part of the extractive distillation column. The entrainer input stage was selected close to the top stage of the column. Other stream conditions and process parameters are given in **Table 5.8**. The sensitivity analysis and optimisation tool of the simulator determined the optimal parameters for the extractive distillation process. The design parameters

were varied in such a manner to achieve the desired purity of top and bottom products of the extractive distillation column with minimum energy requirement.

Table 5.8 Input process parameters

Feed composition (mole fraction)	**IPA**	**0.50**
	Water	**0.50**
Feed flow rate (kmol /hr)	100	
Feed temperature (^oC)	25	
Feed Pressure (atm)	1.1	
Number of stages in extractive distillation column	41	
Number of stages in recovery column	24	
Extractive distillation column pressure(atm)	1.1	
Recovery column pressure (atm)	1.1	

5.4.3. Sensitivity analysis results

The amount of solvent required for achieving the desired purity of the distillate plays a crucial role in determining the economics of the process. Therefore, the solvent requirement was analysed by varying the molar reflux ratio in the range of 0.5 – 2. The effect of solvent flow rate and reflux ratio on the distillate mole fraction (X_D) is shown in **Figure 5.6**. The results indicate that all solvents can be used as entrainers in extractive distillation to achieve the highest purity of distillate. It is evident from the figures that for the same solvent flow rate, distillate purity will be higher at a higher reflux ratio. Further, for the same purity and reflux ratio, the ethaline flow rate requirement is least, followed by EMIM[BF_4] and Glyceline.

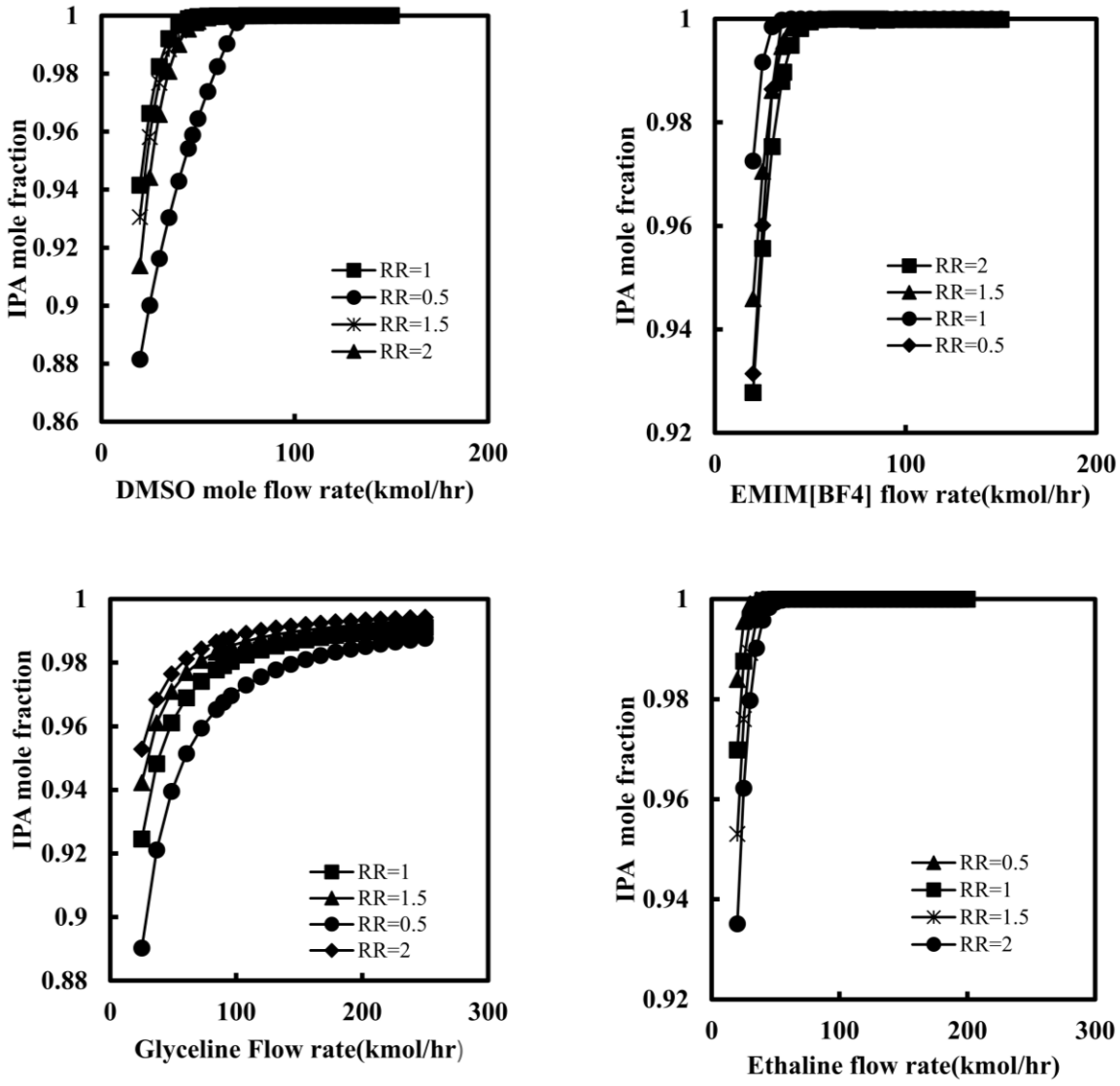

Figure 5.6 Effect of entrainer flow and reflux on distillate purity

The effect of the reflux ratio and solvent flow rate on the reboiler duty has been shown in **Figure 5.7**. In all the cases, the reboiler duty increases almost in a linear fashion with increasing solvent flow rate, as expected. For the given flow rate and reflux ratio, the lowest reboiler duty was observed for the EMIM[BF_4], followed by DMSO, Glyceline, and ethaline. The difference in the reboiler energy consumption was found in the order of 10^2 kW.

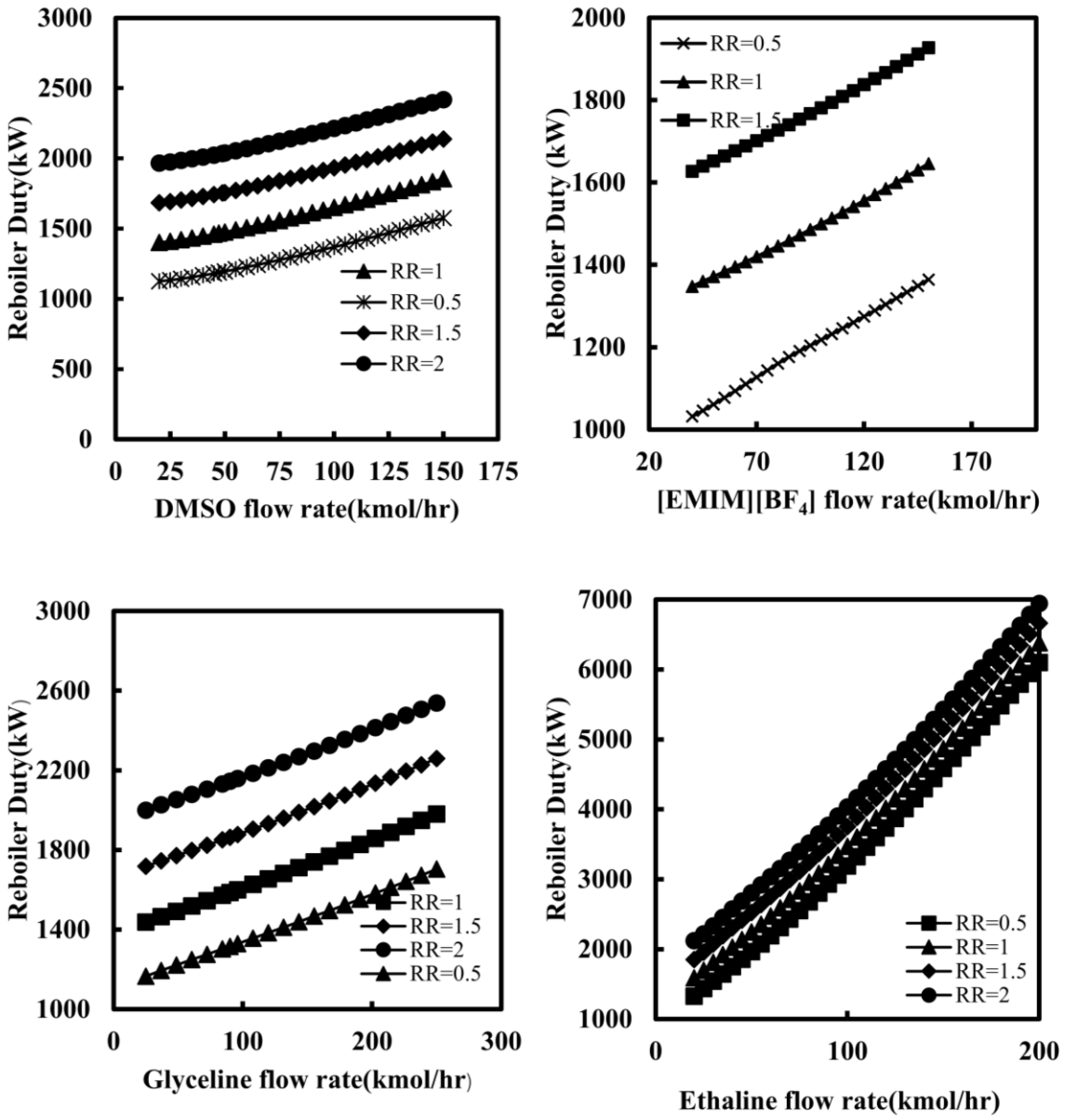

Figure 5.7 Effect of entrainer flow rate and reflux ratio on reboiler duty

The effect of solvent feed stage location on distillate purity has been presented in **Figure 5.8**. Solvent feed location affects the distillate purity only at a lower reflux ratio. There was a slight decrease in the distillate mole fraction with increasing the location of the solvent feed stage.

However, at a higher reflux ratio, the solvent feed stage location does not significantly affect the distillate purity, as shown in **Figure 5.8.**

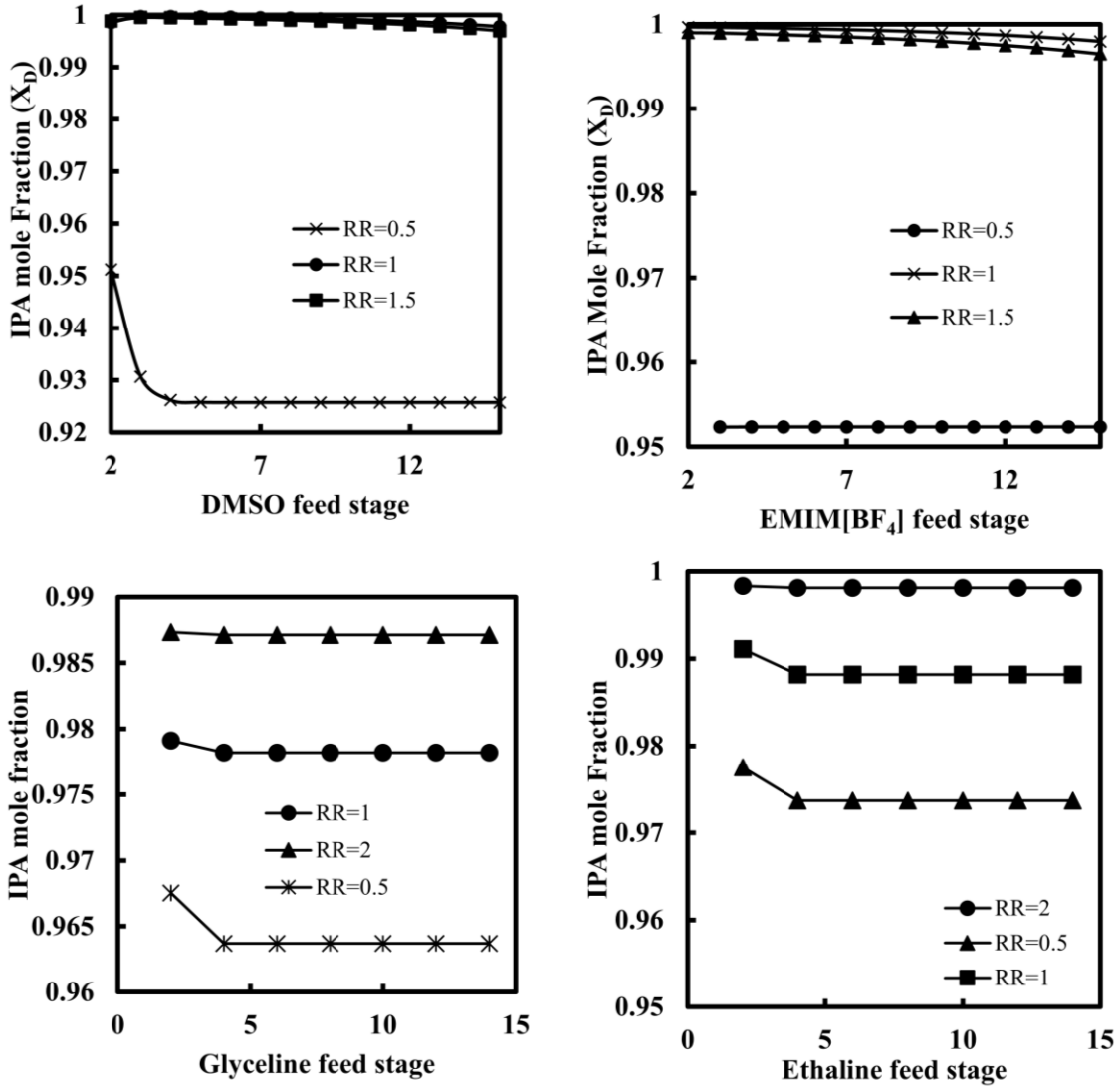

Figure 5.8 Effect of entrainer feed stage and reflux ratio on distillate purity

Figure 5.9 shows the effect of binary feed location on distillate purity. The distillate purity dropped as the binary feed stage was increased due to a decrease in contact time.

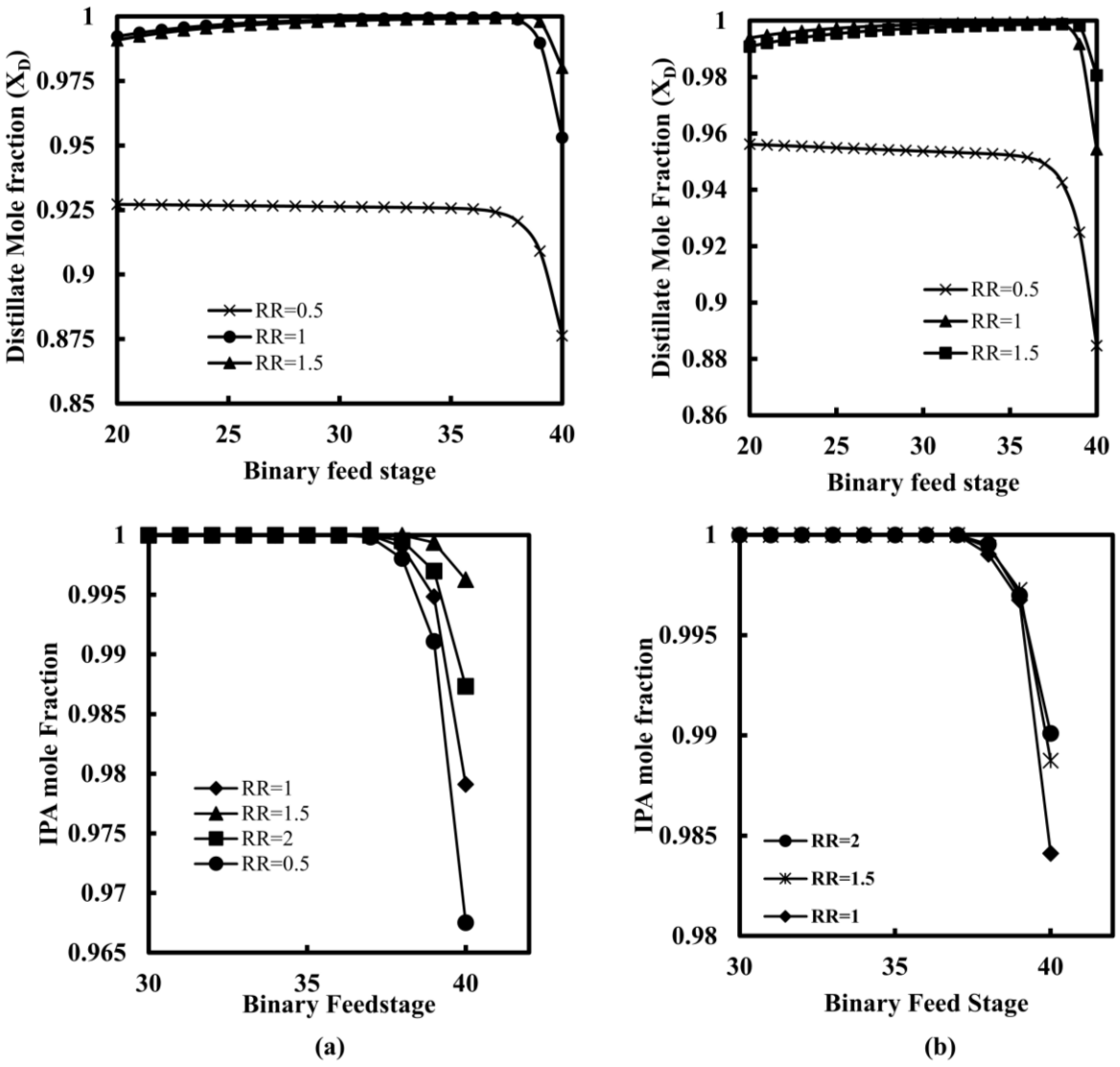

Figure 5.9 Effect of feed stage and reflux ratio on distillate purity: (a) DMSO (b) [EMIM][BF_4])

The composition profiles of the extractive distillation column obtained using [EMIM][BF_4] and DMSO are shown in **Figure 5.10**. Since the solvents have negligible vapour pressure, the entrainer's concentrations do not vary much in the extractive section and can be recovered from the bottom of the column. In addition, the extractive section utilises a larger number of stages compared to the rectifying and stripping sections, to achieve the desired product purity.

(a)

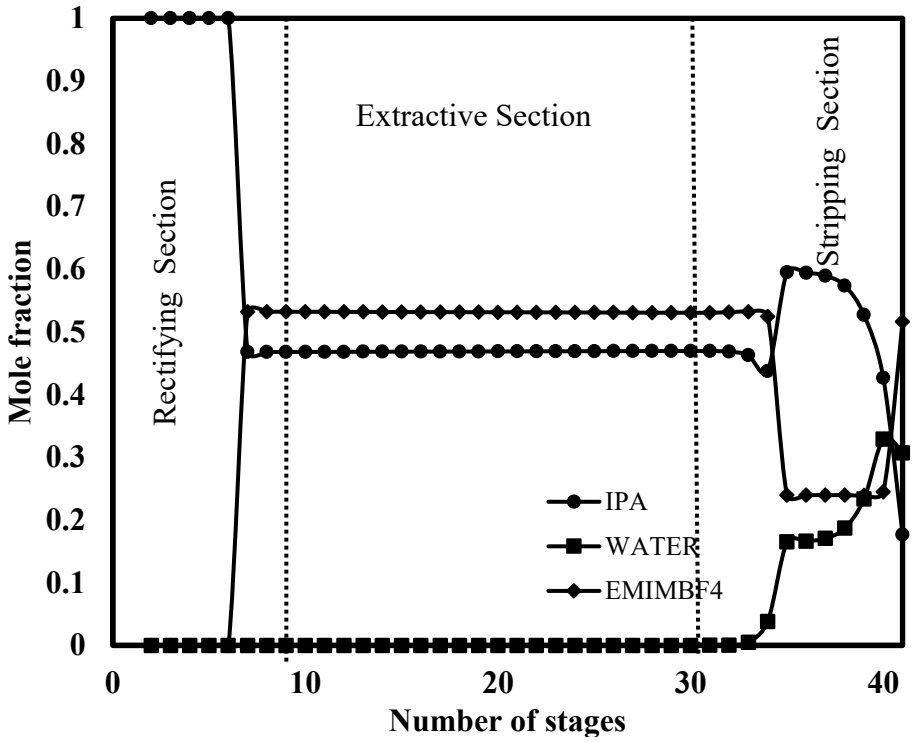

(b)

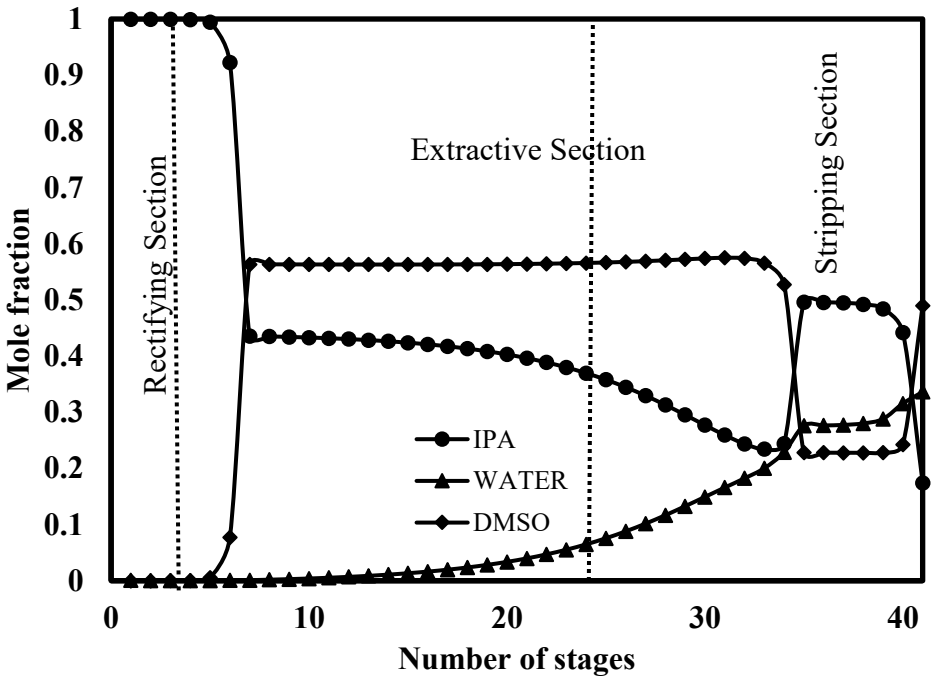

Figure 5.10 Composition profiles of the extractive distillation column of the IPA-water system with (a) [EMIM][BF_4]; (b) DMSO

Figure 5.11 shows the temperature profiles of the extractive distillation columns for different solvents. It can be seen that in the extractive section, the temperature is greater than in the rectifying section and suddenly falls to a lower value close to the binary feed stage, and then rises again to the maximum temperature at the bottom of the column. The observed temperature profile represents the typical behaviour of the extractive distillation column.

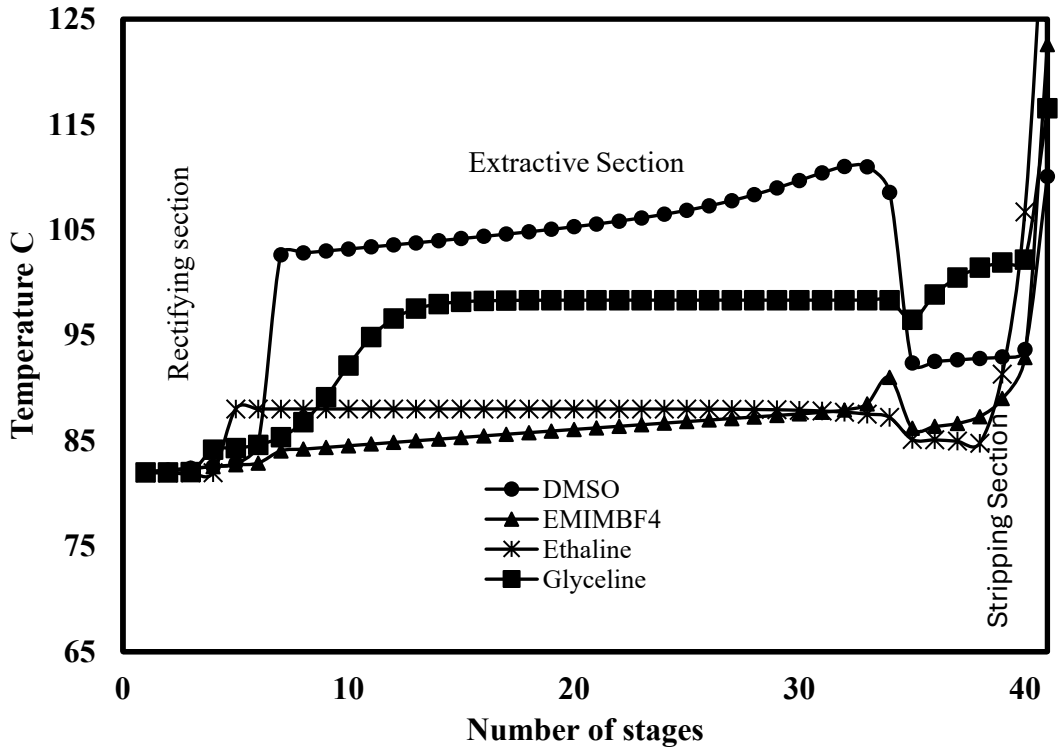

Figure 5.11 Temperature profiles for IPA-water with different entrainers

5.5. Process Optimisation

After analysis of the effect of various parameters, an optimisation study was conducted to calculate the entrainer flow rate, reflux ratio, distillate flow rate, and condenser and reboiler duties of the process for both cases. The parameters were optimised using the optimisation module of Aspen Plus. The objective function (F) was defined by considering the ratio of the sum of heat duties of

the reboiler (Qr) and condenser (Qc) to the specified production of isopropyl alcohol (D) as given below;

$$\text{Min } F = \frac{(Q_r + Q_c)}{D} \tag{5.9}$$

Subject to constraints:

$$X_D \geq 0.999 \tag{5.10}$$

$$X_B \leq 0.001 \tag{5.11}$$

The above objective function minimises the reboiler and condenser duties per unit distillate flow rate. The mass fraction of isopropyl alcohol was fixed at 0.999 and 0.001 at the top (X_D) and at the bottom (X_B) of the column, respectively. The objective function and constraints were inserted in the process by means of the Model Analysis/Optimisation tool of the simulator. The Sequential Quadratic Programming (SQP) search method was used for optimisation purposes. The optimisation considered only the continuous variables: entrainer flow rate and molar reflux ratio.

The optimised process flow diagrams for [EMIM][BF_4] and DMSO are shown in **Figure 5.12 and Figure 5.13**, respectively. The optimal process parameters, such as entrainer flow rate, distillate flow rate, condenser and reboiler duties for both processes are given in **Table 5.9.** The calculated condenser and reboiler duties were found to be considerably less for the [EMIM][BF_4] process compared to the DMSO process. The optimisation study reveals that a mixture of IPA-Water can be separated efficiently using [EMIM][BF_4] as an entrainer, requiring less energy compared to DMSO.

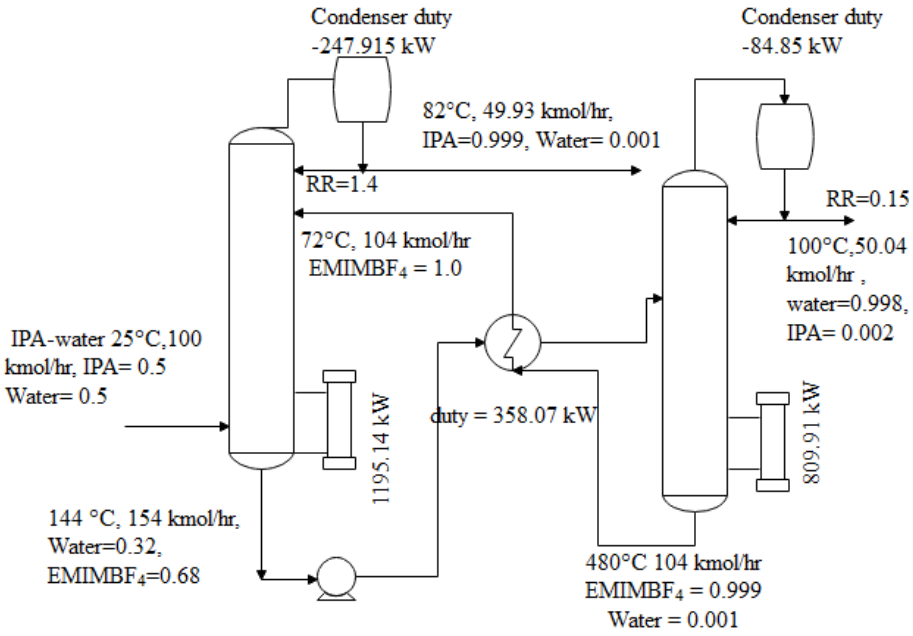

Figure 5.12 Optimal process flowsheet for extractive distillation of IPA-water using [EMIM][BF4] solvent

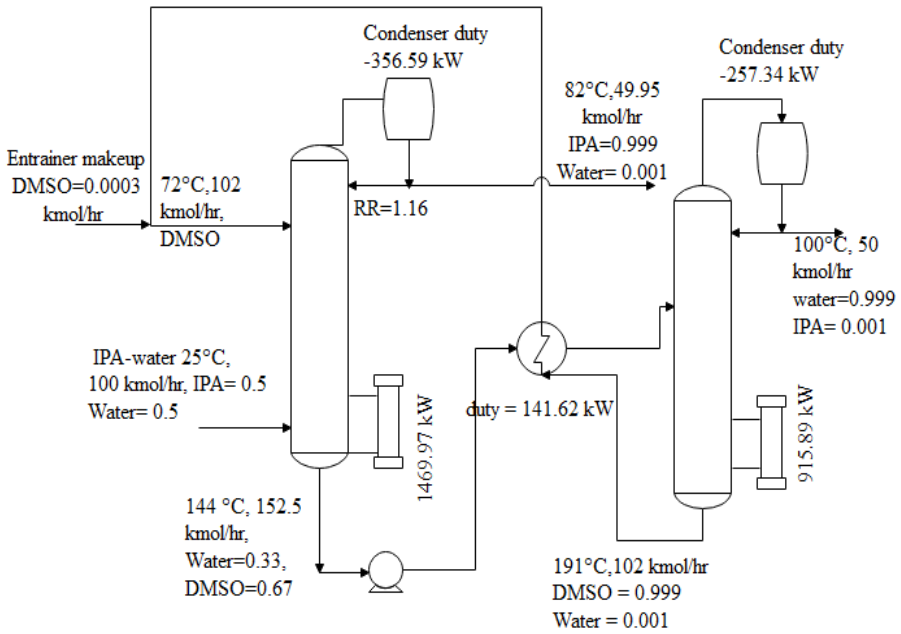

Figure 5.13 Optimal process flowsheet for extractive distillation of IPA-water using DMSO solvent

Table 5.9 Optimisation results of all processes

	Conventional DMSO process	[EMIM][BF_4]		Ethaline	Glyceline
		Conventional process	Alternate process	Alternate process	
Extractive column					
Reboiler (kW)	1469.97	1195.14	1195.14	3799.65	2534.34
Condenser (kW)	356.59	247.92	247.92	1125.80	1688.76
Regeneration column					
Reboiler (kW)	915.89	809.91	--	--	--
Condenser (kW)	257.34	84.85	--	--	--
Flash (kW)	--	--	563.96	400.03	109.93
Heat Exchanger (kW)	141.62	358.07	134.81	463.79	605.04
Distillate flow rate (kmol/hr)	49.98	49.93		49.98	49.98
Entrainer flow rate (kmol/hr)	102.47	104.16		96.04	136.00

5.6. Alternate Process Design of Extractive Distillation

The conventional extractive distillation process using [EMIM][BF_4] as an entrainer was found to be less energy intensive than using DMSO as an entrainer for the separation of the IPA-Water binary mixture. Further, we thought to reduce the energy requirement of the process by exploiting the negligible vapour pressure of [EMIM][BF_4]. Since [EMIM][BF_4] has been considered a non-volatile solvent, it may be recovered by flash column instead of using a stripper column. Therefore, a new process was developed, as shown in **Figure 5.14**, and the stripper column was replaced by the flash column. Also, heat integration of the process was done using a heat exchanger. The regenerated [EMIM][BF_4] was cooled down to the desired temperature using a distillate stream in the heat exchanger. Sensitivity analysis was carried out to calculate the pressure of the isothermal

flash column to achieve the desired purity of [EMIM][BF_4]. The calculated pressure of the flash column was found to be 5 kPa. Further, the complete process was optimised, and total energy requirements were evaluated.

A similar process flow method was also utilised for ethaline and Glyceline, as shown in **Figures 5.15, and 5.16**, respectively. A comparison of the energy requirement for the conventional process as well as for the alternate process has been shown in **Table 5.9** for [EMIM][BF_4]. It is evident from **Table 5.9** that the energy required in the extractive and regeneration unit for the separation of the IPA-Water mixture using [EMIM][BF_4] is lower than using a DMSO entrainer. The energy requirement can be further lowered in the conventional [EMIM][BF_4] process by replacing the regeneration unit with a flash column. In addition, both DESs have shown the capability to be used as an entrainer for breaking the azeotropic composition of IPA-Water with the minimum solvent requirement by the ethaline solvent.

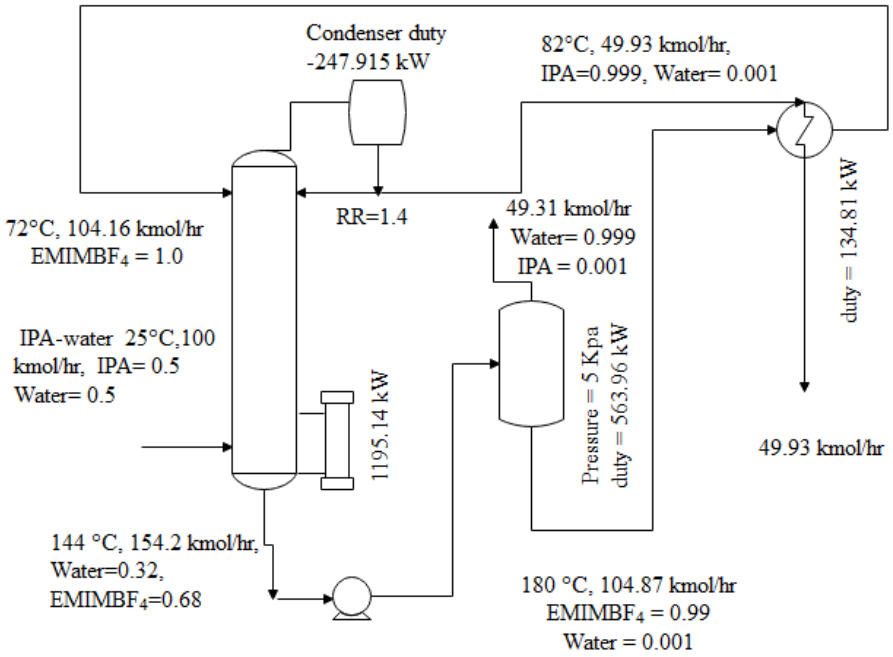

Figure 5.14 Alternate process flow diagram for extractive distillation of IPA-water using [EMIM][BF_4])

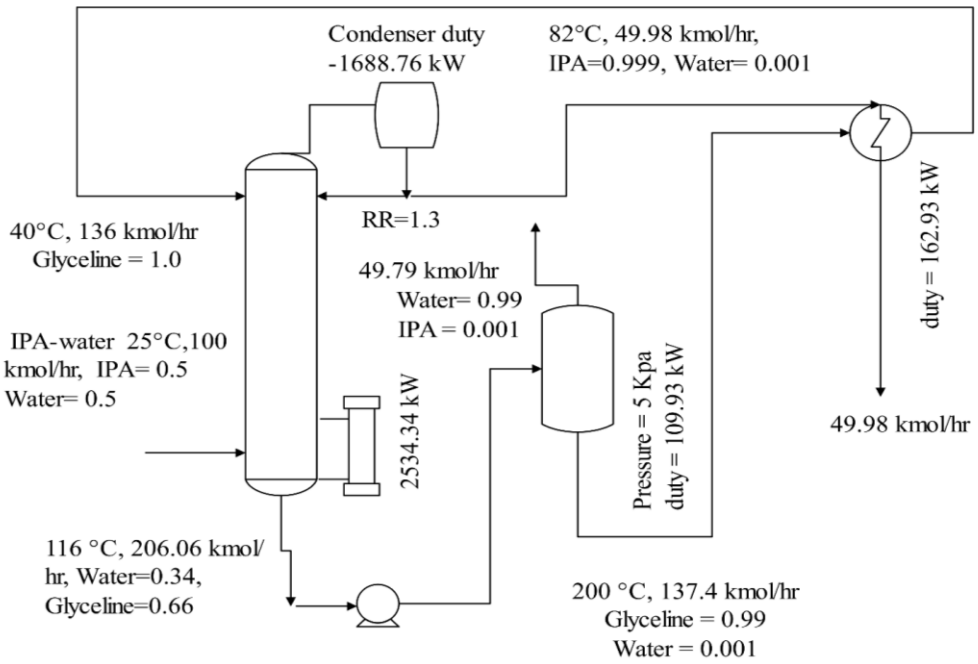

Figure 5.15 Alternate process flow diagram for extractive distillation of IPA-water using Glyceline

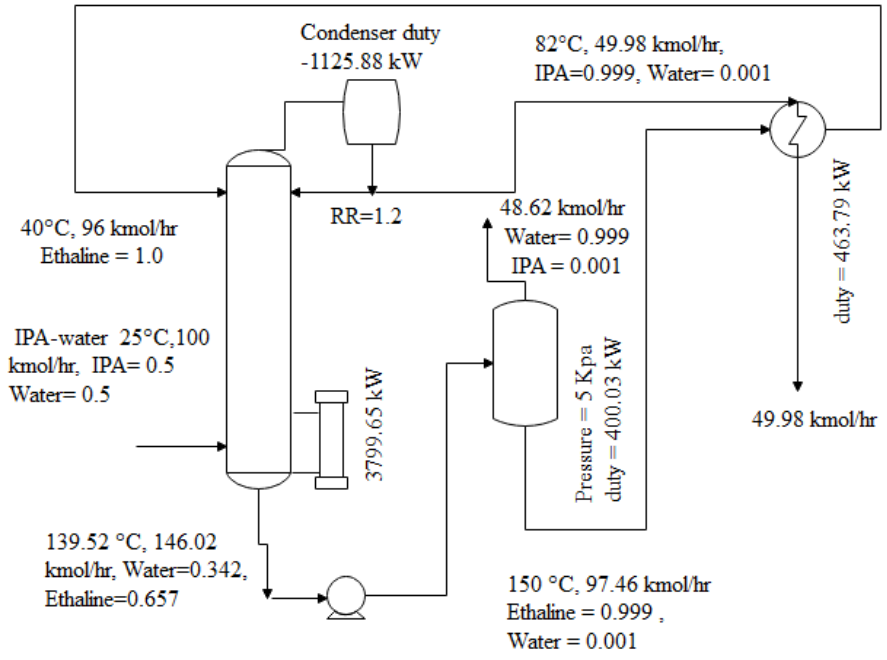

Figure 5.16 Alternate process flow diagram for extractive distillation of IPA-water using ethaline

5.7. Technoeconomic Analysis

Total Annual Cost (TAC) was calculated for the conventional and alternate process design using operating and fixed capital costs generated by Aspen Process Economic Analyzer (APEA) and shown in **Table 5.10** [158], [159]**.** Default cost values available in the APEA for utilities such as electricity, cooling water, and low-pressure steam (100 psi) and high-pressure steam (165 psi) were taken for all the processes. The total annual cost of the alternate process using deep eutectic solvents was found to be comparable to the conventional process of DMSO. However, the TAC of the alternate process using ionic liquid was significantly higher compared to the conventional and alternate process due to the high cost of the ionic liquid solvent.

Table 5.10 Total Annual Cost of conventional and alternate process

Summary	**ChClEG**	**ChClGLY**	**IL**	**DMSO**
	Alternate process			**Conventional process**
Total Capital Cost [USD]	4.87E+06	4.70E+06	4.66E+06	5.26E+06
Total Operating Cost [USD/Year]	3.09E+09	1.62E+09	9.77E+10	3.17E+09
Total Raw Materials Cost [USD/Year]	2.86E+09	1.50E+09	9.05E+10	2.93E+09
Total Utilities Cost [USD/Year]	1.48E+06	1.00E+06	9.67E+05	6.41E+05
Equipment Cost [USD]	4.77E+05	4.38E+05	4.27E+05	5.40E+05
Total Installed Cost [USD]	1.30E+06	1.20E+06	1.18E+06	1.37E+06
Total Annual Cost (TAC)[a] [USD/year]	**3.09E+09**	**1.62E+09**	**9.77E+10**	**3.17E+09**

[a]TAC = 10% Total Installed Equipment Cost + Total Operating Cost[158], [159]

5.8. Conclusion

This chapter examined the separation of IPA-water azeotropic mixture using ionic liquids and deep eutectic solvents through extractive distillation. Using NRTL thermodynamic modeling and Aspen Plus simulations, the study showed that [EMIM][BF_4], Ethaline, and Glyceline can successfully break the azeotrope and produce IPA with more than 99.9 mol% purity. Performance evaluation revealed important insights regarding both energy efficiency and economic viability. While [EMIM][BF_4] demonstrated favorable energy consumption in the extractive column compared to conventional DMSO, its economic feasibility was severely limited by the high cost of ionic liquid procurement. This finding highlights that superior energy performance alone cannot justify solvent selection without considering overall process economics. The alternative process design employing flash-based entrainer recovery proved highly effective for the DES systems. By replacing the conventional regeneration column with a simple flash drum, both capital and operating costs were reduced significantly. Among all configurations tested, the Glyceline alternate process emerged as the most economically attractive option, achieving total annual costs approximately half that of conventional DMSO. This advantage comes from Glyceline's simpler synthesis, lower raw material costs, and reduced energy requirements for entrainer recovery. Ethaline showed comparable economics to DMSO, while requiring the lowest entrainer flow rate among all solvents tested. The results demonstrate that deep eutectic solvents offer viable alternatives to both conventional organic solvents and ionic liquids for azeotrope separation. The flash-based recovery strategy, exploiting the non-volatile nature of DESs, provides a generalizable framework applicable to other challenging separation problems. These findings establish that process configuration and economic considerations are equally important as thermodynamic performance in selecting suitable entrainers for industrial applications.

Having successfully applied deep eutectic solvents for CO_2 capture and azeotrope separation, the next chapter investigates their use as catalysts for biodiesel production from neem oil, presenting experimental results on engine performance and exhaust emissions.

Declaration of Publication

This chapter draws its substance and methodology from the research originally disseminated in the following peer-reviewed publication:

Gomey, A. K., Tripathi, M. M., Haider, M. B., & Kumar, R. (2023). Comparative analysis of isopropyl alcohol dehydration using ionic liquids and deep eutectic solvent. *Journal of Ionic Liquids*, 3(2), 100069. https://doi.org/10.1016/j.jil.2023.100069

Chapter 6

Engine Performance and Emission Study of DES-Synthesized Biodiesel

Graphical Abstract

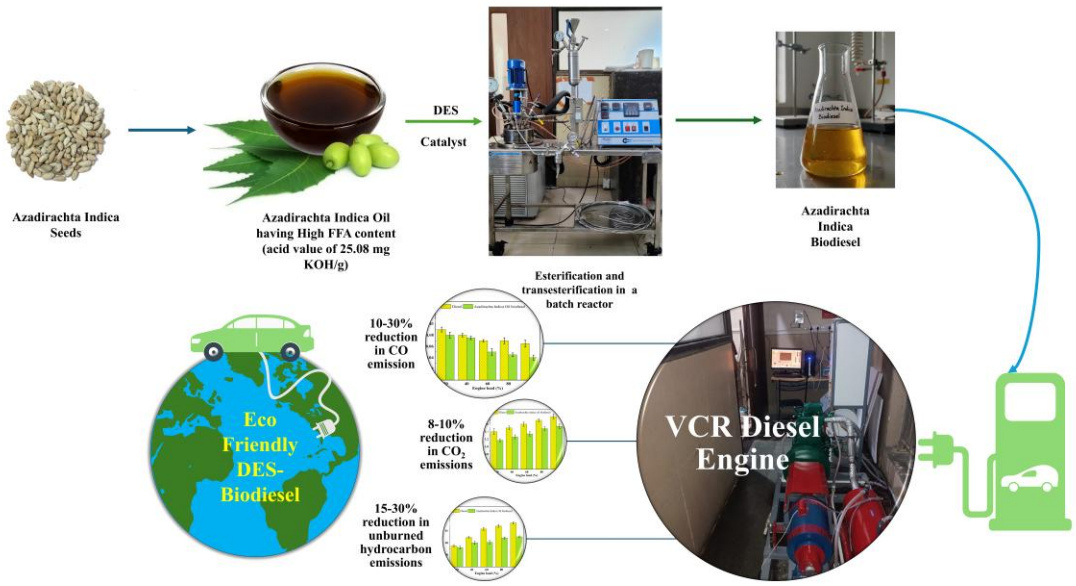

6.1. Introduction

The preceding chapters demonstrated the efficacy of deep eutectic solvents for CO_2 capture and azeotrope separation, establishing their potential as sustainable alternatives to conventional solvents through systematic thermodynamic characterization and process modeling. Beyond gas separation and purification applications, DESs have shown promise as catalysts in chemical synthesis due to their tunable acidity, negligible volatility, and environmentally benign nature. The compelling application lies in biodiesel production, where DES-based catalysts can facilitate the conversion of high-free-fatty-acid feedstocks[160], [161], [162]. The depletion of fossil fuel

reserves and escalating environmental concerns have intensified research into renewable transportation fuels[163]. Biodiesel derived from non-edible oils such as Azadirachta indica (neem) offers an attractive pathway that avoids food-fuel competition while utilizing abundantly available feedstocks[163]. However, the practical viability of any alternative fuel extends beyond synthesis efficiency and must be validated through comprehensive engine testing under realistic operating conditions.

This chapter evaluates biodiesel synthesized from Azadirachta indica oil using deep eutectic solvent catalysts, achieving 90% yield through optimized esterification and transesterification. The fuel was tested on a variable compression ratio diesel engine at 1500 rpm under loads ranging from 20% to 100%. The investigation encompasses three domains: performance characteristics (brake thermal efficiency, specific fuel consumption), combustion characteristics (heat release rate, in-cylinder pressure), and emission profiles (CO, CO_2, HC, NO_x). Fuel properties were characterized against ASTM D6751 and EN 14214 standards. This integrated experimental evaluation demonstrates the practical applicability of DES beyond separation processes, validating DES-catalyzed biodiesel as a viable alternative fuel.

6.2. Materials and Methods

6.2.1. Synthesis of DESs

The DESs were prepared based on the method discussed in **section 4.2.2.** The DESs were synthesized based on hydrogen-bond donors, including phenylacetic acid (carboxylic acid), p-toluenesulfonic acid (strong sulfonic acid), and ethylene glycol (diol), providing a spectrum ranging from strong Brønsted acidity to neutral polyol hydrogen-bonding capability. The hydrogen-bond acceptors comprise choline chloride and tetraethyl/tetrabutyl ammonium bromides

(quaternary ammonium salts), as well as methyltriphenylphosphonium bromide (phosphonium salt), providing varied cation cores and steric environments that tune the polarity and proton availability at the catalytic interface. By pairing these HBAs and HBD, it was aimed to modulate acidity, ion pairing, and hydrogen-bond networks central to esterification catalysis.

6.2.2. Diesel engine setup

The biodiesel produced from the reaction of neem oil and DESs in this work is then studied for its performance in real-time applications. For this, a single-cylinder 4-st diesel engine with a Variable compression ratio (VCR) was employed, featuring a loading unit and an asynchronous motor. **Figure 6.1** illustrates the experimental setup, which employs a single-cylinder diesel engine featuring water cooling and an adjustable compression ratio, as well as the data pathways used for testing Azadirachta indica biodiesel.

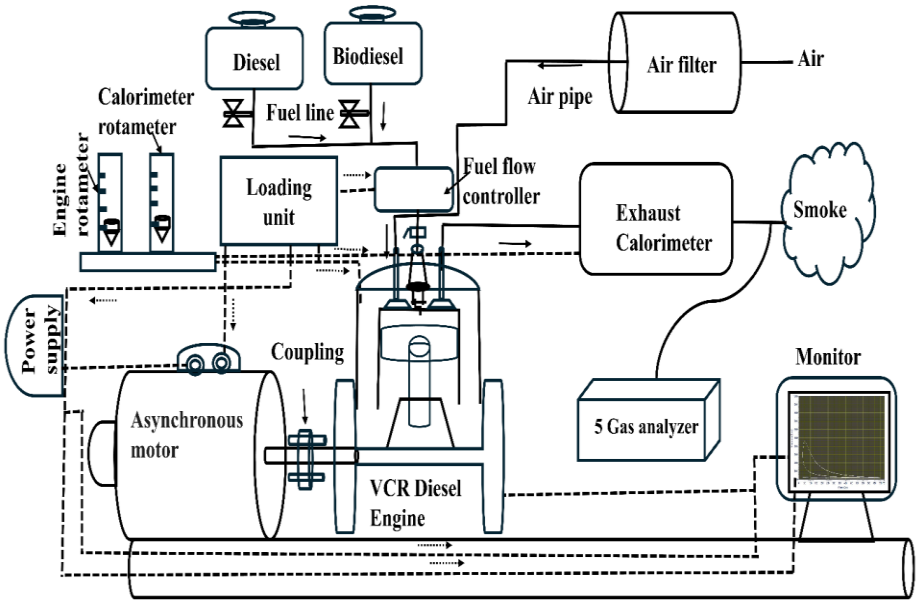

Figure 6.1 Schematic diagram of VCR diesel engine setup

The experimental apparatus features an engine with a single cylinder operating on a four-stroke cycle, equipped with a system that allows adjustment of the compression ratio. This engine is mechanically linked to an asynchronous motor coupled with a load unit with a main-bolt mechanism allowing in-situ compression-ratio adjustment and a water-cooling jacket that stabilizes thermal conditions during steady-state tests. Engine load was measured using a torque apparatus with a range of 2-10 kg. Fuel intake was assessed using a stopwatch and a 50 mL burette. Cooling water circulation and exhaust gas heat monitoring were managed by a cooling jacket (central tube) to maintain an optimal temperature. To assess the biodiesel engine's performance, the engine speed was consistently held at 1500 revolutions per minute, and the load levels were set to 20%, 40%, 60%, 80%, and 100% respectively. Exhaust routing is shown from the manifold to the five-gas analyzer, closing the measurement loop for regulated emissions (CO, HC, CO_2, O_2, NO_x) under steady boundary conditions supported by jacket cooling and speed control.

Tables A5-A6 show the engine's mechanical/operating envelope and the gas analyzer's measurement capabilities to understand and compare across various fuels and loads. The experimental arrangement was equipped with instruments to measure the crankshaft angle, combustion parameters, and fuel injection pressure. The single-cylinder CI unit was rated at 5.2 kW at 1600 rpm, with an 85 mm bore, 110 mm stroke, and 661.5 cc displacement, providing a representative chamber size for fuel property effects to manifest in performance and combustion. The compression ratio is adjustable from 12:1 to 22:1 via the main-bolt arrangement, enabling parametric studies while staying within design limits and ensuring consistent mechanical boundary conditions across fuel comparisons. The lubrication system utilises 3.5 L of 20W40 oil, and the platform is designed to operate with diesel, biodiesel, and blends, aligning with the study's

comparison of diesel versus AIOB at controlled load and speed points. To ensure reproducibility and precision, the experiments were repeated three times.

The gas analyzer is capable of measuring exhaust emissions with high precision, covering ranges such as 0-15000 ppm for general gases (with 1 ppm resolution), 0-15% for carbon monoxide (0.001% sensitivity), 0-20% for carbon dioxide (0.01% sensitivity), 0-25% for oxygen (0.01% sensitivity), and 0-5000 ppm for nitrogen oxides (1 ppm resolution), ensuring effective measurement across the various engine load conditions studied. The analyzer auto-zeros within ≤20 s each cycle and warms up in ≤5 min, draws 4 L/min sample flow, is built with a full-metal body, and operates across 0-50°C, 700-1150 mbar, and 0-90% RH (non-condensing), supporting stable operation during engine tests.

The engine performance and emission characteristics were evaluated under steady-state conditions, following established protocols for variable compression ratio (VCR) engines as detailed in recent analogous studies[164], [165].

6.3. Performance Characteristics

The biodiesel produced using DES was further evaluated for its suitability in engine applications. The performance assessment included key parameters such as brake thermal efficiency (BTE), air-fuel ratio (AFR), and brake-specific fuel consumption (BSFC). These parameters were measured for different blended fuels using a variable compression ratio (VCR) diesel engine. Testing was conducted on the VCR diesel engine at a compression ratio (CR) of 21.5, maintaining a constant speed of 1500 rpm across torque loads of 20%, 40%, 60%, 80%, and 100%, with the injection timing fixed at 23° BTDC and the injection pressure held at 350 bar for all tests.

6.3.1. Brake thermal efficiency (BTE)

BTE describes how much of the fuel's heat energy is converted into the engine's useful mechanical power at the crankshaft. This serves as an indicator of the performance associated with the test fuel and, in addition, provides a more effective assessment of the performance of various fuels, including heating value, compared to fuel consumption. **Figure 6.2 (a)** shows the BTE of the AIOB that were tested at loading of 20%, 40%, 60%, 80% and 100%. The BTE is anticipated to rise with increased load, as within the cylinder, gas temperatures increase at greater loads, improving combustion and thermal efficiency, as illustrated in the Figure. BTE increases monotonically with engine load for both fuels, reflecting higher in-cylinder temperatures and improved combustion at elevated torque, reaching 28.5% for diesel and 26% for AIOB at 100% load. An improvement in BTE for the diesel blend can be attributable to superior atomization, fine fuel droplets, and the resulting more complete combustion[166].In contrast, the relatively larger droplets formed by Azadirachta indica biodiesel slow down vaporisation and weaken combustion efficiency, which ultimately lowers BTE. Similar observations have been reported by several researchers, who noted that higher-ratio biodiesel blends (such as B30) often show a gradual decline in brake thermal efficiency due to their higher viscosity, lower calorific value, greater density, and reduced volatility, all of which contribute to poor atomization and less efficient combustion[167], [168], [169].

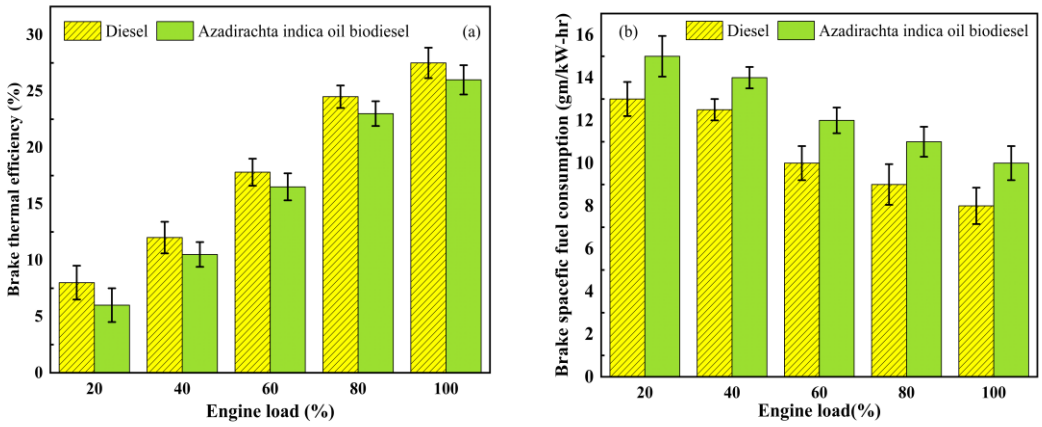

Figure 6.2 Comparative performance characteristics of AIOB and conventional diesel across varying engine loads: (a) BTE (b) BSFC

6.3.2. Brake specific fuel consumption (BSFC)

BSFC indicates how much fuel is consumed to generate a specific amount of engine power[170]. **Figure 6.2 (b)** shows BSFC versus engine load and indicates that Azadirachta indica oil biodiesel (AIOB) consistently demands more fuel per unit power than diesel across the entire load range, reaching about 10.2 g/kWh at full load compared to roughly 8.2 g/kWh for diesel at the same 1500 rpm test point on the VCR engine. This higher BSFC for AIOB reflects its lower calorific value and distinct physical properties that collectively require a greater mass flow to deliver equivalent brake power under identical operating conditions. AIOB has a substantially lower calorific value than diesel (≈35.46 vs 44.40 MJ/kg), so more fuel mass must be supplied to achieve the same brake power, pushing BSFC upward even when combustion proceeds stably at the chosen operating point. The oxygen content of AIOB can aid oxidation during combustion, but it does not offset the energy-per-mass shortfall; thus, the net effect remains an increased mass flow to meet the same power target, reflected in the BSFC bars for AIOB[171]. The oxygen content reported for AIOB

in Table 8 rationalises that less CO and HC will be emitted, which is discussed in the subsequent section; however, oxygenated fuel carries less chemical energy per kilogram, resulting in the net effect on performance being the BSFC increase and BTE decrease[172], [173]. This shows that for work cycles prioritising efficiency, optimising injection strategy, compression ratio, or employing blends can mitigate the BTE gap while leveraging AIOB's emissions benefits, but mass-based consumption will reflect on the net BSFC increase. Additionally, range estimates and storage sizing should account for higher consumptions at typical loads since more mass of fuel must be delivered per unit power.

6.4. Combustion Characteristics

The combustion characteristics are a key factor in assessing the biodiesel's sustainability, and exhaust gas temperature (EGT) quantifies the thermal state of the exhaust gases leaving the engine manifold, providing insights into combustion efficiency. **Figure 6.3** shows the effect of AIOB and diesel fuel on exhaust gas temperature (EGT) under varying engine load conditions. It can be observed from the figure that the EGT rises with load for both fuels; however, AIOB shows a lower EGT than diesel at comparable loads. This can be explained by AIOB having a higher oxygen content, facilitating more complete oxidation at lean to moderately rich conditions, which reduces late-cycle heat release carried into the exhaust stream at these operating points. Furthermore, the lower latent heat of the diesel vaporisation causes it to remain in the liquid phase within the combustion cylinder for a longer duration[174].

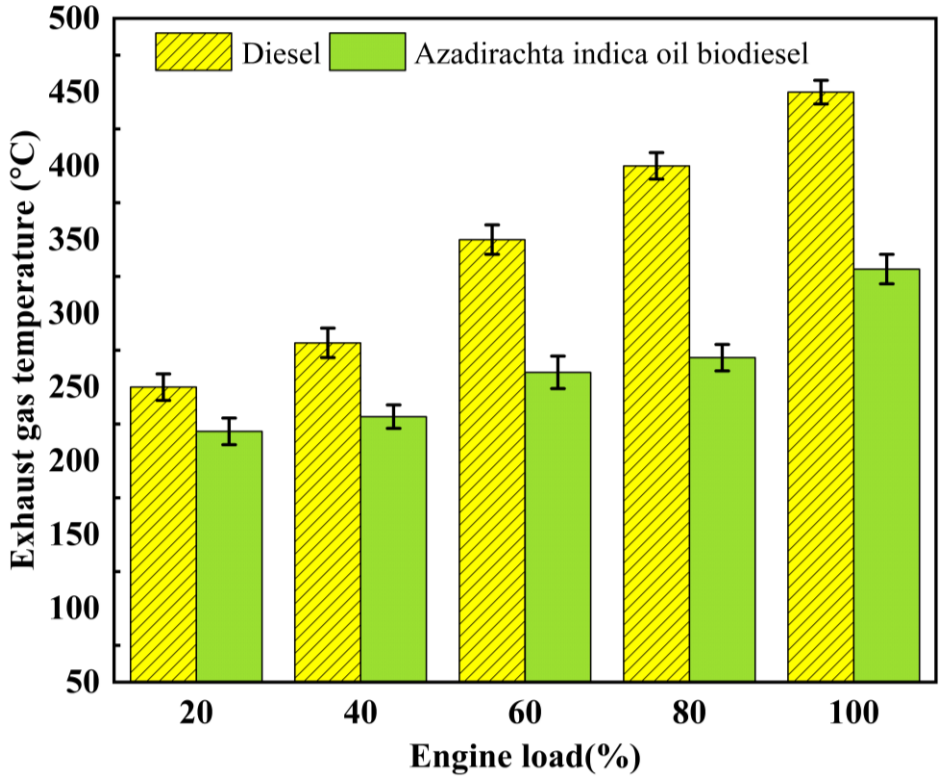

Figure 6.3 Comparative Exhaust gas temperature of AIOB and conventional diesel across varying engine loads

The combustion characteristics of the AIOB are analyzed by studying the heat release rate (HRR) and in-cylinder pressure (Pcp) at different engine load conditions. The result of **Figure 6.3** is consistent with **Figure 6.4 (a)'s** lower net HRR of AIOB at full load, indicating less intense heat liberation near top dead center (TDC) and a cooler burned-gas temperature trajectory that can translate to reduced exhaust enthalpy when expansion phasing is not advanced, especially at mid loads. AIOB exhibits a lower peak net HRR (~40.88 J/deg CA) than diesel (~49.72 J/deg CA), indicating a less aggressive premixed burn and a more distributed diffusion phase at full load, which reflects lower energy per unit mass. Furthermore, the higher density of AIOB led to a denser fuel-air mixture, which may have further affected the combustion process and contributed to the

lower peak cylinder pressures and HRR. This also explains the reduced thermal efficiency in **Figure 6.2 (a)** and the higher fuel consumption in **Figure 6.2 (b)** as less concentrated heat release near optimal phasing diminishes conversion of chemical energy to indicated work under an unchanged injection pressure. The inherent oxygen in AIOB promotes late-stage oxidation, effectively reducing CO and HC emissions. However, its lower mass-specific energy compared to diesel limits the peak HRR, resulting in cleaner but less intense combustion, illustrating the typical trade-off between emissions and performance. Furthermore, Diesel shows a higher peak in-cylinder pressure than AIOB at full load, indicating more rapid heat release and higher local temperatures around the main combustion event, which aligns with Diesel's higher heating value and better atomization/volatility under identical injection settings as shown in **Figure 6.4 (b).** The figure shows the combustion behavior inside the cylinder, representing the variation in specific heat capacity in internal combustion engines, which depends on the crankshaft's position. These CP results are consistent with reported uncertainties (±1.0% for pressure, ±1.28% for HRR), providing confidence that combustion differences arise from fuel properties. These results indicate that if diesel-like BTE and EGT are required, injection phasing, pressure, and possibly multiple injections could be optimised around AIOB's property set to recover some peak HRR/CP while preserving oxygen-driven emissions benefits.

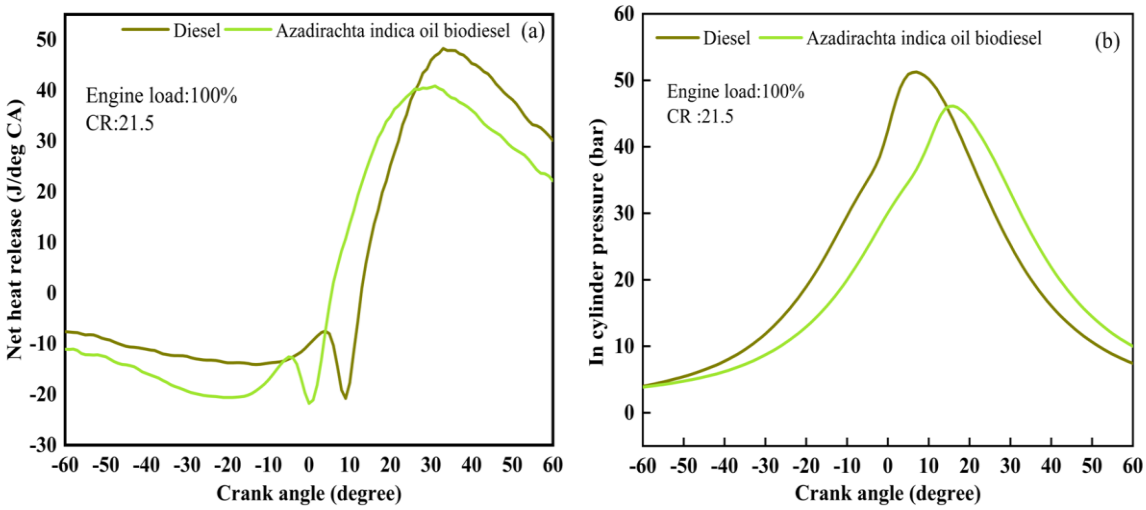

Figure 6.4 Comparative combustion characteristics of AIOB and conventional diesel at various crank angles: (a) Net HRR (b) In-cylinder pressure under full-load conditions.

6.5. Emission Characteristics

The emission from the biodiesel is one of the major factors that qualify it as sustainable. The emission characteristics of AIOB are depicted in **Figure 6.5. Figure 6.5 (a)** shows that CO emissions decline with increasing engine load for both fuels, with AIOB consistently exhibiting lower CO levels than diesel due to its higher oxygen content, which enhances the oxidation of CO to CO_2. The lower CP/HRR and more distributed heat release **(Figure 6.4 (a) and (b))** do not hinder CO clean-up for AIOB because chemically bound oxygen and higher local oxidising potential mitigate incomplete combustion pathways in the diffusion-controlled regions, especially as in-cylinder temperatures rise with increasing load.

The generation of unburned hydrocarbon (UHC) emissions is affected by several parameters, such as inadequate fuel-air mixture, flame cooling, and crevice volumes[175]. In comparison to

Azadirachta indica biodiesel (AIOB), diesel fuel tends to generate higher UHC emissions at higher engine loads, as shown in **Figure 6.5 (b)**. Maximum UHC concentrations (ppm/vol.) were observed to be 83 for diesel and 65 ppm/vol. for AIOB at 100% load, respectively. Since AIOB has a higher oxidation capacity compared to diesel during the combustion process, diesel contributes to a higher formation of hydrocarbons (HC) in the exhaust gases[176]. Similar findings were reported by Dewangan et al., who observed that biodiesel blends consistently generate lower HC emissions compared to neat diesel[177].

The NO_x emitted by diesel as well as biodiesel is shown in **Figure 6.5 (c).** An increased engine load elevates the combustion chamber temperature, and nitrogen reacts with oxygen at higher temperatures to form nitrogen oxide[178]. The figure depicts a reduced NO_x emission for diesel fuel compared to AIOB. It was noted that NO_x emissions were reduced for diesel compared to biodiesel since diesel has fewer nitrogen compounds compared to the AIOB. Although AIOB exhibits lower peak HRR and CP at full load, oxygen availability and potential local temperature increases late in diffusion burn can offset average temperature reductions and increase NO_x, especially as load raises in-cylinder thermal state and residence time at elevated temperatures. Similarly, Oni et al. observed an increased NO_x emissions from Azadirachta indica and Camelina sativa biodiesel compared to diesel in their work[179]. Numerous other studies have also corroborated the upward trend of NO_x emissions when using biodiesel blends[180].

The average CO_2 (%vol) emissions for diesel and AIOB at 100% engine load were determined to be 1.3 for diesel and 1.2 for AIOB, respectively, as shown in **Figure 6.5 (d)**. AIOB has lower CO_2 emission compared to diesel at full load (1.2 vs 1.3 vol%), which can occur when higher BSFC does not fully translate into higher exhaust CO_2 due to differences in carbon content per unit mass

and combustion phasing, alongside potential air–fuel management and dilution effects at the measurement plane. This behaviour aligns with findings from several other researchers, who consistently report that biodiesel contains less carbon per unit mass than diesel, and therefore tends to produce comparatively lower CO_2 emissions[177], [181]. This behaviour aligns with findings from several other researchers, who consistently report that biodiesel contains less carbon per unit mass than diesel, and therefore tends to produce comparatively lower CO_2 emissions[177], [181].

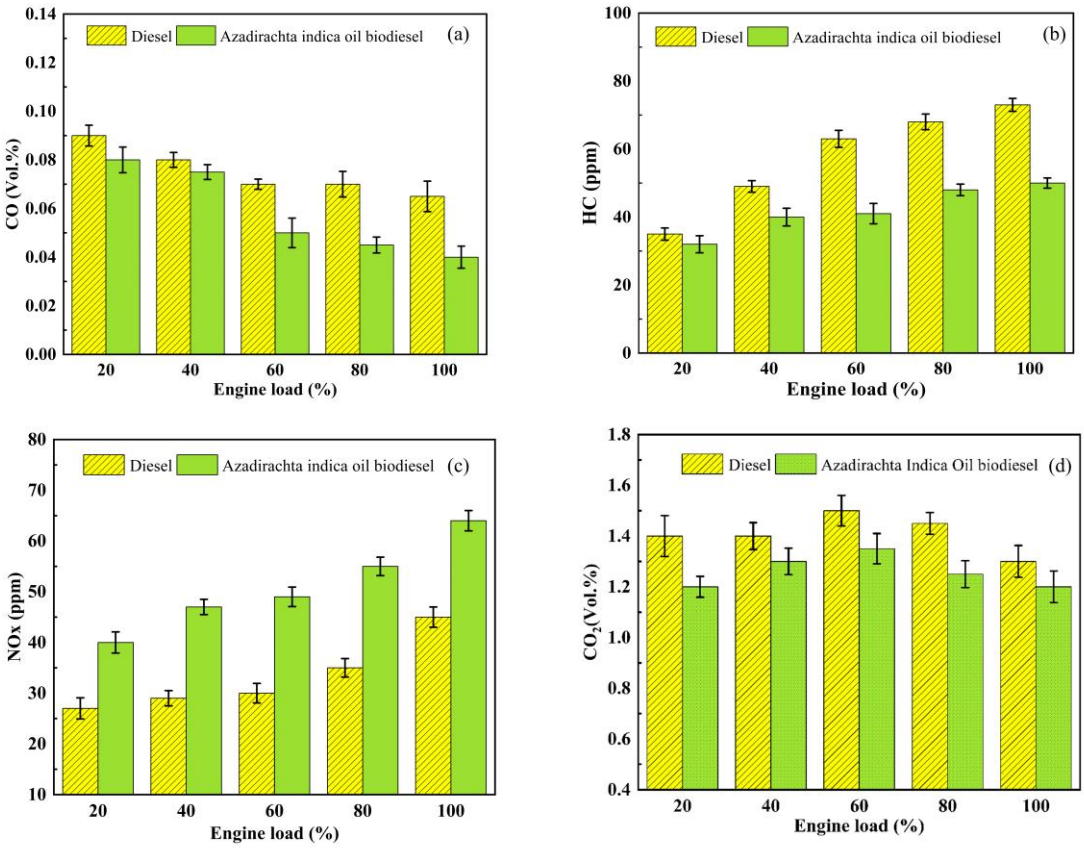

Figure 6.5 Comparative emission characteristics of AIOB and conventional diesel across varying engine loads: (a) CO (b) HC (c) NO_x (d) CO_2

6.6. Conclusion

This chapter evaluated the engine performance and emission characteristics of biodiesel synthesized from Azadirachta indica oil using deep eutectic solvent catalysts. The fuel was tested on a variable compression ratio diesel engine at 1500 rpm under load conditions ranging from 20% to 100%.

Performance analysis revealed that AIOB achieved lower brake thermal efficiency (26% versus 28.5% for diesel at full load) and higher brake-specific fuel consumption (10.2 g/kWh compared to 8.2 g/kWh). These differences come from biodiesel's lower calorific value, requiring greater fuel mass to deliver equivalent power output.

Combustion characteristics showed AIOB exhibited reduced peak heat release rate (40.88 J/deg CA versus 49.72 J/deg CA) and lower maximum in-cylinder pressure compared to diesel. This gradual combustion profile explains the observed efficiency reduction. Exhaust gas temperatures were consistently lower for AIOB, indicating more complete oxidation.

AIOB produced significantly lower carbon monoxide, unburned hydrocarbons, and carbon dioxide emissions, with approximately 22% reduction in HC at full load due to fuel-bound oxygen facilitating complete combustion. However, nitrogen oxide emissions were elevated, attributed to higher local combustion temperatures and enhanced oxygen availability.

These findings demonstrate that DES-catalyzed biodiesel functions effectively in compression ignition engines. While modest performance penalties exist, the notable reductions in CO, HC, and CO_2 emissions offer clear environmental advantages supporting sustainable transportation objectives.

Chapter 7

Conclusions and Future Scope

7.1. Conclusions

This thesis successfully developed an integrated computational-experimental framework for the rational design and application of Deep Eutectic Solvents (DESs). By bridging molecular-scale property prediction with process-level performance evaluation, the work established DESs as viable, high-performance alternatives to conventional volatile organic solvents across three critical domains: CO_2 capture, azeotrope separation, and biodiesel production.

7.1.1. Key Contributions

The research first established a robust methodology for estimating critical and thermophysical properties of DESs, presented in **Chapter 2**. This data fueled the Machine Learning models in **Chapter 3**, where Gradient Boosting (R^2 = 0.956) and SHAP analysis identified viscosity and pressure as dominant predictors for gas solubility. A novel Performance Index was introduced to rank candidates, identifying DES7 and DES1 as optimal formulations. Experimental validation in **Chapter 4** confirmed these predictions, with the Methyltriphenylphosphonium bromide-1,6-hexanediol system achieving a Henry's constant of 2.61 MPa, superior to many reported ternary systems. Process simulation (**Chapter 5**) demonstrated that using Glyceline for azeotropic separation reduced Total Annual Costs by 50% compared to DMSO, while a flash-based recovery design lowered heat duties by 40%. Finally, **Chapter 6** validated the dual solvent-catalyst role of DESs in biodiesel production, achieving 93% conversion of neem oil and reducing unburned hydrocarbon emissions by 22% in engine tests.

7.2. Limitations and Scope of the Present Work

The present thesis was designed to establish a systematic computational and experimental framework for the rational design of DESs, with targeted applications in CO_2 capture, azeotropic separation, and biodiesel production. While the work achieves its defined objectives, certain aspects were outside its scope and are identified as promising directions for future investigation.

The critical and thermophysical properties of DESs were estimated using Group Contribution Methods including the Modified Lydersen-Joback-Reid method and Haghbakhsh correlations. These semi-empirical approaches assume additive group contributions and may introduce uncertainty for DESs containing functional groups underrepresented in the training datasets of these correlations. Direct experimental determination of critical properties for all 102 DESs was beyond the scope of this work.

The process simulations conducted for IPA-water azeotrope separation represent a rigorous steady-state computational study. Laboratory or pilot-scale experimental validation of the complete extractive distillation process, along with a detailed sensitivity analysis for varying plant capacities and long-term solvent stability, presents a natural and valuable extension of this work. Furthermore, while Indian market prices were used to establish a realistic cost basis for the techno-economic analysis, the DES synthesis costs at industrial scale, including controlled heating, inert atmosphere maintenance, and vacuum processing infrastructure, were not incorporated and merit consideration in future scale-up studies.

The engine performance study in Chapter 6 was carried out using a single-cylinder VCR research engine with Azadirachta indica oil as the feedstock, which served as a representative proof-of-concept evaluation. Extending this assessment to multi-cylinder engines, varied biodiesel blends,

and diverse high-FFA feedstocks would further consolidate the practical viability of the DES-catalyzed biodiesel route. Lastly, the recyclability of DESs across multiple operational cycles and their long-term physicochemical stability under industrial conditions are important practical considerations that offer rich scope for dedicated future investigations.

7.3. Future Research Directions

The versatility of DESs extends far beyond chemical processing. Future research should prioritize high-value applications across diverse industrial sectors, ranging from advanced material synthesis to sustainable agriculture:

- **Magneto-Responsive Separations (Manufacturing):** To eliminate energy-intensive distillation, paramagnetic DESs incorporating iron-based ionic liquids should be synthesized. In continuous flow reactors, external magnetic fields could instantly separate the solvent/catalyst from the product stream, enabling non-thermal recycling and significantly reducing process energy consumption.
- **Nanomaterial Dispersion (Advanced Materials):** Concepts have been developed regarding the use of DESs as stable media for nanomaterials. Future investigations should focus on suspending graphene and Metal-Organic Frameworks (MOFs) within DES phases. By enhancing the solubility and dispersion of these materials, hybrid fluids can be created with superior thermal conductivity and catalytic surface area, opening new pathways for heat transfer fluids and catalytic supports.
- **Urban Mining and E-Waste Recovery (Sustainability):** DESs offer a greener route for "urban mining." Research should focus on specific acidic DES formulations capable of selectively leaching precious metals (gold, palladium) and critical elements (lithium, cobalt) from electronic

waste. This provides a closed-loop recycling solution that avoids the toxic, strong acids used in conventional hydrometallurgy.

- **Non-Flammable Electrolytes (Energy Storage):** The electrochemical stability of DESs makes them ideal candidates for next-generation batteries. Future scope exists in developing non-flammable, wide-electrochemical-window DES electrolytes for redox flow batteries and supercapacitors, addressing the safety risks (fire/explosion) associated with current volatile organic electrolytes.
- **Functional Coatings (Separation Technology**): The tunable viscosity and negligible volatility of DESs suggest significant potential as functional coating materials. Future work is proposed to investigate DESs as selective coatings for membrane technologies. These functionalized surfaces could allow for high-efficiency separation of specific gas or liquid mixtures, overcoming the limitations of traditional solvent-based extraction.
- **Controlled-Release Agrochemicals (Agriculture):** Research should explore DESs as solvating vehicles for hydrophobic pesticides and fertilizers. By tailoring the water miscibility of the DES carrier, "smart" formulations can be created that control the release rate of agrochemicals into the soil, preventing runoff pollution and improving nutrient absorption efficiency in crops.

7.4. Final Remarks

This thesis demonstrates that rational DES design, guided by computational intelligence, enables the development of tunable solvents that address specific industrial pain points. However, the true potential of DES technology lies in enabling entirely new processing capabilities-from self-optimizing chemical plants to smart drug delivery. As sustainability pressures intensify, the frameworks established here provide a blueprint for transitioning diverse industries toward greener, more efficient manufacturing landscapes.

References

[1] G. M. L. NOAA, "Trends in CO_2 - NOAA Global Monitoring Laboratory." Accessed: Jan. 02, 2026. [Online]. Available: https://gml.noaa.gov/ccgg/trends/gl_trend.html

[2] World Meteorological Organization (WMO), "State of the Global Climate 2024," Geneva, Climate Statement WMO-No. 1368, 2025. Accessed: Jan. 02, 2026. [Online]. Available: https://library.wmo.int/records/item/69455-state-of-the-global-climate-2024

[3] R. Bardan, "Temperatures Rising: NASA Confirms 2024 Warmest Year on Record - NASA," Temperatures Rising: NASA Confirms 2024 Warmest Year on Record. Accessed: Jan. 02, 2026. [Online]. Available: https://www.nasa.gov/news-release/temperatures-rising-nasa-confirms-2024-warmest-year-on-record/

[4] R. Lindsey and L. Dahlman, "Climate change: global temperature | NOAA." Accessed: Jan. 02, 2026. [Online]. Available: https://www.climate.gov/news-features/understanding-climate/climate-change-global-temperature

[5] V. Owino *et al.*, "The impact of climate change on food systems, diet quality, nutrition, and health outcomes: A narrative review," *Front. Clim.*, vol. 4, Aug. 2022, doi: 10.3389/fclim.2022.941842.

[6] World Health Organization, "Climate change," WHO - World Health Organization. Accessed: Jan. 10, 2026. [Online]. Available: https://www.who.int/news-room/fact-sheets/detail/climate-change-and-health

[7] International Energy Agency, "The role of CCUS in low-carbon power systems," International Energy Agency (IEA), Paris, France, Technical report, 2020. Accessed: Jan. 02, 2026. [Online]. Available: https://www.iea.org/reports/the-role-of-ccus-in-low-carbon-power-systems/the-co2-emissions-challenge

[8] International Energy Agency, "How much CO_2 does India emit?," IEA. Accessed: Jan. 02, 2026. [Online]. Available: https://www.iea.org/countries/india/emissions

[9] International Energy Agency, "Global Energy Review 2025," International Energy Agency (IEA), Paris, France, Annual report, 2025. Accessed: Jan. 02, 2026. [Online]. Available: https://www.iea.org/reports/global-energy-review-2025

[10] A. A. Kiss and R. Smith, "Rethinking energy use in distillation processes for a more sustainable chemical industry," *Energy*, vol. 203, p. 117788, Jul. 2020, doi: 10.1016/j.energy.2020.117788.

[11] A. K. Gomey, M. M. Tripathi, M. B. Haider, and R. Kumar, “Comparative analysis of isopropyl alcohol dehydration using ionic liquids and deep eutectic solvent,” *Journal of Ionic Liquids*, vol. 3, no. 2, p. 100069, Dec. 2023, doi: 10.1016/J.JIL.2023.100069.

[12] Fact.MR, “Isopropanol Market Size, Share and Growth Statistics 2035,” Fact.MR, FACT836MR, Jul. 2025. Accessed: Jan. 02, 2026. [Online]. Available: https://www.factmr.com/report/836/isopropanol-market

[13] M. Karim, R. S. Boikess, R. A. Schwartz, and P. J. Cohen, “Dimethyl sulfoxide (DMSO): a solvent that may solve selected cutaneous clinical challenges,” *Arch Dermatol Res*, vol. 315, no. 6, pp. 1465–1472, Aug. 2023, doi: 10.1007/s00403-022-02494-1.

[14] M. Verheijen *et al.*, “DMSO induces drastic changes in human cellular processes and epigenetic landscape in vitro,” *Sci Rep*, vol. 9, no. 1, p. 4641, Mar. 2019, doi: 10.1038/s41598-019-40660-0.

[15] A. V. Polkovnichenko, E. V. Lupachev, A. A. Voshkin, and N. N. Kulov, “Effect of Sulfolane, Dimethyl Sulfoxide, and N-Methyl-2-pyrrolidone on Relative Volatility of a 2,2,2-Trifluoroethanol–Isopropanol Azeotropic System,” *J. Chem. Eng. Data*, vol. 66, no. 3, pp. 1238–1248, Mar. 2021, doi: 10.1021/acs.jced.0c00790.

[16] F. Cilurzo *et al.*, “An Insight into the Skin Penetration Enhancement Mechanism of N-Methylpyrrolidone,” *Mol. Pharmaceutics*, vol. 11, no. 3, pp. 1014–1021, Mar. 2014, doi: 10.1021/mp400675d.

[17] Fortune Business Insights, “Biodiesel Market Size, Share & Industry Analysis, By Feedstock, By Blend Type, By Application, and Regional Forecast, 2025–2032,” Fortune Business Insights, Pune, India, FBI101631, Dec. 2025. Accessed: Jan. 03, 2026. [Online]. Available: https://www.fortunebusinessinsights.com/industry-reports/biodiesel-market-101631

[18] V. Mandari and S. K. Devarai, “Biodiesel Production Using Homogeneous, Heterogeneous, and Enzyme Catalysts via Transesterification and Esterification Reactions: a Critical Review,” *Bioenerg. Res.*, vol. 15, no. 2, pp. 935–961, Jun. 2022, doi: 10.1007/s12155-021-10333-w.

[19] D. T. Oyekunle, M. Barasa, E. A. Gendy, and S. K. Tiong, “Heterogeneous catalytic transesterification for biodiesel production: Feedstock properties, catalysts and process parameters,” *Process Safety and Environmental Protection*, vol. 177, pp. 844–867, Sep. 2023, doi: 10.1016/j.psep.2023.07.064.

[20] N. A. Roslan, S. Zainal Abidin, N. Abdullah, O. U. Osazuwa, R. Abdul Rasid, and N. M. Yunus, “Esterification reaction of free fatty acid in used cooking oil using sulfonated

hypercrosslinked exchange resin as catalyst," *Chemical Engineering Research and Design*, vol. 180, pp. 414–424, Apr. 2022, doi: 10.1016/j.cherd.2021.10.020.

[21] B. Changmai, C. Vanlalveni, A. P. Ingle, R. Bhagat, and L. Rokhum, "Widely used catalysts in biodiesel production: A review," *RSC Advances*, vol. 10, no. 68, pp. 41625–41679, 2020, doi: 10.1039/d0ra07931f.

[22] X. Yang, R. J. Rees, W. Conway, G. Puxty, Q. Yang, and D. A. Winkler, "Computational Modeling and Simulation of CO_2 Capture by Aqueous Amines," *Chem. Rev.*, vol. 117, no. 14, pp. 9524–9593, Jul. 2017, doi: 10.1021/acs.chemrev.6b00662.

[23] Y. Huang *et al.*, "The structure–activity relationships of reaction heat in secondary amine aqueous solutions for CO_2 capture," *Separation and Purification Technology*, vol. 352, p. 128016, Jan. 2025, doi: 10.1016/j.seppur.2024.128016.

[24] F. Meng, Y. Meng, T. Ju, S. Han, L. Lin, and J. Jiang, "Research progress of aqueous amine solution for CO_2 capture: A review," *Renewable and Sustainable Energy Reviews*, vol. 168, p. 112902, Oct. 2022, doi: 10.1016/j.rser.2022.112902.

[25] L. Wang *et al.*, "Advanced Monoethanolamine Absorption Using Sulfolane as a Phase Splitter for CO_2 Capture," *Environ. Sci. Technol.*, vol. 52, no. 24, pp. 14556–14563, Dec. 2018, doi: 10.1021/acs.est.8b05654.

[26] Intergovernmental Panel on Climate Change (IPCC), "IPCC Special Report on Carbon Dioxide Capture and Storage," Intergovernmental Panel on Climate Change, Cambridge, United Kingdom; New York, NY, USA, Special Report (Working Group III) 978-0-521-68551–1, 2018. Accessed: Jan. 03, 2026. [Online]. Available: https://www.ipcc.ch/site/assets/uploads/2018/03/srccs_wholereport-1.pdf

[27] P. Wasserscheid and W. Keim, "Ionic Liquids—New 'Solutions' for Transition Metal Catalysis," *Angewandte Chemie International Edition*, vol. 39, no. 21, pp. 3772–3789, 2000, doi: 10.1002/1521-3773(20001103)39:21<3C3772::AID-ANIE3772>3E3.0.CO;2-5.

[28] L. A. Blanchard, D. Hancu, E. J. Beckman, and J. F. Brennecke, "Green processing using ionic liquids and CO_2," *Nature*, vol. 399, no. 6731, pp. 28–29, May 1999, doi: 10.1038/19887.

[29] K. Stagel, A. Szpecht, D. Zielinski, M. Smiglak, M. Schnürch, and K. Bica-Schröder, "Halide-Free Continuous Synthesis of Hydrophobic Ionic Liquids," *ACS Sustainable Chem. Eng.*, vol. 10, no. 34, pp. 11215–11222, Aug. 2022, doi: 10.1021/acssuschemeng.2c02871.

[30] R. A. Sheldon, "Green solvents for sustainable organic synthesis: state of the art," *Green Chem.*, vol. 7, no. 5, pp. 267–278, May 2005, doi: 10.1039/B418069K.

[31] C. Yao, Y. Zhao, and G. Chen, “Multiphase processes with ionic liquids in microreactors: hydrodynamics, mass transfer and applications,” *Chemical Engineering Science*, vol. 189, pp. 340–359, Nov. 2018, doi: 10.1016/j.ces.2018.06.007.

[32] D. F. Ordóñez, A. R. N. Pontillo, N. M. Dowell, T. Welton, and K.-Y. Lee, “Unveiling the environmental costs of lignocellulosic film production with ionic liquids: the case of 1-ethyl-3-methylimidazolium acetate,” *RSC Sustainability*, vol. 3, no. 7, pp. 3002–3008, Jul. 2025, doi: 10.1039/D5SU00212E.

[33] C. Guo, X. Liu, F. Wang, Y. Cao, S. Zheng, and G. He, “Economic Analysis and Life Cycle Environmental Assessment of Imidazolium-Based Ionic Liquids for Separation of the Methanol/Dimethyl Carbonate Azeotrope,” *ACS Sustainable Chem. Eng.*, vol. 11, no. 28, pp. 10482–10495, Jul. 2023, doi: 10.1021/acssuschemeng.3c02059.

[34] N. Aggarwal, “Ionic Liquid-Based Green Solvents for Extraction and Purification of Natural Plant Products,” *Current Physical Chemistry*, vol. 14, no. 3, pp. 184–193, Nov. 2024, doi: 10.2174/0118779468304352240423084047.

[35] A. R. P. Gonçalves, X. Paredes, A. F. Cristino, F. J. V. Santos, and C. S. G. P. Queirós, “Ionic Liquids—A Review of Their Toxicity to Living Organisms,” *International Journal of Molecular Sciences*, vol. 22, no. 11, p. 5612, Jan. 2021, doi: 10.3390/ijms22115612.

[36] A. P. Abbott, D. Boothby, G. Capper, D. L. Davies, and R. K. Rasheed, “Deep Eutectic Solvents formed between choline chloride and carboxylic acids: Versatile alternatives to ionic liquids,” *Journal of the American Chemical Society*, vol. 126, no. 29, pp. 9142–9147, Jul. 2004, doi: 10.1021/ja048266j.

[37] A. K. Gomey, M. B. Haider, and R. Kumar, “Designing of energy-efficient deep eutectic solvents for CO_2 capture: insights from physical and thermodynamic property evaluation,” *Journal of Molecular Liquids*, vol. 434, p. 127996, Sep. 2025, doi: 10.1016/j.molliq.2025.127996.

[38] E. L. Smith, A. P. Abbott, and K. S. Ryder, “Deep Eutectic Solvents (DESs) and Their Applications,” *Chemical Reviews*, vol. 114, no. 21, pp. 11060–11082, 2014, doi: 10.1021/cr300162p.

[39] A. P. Abbott, G. Capper, D. L. Davies, R. K. Rasheed, and V. Tambyrajah, “Novel solvent properties of choline chloride/urea mixtures,” *Chemical Communications*, no. 1, pp. 70–71, 2003, doi: 10.1039/b210714g.

[40] B. D. Like, C. E. Uhlenbrock, and M. J. Panzer, “A quantitative thermodynamic metric for identifying deep eutectic solvents,” *Phys. Chem. Chem. Phys.*, vol. 25, no. 11, pp. 7946–7950, Mar. 2023, doi: 10.1039/D3CP00555K.

[41] X. Li, M. Hou, B. Han, X. Wang, and L. Zou, "Solubility of CO_2 in a choline chloride + urea eutectic mixture," *Journal of Chemical and Engineering Data*, vol. 53, no. 2, pp. 548–550, Feb. 2008, doi: 10.1021/je700638u.

[42] P. Liu, J. W. Hao, L. P. Mo, and Z. H. Zhang, "Recent advances in the application of deep eutectic solvents as sustainable media as well as catalysts in organic reactions," *RSC Advances*, vol. 5, no. 60, pp. 48675–48704, 2015, doi: 10.1039/c5ra05746a.

[43] R. B. Leron and M. H. Li, "Solubility of carbon dioxide in a eutectic mixture of choline chloride and glycerol at moderate pressures," *Journal of Chemical Thermodynamics*, vol. 57, pp. 131–136, Feb. 2013, doi: 10.1016/j.jct.2012.08.025.

[44] R. B. Leron and M. H. Li, "Solubility of carbon dioxide in a choline chloride-ethylene glycol based deep eutectic solvent," *Thermochimica Acta*, vol. 551, pp. 14–19, Jan. 2013, doi: 10.1016/j.tca.2012.09.041.

[45] Á. Pérez-Salado Kamps, D. Tuma, J. Xia, and G. Maurer, "Solubility of CO_2 in the Ionic Liquid [bmim][PF6]," *J. Chem. Eng. Data*, vol. 48, no. 3, pp. 746–749, Mar. 2003, doi: 10.1021/je034023f.

[46] S. N. V. K. Aki, B. R. Mellein, E. M. Saurer, and J. F. Brennecke, "High-Pressure Phase Behavior of Carbon Dioxide with Imidazolium-Based Ionic Liquids," *J. Phys. Chem. B*, vol. 108, no. 52, pp. 20355–20365, Dec. 2004, doi: 10.1021/jp046895+.

[47] M. Lu, G. Han, Y. Jiang, X. Zhang, D. Deng, and N. Ai, "Solubilities of carbon dioxide in the eutectic mixture of levulinic acid (or furfuryl alcohol) and choline chloride," *Journal of Chemical Thermodynamics*, vol. 88, pp. 72–77, Sep. 2015, doi: 10.1016/j.jct.2015.04.021.

[48] Y. Chen, N. Ai, G. Li, H. Shan, Y. Cui, and D. Deng, "Solubilities of carbon dioxide in eutectic mixtures of choline chloride and dihydric alcohols," *Journal of Chemical and Engineering Data*, vol. 59, no. 4, pp. 1247–1253, Apr. 2014, doi: 10.1021/je400884v.

[49] M. B. Haider, D. Jha, B. Marriyappan Sivagnanam, and R. Kumar, "Thermodynamic and Kinetic Studies of CO_2 Capture by Glycol and Amine-Based Deep Eutectic Solvents," *Journal of Chemical and Engineering Data*, vol. 63, no. 8, pp. 2671–2680, 2018, doi: 10.1021/acs.jced.8b00015.

[50] S. Sarmad, Y. Xie, J. P. Mikkola, and X. Ji, "Screening of deep eutectic solvents (DESs) as green CO_2 sorbents: from solubility to viscosity," *New Journal of Chemistry*, vol. 41, no. 1, pp. 290–301, 2016, doi: 10.1039/c6nj03140d.

[51] G. Li, D. Deng, Y. Chen, H. Shan, and N. Ai, "Solubilities and thermodynamic properties of CO_2 in choline-chloride based deep eutectic solvents," *Journal of Chemical Thermodynamics*, vol. 75, pp. 58–62, 2014, doi: 10.1016/j.jct.2014.04.012.

[52] R. B. Leron, A. Caparanga, and M. H. Li, "Carbon dioxide solubility in a deep eutectic solvent based on choline chloride and urea at T = 303.15-343.15K and moderate pressures," *Journal of the Taiwan Institute of Chemical Engineers*, vol. 44, no. 6, pp. 879–885, Nov. 2013, doi: 10.1016/j.jtice.2013.02.005.

[53] E. Ali *et al.*, "Solubility of CO_2 in deep eutectic solvents: Experiments and modelling using the Peng-Robinson equation of state," *Chemical Engineering Research and Design*, vol. 92, no. 10, pp. 1898–1906, Oct. 2014, doi: 10.1016/j.cherd.2014.02.004.

[54] L. L. Sze *et al.*, "Ternary deep eutectic solvents tasked for carbon dioxide capture," *ACS Sustainable Chemistry and Engineering*, vol. 2, no. 9, pp. 2117–2123, Sep. 2014, doi: 10.1021/sc5001594.

[55] H. Ghaedi, M. Ayoub, S. Sufian, A. M. Shariff, S. M. Hailegiorgis, and S. N. Khan, "CO_2 capture with the help of Phosphonium-based deep eutectic solvents," *Journal of Molecular Liquids*, vol. 243, pp. 564–571, 2017, doi: 10.1016/j.molliq.2017.08.046.

[56] H. Ghaedi, M. Ayoub, S. Sufian, G. Murshid, S. Farrukh, and A. M. Shariff, "Investigation of various process parameters on the solubility of carbon dioxide in phosphonium-based deep eutectic solvents and their aqueous mixtures: Experimental and modeling," *International Journal of Greenhouse Gas Control*, vol. 66, no. May, pp. 147–158, 2017, doi: 10.1016/j.ijggc.2017.09.020.

[57] M. B. Haider, P. Maheshwari, and R. Kumar, "CO_2 capture from flue gas using phosphonium based deep eutectic solvents: Modeling and simulation approach," *Journal of Environmental Chemical Engineering*, vol. 9, no. 6, p. 106727, Dec. 2021, doi: 10.1016/J.JECE.2021.106727.

[58] Y. Cui *et al.*, "Performance and Mechanism Study on Functionalized Phosphonium-Based Deep Eutectic Solvents for CO_2 Absorption," *Int J Thermophys*, vol. 44, no. 7, p. 98, May 2023, doi: 10.1007/s10765-023-03207-0.

[59] T. Ahmad *et al.*, "Performance evaluation of phosphonium based deep eutectic solvents coated cerium oxide nanoparticles for CO_2 capture," *Environmental Research*, vol. 222, no. January, p. 115314, 2023, doi: 10.1016/j.envres.2023.115314.

[60] Z. Yang, B. Chen, H. Chen, and H. Li, "A critical review on machine-learning-assisted screening and design of effective sorbents for carbon dioxide (CO_2) capture," *Front. Energy Res.*, vol. 10, Jan. 2023, doi: 10.3389/fenrg.2022.1043064.

[61] I. Adeyemi, M. R. M. Abu-Zahra, and I. M. AlNashef, “Physicochemical properties of alkanolamine-choline chloride deep eutectic solvents: Measurements, group contribution and artificial intelligence prediction techniques,” *Journal of Molecular Liquids*, vol. 256, no. 2017, pp. 581–590, 2018, doi: 10.1016/j.molliq.2018.02.085.

[62] J. Wang, Z. Song, L. Chen, T. Xu, L. Deng, and Z. Qi, “Prediction of CO_2 solubility in deep eutectic solvents using random forest model based on COSMO-RS-derived descriptors,” *Green Chemical Engineering*, vol. 2, no. 4, pp. 431–440, 2021, doi: 10.1016/j.gce.2021.08.002.

[63] M. Mohan, O. Demerdash, B. A. Simmons, J. C. Smith, M. K. Kidder, and S. Singh, “Accurate prediction of carbon dioxide capture by deep eutectic solvents using quantum chemistry and a neural network,” *Green Chem.*, vol. 25, no. 9, pp. 3475–3492, May 2023, doi: 10.1039/D2GC04425K.

[64] T. Lemaoui *et al.*, “Predicting the CO_2 Capture Capability of Deep Eutectic Solvents and Screening over 1000 of their Combinations Using Machine Learning,” 2023, doi: 10.1021/acssuschemeng.3c00415.

[65] D. M. Makarov, Y. A. Fadeeva, V. A. Golubev, and A. M. Kolker, “Designing deep eutectic solvents for efficient CO_2 capture: A data-driven screening approach,” *Separation and Purification Technology*, vol. 325, p. 124614, Nov. 2023, doi: 10.1016/j.seppur.2023.124614.

[66] Z. Song, H. Shi, X. Zhang, and T. Zhou, “Prediction of CO_2 solubility in ionic liquids using machine learning methods,” *Chemical Engineering Science*, vol. 223, p. 115752, Sep. 2020, doi: 10.1016/j.ces.2020.115752.

[67] M. Mohan, O. N. Demerdash, B. A. Simmons, S. Singh, M. K. Kidder, and J. C. Smith, “Physics-Based Machine Learning Models Predict Carbon Dioxide Solubility in Chemically Reactive Deep Eutectic Solvents,” *ACS Omega*, vol. 9, no. 17, pp. 19548–19559, Apr. 2024, doi: 10.1021/acsomega.4c01175.

[68] G. Hernández Morales, E. I. Sanchez Medina, A. Jiménez-Gutiérrez, and V. M. Zavala, “Graph neural networks for CO_2 solubility predictions in Deep Eutectic Solvents,” *Computers & Chemical Engineering*, vol. 187, p. 108750, Aug. 2024, doi: 10.1016/j.compchemeng.2024.108750.

[69] V. C. Eze, A. N. Phan, and A. P. Harvey, “Intensified one-step biodiesel production from high water and free fatty acid waste cooking oils,” *Fuel*, vol. 220, pp. 567–574, May 2018, doi: 10.1016/j.fuel.2018.02.050.

[70] H. Guo *et al.*, "Acid-base bifunctional catalyst with coordinatively unsaturated cobalt-nitrogen sites for the simultaneous conversion of microalgal triglycerides and free fatty acids into biodiesel," *Bioresource Technology*, vol. 350, p. 126862, Apr. 2022, doi: 10.1016/j.biortech.2022.126862.

[71] A. Munyentwali, H. Li, and Q. Yang, "Review of advances in bifunctional solid acid/base catalysts for sustainable biodiesel production," *Applied Catalysis A: General*, vol. 633, p. 118525, Mar. 2022, doi: 10.1016/J.APCATA.2022.118525.

[72] X. Liu, B. Gao, Y. Jiang, N. Ai, and D. Deng, "Solubilities and Thermodynamic Properties of Carbon Dioxide in Guaiacol-Based Deep Eutectic Solvents," *Journal of Chemical and Engineering Data*, vol. 62, no. 4, pp. 1448–1455, Apr. 2017, doi: 10.1021/acs.jced.6b01013.

[73] L. F. Zubeir, D. J. G. P. Van Osch, M. A. A. Rocha, F. Banat, and M. C. Kroon, "Carbon Dioxide Solubilities in Decanoic Acid-Based Hydrophobic Deep Eutectic Solvents," *Journal of Chemical and Engineering Data*, vol. 63, no. 4, pp. 913–919, Apr. 2018, doi: 10.1021/acs.jced.7b00534.

[74] F. Luo *et al.*, "Comprehensive Evaluation of a Deep Eutectic Solvent Based CO_2 Capture Process through Experiment and Simulation," *ACS Sustainable Chemistry and Engineering*, vol. 9, no. 30, pp. 10250–10265, 2021, doi: 10.1021/acssuschemeng.1c02722.

[75] H. Qin, Z. Song, H. Cheng, L. Deng, and Z. Qi, "Physical absorption of carbon dioxide in imidazole-PTSA based deep eutectic solvents," *Journal of Molecular Liquids*, vol. 326, Mar. 2021, doi: 10.1016/j.molliq.2021.115292.

[76] X. Li, X. Liu, and D. Deng, "Solubilities and Thermodynamic Properties of CO_2 in Four Azole-Based Deep Eutectic Solvents," *Journal of Chemical and Engineering Data*, vol. 63, no. 6, pp. 2091–2096, Jun. 2018, doi: 10.1021/acs.jced.8b00098.

[77] D. Deng, Y. Jiang, X. Liu, Z. Zhang, and N. Ai, "Investigation of solubilities of carbon dioxide in five levulinic acid-based deep eutectic solvents and their thermodynamic properties," *Journal of Chemical Thermodynamics*, vol. 103, pp. 212–217, Dec. 2016, doi: 10.1016/j.jct.2016.08.015.

[78] R. Haghbakhsh, M. Keshtkar, A. Shariati, and S. Raeissi, "A comprehensive experimental and modeling study on CO_2 solubilities in the deep eutectic solvent based on choline chloride and butane-1,2-diol," *Fluid Phase Equilibria*, vol. 561, Oct. 2022, doi: 10.1016/J.FLUID.2022.113535.

[79] R. Haghbakhsh, M. Keshtkar, A. Shariati, and S. Raeissi, "A study on carbon dioxide solubility in the deep eutectic solvent (1 sodium bromide + 6 ethylene glycol): Experimental

and modeling by the SRK and CPA EoS," *The Journal of Chemical Thermodynamics*, vol. 178, p. 106971, Mar. 2023, doi: 10.1016/j.jct.2022.106971.

[80] H. B. Balaraman, V. Rangarajan, and S. K. Rathnasamy, "A synergetic green approach for enhanced CO_2 capture in protic deep eutectic mixtures – Kinetics and Henry's solubility determination," *Journal of CO_2 Utilization*, vol. 65, p. 102217, Nov. 2022, doi: 10.1016/j.jcou.2022.102217.

[81] G. Yu *et al.*, "CO_2 capture with hydrophobic halogen-free natural deep eutectic solvents: Perturbed-Chain Statistical Associating Fluid Theory modeling and molecular insights," *AIChE Journal*, vol. n/a, no. n/a, p. e18878, doi: 10.1002/aic.18878.

[82] A. A. Manafpour, F. Feyzi, and M. Rezaee, "An environmentally friendly deep eutectic solvent for CO_2 capture," *Sci Rep*, vol. 14, no. 1, p. 19744, Aug. 2024, doi: 10.1038/s41598-024-70761-4.

[83] K. A. Pishro, G. Murshid, F. S. Mjalli, and J. Naser, "Carbon dioxide solubility in amine-based deep eutectic solvents: Experimental and theoretical investigation," *Journal of Molecular Liquids*, vol. 325, p. 115133, Mar. 2021, doi: 10.1016/j.molliq.2020.115133.

[84] A. Alhadid, J. Safarov, L. Mokrushina, K. Müller, and M. Minceva, "Carbon Dioxide Solubility in Nonionic Deep Eutectic Solvents Containing Phenolic Alcohols," *Front. Chem.*, vol. 10, Mar. 2022, doi: 10.3389/fchem.2022.864663.

[85] N. He, Q. Chen, J. Fan, F. Song, Y. Zhang, and H. Mu, "Comprehensive exploration of the adsorption capacity of innovative betaine-based deep eutectic solvents for carbon dioxide capture," *The Journal of Chemical Thermodynamics*, vol. 178, p. 106958, Mar. 2023, doi: 10.1016/j.jct.2022.106958.

[86] Y. Ainai, A. Taniguchi, T. Kuramochi, C. Yokoyama, and D. Kodama, "Density, viscosity, and CO_2 solubility of deep eutectic solvents comprising tetrabutylammonium or phosphonium bromide and ethylene glycol," *Fluid Phase Equilibria*, vol. 584, p. 114122, Sep. 2024, doi: 10.1016/j.fluid.2024.114122.

[87] K. Li, R. Li, X. Duan, and D. Deng, "New Type V Pyrazole/Glycerol Deep Eutectic Solvent: Physiochemical Properties and Gas Solubilities of NH_3 or CO_2," *J Solution Chem*, vol. 52, no. 9, pp. 1033–1047, Sep. 2023, doi: 10.1007/s10953-023-01292-1.

[88] D. Deng, X. Deng, X. Duan, and L. Gong, "Protic guanidine isothiocyanate plus acetamide deep eutectic solvents with low viscosity for efficient NH_3 capture and NH3/CO2 separation," *Journal of Molecular Liquids*, vol. 324, p. 114719, Feb. 2021, doi: 10.1016/j.molliq.2020.114719.

[89] F. Rabhi, F. Mutelet, and H. Sifaoui, “Solubility of Carbon Dioxide in Carboxylic Acid-Based Deep Eutectic Solvents,” *J. Chem. Eng. Data*, vol. 66, no. 1, pp. 702–711, Jan. 2021, doi: 10.1021/acs.jced.0c00844.

[90] J. Fan, X. Zhang, N. He, F. Song, and X. Zhang, “Physical absorption and thermodynamic modeling of CO_2 in new deep eutectic solvents,” *Journal of Molecular Liquids*, vol. 402, p. 124752, May 2024, doi: 10.1016/j.molliq.2024.124752.

[91] B. E. Poling, J. M. Prausnitz, and J. P. O’Connell, *Properties of Gases and Liquids*, 5th Edition. New York: McGraw-Hill Education, 2001. [Online]. Available: https://www.accessengineeringlibrary.com/content/book/9780070116825

[92] K. G. Joback and R. C. Reid, “ESTIMATION OF PURE-COMPONENT PROPERTIES FROM GROUP-CONTRIBUTIONS,” vol. 57, no. 1–6, pp. 233–243, Jul. 2007, doi: 10.1080/00986448708960487.

[93] J. O. Valderrama, L. A. Forero, and R. E. Rojas, “Critical properties and normal boiling temperature of ionic liquids. Update and a new consistency test,” *Industrial and Engineering Chemistry Research*, vol. 51, no. 22, pp. 7838–7844, Jun. 2012, doi: 10.1021/ie202934g.

[94] A.L. Lydersen, Estimation of Critical Properties of Organic Compounds; Report 3*; University of Wisconsin, College of Engineering, Engineering Experimental Station:*, vol. II, no. 1955. 1955.

[95] S. D. Labinov and J. R. Sand, “An analytical method of predicting Lee-Kesler-Plöcker equation-of-state binary interaction coefficients,” *International Journal of Thermophysics*, vol. 16, no. 6, pp. 1393–1411, 1995, doi: 10.1007/BF02083548.

[96] R. Haghbakhsh, S. Raeissi, and A. R. C. Duarte, “Group contribution and atomic contribution models for the prediction of various physical properties of deep eutectic solvents,” *Scientific Reports*, vol. 11, no. 1, pp. 1–19, 2021, doi: 10.1038/s41598-021-85824-z.

[97] Y. Yoo, “A novel approach based on detailed structural and molar free volume analyses to characteristics of deep eutectic solvents specialized for CO_2 absorption,” *Chemical Engineering Journal*, vol. 461, p. 141802, Apr. 2023, doi: 10.1016/j.cej.2023.141802.

[98] D. Beysens and P. Calmettes, “Temperature dependence of the refractive indices of liquids: Deviation from the Lorentz–Lorenz formula,” *The Journal of Chemical Physics*, vol. 66, no. 2, pp. 766–771, Jan. 1977, doi: 10.1063/1.433954.

[99] X. J. Hou, L. Y. Yu, Y. X. Wang, K. J. Wu, and C. H. He, “Comprehensive Prediction of Densities for Deep Eutectic Solvents: A New Bonding-Group Interaction Contribution Scheme,” *Industrial and Engineering Chemistry Research*, vol. 60, no. 35, pp. 13127–13139, 2021, doi: 10.1021/acs.iecr.1c02260.

[100] X. Wu *et al.*, “1-ethyl-3-methylimidazolium chloride plus imidazole deep eutectic solvents as physical solvents for remarkable separation of H_2S from CO_2,” *Separation and Purification Technology*, vol. 276, p. 119313, Dec. 2021, doi: 10.1016/j.seppur.2021.119313.

[101] B. Nowosielski, M. Jamrógiewicz, J. Łuczak, M. Śmiechowski, and D. Warmińska, “Experimental and predicted physicochemical properties of monopropanolamine-based deep eutectic solvents,” *Journal of Molecular Liquids*, vol. 309, pp. 1–12, 2020, doi: 10.1016/j.molliq.2020.113110.

[102] K. A. Omar and R. Sadeghi, “Physicochemical properties of deep eutectic solvents: A review,” *Journal of Molecular Liquids*, vol. 360, p. 119524, 2022, doi: 10.1016/j.molliq.2022.119524.

[103] K. A. Omar and R. Sadeghi, “Database of deep eutectic solvents and their physical properties: A review,” *Journal of Molecular Liquids*, vol. 384, p. 121899, Aug. 2023, doi: 10.1016/j.molliq.2023.121899.

[104] K. A. Omar and R. Sadeghi, “Novel Nonanol-Based deep eutectic solvents: Thermophysical properties and their applications in Liquid-Liquid extraction and amino acid detection,” *Journal of Molecular Liquids*, vol. 336, p. 116359, Aug. 2021, doi: 10.1016/j.molliq.2021.116359.

[105] Y. Chen *et al.*, “Tuning refractive index of deep eutectic solvents,” *Journal of Molecular Liquids*, vol. 348, p. 118031, Feb. 2022, doi: 10.1016/j.molliq.2021.118031.

[106] S. P. Ijardar, V. Singh, and R. L. Gardas, “Revisiting the Physicochemical Properties and Applications of Deep Eutectic Solvents,” *Molecules*, vol. 27, no. 4, Art. no. 4, Jan. 2022, doi: 10.3390/molecules27041368.

[107] L.-Y. Yu, X.-J. Hou, G.-P. Ren, K.-J. Wu, and C.-H. He, “Viscosity model of deep eutectic solvents from group contribution method,” *AIChE Journal*, vol. 68, no. 9, p. e17744, 2022, doi: 10.1002/aic.17744.

[108] A. Yadav and S. Pandey, “Densities and Viscosities of (Choline Chloride + Urea) Deep Eutectic Solvent and Its Aqueous Mixtures in the Temperature Range 293.15 K to 363.15 K,” *J. Chem. Eng. Data*, vol. 59, no. 7, pp. 2221–2229, Jul. 2014, doi: 10.1021/je5001796.

[109] A. Yadav, S. Trivedi, R. Rai, and S. Pandey, "Densities and dynamic viscosities of (choline chloride + glycerol) deep eutectic solvent and its aqueous mixtures in the temperature range (283.15–363.15) K," *Fluid Phase Equilibria*, vol. 367, pp. 135–142, Apr. 2014, doi: 10.1016/j.fluid.2014.01.028.

[110] D. Peng, Z. Yu, A. Alhadid, and M. Minceva, "Modeling the Viscosity of ChCl-Based Deep Eutectic Solvents and Their Mixtures with Water," *Ind. Eng. Chem. Res.*, vol. 63, no. 3, pp. 1623–1633, Jan. 2024, doi: 10.1021/acs.iecr.3c03652.

[111] P. M. Mathias and J. P. O'connell, "The Gibbs−Helmholtz Equation and the Thermodynamic Consistency of Chemical Absorption Data," 2012, doi: 10.1021/ie202668k.

[112] M. Farsi and E. Soroush, "CO_2 absorption by ionic liquids and deep eutectic solvents," *Advances in Carbon Capture: Methods, Technologies and Applications*, pp. 89–105, Jan. 2020, doi: 10.1016/B978-0-12-819657-1.00004-9.

[113] X. Li *et al.*, "Low energy-consuming CO_2 capture by phase change absorbents of amine/alcohol/H2O," *Separation and Purification Technology*, vol. 275, p. 119181, Nov. 2021, doi: 10.1016/J.SEPPUR.2021.119181.

[114] P. López-Porfiri, J. F. Brennecke, and M. Gonzalez-Miquel, "Excess molar enthalpies of deep eutectic solvents (DESs) composed of quaternary ammonium salts and glycerol or ethylene glycol," *Journal of Chemical and Engineering Data*, vol. 61, no. 12, pp. 4245–4251, Dec. 2016, doi: 10.1021/acs.jced.6b00608.

[115] J. J. Chen, W. W. Li, X. L. Li, and H. Q. Yu, "Carbon dioxide capture by aminoalkyl imidazolium-based ionic liquid: a computational investigation," *Physical Chemistry Chemical Physics*, vol. 14, no. 13, pp. 4589–4596, Mar. 2012, doi: 10.1039/C2CP23642G.

[116] Y. Wang, J. Yi, X. Peng, X. Ma, and S. Peng, "Structure–property relationships of novel fluorinated polycarbonate polyurethane films with high transparency and thermal stability," *Res Chem Intermed*, vol. 45, no. 2, pp. 845–862, Feb. 2019, doi: 10.1007/s11164-018-3647-y.

[117] G. Latini *et al.*, "Efficient and reversible CO_2 capture in bio-based ionic liquids solutions," *Journal of CO_2 Utilization*, vol. 55, p. 101815, Jan. 2022, doi: 10.1016/j.jcou.2021.101815.

[118] P. E. Mason, C. E. Dempsey, L. Vrbka, J. Heyda, J. W. Brady, and P. Jungwirth, "Specificity of Ion−Protein Interactions: Complementary and Competitive Effects of Tetrapropylammonium, Guanidinium, Sulfate, and Chloride Ions," *J. Phys. Chem. B*, vol. 113, no. 10, pp. 3227–3234, Mar. 2009, doi: 10.1021/jp8112232.

[119] M. S. M. Misenan, R. Hempelmann, M. Gallei, and T. Eren, “Phosphonium-Based Polyelectrolytes: Preparation, Properties, and Usage in Lithium-Ion Batteries,” *Polymers*, vol. 15, no. 13, p. 2920, Jan. 2023, doi: 10.3390/polym15132920.

[120] P. J. Griffin, A. P. Holt, K. Tsunashima, J. R. Sangoro, F. Kremer, and A. P. Sokolov, “Ion transport and structural dynamics in homologous ammonium and phosphonium-based room temperature ionic liquids,” *J. Chem. Phys.*, vol. 142, no. 8, p. 084501, Feb. 2015, doi: 10.1063/1.4913239.

[121] R. K. Blundell and P. Licence, “Quaternary ammonium and phosphonium based ionic liquids: a comparison of common anions,” *Phys. Chem. Chem. Phys.*, vol. 16, no. 29, pp. 15278–15288, Jul. 2014, doi: 10.1039/C4CP01901F.

[122] V. Gosu, R. Kumar, A. Ramalingam, U. K. A. Kumar, A. K. Kashyap, and V. Subbaramaiah, “Desulfurization of Gasoline Using Deep Eutectic Solvents Based on Tetrabutylammonium Bromide,” *J. Chem. Eng. Data*, vol. 67, no. 9, pp. 2486–2494, Sep. 2022, doi: 10.1021/acs.jced.2c00172.

[123] D. Peng and M. Minceva, “Predicting the density and viscosity of deep eutectic solvents at atmospheric and elevated pressures,” *Fluid Phase Equilibria*, vol. 582, p. 114086, Jul. 2024, doi: 10.1016/j.fluid.2024.114086.

[124] I. Wazeer, I. M. AlNashef, A. A. Al-Zahrani, and M. K. Hadj-Kali, “The subtle but substantial distinction between ammonium- and phosphonium-based deep eutectic solvents,” *Journal of Molecular Liquids*, vol. 332, p. 115838, Jun. 2021, doi: 10.1016/j.molliq.2021.115838.

[125] A. L. Sazali *et al.*, “Physicochemical and thermal characteristics of choline chloride-based deep eutectic solvents,” *Chemosphere*, vol. 338, p. 139485, Oct. 2023, doi: 10.1016/j.chemosphere.2023.139485.

[126] D. M. Makarov and A. M. Kolker, “Viscosity of deep eutectic solvents: Predictive modeling with experimental validation,” *Fluid Phase Equilibria*, vol. 587, p. 114217, Jan. 2025, doi: 10.1016/j.fluid.2024.114217.

[127] J. N. Al-Dawsari, A. Bessadok-Jemai, I. Wazeer, S. Mokraoui, M. A. AlMansour, and M. K. Hadj-Kali, “Fitting of experimental viscosity to temperature data for deep eutectic solvents,” *Journal of Molecular Liquids*, vol. 310, p. 113127, Jul. 2020, doi: 10.1016/j.molliq.2020.113127.

[128] J. Wang, H. Cheng, Z. Song, L. Chen, L. Deng, and Z. Qi, “Carbon Dioxide Solubility in Phosphonium-Based Deep Eutectic Solvents: An Experimental and Molecular Dynamics

Study," *Ind. Eng. Chem. Res.*, vol. 58, no. 37, pp. 17514–17523, Sep. 2019, doi: 10.1021/acs.iecr.9b03740.

[129] X. Wang *et al.*, "Quantifying and Decoupling Molecular Interactions of Ionic Liquids with Gold Electrodes," *Langmuir*, vol. 40, no. 23, pp. 12017–12026, Jun. 2024, doi: 10.1021/acs.langmuir.4c00688.

[130] M. Gong *et al.*, "Cation Chain Length of Nonhalogenated Ionic Liquids Matters in Enhancing SERS of Cytochrome c on Zr–Al–Co–O Nanotube Arrays," *Langmuir*, vol. 40, no. 17, pp. 8886–8896, Apr. 2024, doi: 10.1021/acs.langmuir.4c00067.

[131] Y. Zhang *et al.*, "Amine-based deep eutectic solvents for CO_2 capture: Experiments and molecular thermodynamics," *Separation and Purification Technology*, vol. 359, p. 130559, Jun. 2025, doi: 10.1016/j.seppur.2024.130559.

[132] F. P. Pelaquim, A. M. Barbosa Neto, I. A. L. Dalmolin, and M. C. da Costa, "Gas Solubility Using Deep Eutectic Solvents: Review and Analysis," *Industrial and Engineering Chemistry Research*, vol. 60, no. 24, pp. 8607–8620, 2021, doi: 10.1021/acs.iecr.1c00947.

[133] H. Zhao, H. Shen, A. You, and Y. Yu, "Effect of Substitution Group on Intramolecular Hydrogen Bond of Amino Alcohols from Raman spectroscopy," Mar. 21, 2024, *arXiv*: arXiv:2403.14129. doi: 10.48550/arXiv.2403.14129.

[134] N. He *et al.*, "Investigation of effective CO_2 capture by ternary deep eutectic solvents based on superbase," *Journal of Molecular Liquids*, vol. 401, p. 124755, May 2024, doi: 10.1016/j.molliq.2024.124755.

[135] J. Gao *et al.*, "Physicochemical and thermodynamic properties of binary amine-based deep eutectic solvents for carbon capture," *Journal of Molecular Liquids*, vol. 399, p. 124346, Apr. 2024, doi: 10.1016/j.molliq.2024.124346.

[136] A. H. Sheikhshoaei and A. Sanati, "Data-driven insights into CO_2 solubility in deep eutectic solvents," *Journal of CO_2 Utilization*, vol. 102, p. 103285, Dec. 2025, doi: 10.1016/j.jcou.2025.103285.

[137] D. Hu, D. Cao, S. Lu, Q. Wang, and B. Yoon, "Quantum Chemistry-Guided Machine Learning for Accelerated Design of CO_2-Solubilizing Deep Eutectic Solvents," *ACS Sustainable Chem. Eng.*, vol. 13, no. 25, pp. 9705–9718, Jun. 2025, doi: 10.1021/acssuschemeng.5c02555.

[138] D. M. Makarov, Y. A. Fadeeva, and A. M. Kolker, "Machine Learning Prediction of Henry's Law Constant for CO_2 in Ionic Liquids and Deep Eutectic Solvents," *Liquids*, vol. 5, no. 2, p. 16, Jun. 2025, doi: 10.3390/liquids5020016.

[139] D. Weisburd, C. Britt, D. B. Wilson, and A. Wooditch, “Measuring Association for Scaled Data: Pearson’s Correlation Coefficient,” in *Basic Statistics in Criminology and Criminal Justice*, D. Weisburd, C. Britt, D. B. Wilson, and A. Wooditch, Eds., Cham: Springer International Publishing, 2020, pp. 479–530. doi: 10.1007/978-3-030-47967-1_14.

[140] P. Schober, C. Boer, and L. A. Schwarte, “Correlation Coefficients: Appropriate Use and Interpretation,” *Anesthesia & Analgesia*, vol. 126, no. 5, p. 1763, May 2018, doi: 10.1213/ANE.0000000000002864.

[141] C.-Y. Hsu *et al.*, “General models for predicting the liquid thermal conductivity of fatty acid esters based on smart methods,” *Energy Conversion and Management: X*, vol. 26, p. 101023, Apr. 2025, doi: 10.1016/j.ecmx.2025.101023.

[142] B. Branowski, M. Zabłocki, and M. Sydor, “The Material Indices Method in the Sustainable Engineering Design Process: A Review,” *Sustainability*, vol. 11, no. 19, Art. no. 19, Jan. 2019, doi: 10.3390/su11195465.

[143] V. Agieienko and R. Buchner, “Variation of Density, Viscosity, and Electrical Conductivity of the Deep Eutectic Solvent Reline, Composed of Choline Chloride and Urea at a Molar Ratio of 1:2, Mixed with Dimethylsulfoxide as a Cosolvent,” *J. Chem. Eng. Data*, vol. 65, no. 4, pp. 1900–1910, Apr. 2020, doi: 10.1021/acs.jced.9b01105.

[144] S. Huang, P. Wang, Y. Zhang, Y. Wang, X. Liu, and M. He, “Energy, Exergy, and Economic Analysis of a Low-Energy Consumption CO_2 Capture System with Ionic Liquid [DEME][TF2N],” *ACS Sustainable Chem. Eng.*, vol. 12, no. 39, pp. 14380–14395, Sep. 2024, doi: 10.1021/acssuschemeng.4c03477.

[145] J. O. Valderrama and P. A. Robles, “Critical properties, normal boiling temperatures, and acentric factors of fifty ionic liquids,” *Industrial and Engineering Chemistry Research*, vol. 46, no. 4, pp. 1338–1344, 2007, doi: 10.1021/ie0603058.

[146] S. E. Stein, “Infrared Spectra,” in NIST Chemistry WebBook, NIST Standard Reference Database Number 69, P. J. Linstrom and W. G. Mallard, Eds. Gaithersburg MD: National Institute of Standards and Technology, 2005.

[147] W. L. Luyben and I. L. Chien, Design and Control of Distillation Systems for Separating Azeotropes. Hoboken, NJ: John Wiley & Sons, 2010.

[148] R. E. Treybal, *Mass-Transfer Operations*, vol. 5, no. 5. 1980. doi: 10.1016/0009-2509(56)80037-7.

[149] L. Zhang, J. Han, R. Wang, X. Qiu, and J. Ji, “Isobaric Vapor−Liquid Equilibria for Three Ternary Systems: Water + 2Propanol + 1Ethyl3-methylimidazolium Tetrafluoroborate,

Water + 1Propanol + 1Ethyl3-methylimidazolium Tetrafluoroborate, and Water + 1Propanol + 1Butyl3-methylimidazolium Tetrafluoroborate" *Journal of Chemical & Engineering Data*, vol. 52, no. 4, pp. 1401–1407, 2007, doi: 10.1021/je700092d.

[150] L. Zhang, Z. Zhang, D. Shen, and M. Lan, "2-Propanol Dehydration via Extractive Distillation Using a Renewable Glycerol-Choline Chloride Deep Eutectic Solvent: Vapor-Liquid Equilibrium," *Journal of Chemical and Engineering Data*, vol. 62, no. 2, pp. 872–877, 2017, doi: 10.1021/acs.jced.6b00912.

[151] L. Zhang, M. Lan, X. Wu, and Y. Zhang, "Vapor–Liquid Equilibria for 2-Propanol Dehydration through Extractive Distillation Using Mixed Solvent of Ethylene Glycol and Choline Chloride," *Journal of Chemical & Engineering Data*, vol. 63, no. 8, pp. 2825–2832, 2018, doi: 10.1021/acs.jced.8b00162.

[152] M. Shamsipur, A. A. M. Beigi, M. Teymouri, S. M. Pourmortazavi, and M. Irandoust, "Physical and electrochemical properties of ionic liquids 1-ethyl-3-methylimidazolium tetrafluoroborate, 1-butyl-3-methylimidazolium trifluoromethanesulfonate and 1-butyl-1-methylpyrrolidinium bis(trifluoromethylsulfonyl)imide," *Journal of Molecular Liquids*, vol. 157, no. 1, pp. 43–50, 2010, doi: 10.1016/j.molliq.2010.08.005.

[153] N. G. Tsierkezos, A. E. Kelarakis, and M. M. Palaiologou, "Nikos G. Tsierkezos, Antonis E. Kelarakis, and Maria M. Palaiologou*," *Engineering*, pp. 395–398, 2000, doi: 10.1021/je990271t.

[154] M. K. Alomar, M. Hayyan, M. A. Alsaadi, S. Akib, A. Hayyan, and M. A. Hashim, "Glycerol-based deep eutectic solvents: Physical properties," *Journal of Molecular Liquids*, vol. 215, pp. 98–103, 2016, doi: 10.1016/j.molliq.2015.11.032.

[155] R. B. Leron, D. S. H. Wong, and M. H. Li, "Densities of a deep eutectic solvent based on choline chloride and glycerol and its aqueous mixtures at elevated pressures," *Fluid Phase Equilibria*, vol. 335, pp. 32–38, 2012, doi: 10.1016/j.fluid.2012.08.016.

[156] M. B. Haider, D. Jha, B. Marriyappan Sivagnanam, and R. Kumar, "Modelling and simulation of CO_2 removal from shale gas using deep eutectic solvents," *Journal of Environmental Chemical Engineering*, vol. 7, no. 1, p. 102747, 2019, doi: 10.1016/j.jece.2018.10.061.

[157] K. Liang, W. Li, H. Luo, M. Xia, and C. Xu, "Energy-Efficient Extractive Distillation Process by Combining Preconcentration Column and Entrainer Recovery Column," *Industrial & Engineering Chemistry Research*, vol. 53, no. 17, pp. 7121–7131, 2014, doi: 10.1021/ie5002372.

[158] Y. Qin, Y. Zhuang, C. Wang, L. Zhang, L. Liu, and J. Du, "Multi-objective optimization and comparison of the entrainer-assisted pressure-swing distillation and extractive distillation separation sequences for separating a pressure-insensitive binary azeotrope," *Computers & Chemical Engineering*, vol. 165, p. 107959, Sep. 2022, doi: 10.1016/j.compchemeng.2022.107959.

[159] I. Dejanović, L. Matijašević, H. Jansen, and Ž. Olujić, "Designing a packed dividing wall column for an aromatics processing plant," *Industrial and Engineering Chemistry Research*, vol. 50, no. 9, pp. 5680–5692, May 2011, doi: 10.1021/ie1020206.

[160] T. Long, Y. Deng, S. Gan, and J. Chen, "Application of Choline Chloride·x$ZnCl_2$ Ionic Liquids for Preparation of Biodiesel," *Chinese Journal of Chemical Engineering*, vol. 18, no. 2, pp. 322–327, Apr. 2010, doi: 10.1016/S1004-9541(08)60359-6.

[161] A. Hayyan, M. Ali Hashim, F. S. Mjalli, M. Hayyan, and I. M. AlNashef, "A novel phosphonium-based deep eutectic catalyst for biodiesel production from industrial low grade crude palm oil," *Chemical Engineering Science*, vol. 92, pp. 81–88, 2013, doi: 10.1016/j.ces.2012.12.024.

[162] N. Rodriguez Rodriguez, L. Machiels, and K. Binnemans, "p-Toluenesulfonic Acid-Based Deep-Eutectic Solvents for Solubilizing Metal Oxides," *ACS Sustainable Chem. Eng.*, vol. 7, no. 4, pp. 3940–3948, Feb. 2019, doi: 10.1021/acssuschemeng.8b05072.

[163] S. M. Asaad, A. Inayat, F. Jamil, and P. Hellier, "Process Optimization of Biodiesel Production from Waste Cooking Oil and Neem Oil Blend," *Energies*, vol. 18, no. 18, p. 4944, Jan. 2025, doi: 10.3390/en18184944.

[164] T. Sathish *et al.*, "Impacts of novel calotropis gigantea seed biodiesel usage as a fuel substitute along with various metal-oxide nanoparticles on the DICI engine characteristics," *Case Studies in Thermal Engineering*, vol. 63, p. 105249, Nov. 2024, doi: 10.1016/j.csite.2024.105249.

[165] T. Sathish, Ü. Ağbulut, M. Ubaidullah, R. Saravanan, J. Giri, and S. F. Shaikh, "Waste to fuel: A detailed combustion, performance, and emission characteristics of a CI engine fuelled with sustainable fish waste management augmentation with alcohols and nanoparticles," *Energy*, vol. 299, p. 131412, Jul. 2024, doi: 10.1016/j.energy.2024.131412.

[166] H. Abebe Debella, V. Ramayya Ancha, S. Mekbib Atnaw, and D. Seyoum Zeleke, "Experimental study on performance and emissions from Prosopis Juliflora biodiesel blends with diethyl ether additives," *Energy Conversion and Management: X*, vol. 22, p. 100581, Apr. 2024, doi: 10.1016/j.ecmx.2024.100581.

[167] S. B. A.v.s.l, N. Subramaniapillai, M. S. B. Khadhar Mohamed, and A. Narayanan, "Effect of rubber seed oil biodiesel on engine performance and emission analysis," *Fuel*, vol. 296, p. 120708, Jul. 2021, doi: 10.1016/j.fuel.2021.120708.

[168] S. Kesharvani, G. Dwivedi, T. N. Verma, and P. Verma, "The Experimental Investigation of a Diesel Engine Using Ternary Blends of Algae Biodiesel, Ethanol and Diesel Fuels," *Energies*, vol. 16, no. 1, p. 229, Jan. 2023, doi: 10.3390/en16010229.

[169] P. Shrivastava, T. N. Verma, and A. Pugazhendhi, "An experimental evaluation of engine performance and emisssion characteristics of CI engine operated with Roselle and Karanja biodiesel," *Fuel*, vol. 254, p. 115652, Oct. 2019, doi: 10.1016/j.fuel.2019.115652.

[170] A. K. Prajapati, S. Yadav, A. K. Gomey, A. K. Choubey, and R. Kumar, "Assessment of performance and emission characteristics of CI engine using tyre pyrolysis oil and biodiesel blends by nano additives: An experimental study," *Journal of the Energy Institute*, vol. 117, p. 101825, Dec. 2024, doi: 10.1016/j.joei.2024.101825.

[171] M. Muhammed Niyas and A. Shaija, "Performance evaluation of diesel engine using biodiesels from waste coconut, sunflower, and palm cooking oils, and their hybrids," *Sustainable Energy Technologies and Assessments*, vol. 53, p. 102681, Oct. 2022, doi: 10.1016/j.seta.2022.102681.

[172] A. Zare, T. A. Bodisco, M. N. Nabi, F. M. Hossain, Z. D. Ristovski, and R. J. Brown, "A comparative investigation into cold-start and hot-start operation of diesel engine performance with oxygenated fuels during transient and steady-state operation," *Fuel*, vol. 228, pp. 390–404, Sep. 2018, doi: 10.1016/j.fuel.2018.05.004.

[173] M. K. Yesilyurt and M. Aydin, "Experimental investigation on the performance, combustion and exhaust emission characteristics of a compression-ignition engine fueled with cottonseed oil biodiesel/diethyl ether/diesel fuel blends," *Energy Conversion and Management*, vol. 205, p. 112355, Feb. 2020, doi: 10.1016/j.enconman.2019.112355.

[174] A. Krishnasamy and K. R. Bukkarapu, "A comprehensive review of biodiesel property prediction models for combustion modeling studies," *Fuel*, vol. 302, p. 121085, Oct. 2021, doi: 10.1016/j.fuel.2021.121085.

[175] S. Prabakaran and T. Mohanraj, "Optimization of biodiesel production from Azolla pinnata: investigation of CI engine characteristics using nano dosed biodiesel," *J Mech Sci Technol*, vol. 35, no. 10, pp. 4765–4773, Oct. 2021, doi: 10.1007/s12206-021-0942-0.

[176] W. N. M. Wan Ghazali, R. Mamat, H. H. Masjuki, and G. Najafi, "Effects of biodiesel from different feedstocks on engine performance and emissions: A review," *Renewable and*

Sustainable Energy Reviews, vol. 51, pp. 585–602, Nov. 2015, doi: 10.1016/j.rser.2015.06.031.

[177] A. Dewangan *et al.*, "Comparative analysis of the performance and emissions of a multi-cylinder diesel engine using biodiesel from underutilized feedstocks," *RSC Adv.*, vol. 15, no. 49, pp. 41621–41647, Oct. 2025, doi: 10.1039/D5RA04352B.

[178] H. Chen, B. Xie, J. Ma, and Y. Chen, "NOx emission of biodiesel compared to diesel: Higher or lower?," *Applied Thermal Engineering*, vol. 137, pp. 584–593, Jun. 2018, doi: 10.1016/j.applthermaleng.2018.04.022.

[179] B. A. Oni and D. Oluwatosin, "Emission characteristics and performance of neem seed (Azadirachta indica) and Camelina (Camelina sativa) based biodiesel in diesel engine," *Renewable Energy*, vol. 149, pp. 725–734, Apr. 2020, doi: 10.1016/j.renene.2019.12.012.

[180] S. Rathinam, J. B. Sajin, G. Subbiah, A. Rajeev, S. Prakash, and D. Christopherselvam, "Assessment of the emission characteristics of the diesel engine with nano-particle in neem biodiesel," *Energy Sources, Part A: Recovery, Utilization and Environmental Effects*, vol. 42, no. 21, pp. 2623–2631, Nov. 2020, doi: 10.1080/15567036.2019.1612487.

[181] M. Suresh, C. P. Jawahar, and A. Richard, "A review on biodiesel production, combustion, performance, and emission characteristics of non-edible oils in variable compression ratio diesel engine using biodiesel and its blends," *Renewable and Sustainable Energy Reviews*, vol. 92, pp. 38–49, Sep. 2018, doi: 10.1016/j.rser.2018.04.048.

Appendix

Table A1 Critical properties of the DESs

DES Name	M_{wDES} (g/mol)	V_{cDES} (cm^3/mol)	T_{cDES} (K)	P_{cDES} (bar)	ω_{DES}
DES1	91.88	271.37	641.30	46.02	0.66
DES2	86.58	254.37	644.44	49.54	0.65
DES3	82.79	242.44	646.90	52.32	0.64
DES4	107.94	315.17	680.67	33.46	1.23
DES5	87.92	259.67	602.00	41.00	0.92
DES6	109.28	331.67	647.03	37.90	0.67
DES7	105.49	318.80	650.57	39.81	0.66
DES8	103.22	311.16	652.77	41.03	0.65
DES9	114.50	342.45	658.58	33.29	0.97
DES10	112.82	336.21	661.22	33.85	0.98
DES11	147.54	441.22	712.69	27.38	1.02
DES12	148.07	441.26	718.89	27.41	1.04
DES13	121.99	377.88	726.11	35.34	0.82
DES14	120.82	373.82	733.48	36.04	0.82
DES15	120.04	371.11	738.42	36.51	0.82
DES16	108.48	310.52	647.43	40.14	0.69
DES17	106.41	302.40	649.45	41.42	0.69
DES18	105.02	297.02	650.84	42.30	0.69
DES19	102.50	330.35	637.97	33.67	0.95
DES20	100.02	323.38	639.21	34.29	0.96
DES21	102.50	327.68	640.23	34.36	0.93
DES22	100.02	320.56	641.64	35.04	0.94
DES23	91.98	284.11	620.93	38.44	0.93
DES24	88.80	274.52	621.24	39.62	0.94
DES25	128.01	373.78	691.03	35.42	0.71
DES26	127.24	369.45	695.86	36.13	0.70
DES27	126.72	366.58	699.11	36.61	0.70
DES28	120.50	355.67	680.26	37.65	0.63
DES29	121.23	355.00	687.25	37.96	0.64
DES30	121.72	354.56	691.93	38.16	0.65
DES31	138.52	401.78	709.32	34.36	0.66
DES32	135.64	391.73	710.46	35.23	0.67
DES33	133.73	385.07	711.25	35.84	0.67

DES34	207.49	761.94	776.68	18.22	0.89
DES35	282.30	1019.68	907.13	16.04	0.87
DES36	304.30	1104.06	934.47	15.31	0.86
DES37	297.12	1023.59	917.68	16.09	0.88
DES38	184.90	598.95	728.20	22.51	0.80
DES39	167.71	547.56	718.07	24.37	0.79
DES40	157.40	517.43	712.21	25.63	0.78
DES41	132.68	462.49	656.95	27.45	0.68
DES42	126.07	438.03	670.15	29.23	0.71
DES43	94.11	259.39	700.10	57.39	0.41
DES44	91.22	253.06	691.22	58.19	0.40
DES45	88.90	248.03	684.15	58.85	0.40
DES46	105.94	310.37	641.14	43.55	0.43
DES47	96.48	282.58	635.41	47.71	0.42
DES48	113.51	333.19	646.03	40.67	0.45
DES49	125.37	368.17	682.86	38.48	0.48
DES50	132.50	405.98	744.57	34.30	0.77
DES51	128.52	412.43	716.34	32.66	0.76
DES52	139.63	415.65	728.30	32.91	0.76
DES53	156.57	507.59	759.05	27.25	0.84
DES54	167.68	510.46	769.29	27.43	0.84
DES55	100.02	321.97	640.41	34.66	0.95
DES56	67.90	N.A	799.82	51.46	0.86
DES57	126.17	427.36	745.37	31.48	0.86
DES58	107.14	355.62	697.01	36.42	0.79
DES59	129.16	416.27	774.29	33.68	0.86
DES60	157.54	547.80	889.07	29.32	0.86
DES61	108.75	289.45	805.93	43.71	1.20
DES62	89.72	226.96	761.09	54.42	1.12
DES63	111.74	279.70	838.80	47.25	1.19
DES64	140.13	396.71	951.83	37.70	1.19
DES65	163.58	578.61	803.27	24.12	0.96
DES66	144.54	498.61	752.62	27.03	0.88
DES67	166.57	566.33	831.81	25.61	0.95
DES68	194.95	710.73	950.24	23.25	0.96
DES69	182.28	651.98	831.94	21.73	1.01
DES70	163.25	568.39	780.46	24.11	0.93
DES71	185.27	639.17	860.46	23.00	1.00
DES72	213.65	789.12	980.38	21.18	1.01
DES73	192.96	698.88	822.60	21.18	0.87
DES74	161.60	562.80	736.19	24.50	0.77
DES75	160.27	554.51	731.01	24.85	0.75

DES76	156.15	405.80	606.30	29.36	0.64
DES77	119.44	289.91	569.05	38.92	0.61
DES78	180.03	736.35	871.53	20.60	0.95
DES79	152.24	480.85	747.01	30.76	0.62
DES80	136.19	422.05	737.45	34.20	0.65
DES81	86.36	269.97	620.61	41.78	0.85
DES82	84.31	263.30	621.07	42.40	0.87
DES83	82.94	258.89	621.40	42.84	0.89
DES84	81.96	255.75	621.65	43.15	0.91
DES85	108.33	324.23	660.73	36.03	0.92
DES86	107.70	320.60	663.98	36.11	0.95
DES87	127.15	355.99	637.85	31.10	0.96
DES88	131.39	363.06	645.17	30.94	0.95
DES89	80.09	230.49	668.34	51.43	0.91
DES90	84.09	239.50	684.10	46.96	1.09
DES91	78.77	286.41	706.24	51.40	0.47
DES92	73.84	261.87	678.40	54.17	0.46
DES93	70.89	247.48	661.93	56.03	0.45
DES94	203.60	684.00	759.60	20.20	0.84
DES95	222.30	766.30	789.94	18.40	0.89
DES96	170.95	598.82	750.24	23.24	0.79
DES97	96.71	286.24	656.70	40.56	0.92
DES98	98.28	290.41	659.27	39.80	0.94
DES99	72.69	227.97	618.16	48.74	0.87
DES100	73.26	229.50	619.02	48.13	0.89
DES101	72.69	229.32	616.86	63.13	0.10
DES102	73.26	230.90	617.67	63.04	0.08

Table A2 Calculated densities of DESs at 303.15K

DES	ρ^{calc} (g/cm^3)	ρ^{exp} (g/cm^3)	Error	RD%	ARD%
DES1	1.186	NA.	NA.	NA.	NA.
DES2	1.205	NA.	NA.	NA.	NA.
DES3	1.229	NA.	NA.	NA.	NA.
DES4	1.172	NA.	NA.	NA.	NA.
DES5	1.107	NA.	NA.	NA.	NA.
DES6	1.118	1.094[51]	0.024	2.175	2.175
DES7	1.110	1.087[51]	0.022	2.068	2.068
DES8	1.108	1.085[51]	0.023	2.095	2.095
DES9	1.107	1.118[51]	-0.011	-0.958	0.958
DES10	1.098	1.113[51]	-0.015	-1.303	1.303
DES11	1.113	1.1262[51]	-0.013	-1.155	1.155
DES12	1.101	1.115[51]	-0.013	-1.183	1.183
DES13	1.160	NA.	NA.	NA.	NA.
DES14	1.189	NA.	NA.	NA.	NA.
DES15	1.223	NA.	NA.	NA.	NA.
DES16	1.124	NA.	NA.	NA.	NA.
DES17	1.123	NA.	NA.	NA.	NA.
DES18	1.124	NA.	NA.	NA.	NA.
DES19	1.045	1.049[48]	-0.004	-0.424	0.424
DES20	1.030	1.041[48]	-0.011	-1.032	1.032
DES21	1.043	1.039[48]	0.004	0.422	0.422
DES22	1.016	1.031[48]	-0.015	-1.483	1.483
DES23	1.068	1.060[48]	0.008	0.726	0.726
DES24	1.050	1.060[48]	-0.010	-0.972	0.972
DES25	1.175	1.148[72]	0.027	2.357	2.357
DES26	1.179	1.148[72]	0.031	2.707	2.707
DES27	1.184	1.143[72]	0.041	3.584	3.584
DES28	1.188	1.093[72]	0.095	8.717	8.717
DES29	1.192	1.098[72]	0.094	8.525	8.525
DES30	1.197	1.104[72]	0.093	8.433	8.433
DES31	1.176	1.146[72]	0.030	2.576	2.576
DES32	1.180	1.145[72]	0.035	3.060	3.060
DES33	1.186	1.148[72]	0.038	3.288	3.288
DES34	1.010	NA.	NA.	NA.	NA.
DES35	0.973	NA.	NA.	NA.	NA.
DES36	0.973	NA.	NA.	NA.	NA.
DES37	1.010	NA.	NA.	NA.	NA.
DES38	1.044	NA.	NA.	NA.	NA.
DES39	1.041	NA.	NA.	NA.	NA.
DES40	1.048	NA.	NA.	NA.	NA.
DES41	1.043	NA.	NA.	NA.	NA.
DES42	1.050	NA.	NA.	NA.	NA.

DES43	1.125	NA.	NA.	NA.	NA.
DES44	1.125	NA.	NA.	NA.	NA.
DES45	1.129	NA.	NA.	NA.	NA.
DES46	1.091	1.206[76]	-0.115	-9.500	9.500
DES47	1.099	1.156[76]	-0.057	-4.938	4.938
DES48	1.096	NA.	NA.	NA.	NA.
DES49	1.104	1.129[76]	-0.025	-2.203	2.203
DES50	1.168	1.137[73]	0.031	2.703	2.703
DES51	1.129	1.090[73]	0.039	3.574	3.574
DES52	1.147	1.170[73]	-0.023	-1.967	1.967
DES53	1.091	1.027[73]	0.063	6.176	6.176
DES54	1.107	1.094[73]	0.014	1.237	1.237
DES55	1.019	N.A	N.A	N.A	N.A
DES56	1.245	N.A	N.A	N.A	N.A
DES57	1.114	1.088[80]	0.026	2.382	2.382
DES58	1.122	1.136[80]	-0.014	-1.246	1.246
DES59	1.131	1.112[80]	0.019	1.686	1.686
DES60	1.172	1.158[80]	0.014	1.232	1.232
DES61	1.445	0.978[80]	0.467	47.700	47.700
DES62	1.979	1.103[80]	0.876	79.357	79.357
DES63	1.437	1.079[80]	0.359	33.260	33.260
DES64	2.095	1.128[80]	0.966	85.626	85.626
DES65	1.071	0.951[80]	0.120	12.637	12.637
DES66	1.071	0.990[80]	0.081	8.150	8.150
DES67	1.085	1.009[80]	0.076	7.500	7.500
DES68	1.111	1.055[80]	0.057	5.383	5.383
DES69	1.057	0.912[80]	0.145	15.854	15.854
DES70	1.056	0.942[80]	0.115	12.169	12.169
DES71	1.070	0.927[80]	0.144	15.513	15.513
DES72	1.093	0.959[80]	0.134	14.017	14.017
DES73	1.116	0.953[81]	0.163	17.060	17.060
DES74	1.165	0.893[81]	0.273	30.534	30.534
DES75	1.184	0.893[81]	0.291	32.609	32.609
DES76	1.103	N.A	N.A	N.A	N.A
DES77	1.101	N.A	N.A	N.A	N.A
DES78	0.992	1.048[83]	-0.055	-5.295	5.295
DES79	1.144	0.940[84]	0.204	21.753	21.753
DES80	1.167	0.984[84]	0.183	18.568	18.568
DES81	1.108	1.069[85]	0.039	3.694	3.694
DES82	1.091	1.066[85]	0.025	2.308	2.308
DES83	1.075	1.060[85]	0.015	1.457	1.457
DES84	1.062	1.056[85]	0.006	0.593	0.593
DES85	1.133	1.126[85]	0.007	0.640	0.640
DES86	1.122	1.122[85]	0.000	0.039	0.039
DES87	1.037	1.065[86]	-0.028	-2.641	2.641
DES88	1.065	1.068[86]	-0.003	-0.300	0.300

DES89	1.199	1.172[87]	0.027	2.277	2.277
DES90	1.227	1.201[87]	0.027	2.228	2.228
DES91	1.142	1.137[88]	0.004	0.377	0.377
DES92	1.153	1.113[88]	0.040	3.637	3.637
DES93	1.179	1.102[88]	0.077	7.006	7.006
DES94	1.035	0.980[89]	0.056	5.672	5.672
DES95	1.028	0.966[89]	0.063	6.497	6.497
DES96	1.157	0.889[89]	0.268	30.115	30.115
DES97	1.174	1.101[90]	0.073	6.611	6.611
DES98	1.161	1.103[90]	0.058	5.260	5.260
DES99	1.134	1.031[90]	0.103	10.026	10.026
DES100	1.111	1.030[90]	0.081	7.853	7.853
DES101	1.119	1.045[90]	0.073	7.006	7.006
DES102	1.106	1.046[90]	0.061	5.815	5.815

***N.A Data not reported in literature**

Table A3 Refractive Index, Molar Volume and Molar Free Volume of DESs

DES Name	n_{DES}	V_m (cm^3/mol)	V_{free} (cm^3/mol)
DES1	1.47	77.50	55.75
DES2	1.48	71.83	51.39
DES3	1.49	67.38	47.90
DES4	1.48	92.07	65.76
DES5	1.48	79.40	57.02
DES6	1.53	97.78	67.38
DES7	1.56	95.05	64.44
DES8	1.58	93.17	62.10
DES9	1.47	103.41	74.67
DES10	1.46	102.70	74.39
DES11	1.47	132.53	95.84
DES12	1.46	134.43	97.51
DES13	1.52	105.17	72.96
DES14	1.56	101.64	68.88
DES15	1.59	98.12	64.91
DES16	1.53	96.53	66.65
DES17	1.55	94.79	64.81
DES18	1.56	93.39	63.23
DES19	1.47	98.12	70.94
DES20	1.46	97.07	70.41
DES21	1.47	98.23	70.84
DES22	1.47	98.48	70.98
DES23	1.47	86.15	62.21
DES24	1.47	84.58	61.16
DES25	1.53	108.99	75.23
DES26	1.55	107.94	73.72
DES27	1.56	106.99	72.29
DES28	1.52	101.40	70.40
DES29	1.54	101.71	69.83
DES30	1.56	101.72	69.06
DES31	1.51	117.83	82.30
DES32	1.53	114.97	79.31
DES33	1.55	112.77	76.83
DES34	1.47	205.33	148.27
DES35	1.47	196.02	141.42
DES36	1.46	199.77	144.74
DES37	1.48	294.28	211.06

DES38	1.48	177.08	127.17
DES39	1.49	161.09	114.64
DES40	1.50	150.24	105.80
DES41	1.47	127.18	91.91
DES42	1.49	120.07	85.11
DES43	1.594	83.68	55.29
DES44	1.602	81.10	53.28
DES45	1.610	78.71	51.42
DES46	1.52	97.06	67.58
DES47	1.55	87.81	59.92
DES48	1.51	103.53	72.81
DES49	1.49	113.51	80.81
DES50	1.54	113.48	77.81
DES51	1.53	113.80	78.92
DES52	1.53	121.74	83.94
DES53	1.53	143.53	99.47
DES54	1.53	151.46	104.35
DES55	1.465	98.12	71.01
DES56	N.A.*	N.A.*	N.A.*
DES57	1.486	113.28	80.75
DES58	1.482	95.47	68.25
DES59	1.511	114.18	79.96
DES60	1.504	134.44	94.64
DES61	1.514	75.28	52.60
DES62	1.510	45.33	31.77
DES63	1.539	77.75	53.39
DES64	1.533	66.90	46.12
DES65	1.487	152.78	108.86
DES66	1.483	134.94	96.42
DES67	1.512	153.51	107.45
DES68	1.505	175.41	123.40
DES69	1.487	172.44	122.83
DES70	1.483	154.58	110.43
DES71	1.512	173.11	121.14
DES72	1.505	195.47	137.47
DES73	1.470	172.94	124.72
DES74	1.429	138.68	102.95
DES75	1.428	135.41	100.56
DES76	1.489	141.63	100.74
DES77	1.494	108.50	76.91

DES78	1.504	181.57	127.76
DES79	1.495	133.02	94.21
DES80	1.544	116.74	79.88
DES81	1.467	77.90	56.27
DES82	1.468	77.30	55.80
DES83	1.470	77.12	55.61
DES84	1.471	77.15	55.58
DES85	1.460	95.59	69.39
DES86	1.458	95.95	69.76
DES87	1.470	122.60	88.42
DES88	1.472	123.40	88.87
DES89	1.758	66.80	39.36
DES90	1.598	68.51	45.13
DES91	1.487	68.99	49.16
DES92	1.501	64.05	45.19
DES93	1.518	60.14	41.92
DES94	1.476	196.62	141.17
DES95	1.476	216.15	155.16
DES96	1.429	147.71	109.65
DES97	1.459	82.37	59.86
DES98	1.458	84.66	61.58
DES99	1.467	64.11	46.33
DES100	1.468	65.92	47.59
DES101	1.459	64.98	47.23
DES102	1.457	66.21	48.17

***N.A.** Not Available

Table A4 Viscosity of the Deep Eutectic Solvents (mPa.s)

DES	293 K	298 K	303 K	308 K	313 K	318 K	323 K	References
DES 1	-	-	-	300	-	-	-	[107]
DES 2	1371.97	962.30	539.95	387.02	242.41	180.71	121.58	[108]
DES 3	-	749.40	-	-	-	161.00	-	[107]
DES 4	480.93	363.27	250.19	191.79	133.37	95.70	81.59	[109]
DES 5	60.00	48.59	39.78	33.15	27.77	23.61	20.30	[110]
DES 19	112.90	87.40	70.16	59.73	47.89	39.53	33.04	[110]
DES 20	99.69	78.77	62.96	51.08	41.67	34.51	28.90	[110]
DES 23	94.05	72.10	56.26	44.50	35.89	29.15	24.25	[110]
DES 24	80.19	61.49	47.74	37.47	30.40	24.70	20.43	[110]
DES 57	5.00	3.00	1.00	0.50	0.20	0.10	0.07	[80]
DES 58	9.00	6.00	3.00	2.00	0.70	0.30	0.12	[80]
DES 59	7.00	4.00	3.00	1.00	0.50	0.20	0.10	[80]
DES 60	13.00	8.00	4.00	2.00	1.00	0.60	0.25	[80]
DES 61	7.00	6.00	3.00	2.00	1.00	0.40	0.18	[80]
DES 62	12.00	6.00	4.00	1.00	0.80	0.30	0.13	[80]
DES 63	10.00	5.00	3.00	1.00	0.70	0.30	0.16	[80]
DES 64	17.00	10.00	5.00	3.00	1.00	0.60	0.21	[80]
DES 65	11.00	6.00	2.00	2.00	0.60	0.20	0.95	[80]
DES 66	14.00	8.00	4.00	2.00	0.90	0.40	0.17	[80]
DES 67	13.00	6.00	3.00	2.00	0.80	0.30	0.12	[80]
DES 68	19.00	10.00	5.00	3.00	1.00	0.70	0.31	[80]
DES 69	14.00	6.00	4.00	2.00	0.80	0.30	0.14	[80]
DES 70	17.00	8.00	5.00	3.00	1.00	0.50	0.28	[80]
DES 71	15.00	7.00	4.00	3.00	1.00	0.40	0.16	[80]
DES 72	21.00	11.00	5.00	3.00	1.00	0.60	0.31	[80]
DES 78	-	-	1.48	-	1.17	-	0.96	[83]
DES 89	-	-	101.60	70.38	50.36	37.06	27.98	[87]
DES 90	-	-	189.60	129.20	91.01	65.55	48.56	[87]
DES 91	25.06	21.05	17.16	14.05	11.66	9.89	8.48	[88]
DES 92	25.56	21.49	17.47	14.41	12.05	10.31	8.95	[88]
DES 93	-	-	16.53	13.36	10.98	9.17	7.72	[88]
DES 97	39.80	-	25.70	-	16.30	-	11.00	[90]
DES 98	33.80	-	24.00	-	16.10	-	11.60	[90]
DES 99	49.40	-	31.40	-	19.00	-	12.50	[90]
DES 100	51.20	-	32.00	-	18.30	-	13.10	[90]

DES 101	42.30	-	29.00	-	18.70	-	13.90	[90]
DES 102	43.50	-	28.40	-	19.90	-	14.40	[90]

Table A5 Experimental data for CO_2 absorption in DES1-DES4 at 30 °C and pressures up to 2 MPa[a]

DES1		DES2		DES3		DES4	
Pressure (MPa)	Mol fraction	Pressure (MPa)	Mol fraction	Pressure (MPa)	Mol fraction	Pressure (MPa)	Mol fraction
0.071	0.025	0.079	0.022	0.080	0.025	0.088	0.025
0.139	0.051	0.147	0.046	0.147	0.052	0.155	0.052
0.206	0.075	0.213	0.070	0.216	0.080	0.223	0.079
0.274	0.099	0.280	0.093	0.287	0.107	0.287	0.104
0.336	0.121	0.345	0.115	0.349	0.131	0.351	0.128
0.395	0.141	0.403	0.135	0.411	0.153	0.413	0.151
0.452	0.160	0.469	0.157	0.471	0.175	0.473	0.172
0.511	0.179	0.534	0.177	0.534	0.197	0.538	0.195
0.585	0.203	0.593	0.196	0.590	0.216	0.609	0.218
0.651	0.223	0.652	0.214	0.655	0.237	0.668	0.238
0.722	0.244	0.716	0.233	0.724	0.259	0.735	0.259
0.787	0.264	0.778	0.251	0.794	0.281	0.808	0.282
0.852	0.282	0.840	0.269	0.857	0.300	0.876	0.302
0.913	0.300	0.897	0.285	0.915	0.317	0.943	0.321
0.983	0.319	0.955	0.301	0.981	0.336	1.009	0.340
1.048	0.336	1.018	0.318	1.038	0.352	1.095	0.364
1.106	0.352	1.076	0.333	1.099	0.369	1.176	0.385
1.170	0.368	1.132	0.348	1.156	0.384	1.261	0.407
1.230	0.383	1.189	0.362	1.213	0.399	1.320	0.422
1.289	0.398	1.248	0.377	1.277	0.415	1.378	0.436
1.354	0.413	1.305	0.391	1.337	0.430	1.439	0.451
1.412	0.427	1.371	0.407	1.402	0.446	1.476	0.460
1.443	0.435	1.431	0.421	1.431	0.448	1.532	0.473
1.478	0.443	1.458	0.428	1.462	0.456	1.588	0.485
1.521	0.453	1.504	0.438	1.505	0.466	1.644	0.497
1.567	0.463	1.547	0.447	1.551	0.477	1.682	0.505
1.617	0.473	1.590	0.457	1.604	0.488	1.738	0.517
1.664	0.483	1.636	0.467	1.647	0.498	1.795	0.528
1.711	0.493	1.677	0.475	1.688	0.506	1.850	0.539
1.765	0.504	1.726	0.485	1.734	0.516	1.895	0.548
1.801	0.512	1.771	0.495	1.783	0.526	1.941	0.557
1.845	0.520	1.814	0.503	1.828	0.535	1.987	0.565
1.883	0.528	1.855	0.511	1.869	0.543	2.043	0.576
1.928	0.536	1.897	0.520	1.924	0.554		

1.983	0.547	1.942	0.529	1.966	0.562
2.020	0.554	1.987	0.537	1.999	0.569
		2.032	0.545	2.040	0.576

[a]Standard uncertainties u are u(T) = 0.1 K, u(P) = 1.0% of reading (relative), u(mass) = 0.003 g, u(volume) = 0.5%. Combined standard uncertainty uc(xCO_2) = 0.008 calculated via error propagation. Measurements performed using SETARAM PCT Pro D6350 with equilibration time of 120 min to ensure true equilibrium.

Table A6 Experimental data for CO_2 absorption in DES5-DES8 at 30 °C and pressures up to 2 MPa[a]

DES5		DES6		DES7		DES8	
Pressure (MPa)	Mol fraction	Pressure (MPa)	Mol fraction	Pressure (MPa)	Mol fraction	Pressure (MPa)	Mol fraction
0.079	0.024	0.071	0.018	0.023	0.049	0.080	0.054
0.145	0.053	0.129	0.037	0.075	0.075	0.147	0.078
0.213	0.081	0.190	0.056	0.129	0.100	0.216	0.098
0.280	0.108	0.251	0.074	0.184	0.123	0.287	0.119
0.345	0.133	0.310	0.092	0.242	0.145	0.349	0.139
0.406	0.157	0.372	0.106	0.300	0.166	0.411	0.158
0.477	0.183	0.439	0.122	0.354	0.185	0.471	0.176
0.533	0.203	0.497	0.135	0.425	0.202	0.534	0.193
0.604	0.227	0.560	0.149	0.489	0.217	0.590	0.211
0.666	0.248	0.619	0.162	0.548	0.231	0.655	0.227
0.728	0.268	0.677	0.175	0.612	0.246	0.724	0.248
0.791	0.288	0.744	0.190	0.681	0.262	0.794	0.264
0.855	0.308	0.810	0.205	0.747	0.277	0.857	0.279
0.923	0.328	0.876	0.219	0.811	0.291	0.915	0.294
0.985	0.346	0.944	0.234	0.870	0.304	0.981	0.311
1.048	0.364	1.008	0.248	0.935	0.318	1.038	0.326
1.109	0.381	1.072	0.261	0.998	0.331	1.099	0.346
1.171	0.397	1.137	0.275	1.058	0.344	1.156	0.361
1.226	0.412	1.194	0.287	1.121	0.357	1.213	0.375
1.287	0.427	1.261	0.301	1.185	0.370	1.277	0.388
1.349	0.443	1.320	0.313	1.250	0.383	1.337	0.407
1.404	0.461	1.409	0.331	1.317	0.397	1.402	0.420
1.441	0.470	1.443	0.338	1.374	0.408	1.431	0.427
1.478	0.479	1.482	0.346	1.441	0.422	1.462	0.435
1.514	0.487	1.527	0.355	1.480	0.430	1.505	0.445
1.549	0.495	1.568	0.363	1.527	0.439	1.551	0.456
1.601	0.506	1.604	0.370	1.572	0.447	1.604	0.464
1.646	0.516	1.654	0.380	1.614	0.455	1.647	0.472
1.694	0.526	1.711	0.390	1.658	0.463	1.688	0.481
1.726	0.532	1.757	0.399	1.694	0.470	1.734	0.488
1.768	0.540	1.793	0.406	1.739	0.478	1.783	0.496
1.810	0.549	1.839	0.414	1.774	0.484	1.828	0.504
1.853	0.557	1.872	0.420	1.828	0.493	1.869	0.512
1.891	0.564	1.918	0.429	1.874	0.501	1.924	0.519

1.948	0.575	1.962	0.437	1.919	0.509	1.966	0.529
1.991	0.583	2.007	0.445	1.963	0.517	1.999	0.535
2.024	0.589			2.009	0.524		

[a]Standard uncertainties u are u(T) = 0.1 K, u(P) = 1.0% of reading (relative), u(mass) = 0.003 g, u(volume) = 0.5%. Combined standard uncertainty uc(xCO_2) = 0.008 calculated via error propagation. Measurements performed using SETARAM PCT Pro D6350 with equilibration time of 120 min to ensure true equilibrium.

Table A7 Experimental viscosity data of DES1-DES4 in the temperature range of 20-50°C[a].

DES1		DES2		DES3		DES4	
T K	Viscosity mPa.s	T K	Viscosity mPa.s	T K	Viscosity mPa.s	T K	Viscosity mPa.s
293.21	219	292.86	220	292.73	293	293.05	288.1
293.62	207.4	293.32	217.9	293.18	279.8	293.49	275.2
294.24	200.8	293.91	209.4	293.79	270.8	294.08	267.5
294.89	193.9	294.63	198.6	294.52	260.8	294.77	257.2
295.59	187.2	295.38	192.6	295.28	247.8	295.5	247.4
296.28	181.2	296.05	184.4	296.03	238.2	296.21	236.1
296.95	172.8	296.79	176.6	296.74	228.1	296.9	226.4
297.6	167	297.47	171.3	297.42	218.7	297.55	218.3
298.28	160.7	298.11	163.8	298.07	209.9	298.17	208.9
298.89	155	298.79	158.2	298.74	201.9	298.83	202.2
299.53	149.7	299.46	152.2	299.42	194.6	299.49	194.3
300.16	144.3	300.11	147.6	300.07	187.3	300.13	187.5
300.78	139	300.73	142.1	300.7	180.7	300.75	180.1
301.44	134.8	301.33	138.3	301.37	174.5	301.41	174.3
302.05	129.4	301.97	133.2	301.97	168.1	302.01	168.1
302.68	125.2	302.62	128.9	302.6	162.7	302.63	162.4
303.31	121.4	303.25	125.2	303.23	157.4	303.26	157.3
303.92	116.8	303.88	120.5	303.84	152	303.87	152.1
304.57	113.1	304.46	116.9	304.43	147.3	304.45	147
305.17	109.8	305.09	113.8	305.06	142.6	305.08	142.5
305.78	106.1	305.67	110.1	305.66	137.8	305.66	138.2
306.41	102.5	306.27	106.5	306.25	133.2	306.25	133.5
307.01	99.6	306.87	103.3	306.87	128.9	306.85	129.2
307.6	96.9	307.47	100.5	307.48	124.8	307.45	125.4
308.17	94.1	308.1	97.4	308.1	120.7	308.06	121.5
308.76	91.1	308.72	94.2	308.72	116.7	308.67	117.4
309.38	88.5	309.32	91.6	309.3	113.2	309.25	113.5
309.99	86.2	309.93	89.3	309.9	109.8	309.87	109.9
310.59	83.9	310.52	87	310.5	106.6	310.49	106.5
311.16	81.4	311.13	84.5	311.11	103.2	311.11	103.2
311.74	79	311.74	82	311.72	100.2	311.74	99.8
312.33	77.1	312.32	80.2	312.3	97.4	312.33	96.9
312.88	75.3	312.91	78.3	312.89	94.8	312.93	94.2
313.44	73.1	313.51	76.1	313.48	91.9	313.53	91.6
314.01	71.1	314.08	74	314.06	89.5	314.1	88.8
314.56	69.7	314.64	72.5	314.62	87.2	314.66	86.5
315.15	68	315.15	71	315.21	85	315.25	84.4

315.68	66.1	315.71	69	315.75	82.6	315.78	82
316.22	64.9	316.29	67.8	316.29	80.8	316.33	80.1
316.76	63.4	316.85	66.3	316.84	78.8	316.87	78.4
317.28	62	317.39	64.8	317.36	77	317.39	76.3
317.82	60.9	317.88	63.8	317.85	75.4	317.88	74.9
318.34	59.4	318.37	62.4	318.35	73.7	318.38	73.1
318.83	58.6	318.89	61.5	318.86	72.2	318.89	71.8
319.31	57.3	319.37	60.2	319.38	70.7	319.4	70.2
319.77	56.4	319.81	59.5	319.86	69.2	319.88	69.1
320.2	55.6	320.25	58.5	320.31	68.1	320.33	67.8
320.59	54.6	320.66	57.4	320.71	66.9	320.73	66.6
320.94	54.1	321	57	321.06	66.1	321.07	66

[a]Standard uncertainties u are u(T) = 0.05 K, u(η) = 1.0% (relative).

to ensure Newtonian behavior.

Table A8 Experimental viscosity data of DES5-DES8 in the temperature range of 20-50°C[a].

DES5		DES6		DES7		DES8	
T K	Viscosity mPa.s	T K	Viscosity mPa.s	T K	Viscosity mPa.s	T K	Viscosity mPa.s
292.8	259.3	293.13	230.8	293.17	86.1	293.25	494.7
293.28	257.4	293.56	222.2	293.62	82.5	293.67	485.1
293.95	247.7	294.13	213.5	294.22	78.1	294.27	467.9
294.64	236.5	294.82	203.3	294.93	72.9	294.9	447.8
295.38	228.8	295.54	190.8	295.64	71.7	295.59	424.8
296.1	218.7	296.24	183	296.27	68.8	296.28	399.7
296.8	209.3	296.92	172.6	296.98	65.1	296.95	380.9
297.47	202.9	297.57	162.8	297.64	63.9	297.59	358.8
298.17	193.9	298.19	156.8	298.26	60.5	298.26	338.5
298.8	186.8	298.85	147.5	298.92	58.6	298.88	319.5
299.44	179.5	299.51	142.2	299.57	56.2	299.51	302.4
300.09	173.3	300.14	134	300.21	54.6	300.14	285.1
300.71	166.7	300.76	129.5	300.82	52.4	300.75	272.9
301.37	161	301.42	123.3	301.42	51.1	301.4	255.6
301.97	155	302.02	118.4	302.06	48.7	302	243.7
302.59	150	302.64	114.4	302.71	47.2	302.62	231.5
303.22	145.4	303.26	109.1	303.35	46	303.24	218.2
303.84	140.3	303.87	105.2	303.96	44.1	303.85	209.5
304.43	136	304.46	101.9	304.55	42.7	304.49	199.3
305.05	132.2	305.09	97.9	305.18	41.6	305.1	187.7
305.7	127.8	305.68	94	305.76	40.3	305.71	179.9
306.34	123.4	306.26	91.3	306.35	38.8	306.33	172.9
306.96	119.5	306.86	88.4	306.95	37.7	306.94	164.9
307.57	115.9	307.5	85.1	307.53	36.9	307.52	156.5
308.16	112.3	308.13	81.8	308.14	35.8	308.1	150.8
308.76	108.5	308.74	79.1	308.75	34.6	308.68	145.9
309.39	105.1	309.34	76.7	309.33	33.6	309.3	140.2
310.01	102.1	309.91	74.4	309.92	32.7	309.91	133.8
310.61	99.1	310.5	71.8	310.51	32	310.5	128.2
311.18	96.3	311.11	69.3	311.12	31	311.08	124
311.74	93.5	311.73	67.4	311.73	30	311.66	119.6
312.28	91.2	312.31	65.5	312.3	29.3	312.27	114.5
312.86	88.9	312.91	63.4	312.9	28.6	312.83	109.5
313.45	86.5	313.5	61.3	313.49	27.9	313.41	106.3
314.02	84	314.08	59.8	314.07	27	313.98	102.6
314.58	82.1	314.63	58.2	314.62	26.5	314.55	97.7
315.17	80.1	315.22	56.2	315.14	26	315.16	94

315.71	78	315.76	54.9	315.69	25.2	315.72	91.5
316.24	76.3	316.3	53.7	316.26	24.7	316.28	87.5
316.78	74.6	316.84	52	316.82	24.2	316.82	85
317.3	72.8	317.36	51.1	317.36	23.6	317.35	82.6
317.85	71.4	317.85	49.7	317.86	23.3	317.91	79.4
318.37	69.7	318.34	48.8	318.36	22.6	318.43	78.1
318.86	68.5	318.85	47.6	318.87	22.4	318.92	75.1
319.35	67	319.36	46.8	319.35	21.9	319.4	74
319.81	66	319.85	45.6	319.78	21.6	319.87	72
320.24	64.8	320.3	45.1	320.22	21.2	320.3	70.1
320.63	63.8	320.69	44.2	320.62	20.8	320.69	69.6
320.99	63.1	321.03	43.4	320.97	20.8	321.04	67.9

[a]Standard uncertainties u are u(T) = 0.05 K, u(η) = 1.0% (relative).

Table A9 Engine specifications

Make type	VCR Four Stroke water-cooled
No of cylinder	Single
Power	5.2 kW@1600 rpm
Bore	85 mm
Stroke	110 mm
Combustion principle	Compression ignition
Cubic capacity	661.5 cc
Compression ratio	12:1 - 22:1 (Variable type)
Fuel	Run on diesel, biodiesel as well as blends
Maximum speed	1800 rpm
Minimum idle speed	750 rpm
Minimum operating speed	1200 rpm
Rated operating speed	1500 rpm
Maximum operating speed	1600 rpm
Fuel timing for standard engine valve timing	23-degree BTDC Inlet open BTDC 4.5 degree Inlet close ABDC 35.5 degree Exhaust open BBDC 35.5 degree Exhaust close ATDC 4.5 degree
Inlet valve clearance	0.18 mm
Exhaust valve clearance	0.20 mm
Lubrication oil	3.5 liter (20w40)

Table A10 Gas Analyser Specifications

Measured components	Gas channel	Range	Resolution
	Hydrocarbon (Hexane)	0 to 15000 ppm	1 ppm
	Carbon Monoxide	0 to 15 %	0.001%
	Carbon Dioxide	0 to 20%	0.01%
	Oxygen	0 to 25%	0.01%
	NOx	0 to 5000 ppm	1 ppm
	Lambda	0.500 to 9.999	0.001
	AFR	7.90 to 27.60	00.01
Accuracy	Hydrogen	± 12 ppm Vol.	
	Carbon Monoxide	± 0.06% Vol.	
	Carbon Dioxide	± 0.40% Vol.	
	Oxygen	± 0.10% Vol.	
Response time **Repeatability**		≤ 15 sec. for Final value ± 1% of the First Sample value	
Auto Zeroing		≤20 Seconds (Performs automatically at every measurement cycle)	
Warm-up time		≤5 Minutes	
Samples flow rate		4 litres/minute	
Fabrication		Full Metal Body	
Dimensions		L 280 mm ×W 250 mm ×H 140	
Operating conditions		Temperature Range: 0 to 50 degrees Celsius Atmospheric pressure: 700 to 1150 mBar Humidity:0 to 90% (non-condensing)	

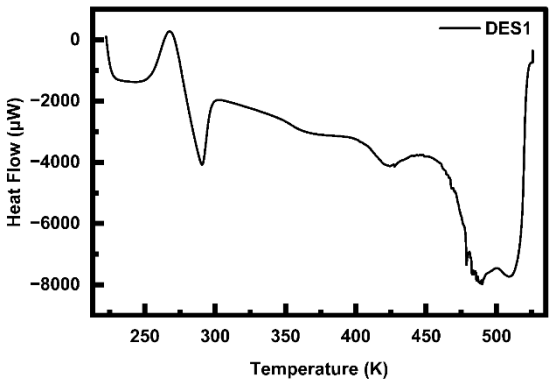

Figure A1 DSC thermogram of DES1

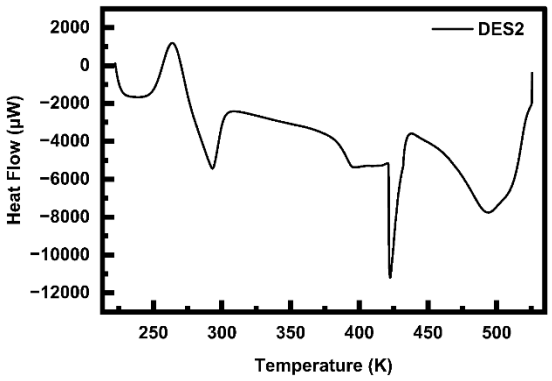

Figure A2 DSC thermogram of DES2

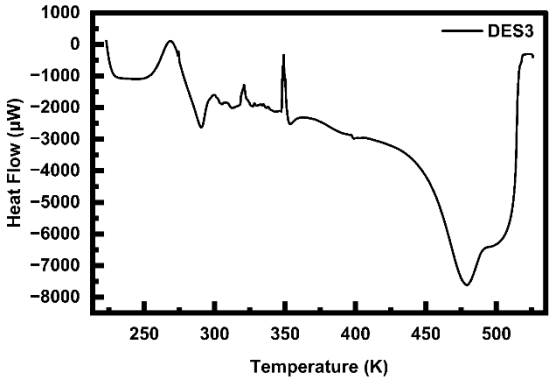

Figure A3 DSC thermogram of DES3

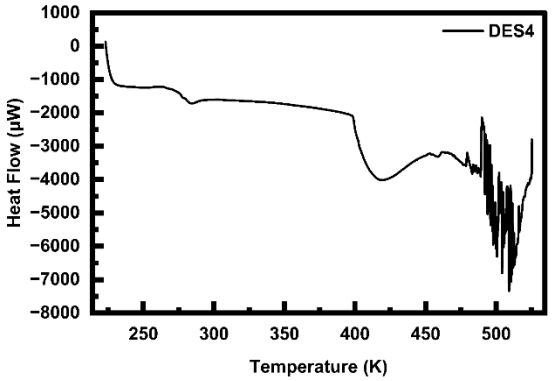

Figure A4 DSC thermogram of DES4

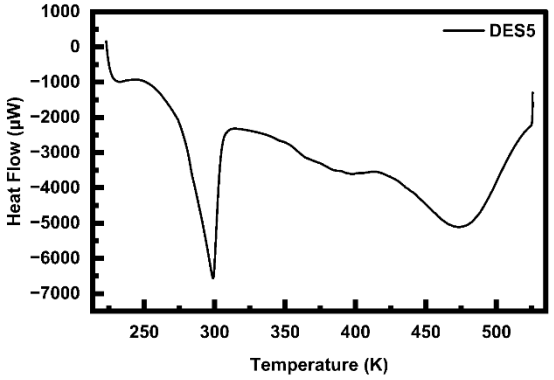

Figure A5 DSC thermogram of DES5

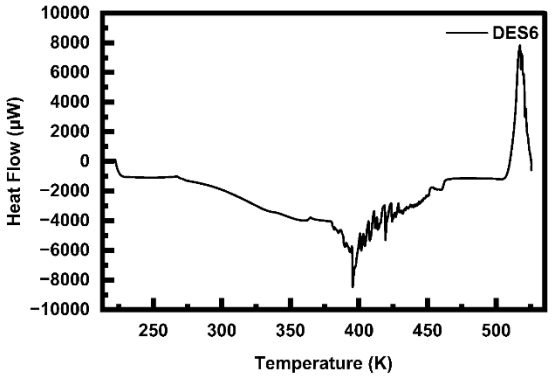

Figure A6 DSC thermogram of DES6

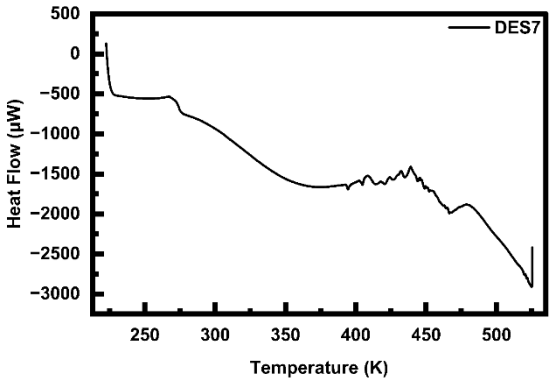

Figure A7 DSC thermogram of DES7

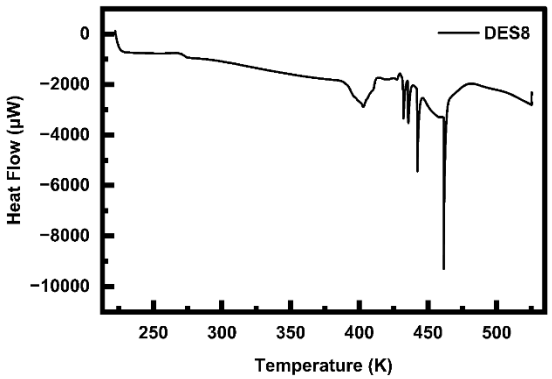

Figure A8 DSC thermogram of DES8

Thesis Outcomes

1. **Gomey, A.K**.; Tripathi, M.M.; Haider, M.B.; Kumar, R. “Comparative analysis of isopropyl alcohol dehydration using ionic liquids and deep eutectic solvent.” *Journal of Ionic Liquids* 3 (2023) 100069. https://doi.org/10.1016/j.jil.2023.100069.
2. **Gomey, A.K**.; Haider, M.B.; Kumar, R. “Designing of energy-efficient deep eutectic solvents for CO_2 capture: Insights from physical and thermodynamic property evaluation.” *Journal of Molecular Liquids* 434 (2025) 127996. https://doi.org/10.1016/j.molliq.2025.127996.
3. **Gomey, A.K.;** Singh, S.K.; Haider, M.B.; Kumar, R. “Rational Design of Deep Eutectic Solvents for CO_2 Capture: Integrated Experimental Analysis and Machine Learning-Guided Screening.” Energy & Fuels (2026). https://doi.org/10.1021/acs.energyfuels.6c01833.
4. **Gomey, A.K**.; Prajapati, A.K.; Tripathi, M.M.; Haider, M.B.; Kumar, R. "Engine Performance and Emission Study of Biodiesel Produced from Azadirachta Indica Oil and Deep Eutectic Solvents." Revision Submitted in *Biomass Conversion and Biorefinery*
5. **Gomey, A.K**.; Medara, S.; Singh, S.K.; Haider, M.B.; Kumar, Sharma, T.; R. “Revisiting the evaluation of CO_2 capture: From amines to ionic liquids and deep eutectic solvents.” Under Review in *ACS Industrial & Engineering Chemistry Research*

List of other Publications and Manuscripts in Progress

1. Prajapati, A.K.; Yadav, S.; **Gomey, A.K**.; Choubey, A.K.; Kumar, R. "Assessment of performance and emission characteristics of CI engine using tyre pyrolysis oil and biodiesel blends by nano additives: An experimental study." Journal of the Energy Institute (2024) 101825.
2. Jha, D.; **Gomey, A.K.**; Kumari, G.; Maheshwari, P.; Haider, M.B.; Kumar, R.; Balathanigaimani, M.S.; Sahu, J.N.. "A review on the role of nanocomposites for desulfurization of liquid transportation fuels." Journal of Environmental Management 375 (2025) 124255.
3. Prajapati, A.K.; **Gomey, A.K.**; Dwivedi, D.; Kumar, R. "Evaluating the performance of batch, tubular coiled and coil flow invertor reactors in biodiesel production from karanja and used cooking oil." Chemical Engineering and Processing - Process Intensification 215 (2025) 110375.
4. Atal, S.; Sharma, S.; **Gomey, A.K.;** Ali, S.S.; Kumar, R.; Dwivedi, D.; Singh, B.P. "Experimental Evaluation of CO_2 Absorption and Thermophysical Properties of TBAB-Based Deep Eutectic Solvents with Amine and Acid Donors." C 12(1) (2026) 28.
5. **Gomey, A.K.**; Shukla, K.; Haider, M.B.; Kumar, R. "Comparative Assessment of Aromatic Hydrocarbon Separation from Low-Aromatic Naphtha Using Conventional Solvents and Ionic Liquids." Submitted in Chemical Engineering Research and Design.
6. Patel, A.; **Gomey, A.K.**; Kumar, R.; Singh, A. "Energy integration in ammonia cracking for hydrogen production: Product stream utilization as feed preheater." Manuscript in progress.
7. **Gomey, A.K.**; Ali, S.S.; Mohammad, A.; Dwivedi, D.; Kumar, M.; Kumar, R. "Effect of deep eutectic solvents on electrode degradation and electrochemical performance: In name of fuel-cell battery." Manuscript in progress.
8. Pandey, S.; **Gomey, A.K.**; Kumar, R.; Ranjan, A. "DES assisted Cu-doped $ZnTiO_3$ for photocatalytic applications." Manuscript in progress.
9. Patel, A.; **Gomey, A.K.**; Kumar, R.; Balathanigaimani, M.S.; Singh, A. "Energy Integration in Ammonia Cracking for Hydrogen Production by Product Stream Utilization." Manuscript in progress.

10. Ali, S.S.; Prajapati, A.K.; Ansari, K.B.; Anwer, S.; **Gomey, A.K.**; Al-Mesfer, M.K.; Khan, M.S.; Raheman, S.A.R.; Shah, M.; Danish, M.; Kumar, R.; Shkir, M. "Evaluating Deep Eutectic Solvents: Property Framework, Emerging Applications, Mechanistic Insights, Machine Learning, Economics, Challenges and Future Perspectives." Submitted in Separation and Purification Technology
11. Abuzar, M.; Ali, S.S.; **Gomey, A.K.**; Haider, M.B.; Kumar, R.; Yusuf, M. "Optimizing Microwave Drying Efficiency of Apples through Power Variation and Geometrical Design." Manuscript in progress.

Book Chapters

1. Gomey, A.K.; Kumari, G.; Medara, S.; Haider, M.B.; Kumar, R. "Amine-Based CO_2 Capture from a Petrochemical Complex." Submitted to Wiley.
2. Pandey, S.K.; Gomey, A.K.; Haider, M.B.; Kumar, R. "Carbon-Based Materials in Biofuel Generation." Submitted to Springer (ISBN:978-3-032-18643-0).
3. Sharma, C.; Gomey, A.K.; Haider, M.B.; Kumar, R. "Solvents for CO_2 Capture." Manuscript in progress.

List of Conferences and Achievements

1. International Conference on “Technological Interventions for Promoting Sustainability” (CHEMCONFLUX22) - Motilal Nehru National Institute of Technology, Allahabad & Universiti Sains Malaysia, Pinang; April 14-16, 2022, **(2nd Prize Winner).**
2. International Conference on “Sustainability in Chemical Processes through Digitalization, Artificial Intelligence and Green Chemistry” (CHEMCON22) - Indian Institute of Chemical Engineers; December 27-30, 2022.
3. International Conference on “Trends in Energy and Environmental Research for Sustainable Development” (TEERSD-2023) - Guru Ghasidas Vishwavidyalaya, Bilaspur; November 2-3, 2023.
4. International Conference on “Energy Transition: Challenges & Opportunities” (CHEMCON23) - Indian Institute of Chemical Engineers; December 27-30, 2023.
5. International Conference on “Catalyzing Sustainable Future with Affordable Energy and Chemicals” (SEFCO-2025) - CSIR-IIP Dehradun; April 23-25, 2025.

List of Workshops Trainings & Webinars

1. Symposium on Ionic Liquids and Deep Eutectic Solvents with Nature
   Organized by IIT Guwahati | March 10–13, 2021
2. Workshop on Research Related Solutions for Faculty and Research Scholars
   Conducted by RGIPT, Jais | January 1 – February 4, 2022
3. Workshop on Optimization in Oil & Gas and Chemical Industry
   Organized by RGIPT, Jais | February 7–11, 2022
4. Workshop on Characterization Technique of Material and Devices
   Held by CSIR–NPL, New Delhi | March 14–15, 2022
5. Workshop on Application of Optimization Techniques in Engineering (AOTE)
   Conducted by AMU, Aligarh | March 28 – April 1, 2022
6. Webinar on Teachings of Chemical Process Design (by Prof. Warren D. Seider and Prof. Daniel R. Lewin)
   Organized by PSE for SPEED | June 17 – September 22, 2022
7. Project on Introduction to Data Analysis using Microsoft Excel
   Coursera | August 23, 2022
8. Webinar on Introduction to AI for Managers
   Organized by CloudxLab (IIT Roorkee) | September 22, 2022
9. Workshop on Python for Beginners (OLC10052)
   Organized by NIELIT Calicut | August 10–14, 2023
10. Online Training Program on Development of eContent: Interactive Resources
    Organized by CIET, NCERT | July 24–28, 2023
11. Webinar on Accelerate to Net Zero: Digital Technologies for CCUS
    Conducted by Chemical Engineering Webinars | August 8, 2023
12. Workshop on Machine Learning using Python (OLC11451)
    Organized by NIELIT Calicut | September 18–22, 2023
13. Workshop on Introduction to MATLAB & Simulink
    Organized by NIELIT Calicut | September 10–14, 2023
14. Webinar on Contaminants of Emerging Concern
    Conducted by Remtech Europe | September 21, 2023
15. Training Course on ACS Author Lab
    Conducted by ACS | May 14, 2024
16. Training Course on ACS Reviewer Lab
    Conducted by ACS | May 14, 2024
17. Workshop on Sustainability Fundamentals: Process Modeling CO_2 Capture & H_2 Production
    Organized by AspenTech University | March 27, 2025